

NIST  
PUBLICATIONS

**NISTIR 5362**

**NIST REACTOR:  
Summary of Activities  
October 1992 through  
September 1993**

U.S. DEPARTMENT OF COMMERCE  
Technology Administration  
National Institute of Standards  
and Technology  
Reactor Radiation Division  
Materials Science and Engineering Laboratory  
Gaithersburg, MD 20899

QC  
100  
.U56  
NO. 5362  
1994





NISTR C  
QC100  
457531  
1992/93  
C.2

**NIST REACTOR:  
Summary of Activities  
October 1992 through  
September 1993**

U.S. DEPARTMENT OF COMMERCE  
Technology Administration  
National Institute of Standards  
and Technology  
Reactor Radiation Division  
Materials Science and Engineering Laboratory  
Gaithersburg, MD 20899

February 1994



**U.S. DEPARTMENT OF COMMERCE**  
**Ronald H. Brown, Secretary**  
**TECHNOLOGY ADMINISTRATION**  
**Mary L. Good, Under Secretary for Technology**  
**NATIONAL INSTITUTE OF STANDARDS**  
**AND TECHNOLOGY**  
**Arati Prabhakar, Director**



## FOREWORD

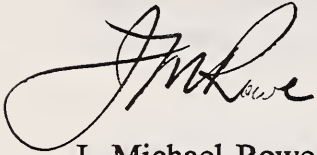
This is the second year for the revised format for the annual report of activities at the NIST Research Reactor. The general reaction to last year's report has encouraged us to continue in this format, but we welcome suggestions for change. Once again, we are including lists of research topics, with affiliations, in lieu of short reports on all topics. In this respect, it should be noted that many of the topics are generic, and represent several "experiments", on different materials or under different sample conditions. Further information may be obtained by writing either directly to the authors, or to Mrs. Carol O'Connor, who will forward your request to the appropriate person.

In spite of a number of problems, the reactor has established a good operating record over the past year, with high reliability (percentage of scheduled time actually operated) and availability (percentage of real time operated). The planning and preparation for the extended shutdown for heat exchanger replacement is on track, with all components either on site or being fabricated. In addition to the heat exchanger replacement, the shim control arms will be replaced and the heavy water will be exchanged during this shutdown, along with a large number of smaller maintenance items. Following this shutdown, the reactor should operate routinely at 20 MW for several years. The start date for the shutdown will be between March 17 and May 20, 1994, with the exact date determined by the availability of all items required to complete the work (including the experimental changes discussed below). The duration of the shutdown is estimated to be between 6 and 9 months.

The science program has made excellent use of the opportunities provided by the performance of the reactor. Among a large number of possible highlights included in the body of the report, I would call special attention to three. The new powder diffractometer is a spectacular success, providing the prototypical free lunch—better resolution with much higher intensity and the number of experiments has grown at an extraordinary pace. The 30 m SANS spectrometers developed primarily for the study of macromolecules and microstructure for materials science, have performed with outstanding success. However, it also makes possible forefront condensed matter physics, as exemplified by the studies of the symmetry and dynamics of flux lattices in superconductors. Finally, the use of a reflectometer to elucidate the origin of the two length scales in the phase transition in Tb illustrates once again that instrument development can drive science, as well as *vice versa*. The unifying theme in all three examples is the close interplay between forefront research and instrument development—both are essential.

In the cold neutron project, three critical milestones were successfully met in the past year. First, the safety case for the liquid hydrogen source has been made successfully, fabrication is near completion, and only local approval is required for final installation. Second, the cold neutron reflectometer is now on line, already oversubscribed, and producing outstanding results on a broad variety of problems. Finally, construction was begun on the final instrument for the CNRF—the spin echo spectrometer—with joint participation of Exxon Research and Engineering and KFA, Jülich. After the scheduled shutdown, with the new source installed and the reactor at 20 MW, researchers at the CNRF can look forward to greatly improved performance (approximately five times better).

In summary, the past year has highly successful, with many gains in every area. As we look forward to the coming year, with its multiple challenges and opportunities, we believe that the successes of the year reported here will be the harbinger of the future.

A handwritten signature in black ink, appearing to read "J. Michael Rowe". The signature is fluid and cursive, with a large initial "J" and "M".

J. Michael Rowe  
Chief  
Reactor Radiation Division

## **ABSTRACT**

This report summarizes all the programs which use the NIST reactor. It covers the period for October 1992 through September 1993. The programs range from the use of neutron beams to study the structure and dynamics of materials through nuclear physics and neutron standards to sample irradiations for activation analysis, isotope production, neutron radiography, and nondestructive evaluation.

**KEY WORDS:** activation analysis; cold neutrons; crystal structure; diffraction; isotopes; molecular dynamics; neutron; neutron radiography; nondestructive evaluation; nuclear reactor; radiation.

## **DISCLAIMER**

Certain trade names and company products are identified in order to adequately specify the experimental procedure. In no case does such identification imply recommendation or endorsement by the National Institute of Standards and Technology, nor does it imply that the products are necessarily the best available for the purpose.





## CONTENTS

<b>FOREWORD</b> .....	<b>iii</b>
<b>ABSTRACT</b> .....	<b>v</b>
<b>CHEMICAL PHYSICS OF MATERIALS</b> .....	<b>1</b>
Fullerenes and Fullerides .....	1
Hydrogen in Solids .....	6
Low Energy Excitations in Glasses .....	10
<b>MAGNETISM AND SUPERCONDUCTIVITY</b> .....	<b>15</b>
Thin Films and Multilayers .....	15
Oxide Systems .....	17
Superconductivity .....	20
<b>CRYSTALLOGRAPHY</b> .....	<b>26</b>
Instrumentation .....	26
Crystal Structures .....	27
The Structure of $\text{La}_3\text{Ti}_5\text{Al}_{15}\text{O}_{37}$ .....	29
Technique Development .....	29
Diffraction Data Center .....	31
<b>SURFACE AND INTERFACIAL STUDIES</b> .....	<b>35</b>
Magnetic Systems .....	35
Ti Oxidation and Dissolution In Situ .....	39
Anomalous Critical Scattering in Tb .....	40
Polymer Systems .....	42
<b>MACROMOLECULAR AND MICROSTRUCTURE STUDIES</b> .....	<b>49</b>
Inorganic Materials .....	49
Biology .....	53
Polymers .....	54
<b>NEUTRON BEAM APPLICATIONS</b> .....	<b>61</b>
Neutron Diffraction Measurement of Residual Stress .....	61
Neutron Diffraction Measurement of Texture .....	65
Neutron Autoradiography of Paintings .....	67
<b>ANALYTICAL CHEMISTRY</b> .....	<b>71</b>
Nuclear Methods Group .....	71
Smithsonian Institution .....	77
Food and Drug Administration .....	78
University of Maryland .....	79
Federal Bureau of Investigation .....	81

<b>NEUTRON METROLOGY AND DOSIMETRY</b> .....	<b>85</b>
Neutron Fields and Standards .....	85
Fundamental Neutron Physics .....	87
<b>POLYMERS DIVISION PROGRAMS</b> .....	<b>89</b>
Equilibrium Phase Behavior .....	89
Kinetics of Phase Separation .....	91
Effect of Flow Field .....	91
Interfacial Characterization, Modification, and Phase Separation with Reaction .....	93
<b>EXXON SANS RESEARCH AT THE CNRF</b> .....	<b>95</b>
Polymers .....	95
Fluids and Microemulsions .....	98
Neutron Tomography/Radiography .....	99
<b>UNIVERSITY OF MINNESOTA PROGRAMS</b> .....	<b>100</b>
SANS .....	100
Reflectometry .....	102
<b>CNRF INSTRUMENTATION DEVELOPMENT</b> .....	<b>104</b>
New Instruments .....	104
Other Instrumentation .....	106
The Hydrogen Cold Source .....	108
<b>GUEST RESEARCHERS AND COLLABORATIONS</b> .....	<b>111</b>
<b>REACTOR OPERATIONS AND ENGINEERING</b> .....	<b>114</b>
<b>PERSONNEL ROSTER</b> .....	<b>115</b>
Staffing .....	115
Research and Engineering Staff .....	118
Technical Staff .....	122
<b>PUBLICATIONS</b> .....	<b>123</b>

## CHEMICAL PHYSICS OF MATERIALS

Research at the NBSR which falls into this category typically involves inelastic neutron scattering measurements of the dynamics of molecular solids, various inclusion compounds, and structurally disordered materials. These studies yield detailed information on the atomic and molecular interactions responsible for many properties of these systems. For cases involving either rotational excitations or hydrogen motions or both, this information is difficult, if not impossible, to obtain by other means. Furthermore, since thermal neutron wavelengths are comparable to interatomic spacings, one is able to ascertain the geometry of the various motions in a way unmatched by other spectroscopic probes. Each of these attributes is featured in one or more of the examples that are highlighted here.

### Fullerenes and Fullerides

- **Rotational Dynamics and the Orientational Potential in  $A_3C_{60}$  Compounds**

There continues to be intense interest in understanding the structure, molecular potentials, and phase transitions in fullerenes and newly synthesized compounds and molecular derivatives based on them.

The alkali-metal fullerides  $A_3C_{60}$  ( $A = K, Rb$ ) crystallize in a face-centered-cubic (fcc) structure in which the alkali metal ions occupy the two tetrahedral and one octahedral sites per  $C_{60}$  ion. The molecules randomly adopt one of two different orientations that are energetically identical and related to one another by a  $90^\circ$  rotation about one of the Cartesian axes as shown in figure 1 (space group  $Fm\bar{3}m$ ) [1]. In contrast to pristine  $C_{60}$ , where an orientational order-disorder transition is encountered at 260 K [2], these compounds remain orientationally ordered at temperatures close to the decomposition temperature [3]. The sodium fullerides  $Na_2CsC_{60}$  [4] and  $Na_2RbC_{60}$  [5], on the other hand, are isostructural with  $C_{60}$ , adopting an orientationally ordered simple cubic (sc) structure (space group  $Pa\bar{3}$ ) at low temperature. Furthermore the latter compounds transform on heating to a fcc orientational "liquid" phase (space group  $Fm\bar{3}m$ ) [4,5]. As in pure  $C_{60}$ , inelastic neutron scattering probes the orientational potentials

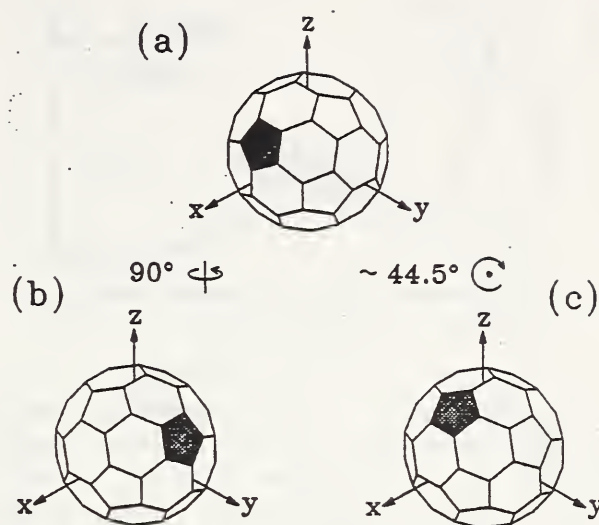


**Figure 1.** Three possible orientations of a  $C_{60}$  in  $A_3C_{60}$  ( $A = K$  or  $Rb$ ), with respect to a fixed set of crystallographic axes. The plane of the drawing is normal to the  $[111]$  direction. The transformation from (a) to (b) involves a  $90^\circ$  rotation about the  $[001]$  direction. The transformation from (a) to (c) involves a  $\sim 44.5^\circ$  rotation about the  $[111]$  direction. One of the pentagons is shaded to illustrate these rotations. The two distinct orientations in this figure are normally called "standard orientations."

which secure these structures, providing information as to how the intermolecular potential in fullerides is modified by intercalation of alkali ions.

Representative spectra for  $Rb_{2.6}K_{0.4}C_{60}$ ,  $K_3C_{60}$ ,  $Na_2RbC_{60}$ , and  $C_{60}$  are shown in figure 2. In each case the symbols are the experimental data, the solid line is the total fit, and the dashed line is the librational component which is represented by a Lorentzian. The librations soften on going from  $Rb_{2.6}K_{0.4}C_{60}$  to  $C_{60}$  and the peak librational energy in  $Na_2RbC_{60}$  is closer to  $C_{60}$  than to  $K_3C_{60}$ . In each case the peak width is not resolution-limited, but the peaks are much broader for the alkali-doped systems than for pure  $C_{60}$ . This is probably due to greater dispersion of the librational branches and to larger anisotropies in the orientational potential. Single crystal measurements are required to ascertain which of these effects is the more important.

An estimate of the rotational barrier in these systems can be obtained assuming that a simple sinusoidal hindrance potential is sufficient to

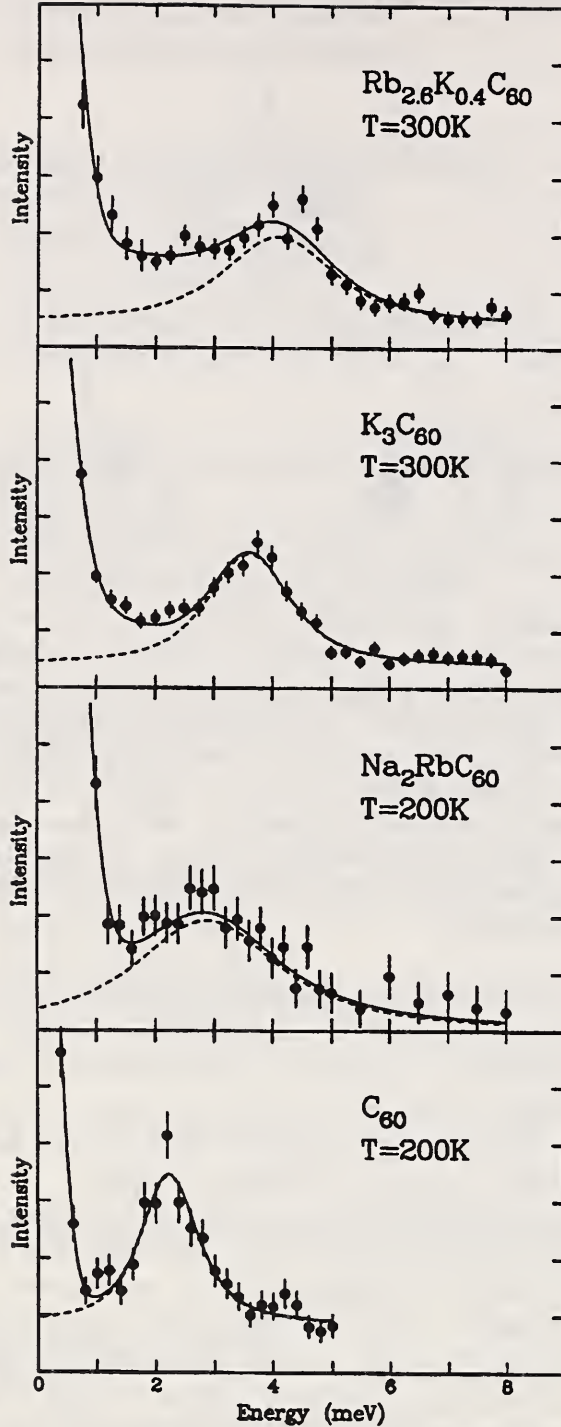
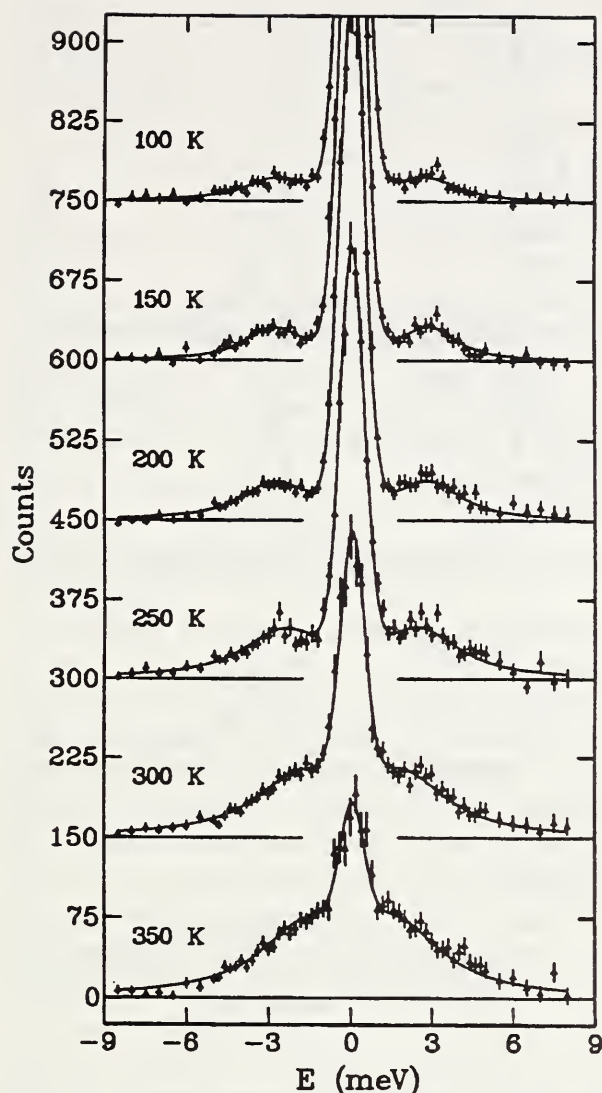


Figure 2. Inelastic neutron scattering spectra for  $\text{Rb}_{2.6}\text{K}_{0.4}\text{C}_{60}$ ,  $\text{K}_3\text{C}_{60}$ ,  $\text{Na}_2\text{RbC}_{60}$ , and  $\text{C}_{60}$  at  $Q \sim 5.7 \text{ \AA}^{-1}$ .

describe the orientational potential [2,6]. For small amplitudes of libration,  $E_a = (E_{\text{lib}}^2/B) \cdot (\Theta/2\pi)^2$ , where  $E_a$  is the potential barrier,  $\Theta$  is the hopping angle between neighboring potential minima,  $B = 0.364 \times 10^3 \text{ meV}$  is the rotational constant for  $\text{C}_{60}$ , and  $E_{\text{lib}}$  is the librational energy. From figure 1, we see that there are two possible jump mechanisms for the merohedrally disordered

systems  $\text{Rb}_{2.6}\text{K}_{0.4}\text{C}_{60}$  and  $\text{K}_3\text{C}_{60}$ . The first involves  $90^\circ$  jumps about one of the twofold molecular axes that are aligned along the crystallographic axes. The second is a  $\sim 44.5^\circ$  jump about one of the threefold molecular axes that is aligned along a  $\langle 111 \rangle$  direction. Using the librational energy of the  $\text{C}_{60}$ 's in  $\text{K}_3\text{C}_{60}$  at 300 K (3.5 meV), we find that  $E_a$  is roughly 520 meV for  $\sim 44.5^\circ$  jumps and 2050 meV for  $90^\circ$  jumps. NMR results [7] on  $\text{K}_3\text{C}_{60}$  show that molecular reorientations occur through large angles with an activation energy of  $(460 \pm 60) \text{ meV}$ , in good agreement with one of the above estimates. Thus the neutron scattering results clearly favor the more physically reasonable model of  $\sim 44.5^\circ$  jumps about threefold axes. It is worth noting that recent 2D NMR measurements [7] suggest that jumps through a smaller angle must also be present. It is also intriguing to note that the principal orientation of the  $\text{C}_{60}$  molecules in the low temperature phase of pure  $\text{C}_{60}$  is approximately halfway between the two possible orientations of the  $\text{C}_{60}$  ions in  $\text{K}_3\text{C}_{60}$  when the molecule is rotated about a  $\langle 111 \rangle$  axis. Perhaps this orientation corresponds to a local minimum in the orientational potential of the  $\text{C}_{60}$ 's in  $\text{K}_3\text{C}_{60}$  as well as to the global minimum in pure  $\text{C}_{60}$ .

Figure 3 shows representative spectra for the sodium fulleride  $\text{Na}_2\text{RbC}_{60}$  at temperatures between 100 and 350 K with  $Q = 5.5 \text{ \AA}^{-1}$ . Well-defined peaks are observed at all temperatures at non-zero energy transfer, and the  $Q$  dependence of the integrated intensities of these peaks leads us to assign them to librational modes of the  $\text{C}_{60}$  ions [8]. The peaks also soften and broaden appreciably as the sample is warmed to 350 K, the maximum temperature of the measurements, and the elastic line has almost completely disappeared by this temperature. The situation is much more reminiscent of solid  $\text{C}_{60}$ , where the full widths of the librations increase by a factor of six [9] on approaching the phase transition (at which temperature they collapse into a single quasielastic line), than of  $\text{Rb}_{2.6}\text{K}_{0.4}\text{C}_{60}$  or  $\text{K}_3\text{C}_{60}$ , where the widths show little change with temperature. These results suggest that  $\text{Na}_2\text{RbC}_{60}$  undergoes an orientational melting transition somewhat above 350 K. This conclusion is consistent with high resolution X-ray diffraction results [5] in which the simple cubic reflections are absent above 400 K. Thus in all respects, except perhaps its isotropy,



**Figure 3.** Representative NIS spectra of  $\text{Na}_2\text{RbC}_{60}$  in the temperature range 100-300 K at constant  $Q = 5.5 \text{ \AA}^{-1}$ . The solid triangles are experimental points and the solid lines are best fits, including a Lorentzian component at non-zero energy transfer.

the orientational potential in  $\text{Na}_2\text{RbC}_{60}$  seems more like that of  $\text{C}_{60}$  than that of  $\text{Rb}_{2.6}\text{K}_{0.4}\text{C}_{60}$  or  $\text{K}_3\text{C}_{60}$ .

The origin of this difference is demonstrated in figure 4 where the measured low temperature librational energies for different fullerides (and  $\text{C}_{60}$ ) are displayed as a function of the ionic radius of the tetrahedral alkali ion. The dashed line at  $1.12 \text{ \AA}$  corresponds to the size of the tetrahedral site in pristine  $\text{C}_{60}$ . When the radius of the tetrahedral ion ( $r_A$ ) is less than this value, the librational energy is roughly constant at  $\sim 2.8 \text{ meV}$ , but when  $r_A > 1.12 \text{ \AA}$ , the energy increases with the size of the ion. Since the size

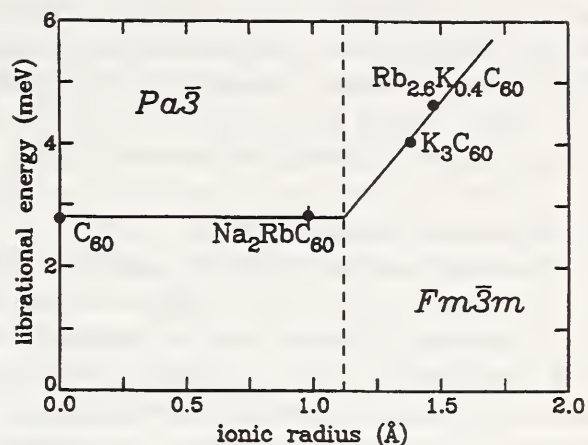


**Figure 4.** Schematic diagram showing the dependence of the librational energy at low temperature on the ionic radius of the alkali ions occupying the tetrahedral interstices in  $\text{A}_3\text{C}_{60}$  fullerides. The dashed line at  $1.12 \text{ \AA}$  corresponds to the size of the tetrahedral hole in pristine  $\text{C}_{60}$  and separates simple cubic ( $\text{Pa}\bar{3}$ ) from fcc ( $\text{Fm}\bar{3}m$ ) solids.

of the ion plays a crucial role in determining the librational energy, the repulsive  $\text{A}^+\text{-C}$  interactions must dominate the orientational potential for fcc merohedrally disordered fullerides. This strong repulsive interaction results in a harder intermolecular potential [2] than in pristine  $\text{C}_{60}$  [8], in which the weaker C-C interactions favor "nesting" of the bonds that fuse hexagons opposite pentagonal (or hexagonal) faces of adjacent molecules [3]. Furthermore, this interaction is minimized by maximizing the A-C distances as the  $\text{C}_{60}$  ions present hexagonal faces to the tetrahedral sites. In  $\text{Na}_2\text{RbC}_{60}$  (and presumably in  $\text{Na}_2\text{CsC}_{60}$ ), the repulsive  $\text{A}^+\text{-C}$  interaction is substantially diminished due to the smaller size of the  $\text{Na}^+$  ion, and it no longer restricts the  $\text{C}_{60}$  ions to the two orientations found in  $\text{K}_3\text{C}_{60}$  and  $\text{Rb}_3\text{C}_{60}$  (Fig. 1). The Coulomb part of the interaction then gains in relative importance [10], leading to the observed  $\text{Pa}\bar{3}$  structure, in which each  $\text{C}_{60}$  ion presents two hexagonal faces and six hexagon-hexagon bonds to its eight neighboring  $\text{Na}^+$  ions. At this same orientation, the  $\text{C}_{60}\text{-C}_{60}$  interactions are also optimized by the nesting of a hexagon-hexagon bonds in the pentagons of the neighboring molecules. The net result is an intermolecular potential, and therefore librational energy, that is comparable with that of pristine  $\text{C}_{60}$ . There is also a substantial decrease in the librational mode energy in  $\text{Na}_2\text{RbC}_{60}$  with increasing temperature,

reflecting considerable softening of the orientational potential, as the interactions become disrupted by increasing amplitudes of libration. This effect is again comparable with the effect in pristine  $C_{60}$ , but markedly larger than in  $K_3C_{60}$ .

#### • Rotational Dynamics of $C_{70}$

X-ray and neutron diffraction measurements on the fcc phase [11,12] of the higher fullerene  $C_{70}$  led to the identification of a well-defined transition to a rhombohedral phase with little change in the unit cell dimension and a rhombohedral angle of  $\sim 85.6^\circ$ . This suggests that the long molecular axis is aligned along the unit cell diagonal. This phase must have uniaxial orientational disorder since the long molecular axis has fivefold symmetry which is incompatible with the  $\bar{3}$  symmetry of the unit cell diagonal. At even lower temperatures, the crystallographic symmetry is found to be monoclinic. In this case, symmetry considerations allow the molecules to lock into a fully orientationally ordered phase.

To investigate the low energy rotational dynamics of  $C_{70}$  we have made neutron scattering measurements on a  $\sim 0.5$  g sample using the BT-4 spectrometer. In figure 5 we show representative spectra at temperatures between 100 and 640 K with  $Q = 5.6 \text{ \AA}^{-1}$ . At all temperatures the  $Q$ -dependence of the energy-integrated scattering intensity implies that the observed scattering is due to rotational motion of the molecules [8,13]. In a situation reminiscent of  $C_{60}$ , librational behavior is observed at temperatures below the orientational ordering transition near 270 K (Figs. 5a and 5b), whereas we find no evidence for this type of motion at and above room temperature (Figs. 5c and 5d). Instead the higher temperature spectra are well described at all  $Q$  by a quasielastic component which is much broader than the instrumental resolution, suggesting that the fullerene molecules are undergoing some form of rotational diffusion at these temperatures.

In spite of the qualitative similarity, there are quantitative differences between our observations for  $C_{60}$  and  $C_{70}$ . For instance, the low temperature librational energy in  $C_{70}$  (1.8 meV at 10 K) is much lower than in  $C_{60}$  (2.8 meV at 20 K). Furthermore the observed full widths are substantially larger in  $C_{70}$  than in  $C_{60}$  (1.8(5) and 0.4(2) meV at 10 and 20 K respectively), and they

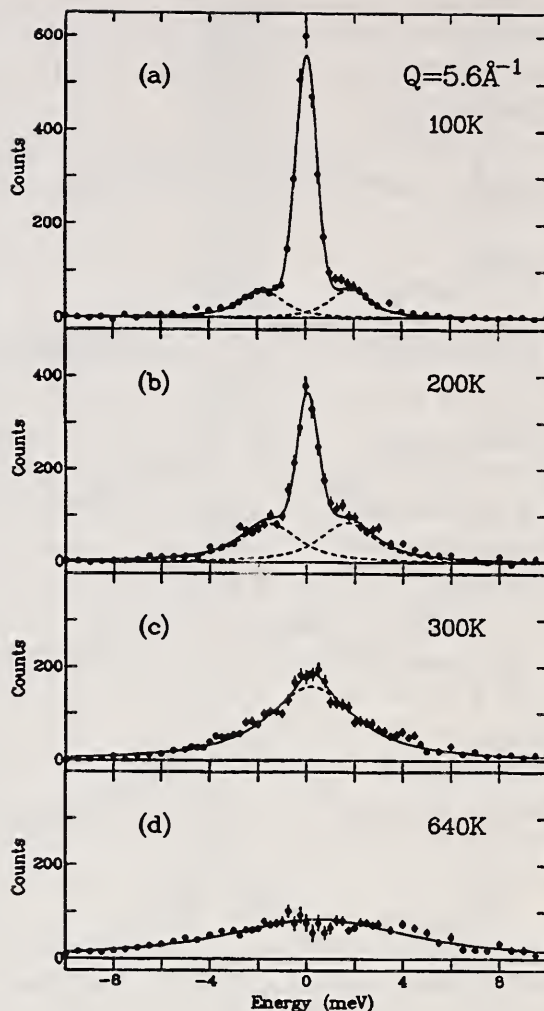


**Figure 5.** Representative inelastic neutron scattering spectra for  $C_{70}$  at constant  $Q = 5.6 \text{ \AA}^{-1}$ : (a)  $T = 100$  K, (b)  $T = 200$  K, (c)  $T = 300$  K, and (d)  $T = 640$  K. The solid circles are experimental points and the solid lines are best fits. The dashed lines show the individual Lorentzian components of the fits.

change less with temperature. The difference in moments of inertia between  $C_{60}$  ( $I = 1.0 \times 10^{-43} \text{ kg m}^2$ ) and  $C_{70}$  ( $I_{||} = 1.24 \times 10^{-43}$  and  $I_{\perp} = 1.44 \times 10^{-43} \text{ kg m}^2$ ) is insufficient to explain the difference in the observed low temperature librational energies, and the difference in  $I_{||}$  and  $I_{\perp}$ , the moments of inertia of the  $C_{70}$  molecule about axes parallel and perpendicular to the fivefold axis, does not by itself account for the observed widths. Thus the orientational potential must be softer and more anisotropic for  $C_{70}$  than for  $C_{60}$ .

These results can also be compared directly to molecular dynamics calculations, providing a stringent test of various interatomic potentials. For

instance, Cheng and Klein [14] have modeled the intermolecular C-C interactions using a standard Lennard-Jones potential. Their calculation results in a librational density of states which peaks at  $\sim 1.2$  meV and has a width of 0.9 meV, both considerably less than the experimental values. This suggests that the model orientational potential is softer by a factor of 2 than indicated by experiment, again reminiscent of the situation in  $C_{60}$  [9,14] where the calculated orientational potential was too small by a factor of 4. The greater deviation between model calculations and experiment in  $C_{60}$  arises from additional anisotropic contributions to the orientational potential associated with the nesting of short ("double") bonds in the pentagons (or hexagons) of adjacent molecules [2].

At 300 K and above, quasielastic scattering is observed. In an attempt to ascertain the geometry of the motion the coherent scattering function has been calculated assuming each  $C_{70}$  molecule undergoes random-walk isotropic rotational diffusion uncorrelated with the motion of its neighbors. This type of model was first developed by Sears [15] and has been successfully applied to describe the rotational motion of  $C_{60}$  in its plastic phase [8,16]. The geometry of the diffusing molecule is taken into account in calculating the powder-averaged rotational component of the coherent neutron scattering function  $S_R(Q, \omega)$  which is expressed as a sum of Lorentzian functions:

$$S_R(Q, \omega) = \sum_{\ell=1}^{\infty} S_{\ell} \frac{1}{\pi} \frac{\tau_{\ell}}{1 + \omega^2 \tau_{\ell}^2} \quad (1)$$

where

$$S_{\ell} = (2\ell + 1) \cdot \sum_{\nu, \nu'=1}^{70} j_{\ell}(QR_{\nu}) j_{\ell}(QR_{\nu'}) P_{\ell}(\cos \theta_{\nu, \nu'}) \quad (2)$$

$$\tau_{\ell}^{-1} = \ell(\ell + 1) D_{\nu} \quad (3)$$

$j_{\ell}$  are spherical Bessel functions,  $P_{\ell}$  are Legendre polynomials,  $D_{\nu}$  is the rotational diffusion constant, and  $\theta_{\nu, \nu'}$  is the angle between the position vectors  $\mathbf{R}_{\nu}$ ,  $\mathbf{R}_{\nu'}$  joining the molecular center to atoms  $\nu$  and

$\nu'$  within the same molecule. In eq. (1), the only terms that are identically zero because of the symmetry of the  $C_{70}$  molecule are those with  $\ell = 1$  and  $\ell = 3$ .

In figure 6 we show the experimental measurements at 525 K and spectra calculated with  $D_r = 1.5 \times 10^{10} \text{ s}^{-1}$ , convoluted with the instrumental resolution. Note that the only two parameters in this comparison are an overall scale factor and  $D_r$ . In selecting a value for the diffusion constant, the complete lineshape was taken into account rather than simply the full width of the quasielastic line. Clearly there is good, though not perfect, agreement between our 525 K data and the isotropic diffusion model, implying that at this temperature the  $C_{70}$  molecules sample all orientations with essentially equal probability, effectively averaging out the anisotropy of the molecule. It should be noted however that the polycrystalline nature of the sample will tend to mask possible correlations or small anisotropies in the motion.

At 300 K the agreement between the measured spectra and the isotropic diffusion model calculation is less good (Fig. 7). Since the shape of the  $C_{70}$  molecule implies that diffusion about the long symmetry axis should occur at a different rate than that of diffusion of the symmetry axis itself, a model for the rotational dynamics of  $C_{70}$  molecules has been developed in which the motions of adjacent molecules remain uncorrelated but each individual molecule performs diffusive motion only about a fixed molecular axis (which may or may not coincide with the long axis). The powder-average rotational component of the incoherent neutron scattering function is then given by eq. (1), with [15,17]:

$$S_{\ell} = (8\pi) \sum_{L=\ell}^{\infty} \left| \sum_{\nu=1}^{70} J_L(QR_{\nu}) Y_{L\ell}(\hat{\mathbf{R}}_{\nu}) \right|^2 \quad (4)$$

and

$$\tau_{\ell}^{-1} = \ell^2 D_r^u \quad (5)$$

where  $Y_{L\ell}(\hat{\mathbf{R}}_{\nu})$  are spherical harmonics with  $\hat{\mathbf{R}}_{\nu}$  specifies the direction of atom  $\nu$ , and  $D_r^u$  is the uniaxial rotational diffusion constant. If the fixed rotation axis is taken to coincide with the fivefold

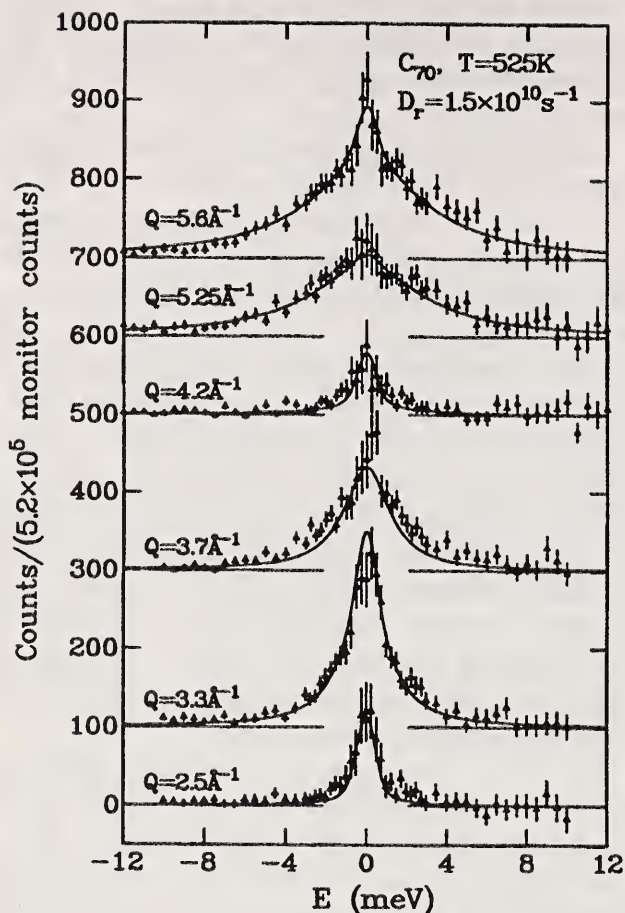


**Figure 6.** Inelastic neutron scattering spectra taken at several values of  $Q$  at 525 K, normalized to the same total monitor count. The solid lines are the calculated spectra convoluted with the instrumental resolution using an isotropic diffusion constant of  $D_r = 1.5 \times 10^{10} \text{ s}^{-1}$ . Note that the only two parameters in this comparison are an overall scale factor and  $D_r$ .

axis of the molecule,  $S_\ell$  is only nonzero when  $\ell$  is an integral multiple of 5. For  $Q \leq 6.5 \text{ \AA}^{-1}$ , contributions from terms with  $\ell > 25$  are essentially negligible.

A detailed comparison between the two models (uniaxial with  $D_r^u = 4.0 \times 10^{10} \text{ s}^{-1}$  and isotropic with  $D_r = 1.0 \times 10^{10} \text{ s}^{-1}$ ) and the experimental data at 300 K is shown in figure 7; the uniaxial model does not describe the experimental data as well as the isotropic model. Discrepancies between the isotropic model predictions and the experimental measurements would perhaps be removed with the introduction of a small amount of anisotropy in the reorientational motion (i.e. introducing two slightly different diffusion constants  $D_{||}$  and  $D_{\perp}$ ), but the present data do not warrant the introduction of a second diffusion parameter. It is

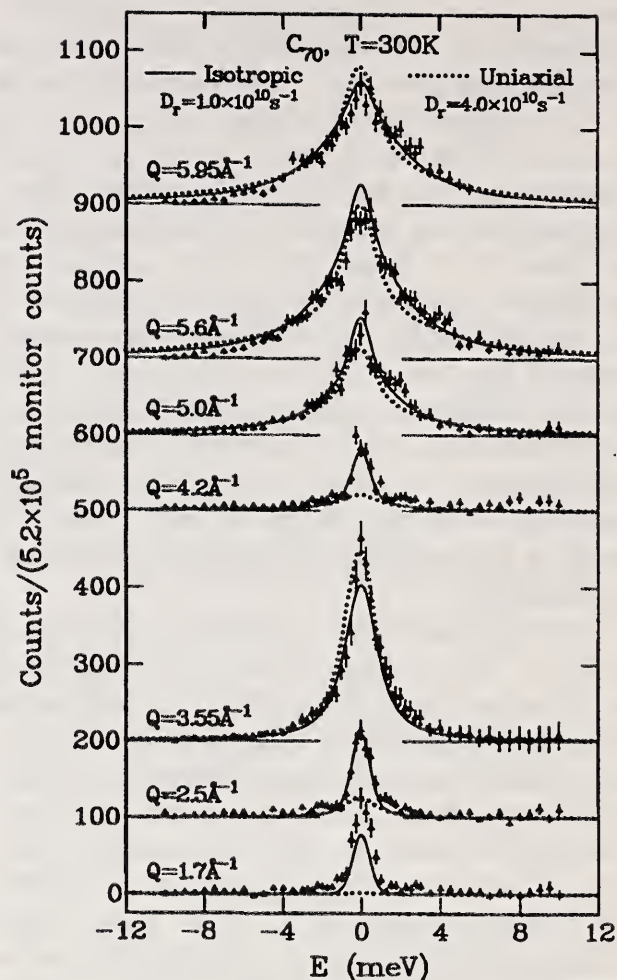


**Figure 7.** Inelastic neutron scattering spectra taken at several values of  $Q$  at 300 K, normalized to the same total monitor count. The solid (dashed) lines are the calculated spectra convoluted with the instrumental resolution using an isotropic (uniaxial) diffusion constant of  $D_r = 1.0 \times 10^{10} \text{ s}^{-1}$  ( $D_r^u = 4.0 \times 10^{10} \text{ s}^{-1}$ ). Note that the only two parameters in this comparison are an overall scale factor and  $D_r$ .

clear that all of the studies on fullerenes and their compounds would be significantly enhanced by the availability of suitably sized single crystals.

## Hydrogen in Solids

### • The Hydration Reaction in Portland Cement

The urgency of renewing the Nation's aging transportation infrastructure has stimulated new interest in the materials science of Portland cement concrete [18], in particular how the material develops its strength as a function of time, chemical composition and ambient environmental conditions. The basic reaction in the formation of



concrete is the hydration of the Portland cement component. The initial anhydrous phase consists primarily of di-calcium silicate, tri-calcium silicate and tri-calcium aluminate, abbreviated in cement chemistry notation by  $C_2S$ ,  $C_3S$ , and  $C_3A$ , respectively. When mixed with water, the  $C_2S$  and the  $C_3S$  react to form calcium silicate hydrate (C-S-H), which has a variable composition, and calcium hydroxide (CH). The  $C_3A$  also reacts very rapidly with water to form CAH. The hydrated compounds appear first as colloidal particles that proceed to link together and eventually form a gel-like structure. The microstructure then determines the properties of the hardened concrete. Although this general process has been known since the time of LeChatelier, the state of the water molecules within the hydrated structure remains uncertain due to the amorphous nature of C-S-H and to the composite nature of concrete. This renders a detailed analysis of diffraction data difficult. We have therefore employed quasielastic neutron scattering (QNS) in order to obtain information on the state of the water molecules as concrete cures.

QNS data were obtained using the BT-2 triple-axis spectrometer. The time required to acquire one scan was typically 3 hours. Measurements were taken continuously for the first three days after mixing. Thereafter, QNS measurements were taken at increasingly longer time intervals. The final data set was acquired 245 days after the specimen had been prepared. The data were fitted to a sum of a Gaussian function,  $G$ , having a resolution-limited width and a Lorentzian,  $L(\Gamma)$ , of width  $\Gamma$  convoluted with the instrumental resolution. Thus the scattering function is given by

$$S_{inc}(Q, \omega) = A \cdot G + B \cdot L(\Gamma). \quad (6)$$

The values of the coefficients  $A$  and  $B$  are directly proportional to the amount of the bound and free water molecules in the specimen respectively. Consequently, this provides a simple index for the amount of bound water in concrete [19]:

$$I = \frac{A}{A+B}. \quad (7)$$

Note that bound water refers either to water molecules immobilized in the C-S-H or to water that is incorporated into the structure as OH.

Figure 8 shows the QNS spectra for early, middle, and late stages of the hydration reaction.

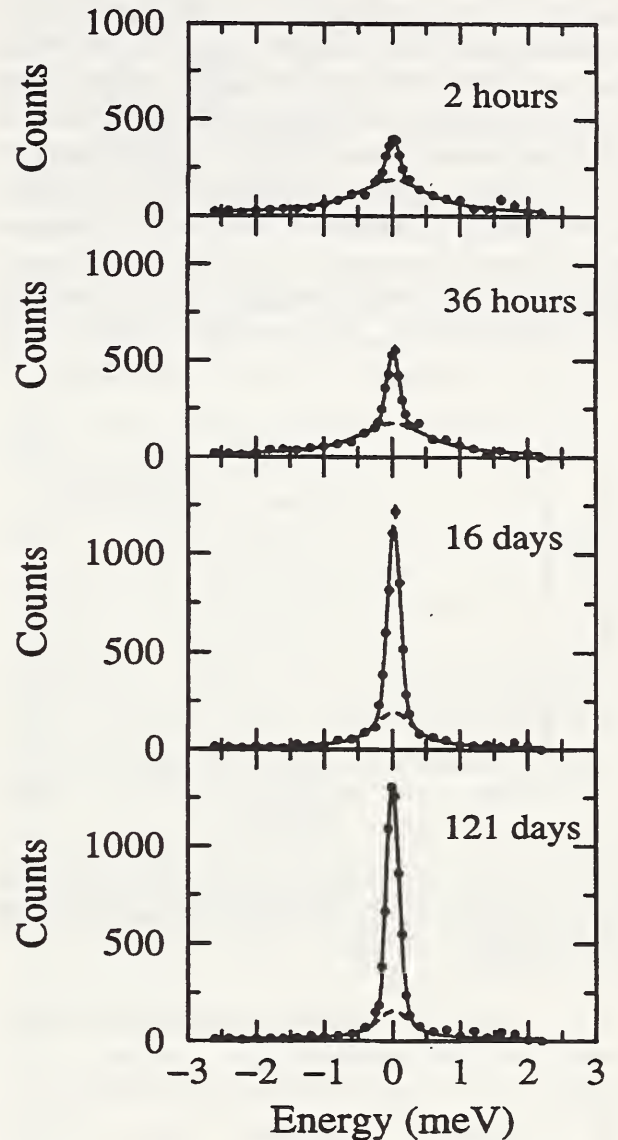


**Figure 8.** Quasielastic neutron scattering spectra at  $Q = 2.25 \text{ \AA}^{-1}$  for Portland cement at various times after mixing. The solid line is the total fit to the data while the dashed line is the Lorentzian component. It is clear that the hydrogen becomes immobilized as a function of time.

Here the symbols represent the data, the dashed line is the Lorentzian component, and the solid line is the total fit. As the hydration reaction proceeds, the major contributor to the intensity shifts dramatically from the Lorentzian to the Gaussian component, clearly demonstrating that the water is becoming immobilized. Furthermore, the width of the Lorentzian component decreases over time,

showing that the timescale of the motion of the remaining unbound water is increasing.

The bound water index is displayed as a function of time in figure 9. For the first day this remained essentially constant at  $\sim 20\%$ , indicating that very little hydration was taking place. After 16 days, however, the reaction has progressed to the point where about 50% of the hydrogen has become bound, and after 90 days, the bound water index reaches a plateau of 70%, which indicates that the hydration reaction has essentially stopped. Thus the majority of the water reacts during the first month, but after the first day.

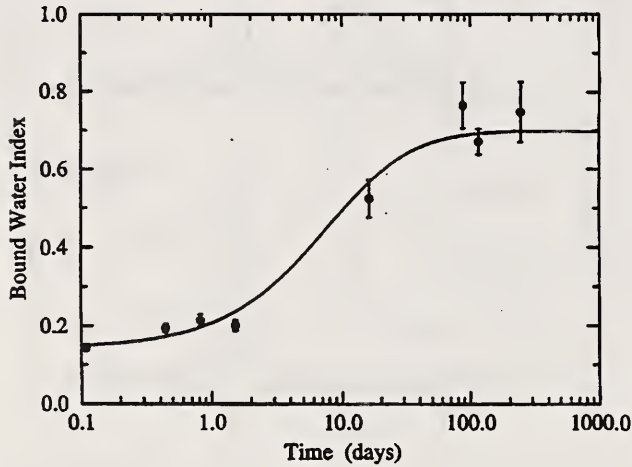


Figure 9. The bound water index as function of time for the hydration reaction of Portland cement. The solid line is a guide to the eye.

In contrast to conventional methods, information on the submicroscopic character of the motion of the water molecule can be obtained from the  $Q$ -dependence of the data. Figure 10 shows the width of the Lorentzian function as a function of  $Q^2$  for the fresh sample. The initial slope of this curve is  $D$ , the diffusion constant. The value of  $D = (3.1 \pm 0.5) \times 10^{-9} \text{m}^2/\text{s}$  is consistent with that of liquid water [20]. Thus in the early stages of hydration the water content actually behaves as though it were bulk water. However, after 116 days the width of the Lorentzian function is more nearly constant, implying that the remaining unbound water is no longer diffusing freely. Instead the water molecules move in a restricted fashion which could be either rotation or limited translation, or a combination of the two.

To distinguish between these two possibilities, the intensity of the elastic peak,  $A$ , is shown as a function of  $Q$  in figure 11 for the data at 245 days.

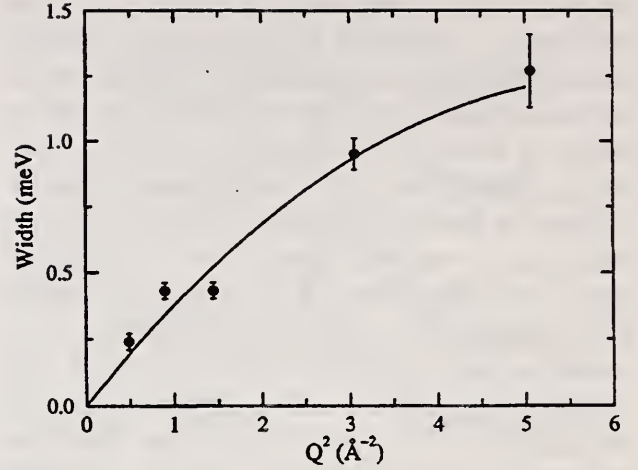


Figure 10. The width of the Lorentzian component as a function of  $Q$  immediately after mixing. The initial slope gives the diffusion constant which is comparable to that of bulk water.

By this time, the  $Q$ -dependence of  $A$  is well described by diffusion within small spherical pores of effective radius,  $R$ , given by [21],

$$A(Q) = \left[ \frac{3j_1(QR)}{QR} \right]^2 + I \quad (8)$$

where  $j_1(QR)$  is a spherical Bessel function. The best fit for this function is a bound water index of 0.75 and an  $R$  which is approximately 1 nm. This value for the range of confined motion for the water molecule agrees with the size of the "gel pores" in concrete, estimated at 2 nm from conventional drying experiments [20].

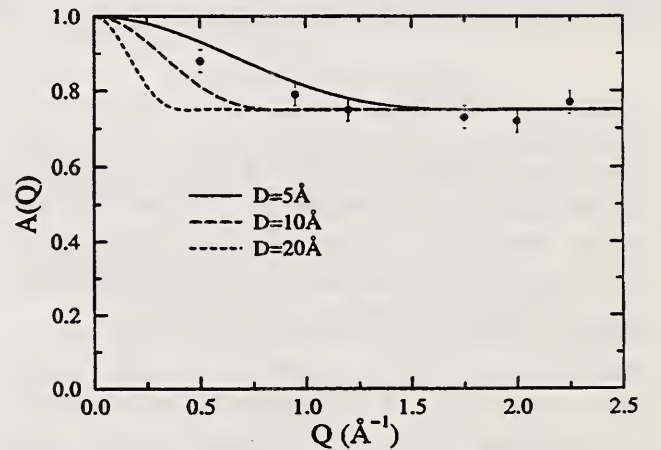
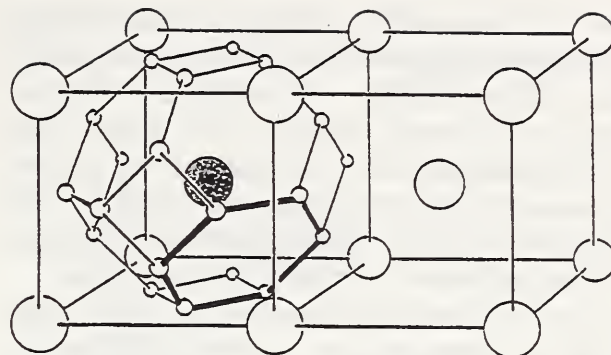


Figure 11. The intensity of the elastic peak as a function of  $Q$  after 245 days of curing. The lines represent the expected dependence for diffusion confined to various pore sizes.

Thus the time evolution of the state of the water molecule hydration in Portland cement concrete has been tracked on the molecular level from the initial liquid condition to the final bound state. These measurements demonstrate that QNS is a powerful tool for investigating the hydration processes of concrete and that it can provide detailed understanding not achieved by other methods. Since the technique is nondestructive, it enables repeated measurements on the same specimens over the course of the reaction. In future research we will use QNS along with other neutron scattering methods to study the influence of various cement compositions and admixtures, as well as environmental factors, on the progress of the hydration reaction and related aspects of microstructure development.

• **Excited-state Tunnel Splitting in Nb(TiH)<sub>x</sub>**

So far, Nb(TiH)<sub>x</sub> is the only known metal-hydrogen system where H atoms undergo low-temperature tunneling when trapped by a substitutional impurity [22]. Unlike tetrahedral H sites close to a Nb interstitial defect such as O or N where a 2-site double-well potential appears to be the adequate description [23,24], there are potentially 24 equivalent tetrahedral H sites close to a substitutional Ti atom (Fig. 12). Previous  $\mu$ SR measurements of Nb<sub>1-x</sub>Ti<sub>x</sub> (x = 0.001, 0.005, and 0.010) [25] have ascertained that  $\mu^+$  (acting as a hydrogen tracer) is not localized over 2 or 24 sites, but rather, over 4 or 6 sites (as illustrated in Fig. 12). At low temperatures, a tunneling peak at 0.2 meV has also been observed [26], as well as indications of further tunneling peaks which must exist for an extended tunneling system. This extended delocalization suggests the possibility of multiple splitting of the excited state levels. We were particularly interested in the first-excited-oscillator state where the tunnel splitting must be larger than in the ground state because the wave functions of the first-excited state are more extended and thus exhibit more overlap. This was indeed found to be the case for the excited-state tunnel splitting ( $4 \pm 0.3$  meV), observed spectroscopically for NbN<sub>0.007</sub>H<sub>0.004</sub> [24] using the BT-4 Be/graphite/Be filter spectrometer at the NBSR. Encouraged by the previous measurements of this interstitially doped Nb system, measurements were



**Figure 12.** Local structure around a substitutional Ti atom (shaded) in Nb with the 24 nearest tetrahedral hydrogen sites.

made of the first-excited state vibration spectrum for a Nb<sub>0.99</sub>Ti<sub>0.01</sub>H<sub>0.01</sub> sample.

The spectrum measured at 4.2 K (Fig. 13a) shows a complex structure. Due to some non-uniformity of the H content in the granular sample, a nonnegligible contribution of an  $\epsilon$ -hydride phase was present. As a measurement on a  $\epsilon$ -NbH<sub>0.109</sub> single crystal at 10 K illustrates (Fig. 13b), the lowest  $\epsilon$ -phase vibration peak contributes a shoulder at an energy of  $\sim 115$  meV. Moreover, Fig. 13b indicates the presence of a previously unknown line at  $\sim 122$  meV, which is currently under further investigation. Nonetheless, after taking account of the  $\epsilon$ -phase contribution to the first-excited-state lineshape, a broad band remains with clear evidence of multiple splitting, suggesting complex tunneling effects.

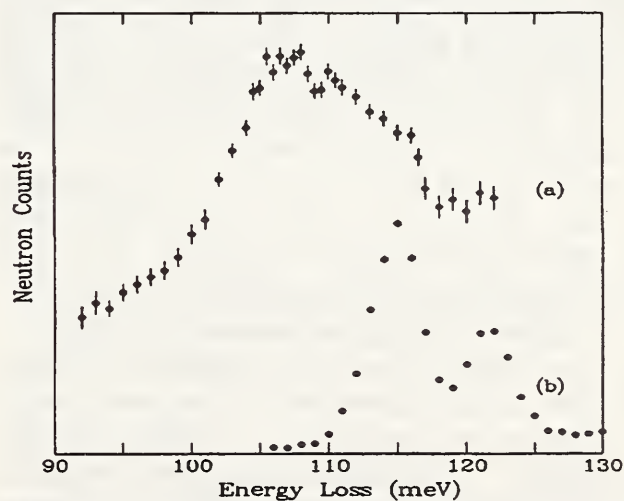


**Figure 13.** High-resolution vibrational spectra at 4.2 K of the first-excited oscillator state of H in (a) NbTi<sub>0.01</sub>H<sub>0.01</sub> and (b)  $\epsilon$ -NbH<sub>0.109</sub>.

This was confirmed by subsequent measurements of the same sample on the MARI spectrometer at RAL (Great Britain). A preliminary Bayesian (maximum entropy) analysis of the most recent MARI spectrum from a sample without  $\epsilon$ -phase contamination gave evidence for a splitting of the vibrational peak into 4 equidistant lines, suggestive of H delocalization over more than two sites.

Further joint measurements using the BT-4 and MARI spectrometers are currently underway to investigate the temperature and  $Q$ -dependence of the lineshape. The temperature dependence data should elucidate the effect on the tunneling state of the electron-hydrogen interaction above the 9-K superconducting transition. The  $Q$ -dependence should provide information about the local extension of the tunneling system as well the nature of the multisite wave function.

### Low Energy Excitations in Glasses

Amorphous materials typically display low energy excitations which exceed the estimated density of states of harmonic vibrations. In fact a broad feature, termed the "Boson" peak, is often observed in the energy range of 0.5-5 meV, whose origin is not yet well understood.

A proposal that tunneling of molecular units might be its origin was tested on a polymer glass polyisobutylene - (PIB) in which a Boson peak appears at  $E \sim 2.3$  meV. The  $Q$ -dependence of this broad inelastic excitation was studied on the BT-4 triple-axis spectrometer and shows that up to  $Q \sim 6 \text{ \AA}^{-1}$  the inelastic structure factor follows the  $Q^2$  dependence expected for vibrational excitations (Fig. 14). On the other hand, one would anticipate an oscillatory behavior with  $Q$  if the scattering were due to the tunneling of molecular units. Furthermore, the intensity varies with temperature following the Bose-factor. Thus, both the temperature and  $Q$ -dependence of the scattering appear to contradict the tunneling proposal.

In order to determine the influence of the side chains on the Boson peak, this low energy scattering was studied for a series of methacrylates: polymethylmethacrylate (PMMA), polyethylmethacrylate (PEMA), and polybutyl methacrylate (PBMA). An increase of the mass of the side chain, as one goes from methyl to ethyl to

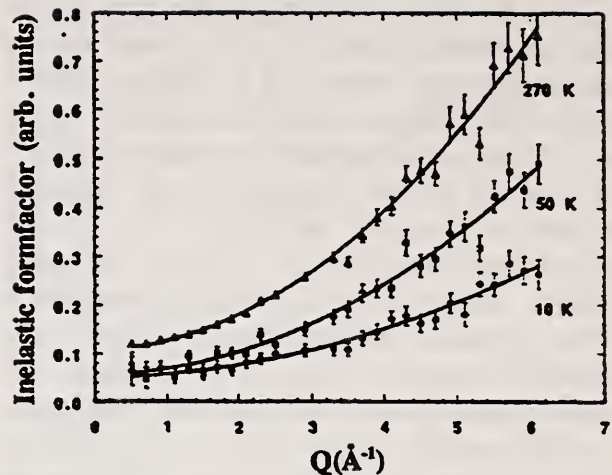


**Figure 14.** The inelastic form factors measured at 2.8 meV for polyisobutylene. The data are corrected for the Debye-Waller factor (the 270 K curve is reduced by a factor of 5 and shifted upwards by .15). The solid lines correspond to parabolic fits, which suggest vibrational behavior as the origin of the scattering.

butyl, should result in a decrease in the energy of the Boson peak if it were indeed due to the side chain reorientations. The observed dependence is opposite to that expected: PMMA and PEMA show a similar shape and position of the Boson peak, but the peak is definitely shifted to higher energy for PBMA (Fig. 15.) Thus the side groups do not significantly contribute to the excess density of states manifested in the Boson peak.

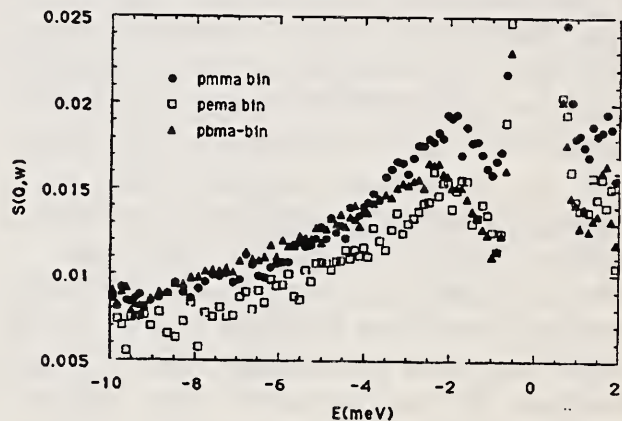


**Figure 15.** The inelastic scattering spectra of PMMA, PEMA, and PBMA exhibiting the Boson peak.

Finally the effect of crystallization on the Boson peak has been studied for ethylbenzene. In this system, an amorphous phase can be produced by quenching the sample in liquid nitrogen. An earlier study of amorphous ethylbenzene, found

that at approximately 135 K, the elastic intensity, which had been monotonically decreasing with increasing temperature, increased dramatically. In the present investigation the origin of this effect is identified as the onset of crystallization from the amorphous phase. A neutron diffraction study of a partially deuterated sample as a function of temperature reveals a liquid like pattern with a broad ( $\sim 2 \text{ \AA}^{-1}$ ) peak centered at  $1.7 \text{ \AA}^{-1}$  for temperatures of 130 K and below, whereas at temperatures at and above 140 K there is a clear pattern of crystalline peaks (Fig. 16).

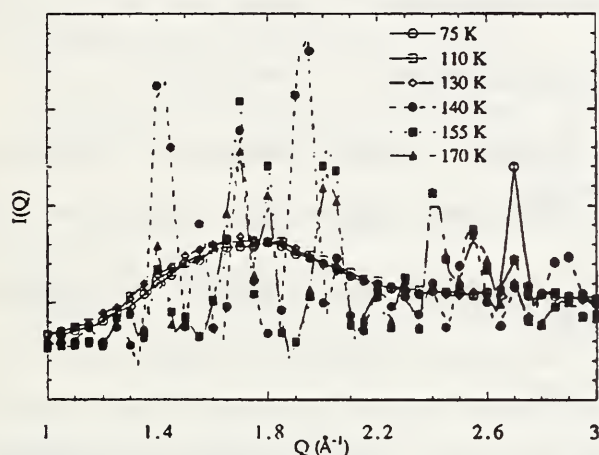


**Figure 16.** A neutron diffraction pattern of ethylbenzene as a function of temperature. The low temperature sample was prepared in the amorphous phase by quenching in liquid nitrogen. It is clear that crystallization occurs between 130 K and 140 K.

This transition has a dramatic effect in the low energy range of the inelastic scattering spectra. Figure 17 shows that there is a strong enhancement of intensity below 5 meV in the amorphous phase compared to the crystalline phase. Since this scattering is characteristic of the glassy phase rather than the material itself, it is identified as the Boson peak. To ascertain the role of the side groups, measurements were made on fully and partially deuterated ethylbenzene. Figures 17 (upper) and 17 (lower) show that the Boson scattering is independent of whether or not the side groups are deuterated, again indicating that it is not due to the side chain dynamics. Thus while the origin of the Boson peak in amorphous materials has not been established, it has been demonstrated that it does not arise from

tunneling of molecular units nor from the dynamics of side groups in these diverse systems.

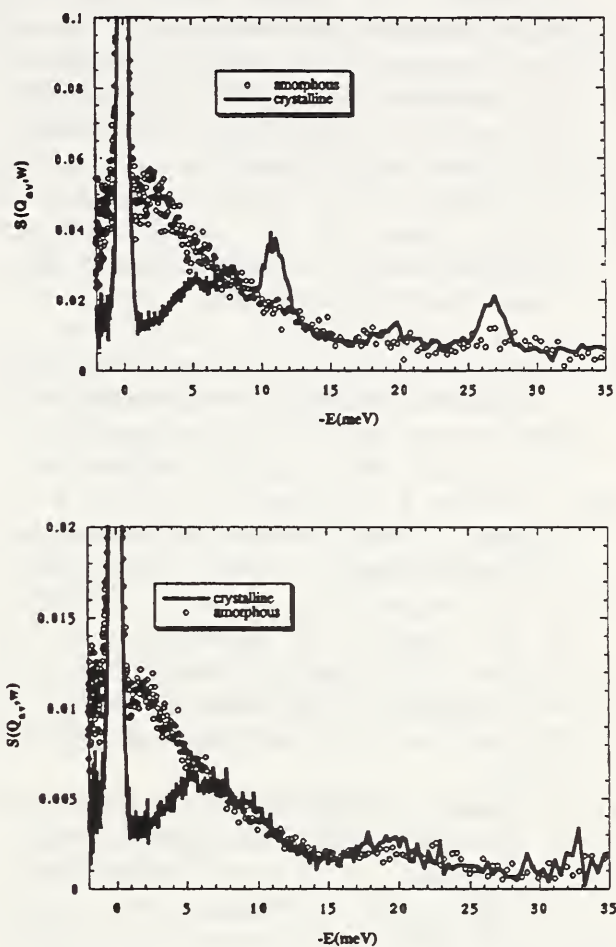


**Figure 17.** The inelastic neutron spectrum obtained on the NIST cold neutron time-of-flight spectrometer. The incident energy is 5 meV. (upper) Ring deuterated ethylbenzene in both the amorphous and crystalline conditions. (lower) Fully deuterated ethylbenzene in both the amorphous and crystalline conditions.

## References

- [1] P. W. Stephens, L. Mihaly, P. L. Lee, R. L. Whetten, S. M. Huang, R. Kanner, F. Deiderich, and K. Holczer, *Nature* **351**, 632 (1992).
- [2] W.I.F. David, R. M. Ibberson, T.J.S. Dennis, J. P. Hare, and K. Prassides, *Europhys. Lett.* **18** 219 (1992).
- [3] C. Christides, D. A. Neumann, K. Prassides, J.R.D. Copley, J. J. Rush, M. J. Rosseinsky, D. W. Murphy, and R.C. Haddon, *Phys. Rev. B* **46**, 12088 (1992).

- [4] K. Prassides, C. Christides, I. M. Thomas, J. Mizuki, K. Tanigaki, I. Hirose, and T. W. Ebbesen, *Science*, submitted for publication.
- [5] K. Kniaz, J. E. Fischer, Q. Zhu, M. J. Rosseinsky, D. W. Murphy, and O. Zhou, *Solid State Commun.* **88**, 47 (1993).
- [6] D. A. Neumann, J.R.D. Copley, D. Reznik, W. A. Kamitakahara, J. J. Rush, R. L. Paul, and R. M. Lindstrom, *J. Phys. Chem. Solids*, in press.
- [7] S. E. Barrett and R. Tycko, *Phys. Rev. Lett.*, **69** 3754 (1992).
- [8] J.R.D. Copley, D. A. Neumann, R. L. Cappelletti, and W. A. Kamitakahara, *J. Phys. Chem. Solids* **53**, 1353 (1992).
- [9] D. A. Neumann, J.R.D. Copley, W. A. Kamitakahara, J. J. Rush, R. L. Cappelletti, W. J. Romanow, N. Coustel, J. P. McCauley, J. E. Fischer, A. B. Smith, K. M. Creegan, and D. M. Cox, *J. Chem. Phys.*, **96** 8631 (1992).
- [10] T. Yildirim, J. E. Fischer, A. B. Harris, P. W. Stephens, D. Liu, L. Brard, R. M. Strongin, and A. B. Smith, *Phys. Rev. Lett.*, **71** 1383 (1993).
- [11] G.B.M. Vaughan, P. A. Heiney, J. E. Fischer, D. E. Luzzi, D. A. Ricketts-Foot, A. R. McGhie, Y.-W. Hui, A. L. Smith, D. E. Cox, W. J. Romanow, B. H. Allen, N. Coustel, J. P. McCauley, and A. B. Smith, *Science*, **254**, 1350 (1992).
- [12] C. Christides, I. M. Thomas, T.J.S. Dennis, and K. Prassides, *Europhys. Lett.* **22**, 611 (1993).
- [13] C. Christides, T. J. S. Dennis, K. Prassides, R. L. Cappelletti, D. A. Neumann, J.R.D. Copley, *Phys. Rev B* (in press).
- [14] A. Cheng and M. L. Klein, *Phys. Rev. B*, **46**, 4958 (1992); A. Cheng and M. L. Klein, *Phys. Rev. B*, **45**, 1889 (1992).
- [15] V. F. Sears, *Can. J. Phys.* **45**, 237 (1967).
- [16] D. A. Neumann, J.R.D. Copley, R. L. Cappelletti, W. A. Kamitakahara, R. M. Lindstrom, K. M. Creegan, D. M. Cox, W. J. Romanow, N. Coustel, J. P. McCauley, N. C. Maliszewskyj, J. E. Fischer, and A. B. Smith, *Phys. Rev. Lett.* **67**, 3808 (1991).
- [17] B. Renker, F. Gompf, R. Heid, P. Adelman, A. Heiming, W. Reichardt, G. Roth, H. Schober, and H. Rietschel, *Z. Phys. B*, **90**, 325 (1993).
- [18] G. Stix, *Sci. American*, **268** [4], 102 (1993); H.F.W. Taylor, *Cement Chemistry*, Academic Press, NY (1990).
- [19] D.H. Harris, C. G. Windsor, and C. D. Lawrence, *Mag. Concrete Res.*, **26**, 65 (1974).
- [20] J. Teixeira, M.-C. Bellisent-Funel, S. H. Chen, and A. J. Dianoux, *Phys. Rev. A* **31**, 1913 (1985).
- [21] F. Volino and A. J. Dianoux, *Mol. Phys.*, **41**, 271 (1980).
- [22] R. Hempelmann, D. Richter, and T. Springer, *Ann. Chim. Fr.* **15**, 53 (1990).
- [23] A. Magerl, A. J. Dianoux, H. Wipf, K. Neumaier, and I. S. Anderson, *Phys. Rev. Lett.* **56**, 159 (1986).
- [24] NISTIR 5120, "NIST REACTOR: Summary of Activities July 1991 through September 1992," pg. 7.
- [25] H.-J. Fell, R. Hempelmann, O. Hartmann, S. Harris, and R. Wäppling, *Ber. Bunsenges. Phys. Chem.* **95**, 1092 (1991).
- [26] R. Hempelmann, D. Richter, and A. J. Dianoux, unpublished.

## Research Topics

### Ca-Ammonia Solvation Complexes in Zirconium Disulfide

E. W. Ong<sup>10</sup>, J. Eckert<sup>10</sup>, and J. M. Nicol<sup>16</sup>.

### Methyl-Amine Solvation Complexes in Titanium Disulfide

E. W. Ong<sup>10</sup>, J. Eckert<sup>10</sup>, L. A. Dotson<sup>3</sup>, and J. M. Nicol<sup>16</sup>.

### Inelastic Neutron Scattering Studies of Mesoporous Molecular Sieves

D. Margolese<sup>23</sup>, H. Quo<sup>23</sup>, G. D. Stucky<sup>23</sup>, J. M. Nicol<sup>16</sup>, and C. J. Glinka<sup>16</sup>.

### Interaction of Hydrogen with Ir<sub>n</sub> Clusters in Zeolites by INS

Z. Xu<sup>24</sup>, S. Kawi<sup>24</sup>, T. Mure<sup>24</sup>, B. C. Gates<sup>24</sup>, R. R. Cavanagh<sup>19</sup>, J. M. Nicol<sup>16</sup>, T. J. Udovic<sup>16</sup>, and J. T. Miller<sup>2</sup>.

### Characterization of High-Surface-Area Magnesium oxide and the Interaction of Hydrogen with Surface Ir Clusters

Z. Xu<sup>24</sup>, B. C. Gates<sup>24</sup>, T. J. Udovic<sup>16</sup>, J. M. Nicol<sup>16</sup>, and R. R. Cavanagh<sup>19</sup>.

### Inelastic Neutron Scattering Studies of the Interaction of Ethane with Zeolite K-L

J. M. Nicol<sup>16</sup>, T. J. Udovic<sup>16</sup>, and R. R. Cavanagh<sup>19</sup>.

### Comparison of the Dynamics of (H<sub>2</sub>O)<sub>2</sub>PW<sub>12</sub>O<sub>40</sub> and [Na<sub>4</sub>(H<sub>3</sub>O)<sub>2</sub>][SiAlO<sub>4</sub>]<sub>6</sub>

T. J. Udovic<sup>16</sup> and J. M. Nicol<sup>16</sup>.

- Dynamics of the  $\text{H}_3\text{O}_2$  Ion in  $\text{Na}_8(\text{AlGeO}_4)_6(\text{OH})_2(\text{H}_2\text{O})_2$**   
T. J. Udovic<sup>16</sup>, J. M. Nicol<sup>16</sup>, and M. Wiebcke<sup>21</sup>.
- Dihydrogen Rotational Tunneling in  $\text{IrH}_2(\mu\text{-H}_2)(\text{PiPr}_3)_2$**   
J. Eckert<sup>10</sup>, T. Le-Husebo<sup>25</sup>, C. M. Jensen<sup>25</sup>, and J. M. Nicol<sup>16</sup>.
- Inelastic Neutron Scattering Study of the Rotational Dynamics of  $\text{C}_{60}$  in  $\text{C}_{60}(\text{I}_2)_2$**   
D. A. Neumann<sup>16</sup>, J.R.D. Copley<sup>16</sup>, and K. Prassides<sup>28</sup>.
- Inelastic Neutron Scattering Study of the Internal Vibrational Nodes in  $\text{Rb}_{2.6}\text{K}_{0.4}\text{C}_{60}$  and  $\text{C}_{60}$**   
W. A. Kamitakahara<sup>16</sup>, D. Reznik<sup>16</sup>, D. A. Neumann<sup>16</sup>, J.R.D. Copley<sup>16</sup>, J. E. Fischer<sup>14</sup>, R. M. Strongin<sup>27</sup>, M. A. Cichy<sup>27</sup>, and A. B. Smith III<sup>27</sup>.
- Diffraction Study of the Orientational Order in  $\text{Rb}_{2.6}\text{K}_{0.4}\text{C}_{60}$**   
W. A. Kamitakahara<sup>16</sup>, D. A. Neumann<sup>16</sup>, J.R.D. Copley<sup>16</sup>, J. E. Fischer<sup>14</sup>, R. M. Strongin<sup>27</sup>, M. A. Cichy<sup>27</sup>, and A. B. Smith III<sup>27</sup>.
- Inelastic Neutron Scattering Study of the Rotational Dynamics of  $\text{C}_{60}$  in  $\text{Rb}_{2.6}\text{K}_{0.4}\text{C}_{60}$**   
D. Reznik<sup>16</sup>, D. A. Neumann<sup>16</sup>, J.R.D. Copley<sup>16</sup>, W. A. Kamitakahara<sup>16</sup>, J. E. Fischer<sup>14</sup>, R. M. Strongin<sup>27</sup>, M. A. Cichy<sup>27</sup>, and A. B. Smith III<sup>27</sup>.
- Neutron and X-ray Diffraction Study of the Structure of Carbon Nanotubes**  
D. Reznik<sup>16</sup>, D. A. Neumann<sup>16</sup>, J.R.D. Copley<sup>16</sup>, M. G. Mitch<sup>14</sup>, and J. S. Lannin<sup>14</sup>.
- Comparison of the Density of States of Graphite and Carbon Nanotubes**  
W. A. Kamitakahara<sup>16</sup>, D. Reznik<sup>16</sup>, D. A. Neumann<sup>16</sup>, J.R.D. Copley<sup>16</sup>, M. G. Mitch<sup>14</sup>, and J. S. Lannin<sup>14</sup>.
- Inelastic Neutron Scattering Study of the Rotational Dynamics of  $\text{C}_{60}$  in  $\text{Na}_2\text{RbC}_{60}$**   
C. Christides<sup>28</sup>, K. Prassides<sup>28</sup>, D. A. Neumann<sup>16</sup>, J.R.D. Copley<sup>16</sup>, J. Mizuki<sup>12</sup>, K. Tanigaki<sup>12</sup>, I. Hirosawa<sup>12</sup>, and T. W. Ebbeson<sup>12</sup>.
- Inelastic Neutron Scattering Study of the Rotational Dynamics of  $\text{P}_4$  Molecules in White Phosphorus**  
F. Gompf<sup>9</sup>, W. A. Kamitakahara<sup>16</sup>, and D. A. Neumann<sup>16</sup>.
- Neutron Diffraction Study of the Orientational Ordering of  $\text{P}_4$  Molecules in White Phosphorus**  
W. A. Kamitakahara<sup>16</sup>, Q. Huang<sup>16,34</sup>, D. A. Neumann<sup>16</sup>, and F. Gompf<sup>9</sup>.
- Inelastic Neutron Scattering Study of  $\text{Ba}_{1-x}\text{K}_x\text{BiO}_3$  for  $x = 0, 0.25, 0.3, 0.4$**   
M. Green<sup>28</sup>, P. Day<sup>28</sup>, K. Prassides<sup>28</sup>, and D. A. Neumann<sup>16</sup>.
- Inelastic Neutron Scattering Study of  $\text{Li}_{1+x}\text{Ti}_{2-x}\text{O}_4$  for  $x = 0, 0.15, 0.33$**   
M. Green<sup>28</sup>, P. Day<sup>28</sup>, K. Prassides<sup>28</sup>, and D. A. Neumann<sup>16</sup>.
- Inelastic Neutron Scattering Study of the Dynamics of the Crown Ethers in  $\text{Cs}(18\text{-crown-6})_2$**   
M. Wagner<sup>11</sup>, J. Dye<sup>11</sup>, D. A. Neumann<sup>16</sup>, and J. A. Borchers<sup>16</sup>.
- Structure of PAN Gels and Foams**  
R. Lagasse<sup>18</sup>, W. A. Kamitakahara<sup>16</sup>, and J. Cook<sup>31,34</sup>.
- Dynamics of Boron Nitride**  
W. A. Kamitakahara<sup>16</sup>, D. A. Neumann<sup>16</sup>, G. Doll<sup>8</sup>, and A. W. Moore<sup>1</sup>.
- Dynamics of  $\text{Ge}_{1-x}\text{Sn}_x\text{Se}_2$  Glasses**  
R. L. Cappelletti<sup>13</sup>, D. Islam<sup>6</sup>, and W. A. Kamitakahara<sup>16</sup>.
- Quasielastic Scattering from Tetrahydrofuran (THF) -  $\text{D}_2\text{O}$  Solutions**  
W. A. Kamitakahara<sup>16</sup> and N. Wada<sup>7</sup>.
- Synergetic Effect of Sucrose and Ethanol in Formation of Triglyceride Microemulsions**  
S. F. Trevino<sup>4</sup> and R. Joubran<sup>20</sup>.
- Dynamics of Rare-Earth Metal Hydrides  $\beta\text{-MH}_{z+x}$  and Their Deuterated Analogs**  
T. J. Udovic<sup>16</sup>, J. J. Rush<sup>16</sup>, and I. S. Anderson<sup>31</sup>.
- Dynamics of Hydrogen in Nanocrystalline Palladium**  
U. Stuhr<sup>30</sup>, H. Wipf<sup>29</sup>, T. J. Udovic<sup>16</sup>, and J. J. Rush<sup>16</sup>.
- Excited-State Tunnel Splitting in  $\text{Nb}(\text{TiH})_x$**   
B. Hayer<sup>33</sup>, R. Hempelmann<sup>32</sup>, D. Richter<sup>33</sup>, T. J. Udovic<sup>16</sup>, and J. J. Rush<sup>16</sup>.

**Quasielastic Neutron Scattering Study of the Hydration Reaction in Portland Cement Concrete**

R. A. Livingston<sup>35</sup>, D. A. Neumann<sup>16</sup>, and J. J. Rush<sup>16</sup>.

**Q-dependence of the Boson Peak in Polyisobutylene**

B. Frick<sup>31</sup> and S. F. Trevino<sup>4</sup>.

**The Dependence of the Energy of the Boson Peak on the Side Chains of Polymer Glasses**

B. Frick<sup>31</sup>, S. F. Trevino<sup>4</sup>, and T. J. Udovic<sup>12</sup>.

**The Effect of Crystallization on the Dynamics of Ethylbenzene**

B. Frick<sup>31</sup> and S. F. Trevino<sup>4</sup>.

**Dynamics of PPVC  $C_6H_4C_2D_2$ <sub>x</sub>**

J. E. Fischer<sup>27</sup>, P. Papanek<sup>27</sup>, J. L. Sauvajol<sup>36</sup>, M. J. Winokur<sup>37</sup>, F. E. Karasz<sup>38</sup>, and T. J. Udovic<sup>16</sup>.

**Affiliations**

<sup>1</sup>Advanced Ceramics Corp.

<sup>2</sup>Amoco Research Center

<sup>3</sup>Arizona State University

<sup>4</sup>Army Armament RD&E Ctr.

<sup>5</sup>Army Research Labs, Aberdeen, MD

<sup>6</sup>Central Michigan University

<sup>7</sup>Colorado School of Mines

<sup>8</sup>General Motors Research Lab

<sup>9</sup>Kernforschungszentrum Karlsruhe

<sup>10</sup>Los Alamos National Laboratory

<sup>11</sup>Michigan State University

<sup>12</sup>Niffon Electric Company

<sup>13</sup>Ohio University

<sup>14</sup>Penn State University

<sup>15</sup>Polymers Division

<sup>16</sup>Reactor Radiation Division

<sup>17</sup>Royal Institution of Great Britain

<sup>18</sup>Sandia National Laboratory

<sup>19</sup>Surface and Microanalysis Sci. Div.

<sup>20</sup>U.S. Dept. of Agriculture

<sup>21</sup>Universität Konstanz

<sup>22</sup>University of California, Davis

<sup>23</sup>University of California, Santa Barbara

<sup>24</sup>University of Delaware

<sup>25</sup>University of Hawaii

<sup>26</sup>University of Illinois

<sup>27</sup>University of Pennsylvania

<sup>28</sup>University of Sussex

<sup>29</sup>Technische Hochschule Darmstadt

<sup>30</sup>Hahn-Meitner Institut

<sup>31</sup>Institut Laue-Langevin

<sup>32</sup>Universität des Saarlandes

<sup>33</sup>IFF Forschungszentrum Jülich

<sup>34</sup>University of Maryland

<sup>35</sup>Federal Highway Administration

<sup>36</sup>Université de Montpellier, France

<sup>37</sup>University of Wisconsin

<sup>38</sup>University of Massachusetts, Amherst



## MAGNETISM AND SUPERCONDUCTIVITY

Research in these areas has continued to cover a wide range of topics, from the structure and nature of magnetic coupling in artificially structured multilayers, to the theory of polarized neutron scattering from London superconductors near the critical angle, to the magnetic ordering and spin dynamics in oxide systems and heavy fermion superconductors. The research topics section provides an idea of the breadth of the ongoing work; following are a few highlights.

### Thin Films and Multilayers

#### • Epitaxial Multilayers

One area of research concerns the magnetic properties of metallic superlattices. Early work focused on rare-earth materials that exhibited long-range exchange interactions, which typically communicated easily through intervening non-magnetic metallic layers. More recent interest has centered on multilayers composed of transition-metal oxides whose exchange interactions are short range in nature. One system of particular interest is superlattices of  $\text{Fe}_3\text{O}_4/\text{NiO}$  grown by molecular beam epitaxy [1]. The magnetic order parameters of the  $\text{Fe}_3\text{O}_4$  spinel and the NiO rocksalt structure have been determined independently by taking advantage of the differing underlying crystal symmetries. The  $\text{Fe}_3\text{O}_4$  and NiO interlayers retain their basic ferrimagnetic and antiferromagnetic magnetic structures, respectively, but the competition between the exchange interactions at the superlattice interfaces leads to anomalous magnetic ordering at temperatures spanning  $T_{\text{Néel}}$  for NiO (520 K) and  $T_{\text{Curie}}$  for  $\text{Fe}_3\text{O}_4$  (858 K).

For these elastic neutron diffraction experiments, the samples were oriented with the [220] in-plane axis and [004] surface normal defining the scattering plane. Figure 1 shows a compilation of neutron diffraction scans taken at 9 K along the growth ( $Q_z$ ) direction through the (222), (111), and (220) peaks. The superlattice sample in this case consists of 300 repeats of 34 Å of  $\text{Fe}_3\text{O}_4$  and 68 Å of NiO. The lineshapes of these reflections differ dramatically. The (222) scattering, which model calculations show is dominated by NiO structural and  $\text{Fe}_3\text{O}_4$  magnetic contributions, has well-defined superlattice

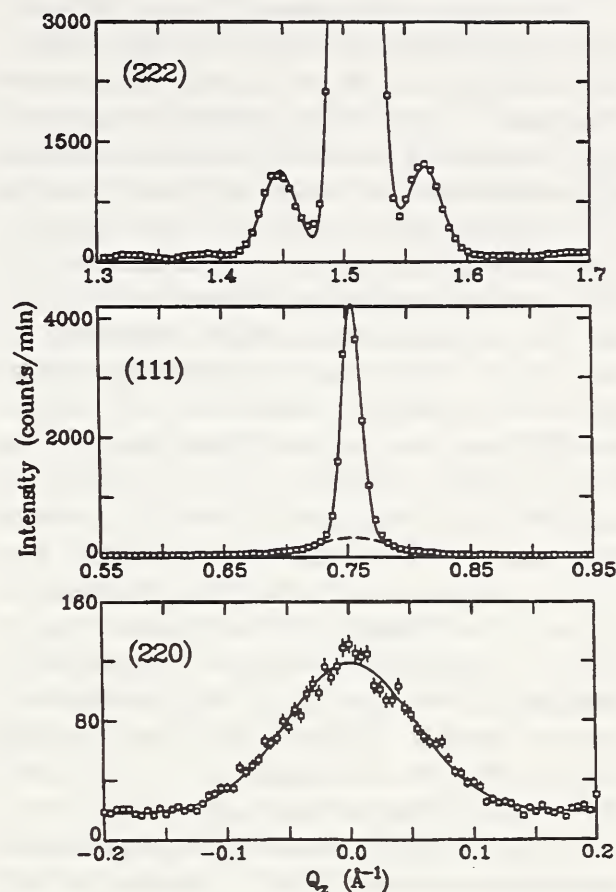


Figure 1. Neutron diffraction scans taken at 9 K along the growth ( $Q_z$ ) direction through the (222), (111), and (220) peaks. The sample consists of 300 repeats of 34 Å of  $\text{Fe}_3\text{O}_4$  and 68 Å of NiO. The curves are fits to Gaussian peaks. The (222) scattering has well-defined superlattice sidebands, while the in-plane (220) scattering is comprised of a single broad peak. The (111) reflection has both a broad (dashed curve) and narrow component [1].

sidebands, while the in-plane (220) scattering, originating from the  $\text{Fe}_3\text{O}_4$  alone, consists of a single broad peak. The coherence length along the growth direction calculated from the full-width-half-maximum of this reflection is  $52 \pm 5$  Å, slightly greater than the width of an  $\text{Fe}_3\text{O}_4$  interlayer. Complementary x-ray characterization confirms that the registry of the  $\text{Fe}_3\text{O}_4$  spinel lattice is not retained across intervening NiO interlayers because the orientation of the Fe tetrahedral sites relative to the NiO rocksalt template is not unique. The coherence of the  $\text{Fe}_3\text{O}_4$  ferrimagnetic order

thus is limited by stacking faults at the NiO/Fe<sub>3</sub>O<sub>4</sub> interfaces.

Contrasting with both the (222) and (220) data, the (111) reflection has two distinct components, broad (dashed curve in Fig. 1) and narrow Gaussians. The width of the broad peak approximates that of the (220) reflection, which suggests that this component originates from the Fe<sub>3</sub>O<sub>4</sub> ferrimagnetic order. In addition, the integrated intensity of this peak remains roughly constant as the temperature is increased from 9 K to 675 K, consistent with the Curie temperature of bulk Fe<sub>3</sub>O<sub>4</sub>. The narrow Gaussian component arises from the collinear antiferromagnetic order in the NiO interlayers, coherent through more than five superlattice bilayers. Upon heating, the intensity of this peak decays smoothly to zero at temperatures near or above T<sub>N</sub> for bulk NiO. The ordering temperatures for the Ni and Fe moments appear to be distinct, but the former tends to increase systematically with the relative Fe<sub>3</sub>O<sub>4</sub> thickness in the bilayer. Mean field simulations of related materials indicate that the exchange coupling of the Ni and Fe spins at the interfaces is responsible for the observed scaling of T<sub>N</sub>.

The basic features of these diffraction data can be understood on the basis of a Hendricks-Teller description of interfacial disorder. Such a model reproduces the distinct superlattice sidebands around the (222) peak, for example, as well as the two-component lineshape of the (111) reflection. However, the agreement is not quantitative. Work is in progress to further develop the model as well as to try and determine the crystalline and magnetic profiles by inversion techniques.

### • Diamagnetic Screening in Thin Film Superconductors

In the last decade or so, polarized neutron reflectometry has developed into a powerful technique to determine the magnetization density profiles in thin films and multilayer systems. The technique is applicable not only to ferromagnetic and ferrimagnetic layers, but also to diamagnetic layers due to screening currents in superconductors. For this latter case the method in principle, provides an absolute measurement of  $\lambda$ , and therefore polarized neutron reflectometry has the capability to make a model-independent determination of  $\lambda(T)$ . To interpret the reflectivity

data, the scattering has generally been calculated numerically from an “optical potential” theory, where the three-dimensional periodic nuclear scattering potential is approximated by an average nuclear potential of a continuum, and the magnetic field inside the superconductor is assumed to have the familiar (London) exponential decrease with distance below the first critical field H<sub>c1</sub>,  $\mathbf{B}(\mathbf{x}) = \mathbf{H} \exp(-x/\lambda)$ . The scattering problem then reduces to a one-dimensional (1-d) Schrödinger equation describing a neutron incident at angle  $\theta$  on a plane-surfaced and semi-infinite superconducting sample placed in an applied magnetic field H; to the incoming neutron the sample is represented as a simple potential barrier which consists of the neutron’s nuclear interaction V<sub>N</sub> with the average nuclear scattering potential and its magnetic interaction with the screening supercurrents in the sample. The change of the potential at the surface is then

$$V(x) = \left(\frac{2\pi\hbar^2}{m}\right)Nb \pm \mu \cdot H[\exp(-\frac{x}{\lambda}) - 1] \quad (1)$$

where the first term is the nuclear potential V<sub>N</sub> and the  $\pm$  for the second (magnetic) term refers to incident neutrons with spin up or spin down. Here N is the number density and b is the coherent nuclear scattering amplitude. When  $\theta$  is small enough such that  $\hbar^2k_x^2/2m$  is below this potential step the neutron is unable to overcome the barrier and therefore is totally reflected. The critical angles  $\theta_c^\pm$  for each neutron spin state are defined when the two energies are equal, and when  $\theta$  exceeds the critical angle then the neutron has a probability for both reflection and transmission. We note that for thermal and cold neutrons  $\theta_c$  is typically below 1°, and this is the conventional regime for neutron reflectometers, while for very-cold neutrons  $\theta_c$  can be much larger than 1°, and for ultra-cold neutrons  $\theta_c \rightarrow 90^\circ$ . The results obtained apply to all these cases.

The potential in Eq. (1) is relatively simple analytically, and we have found an exact solution for  $R^\pm(\theta, \lambda)$  for this problem that is valid throughout the entire angular range of interest [2]. Figure 2 shows the exact reflectivities  $R^+(\theta)$  (dash-dot curve) and  $R^-(\theta)$  (solid curve) for three different choices of the penetration depth  $\lambda$ : (a) 400 Å, (b) 1000 Å, and (c) 1600 Å. In this

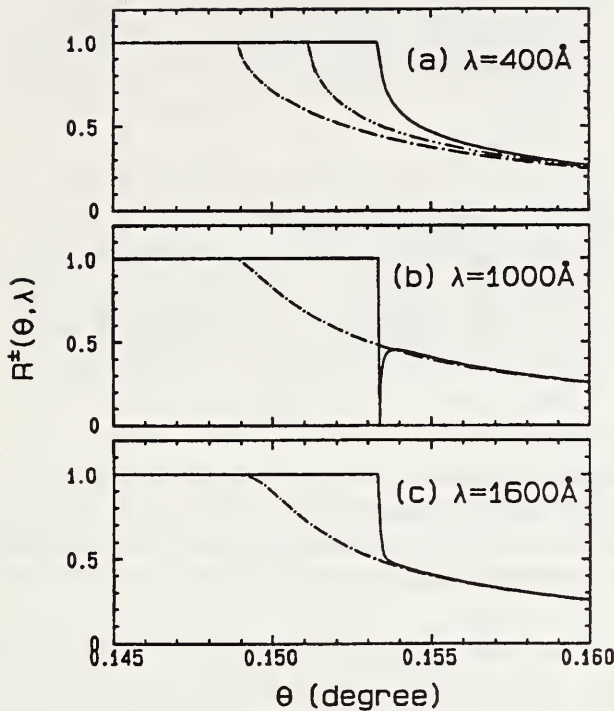


**Figure 2.** Reflectivity calculated for spin-up [ $R^+(\theta, \lambda)$  (dash-dot curves)] and spin-down [ $R^-(\theta, \lambda)$  (solid curves)] neutrons, as a function of  $\theta$ , for three different values of the magnetic penetration depth  $\lambda$ : (a)  $\lambda = 400 \text{ \AA}$ , (b)  $1000 \text{ \AA}$ , and (c)  $1600 \text{ \AA}$ . The dashed-double dotted curve in (a) is the reflectivity for  $H = 0$  [2].

example we have taken typical parameters for the neutron wavelength of  $2.35 \text{ \AA}$ , an applied field of  $H = 500 \text{ Oe}$ , and a nuclear density of  $4.98 \cdot 10^{-5} \text{ \AA}^{-2}$  appropriate for elemental niobium. First consider the curves for  $R^+(\theta)$ . As  $\theta$  exceeds  $\theta_c^+$ ,  $R^+(\theta)$  decreases monotonically, and the larger  $\lambda$  is, the slower  $R^+(\theta)$  decreases above  $\theta_c^+$ . This was the type of behavior expected for both  $R^+(\theta)$  and  $R^-(\theta)$  based on previous (numerical) results. The behavior of  $R^-(\theta)$ , on the other hand, is surprising, as it does not always decrease monotonically as a function of  $\theta$  above  $\theta_c^-$ . For example, at  $\lambda = 1000 \text{ \AA}$ ,  $R^-(\theta)$  almost dips to zero immediately above  $\theta_c^-$  (Fig. 2b). Beyond this dip,  $R^-(\theta)$  is slightly above  $R^+(\theta)$ , reflecting the fact that the asymptotic value of the spin-down potential is above the spin-up potential. Thus these spin-dependent effects are most discernible in the vicinity of the critical angles.

The ‘dip’ in the reflectivity profile for spin-down neutrons shown in figure 2b was an unexpected feature revealed by the analytic expressions for  $R^\pm(\theta, \lambda)$ . In actual reflectivity

measurements from thin films we typically see oscillatory behavior in  $R^\pm(\theta, \lambda)$  due to interference from the waves scattered from the front and back surfaces of the sample. In the present case, however, the sample is assumed to be infinitely thick and hence this structure in  $R^\pm(\theta, \lambda)$  must have a different nature. This  $\lambda$ -dependent resonance effect is worth studying because it has the promise of being developed into a sensitive way to measure  $\lambda$ . It turns out that it is the *shape* of the potential curve that determines whether this total transmission may occur. In contrast to the  $k_x$ -oscillatory type of resonant transmission, we refer to the anomalous transmission discussed above as the potential-profile-dependent and single-dip type. Both have the same physical origin—the reflected waves add up destructively. Indeed we have found a similar anomalous transmission in a very simple two-step potential profile.

We have focused this discussion on neutron reflectometry measurements of the magnetic penetration depth  $\lambda$  in superconductors, as this was the problem which led us to this investigation. However, these results are not restricted to neutron scattering; the exact solution for  $R^\pm(\theta, \lambda)$  can be applied to other scattering problems where the scattering potential has an exponential dependence with distance. Another example for neutrons is the problem of the magnetization at the surface of a ferromagnet, where the magnetization in the surface layer is expected to deviate from the bulk as  $\Delta\mu(z) = \Delta\mu_s \exp(-z/\xi)$ , where  $\xi$  is the magnetic coherence length, and both  $\Delta\mu_s$  and  $\xi$  are temperature dependent. Our solution can be immediately applied to this system with  $\xi$  replacing  $\lambda$ .

## Oxide Systems

### • Spin Dynamics of $V_{2-y}O_3$

One of the most astonishing effects of electronic correlations are their ability to localize electrons in so-called Mott-Hubbard insulators, which cannot be accounted for by the conventional band theory of solids. The discovery of high temperature superconductors in copper oxides has spot-lighted the importance of understanding Mott-Hubbard insulators in transition metal oxides because superconductivity in these systems is believed to occur when doping such an insulator.

$V_2O_3$  does not superconduct, but ever since the discovery of its Metal Insulator Transition (MIT) in 1946 this material has served as a model system for theories of metals in the vicinity of a Mott-Hubbard insulating phase. The insulating phase of this material ( $T < T_{MIT} = 150$  K) is a monoclinic, commensurate antiferromagnet with conventional spin wave excitations. In the metallic phase, however, the magnetic order and spin wave excitations associated with the insulator completely vanish rather than evolving into conventional paramagnetic scattering. This unusual result was taken to indicate the disappearance of conventional localized spins as the d-electrons formed bands. Indeed little was known about electronic correlations in the metallic phase apart from the fact that they lead to strongly renormalized fermionic quasiparticles when the metal is stabilized to low temperatures in cation deficient samples.

The recent discovery of a low temperature antiferromagnetic phase transition in metallic  $V_{2-y}O_3$  has led us to a completely new picture of the metallic phase in the vicinity of the MIT [3]. Magnetic Bragg peaks of the metal were not found at  $(1/2, 1/2, 0)$ , corresponding to the ordered structure of the insulator, but instead appeared at incommensurate positions. The peaks are resolution limited in width, placing a lower limit of  $10^3$  Å on the correlation length. The ordered moment is  $0.148(7) \mu_B$  (for  $y=0.027(3)$ ) and the ordered structure consists of nearly perfect planar Honeycomb antiferromagnetic layers with a local spin direction rotating an angle  $1.43(7) \pi$  from plane to plane. The chromium-like anomaly in the resistivity and the strongly reduced staggered magnetization below  $T_N$  indicate that the magnetic order is an incommensurate spin density wave formed among itinerant 3-d electrons. This is confirmed by the large bandwidth and disproportionately strong spin fluctuation spectrum which we probed by inelastic magnetic neutron scattering. Figure 3 shows a contour map of the normalized dynamic spin correlation function at low temperatures in metallic  $V_{2-y}O_3$ . Contrary to the spin waves of a localized-spin antiferromagnet, which would give rise to two sharp ridges emanating from each incommensurate magnetic Bragg peak, the dynamic spin correlation function consists of a single ridge as a function of energy centered near each incommensurate magnetic zone

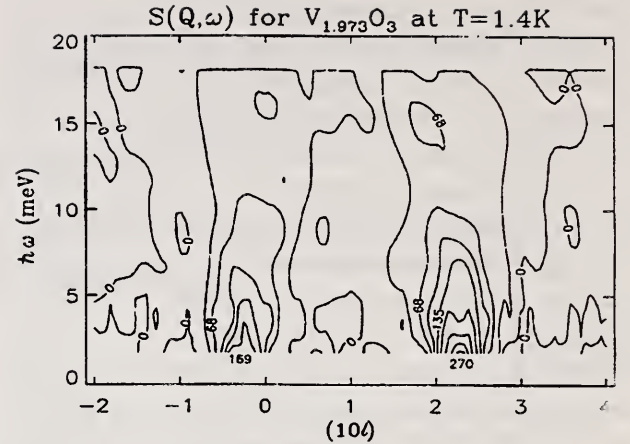


**Figure 3.** Contour map of the measured dynamical spin correlation function,  $S(Q, \omega)$  in  $V_{2-y}O_3$  ( $y = 0.027$ ) at  $T = 1.4$  K [3]. The numbers on contour lines indicate the value of  $S(Q, \omega)$  in mbarn/meV/hexagonal-unit-cell.

center. With increasing energy the peaks broaden and move toward the commensurate antiferromagnetic Bragg point  $(101)$ . This type of response resembles that found in itinerant spin density wave antiferromagnets such as chromium, where a Fermi surface nesting instability gives rise to strong enhancement of the Lindhard susceptibility of the 3-d bands. The bandwidth or inverse rate of broadening of the ridge is, however, far less for  $V_{2-y}O_3$  ( $67(4) \text{ meV-Å}$ ) than for Cr ( $900 \text{ meV-Å}$ ) indicating that quasiparticles on the relevant parts of the Fermi surface have a larger effective mass.

A typical feature of Fermi-surface-related instabilities is that the characteristic wave vector changes with carrier density as the distance between active parts of the Fermi surface changes. The incommensurate wave vector does indeed change with doping, but only by a small amount, because in  $V_{2-y}O_3$  the Fermi surface is large in the vicinity of the MIT. It is therefore not too surprising that the incommensurate spin correlations uncovered at low temperatures in the cation deficient sample turn out to be a characteristic feature throughout the metallic phase of  $V_{2-y}O_3$ . We also have found that this entire Fermi-surface instability is removed when entering the low temperature insulating phase. This contrasts with materials such as  $La_{2-x}Sr_xCuO_4$ , where the Bragg peaks of the commensurate antiferromagnetic insulator emerge close to the place where the Lindhard susceptibility of the metal is enhanced. It appears that the MIT in  $V_2O_3$  results from a competition between two unrelated instabilities of

a strongly correlated electron system: A Fermi-surface nesting instability and a rhombohedral to monoclinic structural transition which wipes out the Fermi surface.

• **Magnetic Excitons in  $\text{Pr}_2\text{CuO}_4$**

Studies of the magnetic properties of the insulating  $\text{R}_2\text{CuO}_4$  compounds and their electron-doped superconducting analogs  $\text{R}_{2-x}\text{Ce}_x\text{CuO}_4$  ( $\text{R}=\text{Pr}$ ,  $\text{Nd}$ , and  $\text{Sm}$ ) have demonstrated that these materials exhibit a variety of interesting magnetic behavior involving both the rare earth and the copper spins. The Cu spins in the insulating compounds order antiferromagnetically at high temperatures, with  $T_N$  in the range of 250-300 K, and have very strong 2-d exchange in the  $a$ - $b$  plane. In the superconducting phase there is no long range Cu order, but the large energy scale provided by the exchange interaction within the  $\text{CuO}_2$  planes has supported speculation that magnetism may be directly connected with Cooper pairing in these materials. The rare earth ions, on the other hand, typically order in both the insulating and superconducting phases at low temperatures (e.g. 6 K for Sm). The coexistence of long-range magnetic order and superconductivity in these systems has provided an interesting situation where the interplay between the two cooperative phenomena can be studied, particularly for the light rare earths such as Sm and Nd where it is clear that exchange interactions are dominant. However, the nature and anisotropy of these rare earth exchange interactions, and their possible effect on the Cu-O planes, was not clear. We have been measuring the dispersion relations for the Pr excitons in a single crystal of the parent electron-superconductor system  $\text{R}_2\text{CuO}_4$ . The dispersion observed for excitations propagating both within the basal plane and along the  $c$ -axis directly demonstrates that substantial R-R exchange interactions exist in these materials, and that these exchange interactions must be mediated through copper-oxygen layers where superconducting pairs form.

The basic crystal-field level scheme for the  $\text{Pr}^{+3}$  ions in  $\text{R}_2\text{CuO}_4$  has already been studied via neutron measurements on polycrystalline specimens by various groups, and the  $\text{Pr}^{+3}$  ground state has been determined to be a non-magnetic singlet and the first excited state is a magnetic

doublet at  $\sim 18$  meV. For the present case where the crystal field dominates the exchange, the elementary collective excitations can be conveniently described by linear combinations of the single-ion crystal-field transitions which propagate through the lattice. The dispersion exhibited by these *magnetic excitons* is a direct measure of the exchange coupling between the magnetic ions. The fortuitous crystal-field level scheme for  $\text{Pr}^{+3}$  in  $\text{R}_2\text{CuO}_4$  provides us with a model cuprate-superconductor system to investigate these magnetic excitons and make a direct determination of the exchange interactions in this class of materials.

Figure 4 displays the measured dispersion relation of the acoustic exciton mode covering more than one Brillouin zone to illustrate the periodicity of the excitations [4]. The vertical dashed lines in the figure mark the zone boundaries. The top portion of the figure shows the dispersion propagating along the [110] direction while the bottom portion corresponds to propagation along the [100] direction. The observed periodicity of the excitons is in agreement with that expected for the reciprocal lattice of the Pr chemical unit cell. Anticipating that the dominant exchange interactions involved are short range in nature, we have used the magnetic exciton model to fit the measured dispersion relations by including up to third-nearest-neighbor exchange constants. The solid curves drawn through the data in figure 4 are calculated with the following parameters:  $D = 18$  meV,  $\alpha^2 J_1 = 0.7$  meV,  $8\alpha^2 J_2 = 0.8$  meV, and  $8\alpha^2 J_3 = -0.8$  meV, where  $J_i$  is the exchange constant between  $i^{\text{th}}$  nearest neighbors. The exchange parameter  $J_3$  is a measure of the coupling between nearest neighbor ions within the  $a$ - $b$  plane while  $J_2$  corresponds to the coupling between those Pr layers that are separated by oxygen layers. The uncertainties in the values of these parameters are  $\sim 0.1$  meV. The remaining parameter  $J_1$  is associated with the coupling between those Pr layers that are separated by the  $\text{CuO}_2$  layers. Thus if  $J_1 \neq 0$  the exciton modes propagating along the  $c$ -axis direction should exhibit dispersion, which we have confirmed.

Finally we note for systems where the rare earth ground state is magnetic, such as for Nd and

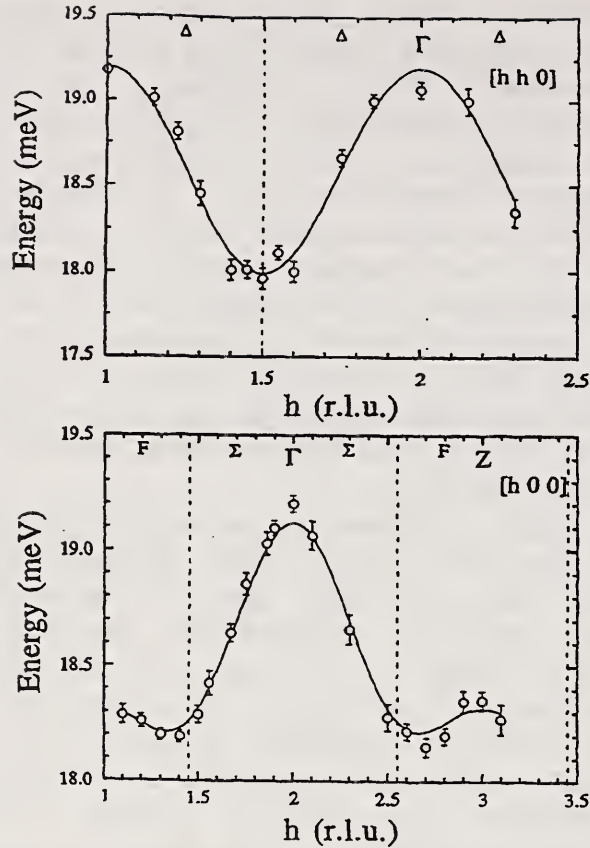


**Figure 4.** Measured low temperature dispersion relation of the  $\text{Pr}^{3+}$  acoustic exciton mode in  $\text{Pr}_2\text{CuO}_4$ , propagating in the  $[110]$  (top) and in the  $[100]$  (bottom) directions. The solid curve is the fit of the magnetic exciton model to the measured dispersion relation [4].

Sm, there is only a very small decrease in the ordering temperature when the rare earth lattice is diluted with (non-magnetic) Ce to form the superconducting materials. This argues that the exchange interactions are likely of the superexchange type, and are not significantly affected by the Ce dilution. For  $\text{Pr}_2\text{CuO}_4$  we have been able to provide direct evidence of substantial R—R exchange interactions in the electron superconductors. If conventional spin-depairing theories of magnetic superconductors were applied, the strength of these interactions would be expected to be quite detrimental to superconductivity, irrespective of the Cu magnetism. The realization that these materials are nevertheless ‘high temperature’ superconductors argues that a different type of superconducting state is present.

## Superconductivity

### • Vortex Lattice in $\text{YBa}_2\text{Cu}_3\text{O}_7$

The nature of the vortex state in the cuprate high-temperature superconductors remains an issue of great theoretical and practical interest. A variety of experimental techniques has been used to investigate the static and dynamic vortex correlations in these materials. In contrast to surface probes such as Bitter decoration or scanning tunnel microscopy, which are restricted to low applied fields, neutron scattering can explore both the low-field and high-field regimes, the latter being a theoretically interesting region where the vortices interact strongly. This is also the relevant region for prospective magnet applications of the copper-oxide superconductors. In fact, the success of these experiments [5] depended critically on the preparation of a large ( $\sim 2.5$  cm diameter,  $\sim 0.9$  cm thick), high-quality single crystal in a program devoted to device applications of bulk  $\text{YBa}_2\text{Cu}_3\text{O}_7$ .

The small-angle neutron experiments were carried out as a function of the angle of the applied magnetic field with respect to the crystalline axes. There are two important angles in these experiments,  $\theta$ , the angle of the field with respect to the twin planes, and  $\chi$ , which is the tilt angle of the  $c$ -axis with respect to the scattering plane. Figure 5 A—F shows data [5] for  $\chi = 0^\circ$ . For  $\theta = \chi = 0^\circ$  (A), the scattering pattern appears to have fourfold symmetry. This result led previous investigators to conclude that the intrinsic lattice is square, which would mean that the binding energy between the twin planes and the vortices would be a maximum. To investigate this point further we oriented the crystal so that  $\chi = 9^\circ$  and  $\theta = 5^\circ$  (G). This small angular offset breaks the twin-boundary symmetry and causes a single-domain triangular lattice to be formed in the entire crystal, as evidenced by the hexagonal diffraction pattern. Hence we conclude that the intrinsic lattice is triangular, not square.

The dependence of the scattering on the angle of the applied field with respect to the  $c$ -axis is also shown in figure 5 (A—F). The eccentricity of the diffraction pattern that develops with increasing field angle is a result of the anisotropy between the  $c$  and  $ab$  axes of the electron effective mass; the ratio is  $\sim 25$ . At small angles  $\theta$  the

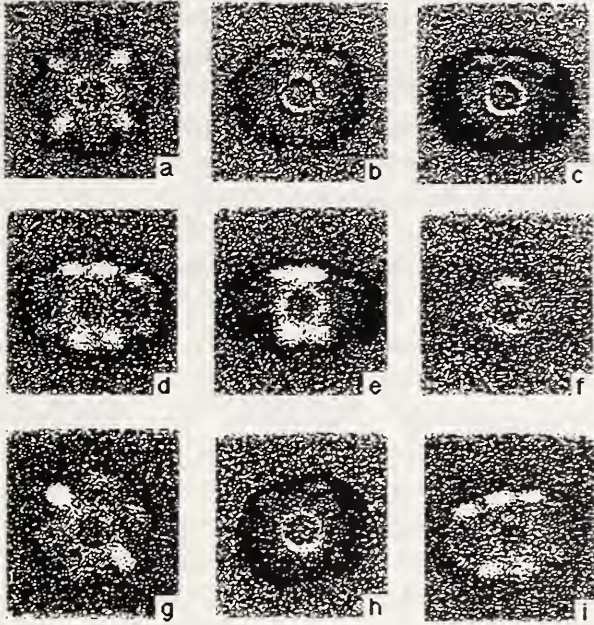


**Figure 5.** Small angle diffraction patterns of the vortex lattice of  $\text{YBa}_2\text{Cu}_3\text{O}_7$  at 10 K. A through F are for  $\chi = 0^\circ$ , and G through I are for  $\chi = 9^\circ$ . A–F are for  $\theta$  of  $0^\circ$ ,  $40^\circ$ ,  $50^\circ$ ,  $60^\circ$ ,  $70^\circ$ , and  $80^\circ$ , respectively. G–I are for  $\theta$  of  $5^\circ$ ,  $30^\circ$ , and  $60^\circ$ , respectively [5].

orientation of the vortex lattice is determined by pinning interactions between vortices and twin planes, and the smooth variation of the data strongly suggests that this pinning dominates for  $\theta \leq 70^\circ$ . For higher angles (F) the vortex lattice consists of independent chains in the orientation predicted by anisotropic London theory.

### • Vortex Melting in Niobium

One of the most interesting and fundamental questions concerning the vortex structures in superconductors is whether or not they undergo a melting transition. Early work in the cuprate systems identified an irreversibility line, suggesting that the basic vortex behavior was quite different than for conventional superconductors. In the low field regime below the irreversibility line ( $T_{\text{irr}}$ ) the vortices are thought to exist in a lattice or glass, while in the high field regime above  $T_{\text{irr}}$  they melt into some kind of a fluid phase. However, it has proved difficult to probe the structure of these phases directly because techniques such as Bitter decoration are restricted to low fields, while neutron scattering experiments have suffered from the low signal-to-noise presently available for high  $T_c$  samples. This

melting behavior was thought to originate from the unique physical properties of the cuprates, namely the large  $\kappa$ , intrinsic anisotropy, and high thermal energies available near  $T_c$ , but a reexamination of conventional superconductors has revealed that they also undergo a melting phenomenon. We have therefore been carrying out an extensive series of small angle neutron scattering measurements on a high quality single crystal of niobium [6], where the signal-to-noise is several orders-of-magnitude better than currently available from the best high  $T_c$  crystals.

The temperature dependence of the observed widths of the magnetic vortex peaks is shown in figure 6, obtained by cooling in an applied field of 2000 Oe. At low temperatures these widths are instrumentally limited, and this is the best resolution available on these SANS instruments. At higher temperatures the width of the peaks in the transverse direction begins to increase, while the radial width remains resolution limited. We have also taken a limited number of isothermal measurements, and have found that above a certain temperature the intensity and positions of the peaks are reversible, while below they are irreversible. The onset of broadening in the field-cooled data is very close to where we observe this crossover from reversible to irreversible behavior in this sample, and thus we associate this broadening with the irreversibility line and melting identified in bulk measurements. However, the scattering still exhibits sixfold symmetry, while an isotropic liquid would exhibit a ring of intensity rather than spots. Thus we describe this phase as a correlated flux fluid. We see from the figure that an intrinsic radial width is only observed close to  $T_c$ , but even here the sixfold symmetry is still preserved. Indeed we find no evidence of a liquid-like ring of scattering under any conditions.

The phase diagram we have determined is also shown in figure 6 (bottom). The  $H_{c2}$  phase boundary is determined by SQUID measurements,  $I(T)$  data, and by the field where the isothermal scattering vanishes. Good agreement is obtained between these data, demonstrating that within our experimental sensitivity the vortex scattering disappears at  $H_{c2}$ . We also show in the figure the field where the flux begins to penetrate the sample, which is identified as the sudden onset of vortex scattering

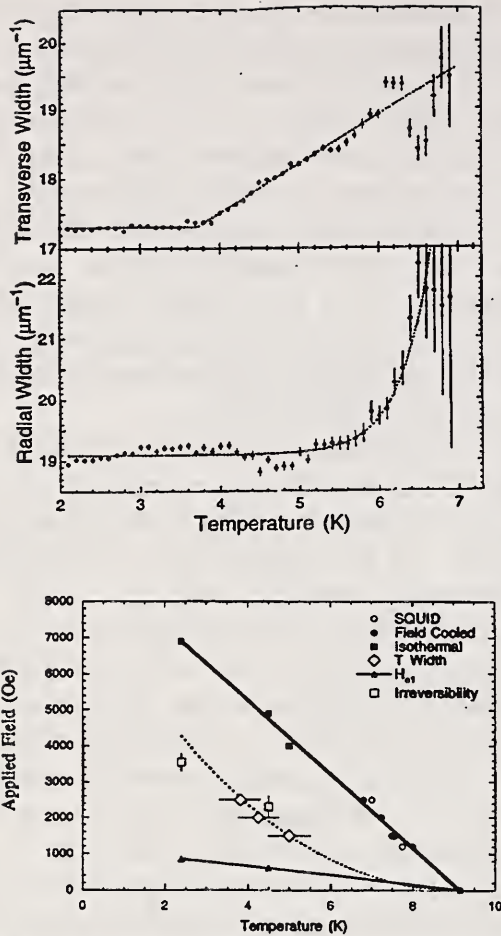


**Figure 6.** Measured radial and transverse (angular) widths as a function of temperature for an applied field of 2000 Oe. The solid curves are a guide to the eye. The bottom part of the figure shows the superconducting phase diagram for Nb [6].

as  $H$  increases above the observed  $H_{c1}$ . The irreversibility line (open squares) as determined by our isothermal measurements, and the onset temperature of the intrinsic transverse width (open diamonds), are also shown in the phase diagram. It is clear that they occur in close proximity to each other, and both are well below  $H_{c2}$ . Thus we identify the onset of an intrinsic transverse width with the irreversibility/melting curve identified in bulk measurements, and the dotted curve is a fit to a melting theory for comparison purposes.

The temperature dependence of the widths of the vortex peaks must originate from the vortex dynamics, and there are two alternative explanations for these data. The first is that the development of the transverse widths, coupled with the irreversibility line we observe, signals the transition to a fluid phase. In this case the intrinsic radial width would simply be below our

instrumental limit until  $T$  is sufficiently close to  $T_c$ . A second possibility is that the transverse width is due to strong inelastic scattering associated with the soft shear mode of the lattice, the same mode that would be involved in melting. The observed intensity from such modes would be strongest in the transverse direction. Thus if we had sufficiently high resolution and could distinguish elastic from inelastic scattering, we would expect to see a true  $\delta$ -function Bragg peak, with wings of inelastic scattering. This scattering would be convolved into a single broadened peak with the present resolution. The implication would be that the lattice has not yet melted, and that the observed irreversibility curve would not be associated with melting. The melting might then be identified with the increase of the width in the radial direction. This would correspond more closely to the melting line identified in bulk measurements on high  $\kappa$  samples, and would suggest that the melting curve is not strongly dependent on  $\kappa$ . While we favor the first interpretation, we cannot rule out the second yet, but in either scenario we have found that the basic six-fold symmetry is preserved throughout. If this vortex correlation originates from the underlying crystal symmetry then an isotropic liquid would only be observed if the crystalline anisotropy were negligible. In all other cases a correlated flux liquid is realized.

## References

- [1]. J. A. Borchers, R. W. Erwin, S. D. Berry, D. M. Lind, E. Lochner, and K. A. Shaw, *Appl. Phys. Lett.* (to be published).
- [2]. H. Zhang and J. W. Lynn, *Phys. Rev. Lett.* **70**, 77 (1993).
- [3]. W. Bao, C. L. Broholm, S. A. Carter, T. F. Rosenbaum, G. Aeppli, S. F. Trevino, P. Metcalf, J. M. Honig, and J. Spalek, *Phys. Rev. Lett.* **71**, 766 (1993).
- [4]. I. W. Sumarlin, J. W. Lynn, T. Chattopadhyay, S. N. Barilo, and D. I. Zhigunov, *Physica C* (to be published).
- [5]. B. Keimer, F. Dogan, I. A. Aksay, R. W. Erwin, J. W. Lynn, and M. Sarikaya, *Science* **322**, 83 (1993).
- [6]. J. W. Lynn, N. Rosov, T. E. Grigereit, H. Zhang, and T. W. Clinton (preprint).



## Research Topics

### Polarization Analysis of the Magnetic Excitations in Invar

J. W. Lynn<sup>27</sup>, N. Rosov<sup>27</sup>, M. Acet<sup>38</sup>, and H. Bach<sup>28</sup>.

### New Exact Solution of the one Dimensional Schrödinger Equation and Its Application to Polarized Neutron Reflectometry

H. Zhang<sup>43,27</sup> and J. W. Lynn<sup>27</sup>.

### Vortex Lattice and Melting in Nb

J. W. Lynn<sup>27</sup>, N. Rosov<sup>27</sup>, T. E. Grigereit<sup>43</sup>, H. Zhang<sup>43,27</sup>, and T. W. Clinton<sup>43</sup>.

### Phonon Density of States in the Superconductor $\text{HgBa}_2\text{CaCu}_2\text{O}_{4.3}$

J. W. Lynn<sup>27</sup>, T. J. Udovic<sup>27</sup>, J. J. Rush<sup>27</sup>, R. L. Meng<sup>41</sup>, and C. W. Chu<sup>41</sup>.

### Nature of the Vortex Lattice in $\text{YBa}_2\text{Cu}_3\text{O}_7$

B. Keimer<sup>25</sup>, I. Aksay<sup>25</sup>, F. Dogan<sup>25</sup>, R. W. Erwin<sup>27</sup>, J. W. Lynn<sup>27</sup>, and M. Sarikaya<sup>25</sup>.

### Magnetic Structure of the Heavy Fermion Compound $\text{CeCu}_{5.5}\text{Au}_{0.5}$

A. Schröder<sup>18</sup>, J. W. Lynn<sup>27</sup>, M. Loewenhaupt<sup>14</sup>, and H. V. Löhneysen<sup>39</sup>.

### Temperature Dependence of the Magnetic Excitations in Ordered and Disordered $\text{Fe}_3\text{Pt}$

N. Rosov<sup>27</sup>, J. W. Lynn<sup>27</sup>, J. Kästner<sup>38</sup>, E. F. Wassermann<sup>38</sup>, and H. Bach<sup>28</sup>.

### Dispersion of the Magnetic Excitations of the Pr and Cu ions in $\text{Pr}_2\text{CuO}_4$

I. W. Sumarlin<sup>43</sup>, J. W. Lynn<sup>27</sup>, T. Chattopadhyay<sup>12</sup>, S. N. Barilo<sup>6</sup>, and D. I. Zhigunov<sup>6</sup>.

### Magnetic Properties of Single-crystalline $\text{UCu}_3\text{Al}_2$

H. Nakotte<sup>41</sup>, E. Brück<sup>41</sup>, J.H.V.J. Brabers<sup>41</sup>, K. Prokeš<sup>41</sup>, F. R. de Boer<sup>41</sup>, V. Sechovsky<sup>8</sup>, K.H.J. Buschow<sup>24</sup>, A. V. Andreev<sup>49</sup>, R. A. Robinson<sup>17</sup>, A. Purwanto<sup>17</sup>, and J. W. Lynn<sup>27</sup>.

### Neutron Powder Diffraction Study of the Nuclear and Magnetic Structures of the Substitutional Compounds $(\text{Y}_{1-x}\text{Ca}_x)\text{Ba}_2\text{Fe}_3\text{O}_{8+\delta}$

I. Natali Sora<sup>31</sup>, Q. Huang<sup>43,27</sup>, J. W. Lynn<sup>27</sup>, N. Rosov<sup>27</sup>, P. Karen<sup>47</sup>, A. Kjekshus<sup>47</sup>, V. L. Karen<sup>27</sup>, A. D. Mighell<sup>27</sup>, and A. Santoro<sup>27</sup>.

### Magnetic Studies of Ce Spins in Heavy-Fermion Compounds $(\text{Ce-La})_3\text{M}$ With $\text{M}=\text{Al, In, and Sn}$

W.-H. Li<sup>20</sup>, W. T. Hsieh<sup>20</sup>, K. J. Chang<sup>20</sup>, and J. W. Lynn<sup>27</sup>.

### Crystal Structure and Magnetic Ordering of the Rare Earth and Cu Moments in $\text{RBa}_2\text{Cu}_2\text{NbO}_{10}$ ( $R = \text{Nd, Pr}$ )

N. Rosov<sup>27</sup>, J. W. Lynn<sup>27</sup>, H. B. Radousky<sup>15</sup>, M. Bennahmias<sup>38</sup>, T. J. Goodwin<sup>38</sup>, P. Klavins<sup>38</sup>, and R. N. Shelton<sup>38</sup>.

### Magnetic Ordering of Pr and Cu in $\text{TlBa}_2\text{PrCu}_2\text{O}_{7-y}$

K. J. Chang<sup>20</sup>, W. T. Hsieh<sup>20</sup>, W.-H. Li<sup>20</sup>, K. C. Lee<sup>20</sup>, J. W. Lynn<sup>27</sup>, C. C. Lai<sup>20</sup>, and H. C. Ku<sup>20</sup>.

### Two-dimensional Magnetic Order in $\text{Pb}_2\text{Sr}_2\text{TbCu}_3\text{O}_8$

S. Y. Wu<sup>20</sup>, W. T. Hsieh<sup>20</sup>, W.-H. Li<sup>20</sup>, K. C. Lee<sup>20</sup>, J. W. Lynn<sup>27</sup>, and H. D. Yang<sup>21</sup>.

### Effects of Metallic Doping on the Pr Magnetism in $\text{PrBa}_2(\text{Cu}_{1-x}\text{M}_x)_3\text{O}_7$

W. T. Hsieh<sup>20</sup>, K. J. Chang<sup>20</sup>, W.-H. Li<sup>20</sup>, and J. W. Lynn<sup>27</sup>.

### Temperature and Field Dependence of the Magnetic Order in $\text{UPdSn}$

R. A. Robinson<sup>17</sup>, A. C. Lawson<sup>17</sup>, J. W. Lynn<sup>27</sup>, K.H.J. Buschow<sup>24</sup>, E. Brück<sup>41</sup>, and F. R. de Boer<sup>41</sup>.

### Magnetic Ordering of Sm and Cu in $\text{Sm}_2\text{CuO}_4$

S. Skanthakumar<sup>43,3</sup>, J. W. Lynn<sup>27</sup>, I. W. Sumarlin<sup>43</sup>, J. L. Peng<sup>43</sup>, and Z. Y. Li<sup>43</sup>.

### Non-collinear Magnetic Structure of the Cu Spins in $\text{R}_2\text{CuO}_4$ ( $R = \text{Nd, Sm, Pr}$ )

S. Skanthakumar<sup>43,3</sup>, J. W. Lynn<sup>27</sup>, I. W. Sumarlin<sup>43</sup>, J. L. Peng<sup>43</sup>, and Z. Y. Li<sup>43</sup>.

### Phonon Density-of-States in $\text{R}_2\text{CuO}_4$ and Superconducting $\text{R}_{1.85}\text{Ce}_{0.15}\text{CuO}_4$ ( $R = \text{Nd, Pr}$ )

I. W. Sumarlin<sup>43</sup>, J. W. Lynn<sup>27</sup>, D. A. Neumann<sup>27</sup>, J. J. Rush<sup>27</sup>, J. L. Peng<sup>43</sup>, and Z. Y. Li<sup>43</sup>.

### Magnetic Ordering in $\text{Eu}_2\text{CuO}_4$

T. Chattopadhyay<sup>12</sup>, J. W. Lynn<sup>27</sup>, N. Rosov<sup>27</sup>, S. N. Barilo<sup>6</sup>, and D. I. Zhigunov<sup>6</sup>.

### Magnetic Field Penetration Depth in Superconductors by Polarized Neutron Reflectometry

H. Zhang<sup>43,27</sup>, J. W. Lynn<sup>27</sup>, C. F. Majkrzak<sup>27</sup>, S. K. Satija<sup>27</sup>, and J. H. Kang<sup>50</sup>.

- Magnetic Fluctuations in U(Cu-Pd)<sub>5</sub> Alloys**  
M. Aronson<sup>44</sup>, J. W. Lynn<sup>27</sup>, R. A. Robinson<sup>17</sup>, C. Seaman<sup>39</sup>, M. B. Maple<sup>39</sup>, and R. Osborn<sup>3</sup>.
- Cerium and Oxygen Dependence of the Nd and Cu Magnetic Order in Nd<sub>2-x</sub>Ce<sub>x</sub>O<sub>4-y</sub>**  
S. Skanthakumar<sup>43,3</sup>, J. W. Lynn<sup>27</sup>, J. L. Peng<sup>43</sup>, and Z. Y. Li<sup>43</sup>.
- Neutron Powder Diffraction Study of the Nuclear and Magnetic Structures of the Oxygen-Deficient Perovskite YBaCuCoO<sub>5</sub>**  
Q. Huang<sup>43,27</sup>, P. Karen<sup>47</sup>, V. L. Karen<sup>27</sup>, A. Kjekshus<sup>47</sup>, J. W. Lynn<sup>27</sup>, A. D. Mighel<sup>27</sup>, I. Natali Sora<sup>31</sup>, N. Rosov<sup>27</sup>, and A. Santoro<sup>27</sup>.
- Crystal and Magnetic Structures of NiF<sub>3</sub>**  
L. Chacon<sup>37</sup>, N. Rosov<sup>27</sup>, and J. W. Lynn<sup>27</sup>.
- Magnetic Small Angle Scattering in the Nanocrystalline Amorphous System Fe<sub>73.5</sub>B<sub>9</sub>Si<sub>13.5</sub>Cu<sub>1</sub>Nb<sub>3</sub>**  
N. Rosov<sup>27</sup>, J. W. Lynn<sup>27</sup>, and G. Fish<sup>1</sup>.
- Magnetic Ordering in Dy<sub>5</sub>Os<sub>4</sub>Ge<sub>10</sub>**  
J. W. Lynn<sup>27</sup>, L. C. Gupta<sup>30</sup>, M. Lin<sup>10</sup>, and S. K. Sinha<sup>10</sup>.
- Search for Magnetic Order in Nd<sub>1.5</sub>Ba<sub>1.5</sub>Cu<sub>3</sub>O<sub>7</sub>**  
J. W. Lynn<sup>27</sup>, K. K. Singh<sup>19</sup>, and D. E. Morris<sup>19</sup>.
- Magnetic Ordering in RPO<sub>4</sub> and RVO<sub>4</sub> Systems**  
S. Skanthakumar<sup>43,3</sup>, C.-K. Loong<sup>3</sup>, L. Soderholm<sup>3</sup>, and J. W. Lynn<sup>27</sup>.
- Search for Magnetic Order in YbBiPt**  
R. A. Robinson<sup>17</sup>, J. W. Lynn<sup>27</sup>, and R. W. Erwin<sup>27</sup>.
- Magnetic Ordering in UAuCu<sub>4</sub> and UAgCu<sub>4</sub>**  
M. Aronson<sup>44</sup>, J. W. Lynn<sup>27</sup>, Y. Dalichaouch<sup>39</sup>, and M. B. Maple<sup>39</sup>.
- Cerium and Oxygen Dependence of the Nd and Cu Order in Nd<sub>2-x</sub>Ce<sub>x</sub>CuO<sub>4-y</sub>**  
S. Skanthakumar<sup>43,3</sup>, J. W. Lynn<sup>27</sup>, J. L. Peng<sup>43</sup>, and Z. Y. Li<sup>43</sup>.
- Structural and Magnetic Phase Transitions in KMnF<sub>3</sub>**  
P. M. Gehring<sup>27</sup>, S. M. Shapiro<sup>8</sup>, B. J. Sternleib<sup>9</sup>, A. Gibaud<sup>40</sup>, and J. Nouet<sup>40</sup>.
- Effects of Nb Dipole Impurities on the Lattice Dynamics of the Incipient Ferroelectric KTaO<sub>3</sub>**  
P. M. Gehring<sup>27</sup>, S. M. Shapiro<sup>8</sup>, H. Chou<sup>8</sup>, J. Toulouse<sup>16</sup>, and L. A. Boatner<sup>23</sup>.
- Effects of Random Magnetic Anisotropy on the Magnetism of Dy<sub>x</sub>Y<sub>1-x</sub>Al<sub>2</sub> Single Crystals**  
P. M. Gehring<sup>27</sup> and A. del Moral<sup>48</sup>.
- Anharmonicity of the Soft Ferroelectric Modes in PbTiO<sub>3</sub>**  
C. M. Foster<sup>3</sup>, P. M. Gehring<sup>27</sup>, and D. A. Neumann<sup>27</sup>.
- Magnetic Frustration in NiS<sub>2</sub>**  
T. Thio<sup>22</sup>, T. R. Thurston<sup>8</sup>, and P. M. Gehring<sup>27</sup>.
- Anomalous Critical Scattering in Tb**  
P. M. Gehring<sup>27</sup>, C. F. Majkrzak<sup>27</sup>, K. Hirota<sup>8</sup>, and G. Shirane<sup>8</sup>.
- Anomalous Critical Scattering in Ho Thin Films**  
L. D. Gibbs<sup>8</sup>, T. R. Thurston<sup>8</sup>, J. Hill<sup>8</sup>, G. Helgesen<sup>8</sup>, P. M. Gehring<sup>27</sup>, and C. F. Majkrzak<sup>27</sup>.
- Magnetic Structure Determination in Fe<sub>3</sub>O<sub>4</sub>/NiO Superlattices**  
J. A. Borchers<sup>27</sup>, R. W. Erwin<sup>27</sup>, S. D. Berry<sup>11</sup>, and D. M. Lind<sup>11</sup>.
- Spatially Modulated Antiferromagnetic Order in NiO/CoO Superlattices**  
J. A. Borchers<sup>27</sup>, M. J. Carey<sup>39</sup>, R. W. Erwin<sup>27</sup>, A. E. Berkowitz<sup>39</sup>, and C. F. Majkrzak<sup>27</sup>.
- Identification of the Antiferromagnetic Phase in SmMn<sub>2</sub>Ge**  
J. A. Borchers<sup>27</sup>, R. W. Erwin<sup>27</sup>, and R. B. van Dover<sup>5</sup>.
- Quasielastic Diffraction Studies of Bulk Holmium through T<sub>N</sub>**  
T. R. Thurston<sup>7</sup>, J. P. Hill<sup>7</sup>, L.D. Gibbs<sup>7</sup>, R. W. Erwin<sup>27</sup>, and J. A. Borchers<sup>27</sup>.
- Exchange Coupling in Dy/Er Superlattices**  
K. Dumesnil<sup>46</sup>, C. Dufour<sup>46</sup>, Ph. Mangin<sup>46</sup>, G. Marchal<sup>46</sup>, W. T. Lee<sup>45</sup>, H. Kaiser<sup>45</sup>, J. J. Rhyne<sup>45</sup>, R. W. Erwin<sup>27</sup>, and J. A. Borchers<sup>27</sup>.

**Enhanced Curie Temperatures and Magnetoelastic Domains in Dy/Lu Superlattices and Films**

R. S. Beach<sup>42</sup>, J. A. Borchers<sup>27</sup>, R. W. Erwin<sup>27</sup>, A. Matheny<sup>42</sup>, M. B. Salamon<sup>42</sup>, C. P. Flynn<sup>42</sup>, and J. J. Rhyne<sup>45</sup>.

**Magnetic Properties of Dy<sub>x</sub>Lu<sub>1-x</sub> Films**

B. A. Everitt<sup>42</sup>, M. B. Salamon<sup>42</sup>, C. P. Flynn<sup>42</sup>, B. J. Park<sup>42</sup>, J. A. Borchers<sup>27</sup>, and R. W. Erwin<sup>27</sup>.

**Characterization of the Magnetic Structures in Nd Films and Nd/Y Superlattices**

B. A. Everitt<sup>42</sup>, J. A. Borchers<sup>27</sup>, R. W. Erwin<sup>27</sup>, M. B. Salamon<sup>42</sup>, B. J. Park<sup>42</sup>, C. P. Flynn<sup>42</sup>, and J. J. Rhyne<sup>45</sup>.

**On the Topology of London Fluxoids as Applied to Superconducting Shields Employed in an Experiment Using Local Theory to Bound a Possible "Low Temperature" Photon Mass**

R. C. Casella<sup>27</sup>.

**On the Wagh-Rakhecha Phase and Its Relation to the Casella-Werner Analysis of the Anandan Acceleration of Neutrons in Constant Electric and Magnetic Fields**

R. C. Casella<sup>27</sup> and S. W. Werner<sup>51</sup>.

**Search for Magnetic Ordering in CuCl<sub>2</sub> Graphite Intercalate**

D. G. Wiesler<sup>27</sup>, N. Rosov<sup>27</sup>, M. Suzuki<sup>29</sup>, and I. Suzuki<sup>29</sup>.

**Incommensurate Magnetic Order in MnCl<sub>2</sub> Graphite Intercalate**

D. G. Wiesler<sup>27</sup>, N. Rosov<sup>27</sup>, M. Suzuki<sup>29</sup>, and I. Suzuki<sup>29</sup>.

**Spin Correlations in Metallic and Insulating V<sub>2-y</sub>O<sub>3</sub>**

W. Bao<sup>13</sup>, C. L. Broholm<sup>13</sup>, S. A. Carter<sup>40</sup>, T. F. Rosenbaum<sup>40</sup>, G. Aeppli<sup>5</sup>, J. M. Honig<sup>26</sup>, J. Spalek<sup>26</sup>, and S. F. Trevino<sup>27,2</sup>.

**Spin Dynamics in a Doped Haldane Chain**

J. F. Ditusa<sup>5</sup>, S. W. Cheong<sup>5</sup>, H. W. Hwang<sup>5</sup>, G. Aeppli<sup>5</sup>, and C. L. Broholm<sup>13</sup>.

**Crystal Structure of SrCr<sub>8-x</sub>Ga<sub>4+x</sub>O<sub>19</sub>**

S. H. Lee<sup>13</sup>, C. L. Broholm<sup>13</sup>, G. Aeppli<sup>5</sup>, A. P. Ramirez<sup>5</sup>, and B. Hessen<sup>5</sup>.

**Antiferromagnetism in the Stacked Kagome Antiferromagnet KCr<sub>3</sub>(OH)<sub>6</sub>(SO<sub>4</sub>)<sub>2</sub>**

S. H. Lee<sup>13</sup>, C. L. Broholm<sup>13</sup>, M. F. Collins<sup>18</sup>, L. Heller<sup>18</sup>, C. Kloc<sup>5</sup>, E. Bucher<sup>5</sup>, and R. W. Erwin<sup>27</sup>.

**Affiliations**

<sup>1</sup>Allied Signal Corp.

<sup>2</sup>Army Armament RD&E Center

<sup>3</sup>Argonne National Lab

<sup>4</sup>Arizona State University

<sup>5</sup>AT&T Bell Laboratories

<sup>6</sup>Belarus Academy of Sciences

<sup>7</sup>Brookhaven National Lab

<sup>8</sup>Charles University, Prague

<sup>9</sup>Columbia University

<sup>10</sup>Exxon Research & Engineering Co.

<sup>11</sup>Florida State University

<sup>12</sup>Institut Laue-Langevin

<sup>13</sup>Johns Hopkins University

<sup>14</sup>KFA Jülich

<sup>15</sup>Lawrence Livermore Laboratory

<sup>16</sup>Lehigh University

<sup>17</sup>Los Alamos National Laboratory

<sup>18</sup>McMaster University

<sup>19</sup>Morris Research, Berkeley

<sup>20</sup>National Central U., Taiwan

<sup>21</sup>Nat'l Sun Yat-Sen U, Taiwan

<sup>22</sup>Niffon Electric Co.

<sup>23</sup>Oak Ridge National Lab

<sup>24</sup>Philips Research Labs

<sup>25</sup>Princeton University

<sup>26</sup>Purdue University

<sup>27</sup>Reactor Radiation Division

<sup>28</sup>Ruhr Universität

<sup>29</sup>SUNY at Binghamton

<sup>30</sup>Tata Institute of Fundamental Research, Bombay

<sup>31</sup>Universita di Brescia, Italy

<sup>32</sup>Universität Bochum, Germany

<sup>33</sup>Universität Duisberg, Germany

<sup>34</sup>Universität Karlsruhe, Germany

<sup>35</sup>Université du Maine

<sup>36</sup>University of Amsterdam

<sup>37</sup>University of California, Berkeley

<sup>38</sup>University of California, Davis

<sup>39</sup>University of California, San Diego

<sup>40</sup>University of Chicago

<sup>41</sup>University of Houston

<sup>42</sup>University of Illinois

<sup>43</sup>University of Maryland

<sup>44</sup>University of Michigan

<sup>45</sup>MURR, University of Missouri

<sup>46</sup>University of Nancy I, France

<sup>47</sup>University of Oslo

<sup>48</sup>University of Zaragoza, Spain

<sup>49</sup>Ural State University, Russia

<sup>50</sup>Westinghouse

<sup>51</sup>Physics & Astronomy Dept., University of Missouri, Columbia

## Instrumentation

Installation of the new 32-detector powder diffractometer at BT-1 was completed in the winter of 1992/1993, followed by calibration and modifications to reduce background during the spring. Routine operation was begun in June 1993; in the ensuing four-month period, over 200 data sets were collected on 95 materials, in spite of continuing testing time during this period. This dramatic increase in productivity over the old diffractometer is the direct result of greater intensity from the focusing monochromators and the ability to scan a smaller angular  $2\theta$  range owing to the expansion from five to 32 detectors. The time required for a full data set now ranges from 2-16 hr (depending upon desired resolution and sample size), compared to 24-48 hr on the previous instrument. Patterns under the resolution condition of the old diffractometer can be taken about 20-25 times faster. Backgrounds are also lower for the new instrument. Further improvements in intensity this year will allow full patterns to be taken in about 1 hr. At this writing scientists from over 20 organizations have participated in research with the new instrument. Experiments are now being performed that would have not been feasible in the past, for example, collection of data on samples as small as 0.2 g or at 10 or more temperatures in a single day. An important additional bonus is that data are obtained over a larger angular range, with useful data up to about  $160^\circ$

$2\theta$  compared to the previous  $120^\circ$  limit. These additional data are particularly important for refinement of site occupancies and the determination of relatively large crystal structures. The design of the diffractometer was described in the previous Summary of Activities (NISTIR 5120).

The three automatically-selectable monochromator choices (see Table 1) produce Gaussian line shapes at both  $7'$  and  $15'$  incident collimation.

Table 1. Monochromator data

mono-chromator	take-off angle	wavelength	relative intensity
Cu 220	$75^\circ$	1.5547 Å	100
Cu 311	$90^\circ$	1.5398 Å	63
Si 531	$120^\circ$	1.5899 Å	30

Figure 1 shows a region of the diffraction pattern of  $Tb_2Ti_2O_7$  for four possible instrument configurations. The experimental resolution curves are presented in figure 2. These curves closely approximate the calculated resolutions. The actual resolution for an "ideal" powder may be slightly better. FWHM's are as low as 10 min. Most data sets have been collected using the Cu 311 monochromator with  $15'$  incident collimation, which provides a good compromise between intensity and resolution. The resolution available on the new instrument is about two to four times better than that of the old one at higher  $2\theta$  (Q).

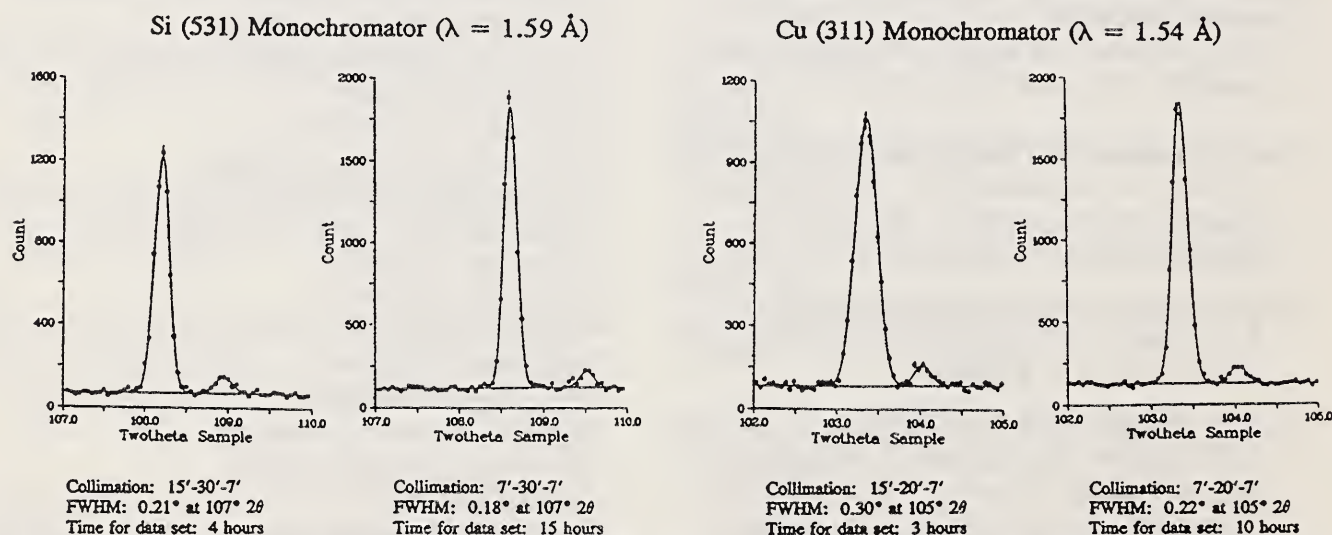
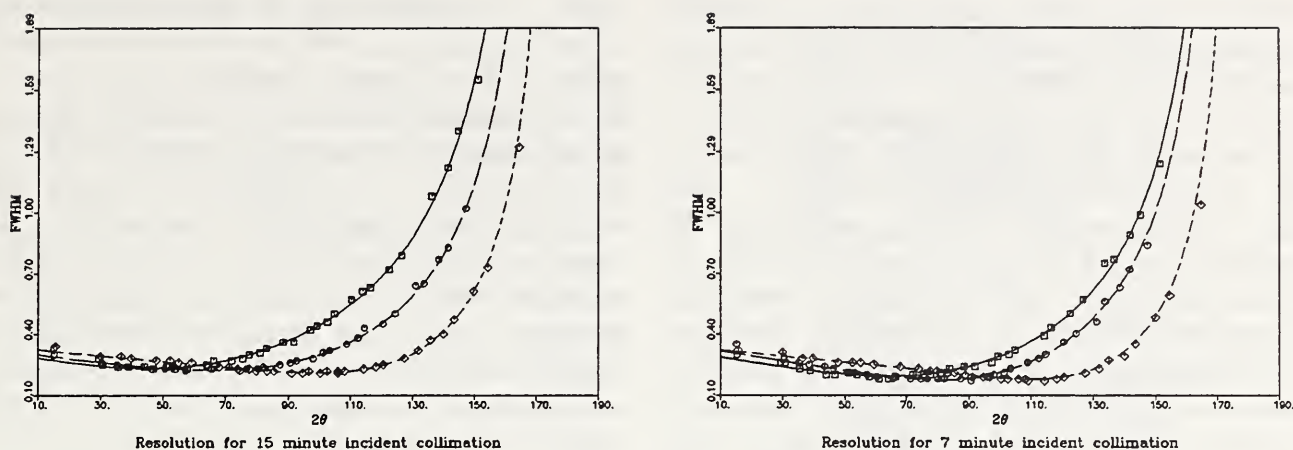


Figure 1. Experimental data points with Gaussian fits of two peaks in the neutron powder diffraction pattern of  $Tb_2Ti_2O_7$  for four possible BT-1 configurations. The times given for collection of a complete data set are approximate, and should in fact decrease significantly with further instrument modifications.



**Figure 2.** Experimental instrument resolution (full width at half maximum, in degrees) for 15' and 7' incident collimation for the Cu 220 ( $\square$ ), Cu 311 ( $\circ$ ), and Si 531 ( $\diamond$ ) monochromators, obtained from the diffraction pattern of  $\text{Tb}_2\text{Ti}_2\text{O}_7$ . For comparison between the two incident collimations, the resolution curve for the Cu 220 monochromator at 7' incident collimation is nearly coincident with that of the Cu 311 monochromator at 15' incident collimation.

## Crystal Structures

### • New Hg Superconductors

Since the discovery of superconductivity in the copper-oxide systems, the expectation has been that these new materials would make widespread commercial applications of superconductivity viable. Due to the anisotropic superconducting properties combined with generally unfavorable mechanical and materials properties, however, progress has been frustratingly slow, but now applications involving not only thin films but also wires are becoming a reality. From the materials science standpoint, the hope is that new classes of superconductors will be discovered with improved superconducting and/or mechanical properties, and therefore the community has been excited by the recent discovery of superconductivity in a new series of mercury-containing compounds, with superconducting transition temperatures as high as 140 K at ambient pressure and over 160 K under high pressure. One of the first orders of business is to determine the crystal structure and phase diagram of these new materials, in particular with respect to the role of oxygen on the electronic properties. Consequently we have undertaken neutron powder profile refinements of these materials in this laboratory.

The Hg-based series of materials is quite similar to some of the other cuprate superconductors, in that it consists of a homologous

series of general formula  $\text{HgBa}_2\text{X}_{n-1}\text{Cu}_n\text{O}_{2n+2+\delta}$  (where X is an element such as Ca), with the superconducting transition temperature increasing with the number of Cu layers in the unit cell. Figure 3 shows the results [1,2] for the single layer material (on the left)  $\text{HgBa}_2\text{CuO}_{4.06}$ , designated 1201. The crystal structure is tetragonal ( $a = 3.883 \text{ \AA}$ ,  $c = 9.513 \text{ \AA}$ ), and is similar in some respects to the electron-superconductor materials, with the same space group ( $P4/mmm$ ). The single Cu-O layer is to a first approximation in square-planar coordination, with a Cu-O separation of  $1.94 \text{ \AA}$ ; the oxygen ions surrounding the Cu actually form a distorted octahedron, but the apical Cu-O(2) distance is  $2.78 \text{ \AA}$ . In all the superconducting samples we studied we found no evidence of Cu occupying the Hg sites, in contrast to a suggestion made in some early work [3] on impure samples. One of the difficulties found in the refinements for all these early studies was the persistence of anomalous Debye Waller factors for some of the atoms, which we traced to the influence of a relatively small amount of an unrefineable impurity phase in the samples. On high purity samples these difficulties with the thermal parameters do not occur, and the results unambiguously demonstrate that Cu does not reside on the Hg sites in the superconducting systems [2].

There are a number of interesting features of this single-layer material. One aspect concerns the doping, which is accomplished by adding a small

amount of extra oxygen (less than 0.1 for optimum doping) into the centered position in the Hg plane as shown in the figure 3. The doping appears to be similar to the “superoxygenated”  $\text{La}_2\text{CuO}_{4+\delta}$  system, rather than substitutional doping such as for  $(\text{La-Sr})_2\text{CuO}_{4+\delta}$  or  $(\text{Nd-Ce})_2\text{CuO}_{4+\delta}$ . This raises an important question concerning the possible role that the Hg-O layers might play in enhancing the superconducting transition temperature. This is particularly significant considering that the superconducting transition temperature is 94 K, the highest of any single-layer system, while the unit cell contains but a single layer of Cu-O separated by the rather large distance of 9.5 Å.

The structures of the double layer (1212) [4, 5] and triple layer (1223) [6] materials are also shown in figure 3. There is a direct analogy between this

series of materials and the homologous series  $\text{TlBa}_2\text{Ca}_{n-1}\text{Cu}_n\text{O}_{2n+3-\delta}$ , with the same P4/mmm space group. The basic crystal chemistry is the same as for the single layer Hg system in that the doping is accomplished by oxygen in the centered position of the Hg layers. The added  $\text{CuO}_2$  layers and additional doping on the Hg layer increases the superconducting transition from  $\sim 126$  K for the two-layer material to  $\sim 133$  K for the three-layer material. One of the interesting observations is that the transition can be increased dramatically with pressure [7], with  $T_c$ 's up to 164 K having been observed already. The question now is whether these higher  $T_c$ 's can be produced at ambient pressure by appropriate chemical substitutions, and our present emphasis is on investigating the crystallography of such chemically substituted systems.

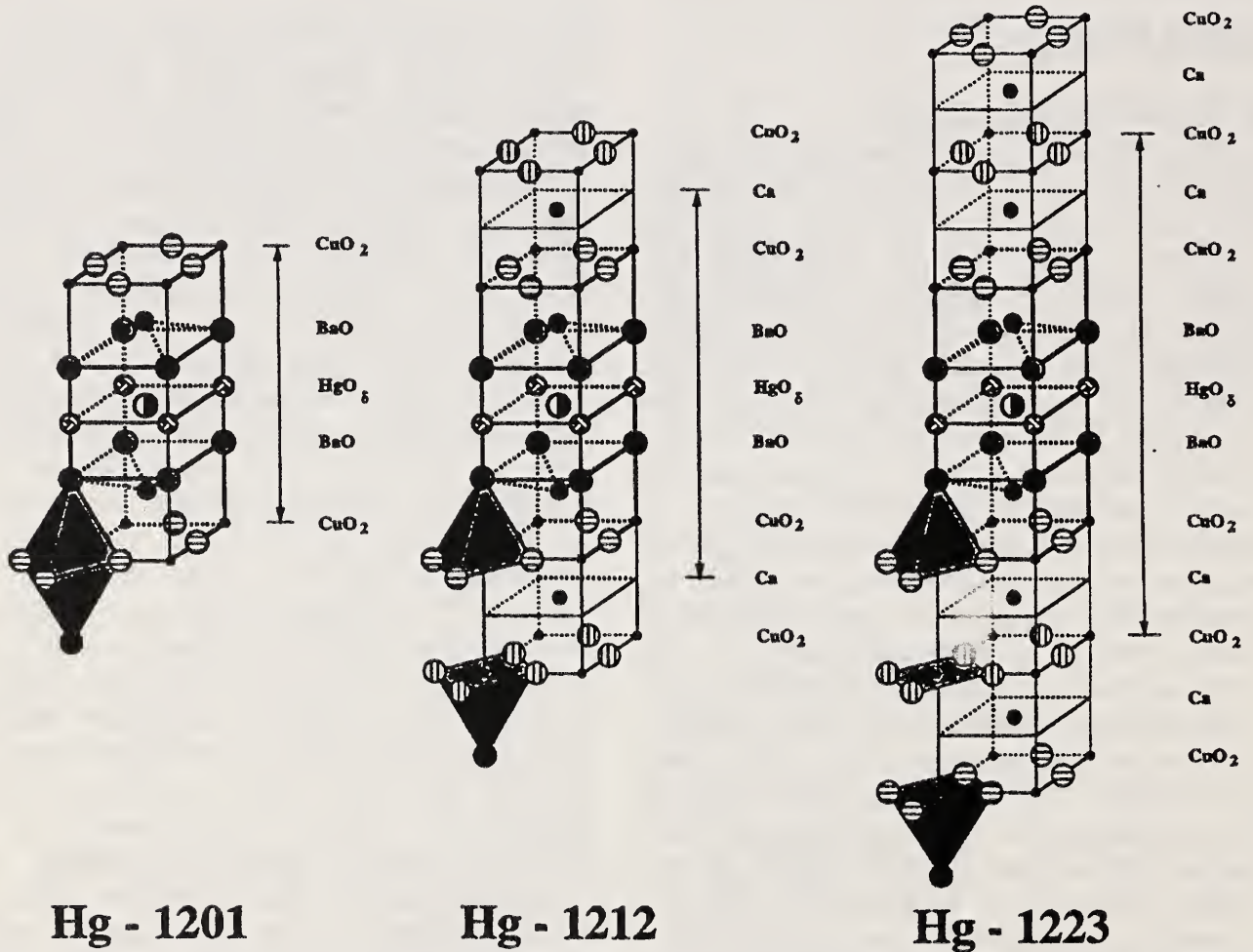


Figure 3. Crystal structures of the single layer (left), double layer (middle), and triple layer (right) mercury superconductors.

## The Structure of $\text{La}_3\text{Ti}_5\text{Al}_{15}\text{O}_{37}$

The use of powder diffraction in structural crystallography has again been extended with the determination and refinement of the structure of  $\text{La}_3\text{Ti}_5\text{Al}_{15}\text{O}_{37}$ , which has 60 atoms in the asymmetric unit. This compound crystallizes in space group Cc, with  $a = 22.5655(3) \text{ \AA}$ ,  $b = 10.9863(2) \text{ \AA}$ ,  $c = 9.7189(2) \text{ \AA}$ ,  $\beta = 98.569(2)^\circ$ . A starting model was obtained by applying direct methods to a set of 1902 independent reflections whose integrated intensities were measured on an X-ray powder pattern collected at the Synchrotron Radiation Source in Daresbury, UK. Neutron diffraction powder patterns were collected on BT-1 using both the Cu 311 monochromator ( $\lambda = 1.539 \text{ \AA}$ ) and the Si 531 monochromator ( $\lambda = 1.589 \text{ \AA}$ ), and the structure was refined using both data sets simultaneously. The final agreement factors with 162 independent structural parameters were  $R_B = 6.69\%$ ,  $R_{wp} = 8.79\%$ ,  $R_e = 3.82\%$ ,  $\chi = 2.23$ .

$\text{La}_3\text{Ti}_5\text{Al}_{15}\text{O}_{37}$  consists of blocks of  $\text{La}_2\text{Ti}_2\text{O}_7$  interleaved with regions of  $\text{LaAlO}_3$  and  $\text{Al}_2\text{TiO}_5$  type structures. The lanthanum atoms, two with 12 coordination and one with 11 coordination, show great similarity to those found in the pyrochlore type phase  $\text{La}_2\text{Ti}_2\text{O}_7$ . These lanthanum coordination polyhedra are linked by sharing of faces to three of the  $\text{TiO}_6$  units. These titanium containing units are also distorted in a manner similar to that seen in  $\text{La}_2\text{Ti}_2\text{O}_7$ , with three long Ti-O bonds and three short Ti-O bonds. The aluminum coordination polyhedra are also highly distorted, with some of them having long (2.2-2.3  $\text{ \AA}$ ) Al-O bonds similar to those seen in the pseudobrookite structure of  $\text{Al}_2\text{TiO}_5$ . Figure 4 is a view of the structure looking down the c axis.

### Technique Development

#### ● Preferred Orientation

Although Rietveld's original program for structure refinement from powder diffraction data contained provision for a preferred orientation parameter, the refinement of a structure when the sample did not consist of randomly oriented grains has never been really satisfactory. In recent years methods have been developed for measuring a quantitative orientational distribution function

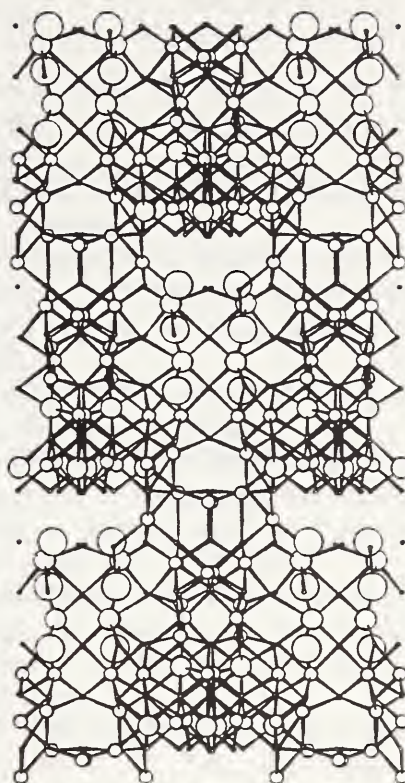
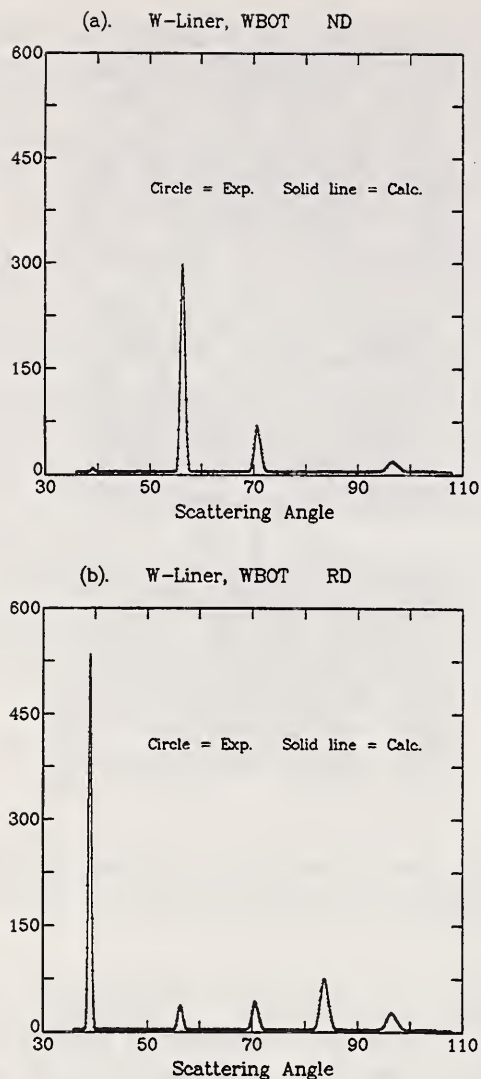


Figure 4. View of  $\text{La}_3\text{Ti}_5\text{Al}_{15}\text{O}_{37}$  looking down [001]. Atoms, in order of decreasing size, are La, Ti, Al, and O.

(ODF) for the crystallites in a textured, solid sample. From this distribution function it is possible to work backwards and, for each set of reflecting planes, calculate an "effective multiplicity" for a sample mounted in a particular orientation with respect to the incident and diffracted beam directions. This effective multiplicity can then be incorporated in a Rietveld refinement program to refine other structural parameters.

As part of an ongoing Department of Defense project, quantitative orientation distribution functions have been measured for a number of components fabricated from heavy metals, such as tungsten and tantalum, in order to study correlations between manufacturing procedures and performance. Powder diffraction data have been collected from these components with special directions, a normal to the surface of a rolled plate or a rolling direction, for example, mounted parallel to the diffraction vector. These data have been refined with a modified Rietveld program with excellent results, showing that there is the possibility of structure refinement in samples that



**Figure 5.** The observed and calculated neutron diffraction intensities from a highly textured tungsten sample. (a) The normal to the plate parallel to the diffraction vector; (b) the rolling direction parallel to the diffraction vector.

are affected by preferred orientation. Figure 5 shows a pair of diffraction patterns collected from a highly textured sample of tungsten in different orientations, compared with fits to the data.

### • Absorption Effects

Multi-detector powder diffractometers which simultaneously sample a wide range of scattering angles  $2\theta$  require a powder container with high symmetry in order to be able to usefully analyze data over the entire angular range. To date, as described in the International Tables for Crystallography and other references [8,9], the magnitude of the mean absorption has only been generally available for the solid cylinder and sphere. This is sufficient for materials with relatively small

absorption lengths  $\mu$ . However, for materials with large absorption, the standard way to reduce the amount of absorption has been to decrease the amount of material, either by using cylinders of smaller diameter or by diluting with some other weakly absorbing and diffracting material.

However, a method which provides superior signal-to-noise is to arrange the material of interest in a cylindrical annulus. This has several advantages over merely using a cylinder of smaller diameter:

1. For a given amount of material, the sample radius can be increased, thereby intercepting more neutrons.
2. There is less probability for true absorption.
3. The requirements for measuring the actual absorption of the sample when the radius of the sample is large are much less demanding, since the sample thickness  $t$  for the absorption measurement may be more precisely determined.

The advantages over dilution of the sample include not needing to render the sample useless for other studies and not having extra scattering lines in the powder pattern. In addition, for a given quantity of sample, over certain angular ranges the absorption is less for the annular sample shape.

We have written a program to numerically calculate the absorption as a function of scattering angle given values for  $\mu t$  and  $t/R$ , where  $\mu$  is the linear absorption coefficient,  $t$  is the thickness of the shell, and  $R$  is the radius of the outermost cylinder [8]. These calculations reduce to those given in [9, 10] when  $t/R = 1$ .

The program has already been used for the analysis of several powder patterns for samples containing Hg [4] on the new BT-1 diffractometer. A threefold gain in intensity was achieved in this case by using the annular geometry. As an extreme example of the benefits of this annular geometry, transmission factors  $A_{hkl}$  for Cd in several geometries and  $\lambda = 1.5 \text{ \AA}$  have been calculated (see Fig. 6). The open circles show  $A_{hkl}$  in the annular geometry with a 2 cm outer diameter and a thickness of 0.011 cm (so  $\mu t = 1$ ). The solid circles show the transmission for the same mass of powder in a solid cylinder, where the absorption is more than two orders-of-magnitude larger at small angles, and roughly a factor of eight more at larger scattering angles. Diluting the sample so that it uniformly fills the 2 cm cylinder provides an intermediate case, denoted



by the open squares, with greater absorption at smaller scattering angles.

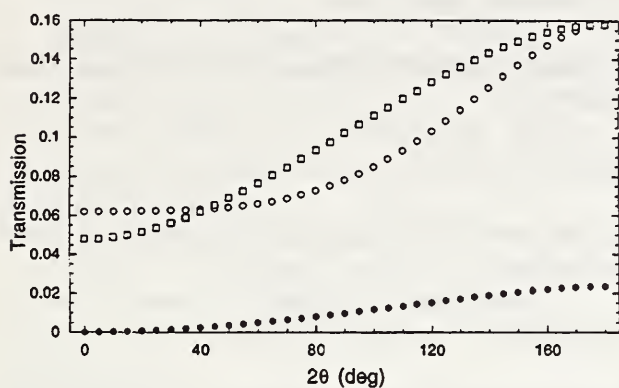


**Figure 6.** Transmission for Cd in various geometries, for the same amount of sample. ○ annulus,  $\mu t = 1.0$ ,  $t/R = 0.0107$ ; ● solid cylinder,  $\mu t = 13.57$ ,  $t/R = 1.0$ ; and □ dilute cylinder,  $\mu t = 1.98$ ,  $t/R = 1.0$ .

## Diffraction Data Center

One of the principal activities of the Data Center was the widespread distribution of the computer program NIST\*LATTICE. This program performs several functions, including: 1) the determination of symmetry and the evaluation of experimental error; 2) the generation of transformation matrices relating any two unit cells; and 3) the calculation of the reduced cell of a lattice and the calculation and reduction of specified derivative supercells or subcells.

It is not at all unusual for crystals to be assigned to the wrong space group. The symmetry determination feature of NIST\*LATTICE can help to prevent this by detecting lattice symmetry that was not observed in the original structure determination. The program has been installed in the office of the Technical Editor of *Acta Crystallographica* and is routinely used to check submitted manuscripts for incorrect symmetry. The International Union of Crystallography is also proceeding to make the program available to other journals that publish crystallographic results in hopes of preventing publication of incorrect information. There are also plans to incorporate the theory and program into the software for driving commercial diffractometers in order to automate the data collection process in a logical manner.

## References

- [1] O. Chmaissem, Q. Huang, S. N. Putilin, M. Marezio, and A. Santoro, *Physica C* **212**, 259 (1993).
- [2] Q. Huang, J. W. Lynn, Q. Xiong, and C. W. Chu (preprint).
- [3] J. L. Wagner, P. G. Radaelli, D. G. Hinks, J. D. Jorgensen, J. F. Mitchell, B. Dabrowski, G. S. Knapp, and M. A. Beno, *Physica C* **210**, 447 (1993).
- [4] Q. Huang, J. W. Lynn, R. L. Meng, and C. W. Chu, *Physica C* (in press).
- [5] E. V. Antipov, J. J. Capponi, C. Chaillout, O. Chmaissem, S. M. Loureiro, M. Marezio, S. N. Putilin, A. Santoro, and J. L. Tholence, *Physica C* (in press).
- [6] O. Chmaissem, Q. Huang, E. V. Antipov, S. N. Putilin, M. Marezio, S. M. Loureiro, J. J. Capponi, J. L. Tholence, and A. Santoro, *Physica C* (in press).
- [7] C. W. Chu, L. Gao, F. Chen, Z. J. Huang, R. L. Meng, and Y. Y. Xue, *Nature* **365**, 323 (1993).
- [8] N. Rosov and J. W. Lynn (preprint).
- [9] K. D. Rouse, M. J. Cooper, E. J. York, and A. Chakera. *Acta Cryst.* (1970), A26, 682.
- [10] A. Hewat. *Acta Cryst.* (1979), A35, 248.

## Research Topics

### Powder Diffraction Studies on the Quasicrystal $\text{Al}_{0.625}\text{Cu}_{0.25}\text{Fe}_{0.125}$ with Isotopic Substitution

B. Mozer<sup>19</sup>, J. L. Soubeyroux<sup>8</sup>, and J. W. Cahn<sup>15</sup>.

### Neutron Powder Diffraction Studies of $\text{RFe}_{10.5}\text{Mo}_{1.5}\text{C}_x$ , R = Ho, Er, Y; x = 0.5, 1.0, 1.5

J. L. Soubeyroux<sup>8</sup>.

### Space Group Adapted Fast Fourier Transforms

E. Prince<sup>19</sup>, C. Lu<sup>22</sup>, M. An<sup>6</sup>, and R. Tolimieri<sup>6</sup>.

### Phase Determination in Macromolecular X-ray Diffraction Data by Maximum Entropy

E. Prince<sup>19</sup> and L. Sjölin<sup>9</sup>.

### Ab Initio Structure Solution of $\text{La}_3\text{Ti}_5\text{Al}_{15}\text{O}_{37}$ Using Synchrotron X-ray and Neutron Powder Diffraction Data

R. Morris<sup>28</sup>, J. Owen<sup>28</sup>, J. K. Stalick<sup>19</sup>, and A. K. Cheetham<sup>28</sup>.

### Neutron Powder Diffraction Studies of $\text{K}(\text{Y}_{1-x}\text{Yb}_x)\text{F}_4$ (x = 0.2, 0.5)

R. Morris<sup>28</sup>, J. Owen<sup>28</sup>, and A. K. Cheetham<sup>28</sup>.

- The Effect of Temperature on Oxygen and Lithium Positions in the Superconducting Spinel  $\text{Li}_{1+x}\text{Ti}_{2-x}\text{O}_4$**   
M. A. Green<sup>20</sup>, M. Dalton<sup>20</sup>, P. Day<sup>20</sup>, and J. K. Stalick<sup>19</sup>.
- Structural Phase Transitions in the  $\text{BaSn}_{1-x}\text{Sb}_x\text{O}_3$  System**  
M. A. Green<sup>20</sup>, K. Prassides<sup>21</sup>, P. Day<sup>20</sup>, and J. K. Stalick<sup>19</sup>.
- Structure of the Ruddleston-Popper Series,  $\text{Sr}_{n+1}\text{Sn}_n\text{O}_{n+1}$  Determined by Powder Neutron Diffraction**  
M. A. Green<sup>20</sup>, K. Prassides<sup>21</sup>, P. Day<sup>20</sup>, and J. K. Stalick<sup>19</sup>.
- High-Resolution Neutron Diffraction Study of Distortions of the ZrPd Lattice**  
L. A. Bendersky<sup>16</sup>, R. M. Waterstrat<sup>2</sup>, and J. K. Stalick<sup>19</sup>.
- Determination of Antiferromagnetic Structure in  $\text{SmMn}_2\text{Ge}$**   
J. A. Borchers<sup>19</sup>, R. W. Erwin<sup>19</sup>, and B. Van Dover<sup>5</sup>.
- The Structure of Neopentane at 4K**  
P. Depondt<sup>24</sup> and S. Trevino<sup>4,19</sup>.
- Study of Structural and Magnetic Phase Transitions in  $\text{KMnF}_3$**   
P. M. Gehring<sup>19</sup>, S. Shapiro<sup>7</sup>, B. Sternlieb<sup>7</sup>, A. Gibaud<sup>23</sup>, J. Nouet<sup>23</sup>, and H. Yu<sup>3</sup>.
- Orientalional Structure of  $\text{Rb}_{2.6}\text{K}_{0.4}\text{C}_{60}$**   
W. A. Kamitakahara<sup>19</sup>, D. A. Neumann<sup>19</sup>, J. R. D. Copley<sup>19</sup>, J. E. Fischer<sup>34</sup>, M. Cichy<sup>34</sup>, R. M. Strongin<sup>34</sup>, and A. B. Smith III<sup>34</sup>.
- Application of ODF to the Rietveld Profile Refinement**  
C. S. Choi<sup>4,19</sup>, E. F. Baker<sup>4</sup>, and J. Orosz<sup>4</sup>.
- Quantitative Phase Analysis of Austempered Ductile Iron**  
C. S. Choi<sup>4,19</sup>, E. F. Baker<sup>4</sup>, and J. Orosz<sup>4</sup>.
- Structural Studies of  $\beta\text{-TbD}_{2+x}$**   
T. J. Udovic<sup>19</sup>, I. S. Anderson<sup>11</sup>, and J. Schefer<sup>17</sup>.
- Structural Studies of  $\text{LaH}_{2+x}$**   
T. J. Udovic<sup>19</sup>, I. S. Anderson<sup>11</sup>, and J. Schefer<sup>17</sup>.
- Neutron Powder Diffraction Study of  $\text{SrCr}_2\text{Ga}_4\text{O}_{19}$**   
C. L. Broholm<sup>12</sup> and S. H. Lee<sup>12</sup>.
- Structure and Ordering in  $\text{Ba}_2\text{LnBiO}_6$  (Ln = Ce, Pr, Tb) Distorted Perovskites**  
K. P. Reis<sup>30</sup>, W.T.A. Harrison<sup>30</sup>, A. J. Jacobson<sup>30</sup>, and J. M. Nicol<sup>19</sup>.
- Structural Characterization of  $\text{RbBiNb}_2\text{O}_7$  and  $\text{RbNdNb}_2\text{O}_7$**   
W.T.A. Harrison<sup>30</sup>, A. J. Jacobson<sup>30</sup>, and J. M. Nicol<sup>19</sup>.
- Determination of Cation Locations in Ion-Exchanged Ferrierites**  
U. Ruschewitz<sup>28</sup>, S. Weigel<sup>28</sup>, R. Morris<sup>28</sup>, A. K. Cheetham<sup>28</sup>, and J. M. Nicol<sup>19</sup>.
- Crystallographic Characterization of Li-Containing Zeolites**  
B. H. Toby<sup>1</sup>, J. MacDougall<sup>1</sup>, and J. M. Nicol<sup>19</sup>.
- Determination of Proton Locations in H/D Ferrierites**  
U. Ruschewitz<sup>28</sup>, A. K. Cheetham<sup>28</sup>, and J. M. Nicol<sup>19</sup>.
- Neutron Powder Diffraction Studies of the Phase Transitions and Structures of  $\text{Pr}_{1.5}\text{Ce}_{0.5}\text{Sr}_2\text{Cu}_2\text{TaO}_{10}$  and  $\text{Pr}_{1.5}\text{Ce}_{0.5}\text{Sr}_2\text{Cu}_2\text{NbO}_{10}$**   
N. Rosov<sup>19</sup>, J. W. Lynn<sup>19</sup>, T. J. Goodwin<sup>27</sup>, R. N. Shelton<sup>27</sup>, and H. B. Radousky<sup>13</sup>.
- Structural Studies of  $\text{NiF}_3$**   
L. Chacon<sup>29</sup>, N. Bartlett<sup>29</sup>, N. Rosov<sup>19</sup>, and J. W. Lynn<sup>19</sup>.
- The Crystal Structures of  $\text{HgBa}_2\text{CuO}_{4+\delta}$  (Hg-1201) and  $\text{HgBaO}_2$**   
O. Chmaissem<sup>8</sup>, Q. Huang<sup>31,21</sup>, S. N. Putilin<sup>32</sup>, M. Marezio<sup>8,6</sup>, and A. Santoro<sup>19</sup>.
- The Crystal Structure of  $\text{HgBa}_2\text{CaCu}_2\text{O}_{6+\delta}$  (Hg-1212)**  
E. V. Antipov<sup>32</sup>, J. J. Capponi<sup>8</sup>, C. Chaillout<sup>8</sup>, O. Chmaissem<sup>8</sup>, S. M. Loureiro<sup>8</sup>, M. Marezio<sup>8,6</sup>, S. N. Putilin<sup>32</sup>, A. Santoro<sup>19</sup>, and J. L. Tholence<sup>8</sup>.
- The Crystal Structure of  $\text{HgBa}_2\text{Ca}_2\text{Cu}_3\text{O}_{8+\delta}$  (Hg-1223)**  
O. Chmaissem<sup>8</sup>, Q. Huang<sup>31,21</sup>, E. V. Antipov<sup>32</sup>, S. N. Putilin<sup>32</sup>, M. Marezio<sup>8,6</sup>, S. M. Loureiro<sup>8</sup>, J. J. Capponi<sup>8</sup>, J. L. Tholence<sup>8</sup>, and A. Santoro<sup>19</sup>.
- The Crystal Structures of  $\text{Sr}_2\text{RuO}_4$  and  $\text{Sr}_2\text{IrO}_4$**   
Q. Huang<sup>31,21</sup>, J. L. Soubeyroux<sup>8</sup>, O. Chmaissem<sup>8</sup>, I. Natali Sora<sup>25</sup>, A. Santoro<sup>19</sup>, R. J. Cava<sup>5</sup>, J. J. Krajewski<sup>5</sup>, and W. F. Peck<sup>5</sup>.

**The Structures of the Defective Perovskites  $\text{Ba}(\text{In}_{0.67}\text{Zr}_{0.33})\text{O}_{2.67}$ ,  $\text{Ba}(\text{In}_{0.67}\text{Ce}_{0.33})\text{O}_{2.67}$  and  $(\text{La}_{0.5}\text{Ba}_{0.5})(\text{Co}_{0.7}\text{Cu}_{0.3})\text{O}_{3-\delta}$**

S. B. Adler<sup>29</sup>, S. L. Russek<sup>29</sup>, J. A. Reimer<sup>29</sup>, M. Fendorf<sup>29</sup>, Q. Huang<sup>31,21</sup>, A. Santoro<sup>19</sup>, J. W. Lynn<sup>19</sup>, J. Baltisberger<sup>29</sup>, P. Grandinetti<sup>29</sup>, U. Werner<sup>29</sup>, and A. Pines<sup>29</sup>.

**The Defective Structure of  $\text{Y}_{1-x}\text{Ca}_x\text{CuO}_{2+\delta}$  ( $x = 0.05, 0.01$ ;  $\delta = 0.5, 0.59$ )**

I. Natali Sora<sup>25</sup>, Q. Huang<sup>31,21</sup>, A. Santoro<sup>19</sup>, R. J. Cava<sup>5</sup>, J. J. Krajewski<sup>5</sup>, and W. F. Peck<sup>5</sup>.

**Study of the  $\text{BaPb}_{1-x}\text{Bi}_x\text{O}_3$  System:  $\text{BaPbO}_3$  and  $\text{BaPb}_{0.8}\text{Bi}_{0.2}\text{O}_3$**

Q. Huang<sup>31,21</sup>, A. Santoro<sup>19</sup>, R. J. Cava<sup>5</sup>, J. J. Krajewski<sup>5</sup>, and W. F. Peck<sup>5</sup>.

**Crystal Structures of  $\text{LaFeO}_3$  and  $\text{YFeO}_3$**

O. Chmaissem<sup>8</sup>, Q. Huang<sup>31,21</sup>, P. Karen<sup>33</sup>, V. L. Karen<sup>19</sup>, A. Kjekshus<sup>33</sup>, A. D. Mighell<sup>19</sup>, and A. Santoro<sup>19</sup>.

**The Crystal Structures of  $\text{La}_{0.1}\text{Y}_{0.9}\text{FeO}_3$  and  $\text{YBa}_2\text{Co}_{1.2}\text{Fe}_{1.8}\text{O}_3$**

O. Chmaissem<sup>8</sup>, Q. Huang<sup>31,21</sup>, P. Karen<sup>33</sup>, V. L. Karen<sup>19</sup>, A. Kjekshus<sup>33</sup>, A. D. Mighell<sup>19</sup>, and A. Santoro<sup>19</sup>.

**The Crystal Structures of  $(\text{Y}_{1-x}\text{La}_x)(\text{Ba}_{1-y}\text{La}_y)\text{Fe}_3\text{O}_{8+\delta}$**

O. Chmaissem<sup>8</sup>, Q. Huang<sup>31,21</sup>, P. Karen<sup>33</sup>, V. L. Karen<sup>19</sup>, A. Kjekshus<sup>33</sup>, A. D. Mighell<sup>19</sup>, and A. Santoro<sup>19</sup>.

**The Crystal Structure of  $\text{LaCuO}_{2.67}$**

Q. Huang<sup>31,21</sup>, A. Santoro<sup>19</sup>, R. J. Cava<sup>5</sup>, J. J. Krajewski<sup>5</sup>, and W. F. Peck<sup>5</sup>.

**Neutron Powder Diffraction Study of the Nuclear and Magnetic Structures of  $\text{YBa}_2\text{Fe}_3\text{O}_8$  at Room Temperature**

Q. Huang<sup>31,21</sup>, P. Karen<sup>33</sup>, V. L. Karen<sup>19</sup>, A. Kjekshus<sup>33</sup>, J. W. Lynn<sup>19</sup>, A. D. Mighell<sup>19</sup>, N. Rosov<sup>19</sup>, and A. Santoro<sup>19</sup>.

**Crystallographic and Magnetic Properties of  $\text{UAuSn}$**

R. A. Robinson<sup>14</sup>, J. W. Lynn<sup>19</sup>, V. Nunez<sup>33</sup>, K.H.J. Buschow<sup>18</sup>, H. Nakotte<sup>26</sup>, and A. C. Lawson<sup>14</sup>.

**Crystal Structure and Magnetic Ordering of the Rare Earth and Cu Moments in  $\text{R}\text{Ba}_2\text{Cu}_2\text{NbO}_8$  ( $\text{R}=\text{Nd}, \text{Pr}$ )**

N. Rosov<sup>19</sup>, J. W. Lynn<sup>19</sup>, H. B. Radousky<sup>13</sup>, M. Bennahmias<sup>5</sup>, T. J. Goodwin<sup>27</sup>, P. Klavins<sup>27</sup>, and R. N. Shelton<sup>27</sup>.

**Neutron Powder Diffraction Study of the Nuclear and Magnetic Structures of the Oxygen-Deficient Perovskite  $\text{YBaCuCoO}_5$**

Q. Huang<sup>31,21</sup>, P. Karen<sup>33</sup>, V. L. Karen<sup>19</sup>, A. Kjekshus<sup>33</sup>, J. W. Lynn<sup>19</sup>, A. D. Mighell<sup>19</sup>, I. Natali Sora<sup>25</sup>, N. Rosov<sup>19</sup>, and A. Santoro<sup>19</sup>.

**Crystal Structure of Annealed and As-Prepared  $\text{HgBa}_2\text{CaCu}_2\text{O}_{6+\delta}$**

Q. Huang<sup>31,21</sup>, J. W. Lynn<sup>19</sup>, R. L. Meng<sup>30</sup>, and C. W. Chu<sup>30</sup>.

**Local Structure, Vacancy Ordering, and Oxide-ion Motion in Defective Perovskites**

S. Adler<sup>29</sup>, S. Russek<sup>29</sup>, J. Reimer<sup>29</sup>, M. Fendorf<sup>29</sup>, A. Stacy<sup>29</sup>, Q. Huang<sup>31,21</sup>, A. Santoro<sup>19</sup>, J. Lynn<sup>19</sup>, J. Baltisberger<sup>29</sup>, P. Grandinetti<sup>29</sup>, U. Werner<sup>29</sup>, and A. Pines<sup>29</sup>.

**Neutron Powder Diffraction Study of the Nuclear and Magnetic Structures of the Substitutional Compounds  $(\text{Y}_{1-x}\text{Ca}_x)\text{Ba}_2\text{Fe}_3\text{O}_{8+\delta}$**

I. Natali Sora<sup>25</sup>, Q. Huang<sup>31,21</sup>, J. W. Lynn<sup>19</sup>, N. Rosov<sup>19</sup>, P. Karen<sup>33</sup>, A. Kjekshus<sup>33</sup>, V. L. Karen<sup>19</sup>, A. D. Mighell<sup>19</sup>, and A. Santoro<sup>19</sup>.

**Neutron Powder Diffraction Study of Phase Transitions and Structures in the Series  $\text{La}_{2-x-y}\text{Nd}_x\text{Sr}_y\text{CuO}_4$ ,  $x = 0, 0.2, 0.4, 0.6$ ;  $y = 0.125$**

Q. Huang<sup>31,21</sup> and M. Crawford<sup>10</sup>.

**The Structure of  $\text{Ba}_{0.5}\text{Sr}_{0.5}\text{Pb}_{1-x}\text{Bi}_x\text{O}_{3-\delta}$  from Neutron Rietveld Refinement**

Q. Huang<sup>31,21</sup> and T. Clinton<sup>31</sup>.

**The NIST X-ray and Electron Diffraction Data Center**

A. D. Mighell<sup>19</sup>, V. L. Karen<sup>19</sup>, and M. E. Mrose<sup>19</sup>.

**Powder X-ray and Neutron Diffraction Studies of the  $(\text{Ba}_{1-x}\text{Sr}_x)_2(\text{Sr}_{0.67}\text{Bi}_{0.33})(\text{Pb}_{1-y}\text{Bi}_y)\text{O}_{6-\delta}$  System with  $(\text{NH}_4)_3\text{FeF}_6$  Structure**

C. Eylem<sup>31</sup>, Q. Huang<sup>21,31</sup>, B. Eichhorn<sup>31</sup>, and T. Clinton<sup>31</sup>.

**Affiliations**

<sup>1</sup>Air Products & Chemicals, Inc.

<sup>2</sup>American Dental Association

<sup>3</sup>Argonne National Laboratory

<sup>4</sup>Army Res. Devel. & Eng. Ctr.

<sup>5</sup>AT&T Bell Laboratories

<sup>6</sup>Aware, Inc.

<sup>7</sup>Brookhaven National Laboratory

<sup>8</sup>C.N.R.S., France

- <sup>9</sup>Chalmers U. of Tech., Sweden
- <sup>10</sup>DuPont
- <sup>11</sup>Institut Laue-Langevin
- <sup>12</sup>Johns Hopkins University
- <sup>13</sup>Lawrence Livermore Nat'l Lab
- <sup>14</sup>Los Alamos National Laboratory
- <sup>15</sup>Materials Sci. & Eng. Lab., NIST
- <sup>16</sup>Metallurgy Division
- <sup>17</sup>Paul Scherrer Institut
- <sup>18</sup>Philips Research Labs
- <sup>19</sup>Reactor Radiation Division
- <sup>20</sup>Royal Institution of Great Britain
- <sup>21</sup>Sussex University, UK
- <sup>22</sup>Towson State University
- <sup>23</sup>U. du Maine, France
- <sup>24</sup>U. Pierre et Marie Curie
- <sup>25</sup>Universita di Brescia, Italy
- <sup>26</sup>University of Amsterdam
- <sup>27</sup>University of California, Davis
- <sup>28</sup>University of California, Santa Barbara
- <sup>29</sup>University of California, Berkeley
- <sup>30</sup>University of Houston
- <sup>31</sup>University of Maryland
- <sup>32</sup>University of Moscow
- <sup>33</sup>University of Oslo
- <sup>34</sup>University of Pennsylvania

## SURFACE AND INTERFACIAL STUDIES

The determination of chemical and magnetic density depth profiles from the analysis of neutron reflectivity data, obtained at glancing angles of incidence, is becoming more and more important in the study of surface and interfacial phenomena on a microscopic scale. That this is so is evident from the very enthusiastic response to the "Workshop on the State-of-the-Art in Neutron Reflectometry" sponsored by NIST in December 1993. Approximately 100 scientists from academia, national labs and industry, both domestic and international, interested in a variety of surface and interfacial problems in chemistry, physics, biology and materials science participated in the two day meeting.

In this section, we will highlight a few of the many interesting neutron reflectivity experiments performed in the last year at the NBSR. Specific examples will be given in the fields of magnetism, electrochemistry, critical behavior, and polymer science.

### Magnetic Systems

#### • Spatial Modulation of the Magnetic Moment in Co/Pd Superlattices Observed by Polarized Neutron Reflectivity

The discovery of perpendicular magnetic anisotropy in Co/Pd superlattices [1,2] has attracted technological interest, while a related topic of fundamental importance has been the polarization of the nonmagnetic Pd atoms [1-3] arising from the proximity of Co at the superlattice interfaces. A "giant moment" as large as  $0.4 \mu_B$  per Pd atom occurs in dilute Pd alloys with magnetic transition metals principally due to the 3d - 4d hybridization of the impurities with the Pd atoms [4]. For a Co monolayer on a Pd substrate, a theoretical study [5] predicts that the Co magnetization is enhanced by as much as  $0.4 \mu_B$  per atom and that the Co induces moments of  $0.33 \mu_B$  and  $0.24 \mu_B$  per atom in the first and second Pd layers respectively.

Bulk magnetization measurements [1-3] provide widely-varying estimates of the Pd moment in Co/Pd superlattices. In contrast with this technique, polarized-neutron reflectivity is sensitive to the depth-dependent moment distribution through

the superlattice and is insensitive to sample volume. Thus it provides a means to probe separately the magnetization through the individual Co and Pd interlayers.

The specular reflectivity of x-rays and spin-polarized neutrons from a Co/Pd superlattice, [Pd 80 Å | Co 60 Å] × 20/Pd 300 Å/Co 10Å/GaAs, grown by molecular-beam epitaxy have been measured and modeled. In order to reduce the number of variables in the neutron data analysis, the spatial profile of the chemical composition of the superlattice was first extracted from the x-ray reflectivity. The fit reveals that the superlattice interfaces are somewhat rounded, with Co atoms present throughout the nominal Pd layer and vice versa. This interfacial "mixing" could originate from a combination of diffusion, atomic-scale roughness or correlated roughness arising from substrate miscut.

The neutron reflectivity studies were performed on the BT-7 reflectometer with the samples magnetized in-plane in a saturating field of 2300 Oe. Since neutrons interact with both the nuclei and electron spins of the scattering material, the refractive indices describing the reflectivity have a structural and magnetic component. For a simple ferromagnet, the refractive index can be written,

$$n_{\pm} = \sqrt{1 - \frac{N\lambda^2}{\pi} (b \pm p)}. \quad (1)$$

where  $N$  is the number density of the scatterers,  $b$  their nuclear scattering length and  $p = \sigma_m \mu$  is the magnetic scattering amplitude where  $\sigma_m = 0.2695 \times 10^{-4} \text{ Å}/\mu_B$  and  $\mu$  is the magnetic moment per atom lying in the sample plane. The plus and minus subscripts designate the indices for neutrons polarized parallel and antiparallel to the sample moment. Measuring both spin states one can, in principle, obtain a spatial profile of the distribution of structural and magnetic scatterers through the sample using a model based upon the one-dimensional wave equation for a stratified medium. A detailed explanation of the model and its application to polarized [6] and unpolarized [7] reflectivity is provided elsewhere.

The polarized neutron scans for at 38 K reveal only a single superlattice reflection above the diffuse background, as shown in figure 1a). The + and - cross sections were fit simultaneously to the structure factor model [6] holding the structural parameters constant. For this sample the fit is guided principally by the critical angles, which are related to the square of the total bilayer moment, and by the relative intensities of the + and - superlattice peaks, which are determined by the difference between the magnetization in the nominal Co and Pd layers. Following simple Fourier-transform arguments, the absence of higher order superlattice reflections limits the sensitivity of the fit to the average moments through the separate Co-rich and Pd-rich interlayers.

The magnetization profile that generates the fit (solid line) in figure 1a) is shown in figure 1b). The average magnetic moment in the nominal Co interlayer equals  $1.37 \pm 0.08 \mu_B$  per Co atom, corresponding to 78% of the Co bulk moment ( $1.74 \mu_B$ ). The remaining 22% of the spins elude experimental detection and are, therefore, either disordered or aligned perpendicular to the sample plane. Figure 1b) also demonstrates that the magnetic density  $\text{Re}(Np)$  of the Pd-rich layer is smaller than would be expected if those Co atoms dispersed through the layer exhibited the same moment as those in the Co-rich layer. A depletion of the magnetic moment in the nominal Pd interlayer is clearly observed, rather than the predicted enhancement. This effect may, in fact, be associated with the structural disorder revealed by x-ray characterization.

In order to place limits on our moment estimates, we have calculated reflectivity curves for  $[\text{Pd } 80\text{\AA} | \text{Co } 60\text{\AA}] \times 20 / \text{Pd } 300\text{\AA} / \text{Co } 10\text{\AA} / \text{GaAs}$  assuming that the Co atoms through the entire bilayer order with 78% of the bulk Co moment [dotted line in Fig. 1b)]. As can be seen from figure 1a), the differences between these curves (dashed lines) and the actual fitted curves (solid lines) are striking. Any enhancement of the magnetization in the nominal Pd layer would further diminish the amplitudes of the + and - superlattice reflections, an effect not evident in our data.

Since this analysis is highly sensitive to differences between the magnetic densities of the

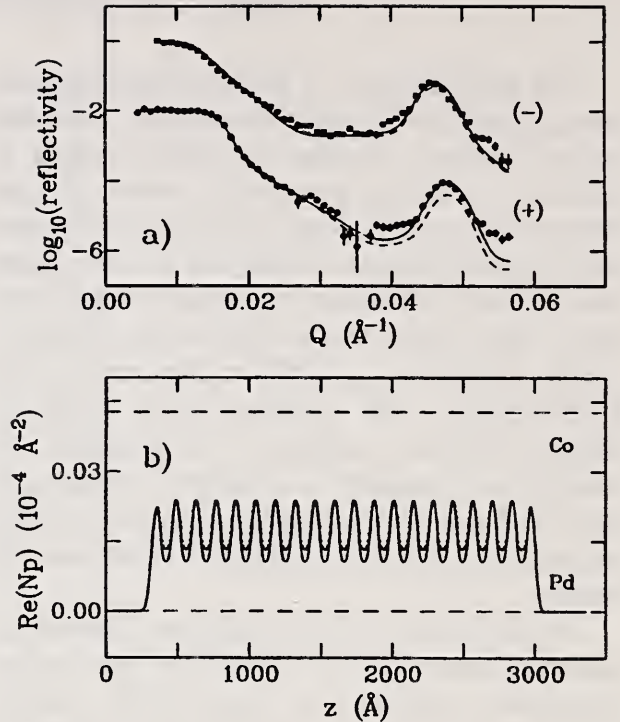


**Figure 1.** (upper) Polarized neutron reflectivity of  $[\text{Pd } 80 \text{\AA} | \text{Co } 60 \text{\AA}] \times 20 / \text{Pd } 300 \text{\AA} / \text{Co } 10 \text{\AA} / \text{GaAs}$  as a function of wavevector  $Q$  at 38 K in a saturating field of 2300 Oe. The + and - cross sections are designated by circles and squares respectively and the former is vertically offset for clarity. The solid lines represent the fit to the data, and the dashed lines describe the reflectivities calculated assuming that the Co atoms present in both the nominal Co and Pd interlayers are magnetized with 78% of the bulk Co moment. b. (lower) Magnetic scattering density profile for the same sample obtained from the reflectivity fit in a). The dashed lines mark the bulk densities of Co and Pd. The dotted line describes the density profile calculated assuming that the Co atoms present in both the nominal Co and Pd interlayers are magnetized with 78% of the bulk Co moment.

Co and Pd interlayers, either the Pd in this sample is not polarized or the effect is very small. Using neutron reflectivity or any other technique, observation of subtle moment enhancements in a narrow interfacial region ( $< 5 \text{\AA}$ ) as predicted by theory [5] requires a level of structural perfection difficult to achieve in any metallic superlattice system. Upon refinement of the structural quality, specular reflectivity provides the means to detect and place limits on these small, localized enhancements and remains a topic for future investigation.

### • Magnetic Semiconductor Multilayers

Artificial superlattice structures fabricated from antiferromagnetic semiconducting compounds offer highly interesting prototypical systems for the study of thin and ultrathin antiferromagnetic layers. Experiments have been conducted on two different classes of such systems: (i) superlattices composed of alternating layers of zinc-blende (ZB) Mn-VI and non-magnetic II-VI materials which essentially show the Type III antiferromagnetic (AF) structure and (ii) EuTe/PbTe multilayers in which both constituent materials crystallize in the NaCl structure and the EuTe layers exhibit Type II AF ordering. Some recent results for EuTe/PbTe and MnTe/CdTe superlattices are described below.

**EuTe/PbTe Superlattices.** The samples were prepared by MBE on single crystal BaF<sub>2</sub> substrates, with a (111) growth plane. EuTe is a FCC Type II antiferromagnet [8] ( $T_N \approx 10$  K) and PbTe, a nonmagnetic semiconductor, is treated at low T as an insulator. In EuTe/PbTe multilayers, both constituent materials crystallize in the NaCl structure. While in a bulk crystal there are four Type II AF domain configurations corresponding to the four equivalent (111) planes, in EuTe/PbTe superlattices the lattice mismatch strain selects a single configuration with the FM sheets parallel to the EuTe layer plane. The superlattices have previously been investigated by magnetic susceptibility [9] and magnetization measurements [10].

An intriguing problem is how the behavior of the superlattices changes with the number of (111) spin planes in the EuTe layers. An odd number of layers will produce a non-zero net magnetic moment and hence may generate relatively strong magnetic fields which decrease with distance as  $H(r) \sim r^{-3}$ . If the thickness of the nonmagnetic PbTe spacers is not too large, the fields could give rise to significant interlayer coupling effects. Such coupling would be indicated by characteristic superlattice peak patterns in the region of the AF reflection points for the Type II structure (e.g.,  $(1/2 \ 1/2 \ 1/2)$ ). In measurements on a [(EuTe)<sub>3</sub>| (PbTe)<sub>9</sub>]<sub>400</sub> specimen, clear superlattice maxima are observed [11]. However, a distinct superlattice peak pattern is also seen from a sample with an *even* number of spin sheets in the EuTe layers (Fig. 2), suggesting that the observed interlayer coupling may involve mechanisms other than those

of the simple model. One possibility is coupling through weak 'multi-pole' fields which are generated by the layers even though the numbers of 'up' and 'down' spins are equal—such fields result from the planes of dipoles being shifted apart in space [12]. Another is transfer of the magnetic interactions through the PbTe layers by carriers, in analogy to the RKKY mechanism in metals—although the carrier concentration in PbTe in the  $T < 10$  K range is only  $\sim 10^{17}/\text{cm}^3$ , so this effect should be much weaker than in metallic magnetic superlattices.

Experiments in high external magnetic fields parallel to the (111) plane show that the superlattice peak pattern in the  $(1/2 \ 1/2 \ 1/2)$  point region weakens with increasing H, and completely disappears when the field reaches the value 6 T. At the same time, a new superlattice peak pattern emerges in the vicinity of the (111) *ferromagnetic*

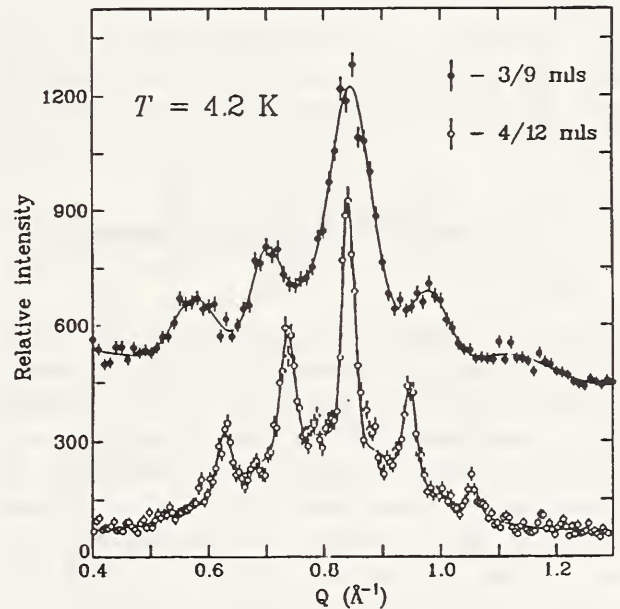


**Figure 2.** Diffraction scan along the [111] axis in  $Q$ -space for a [(EuTe)<sub>3</sub>| (PbTe)<sub>9</sub>]<sub>400</sub> superlattice sample ("3/9" monolayers—upperplot), and a [(EuTe)<sub>4</sub>| (PbTe)<sub>12</sub>]<sub>400</sub> sample ("4/12" monolayers—lower plot), showing a number of distinct superlattice peaks in the region of the  $(1/2 \ 1/2 \ 1/2)$  AF reflection point (the position of this point is at  $Q \approx 0.84 \text{ \AA}^{-1}$ ). The spacing between these peaks,  $\Delta Q = 0.10 \text{ \AA}^{-1}$ , is consistent with the elementary bilayer period in the sample ( $D_{BL} \approx 45 \text{ \AA}$ ). For clarity, the spectrum for the "3/9" sample has been shifted upward in the intensity scale.

reflection point. In samples with EuTe thicknesses of 2 and 4 monolayers the interval between these peaks,  $\Delta Q$ , is consistent with the superlattice periodicity ( $\Delta Q = 2\pi/D_{SL}$ , where  $D_{SL}$  is the elementary bilayer thickness). Surprisingly, for the sample with three monolayers, the spacing between the superlattice peaks is *half* that corresponding to  $D_{SL}$  (see Fig. 3), indicating that the induced magnetization in the EuTe layers is additionally modulated along the [111] axis with a  $2D_{SL}$  period. However, the exact nature of this modulation, and whether it is related to the odd number of spin planes in the EuTe layers, is yet to be understood.

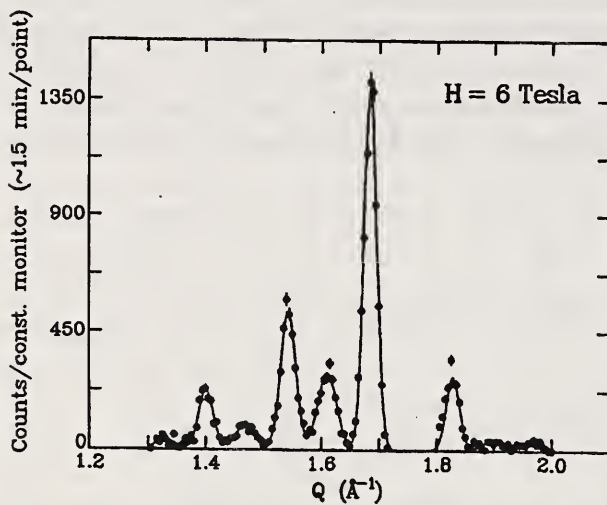


**Figure 3.** Scan along the [111] axis for a  $[(\text{EuTe})_3|(\text{PbTe})_9]_{400}$  sample at 4.2 K at external magnetic field 6 T, showing a number of distinct superlattice peaks induced by the field in the region of a *ferromagnetic* reflection point (111). Surprisingly, the spacing between these peaks,  $\Delta Q = 0.07 \text{ \AA}^{-1}$ , is *twice as small* as that corresponding to the elementary bilayer period in this sample ( $D_{BL} \approx 34 \text{ \AA}$ ). A strong (111) reflection from the  $\text{BaF}_2$  substrate, occurring at  $Q = 1.76 \text{ \AA}^{-1}$ , has been erased.

**MnTe/CdTe Superlattices.** MnTe/CdTe superlattices belong to the family of artificial multilayered structures composed from zinc-blende (ZB) II-VI semiconducting compounds and Mn chalcogenides using MBE or atomic layer epitaxy (ALE).

Other known systems are MnSe/ZnSe, MnTe/ZnTe, and MnSe/ZnTe. While naturally existing crystals of MnTe have the NiAs structure, the ZB form is a FCC Heisenberg antiferromagnet with dominant nearest neighbor (NN) interactions.

Such a lattice is a well known example of an inherently frustrated spin system with a ground state degeneracy. Neutron diffraction studies show that strain has a profound influence on spin ordering phenomena and phase transition behavior in such frustrated systems. Results for the unstrained MnTe lattice and the strained layers of the Mn-VI/Zn-VI superlattices have been reported elsewhere [13-16]. Whereas the Mn-VI/Zn-VI systems were all prepared by MBE, the MnTe/CdTe samples were grown by ALE. In this technique the thickness of the non-magnetic layers can be made very small ( $\geq 2$  single monolayers).

With thinner CdTe spacers, the nonmagnetic layer thickness becomes comparable with the range of the Mn-Mn AF exchange, leading to observable magnetic interlayer coupling effects not seen in the Mn-VI/Zn-VI systems [17]. The widths of the AF diffraction peaks indicate that in such circumstances the magnetic interactions are transferred through the CdTe layers, giving rise to interlayer spin-spin correlations. Studies of interlayer effects varying with CdTe layer thickness have been planned to give insight into the nature of weak long-range magnetic exchange interactions in diluted semiconductors based on II-VI compounds.

MnTe/CdTe is also an example of a system with tensile strain in the magnetic layers which produces a transition to an incommensurate helical AF phase not observed in any other FCC antiferromagnets. The strain (and therefore helical period) increases with thickness of CdTe, but is weak enough to allow investigation of the onset of incommensurate helical effects. Diffraction data also show simultaneous occurrence of peaks corresponding to the commensurate Type III and the incommensurate helical phase—such a coexistence has never been seen before in any Mn-VI/Zn-VI system. Theoretical analysis of the phase diagram of frustrated FCC lattices in the strain vs T coordinates [18] leads to the prediction that in the region of weak tensile strain there is a transition between an incommensurate and commensurate phase; in the vicinity of this phase boundary, small fluctuations of strain may lead to simultaneous occurrence of both phases.

These experiments show that MnTe/CdTe and EuTe/PbTe multilayers offer interesting examples for the study of interlayer coupling phenomena in



antiferromagnetic superlattices. Since ALE makes it possible to grow very thin CdTe layers, the former system offers an excellent prototype for investigating interlayer coupling by short-range exchange interactions. Due to the 'layered' nature of the Type II AF structure in EuTe which enables the growth of layers with 'unbalanced' AF sublattices, the EuTe/PbTe superlattices provide an excellent system for the study of interlayer coupling by dipolar forces.

### Ti Oxidation and Dissolution In Situ

Neutron reflectometry has been employed to study the dissolution and electrochemical breakdown of anodic oxide films on Ti in contact with a sulfuric acid electrolyte [19]. Such films play an important role in corrosion resistance, catalysis, and photochemistry in aqueous environments. A teflon electrochemical cell is clamped to a thick Si wafer, onto which has been sputtered a thin Ti electrode. The region between the cell and the Ti film is filled with 0.1 N H<sub>2</sub>SO<sub>4</sub> electrolyte, and electrical contacts are established between the Ti, a Pt counter electrode, and a saturated calomel reference. Neutrons are incident through the Si substrate. Figure 4 shows a series of reflectivity profiles for films formed by ramping the potential at 1 mV/s to the anodic growth voltages indicated. The solid lines are fits to a four-layer model, consisting of Si, Ti, an oxide layer, and electrolyte. The corresponding layer profiles are shown in figure 5, where  $z$  is the height (Si is the region for  $z < 50$  Å) and  $Q_c^2$  is a scaled scattering length density. As the potential increases, the oxide film thickens linearly at a rate of 14 Å/V. By 4 V the Ti is virtually all converted to oxide, and at 5 V it appears that some of the Si has oxidized as well, as indicated by the "bump" in the scattering density. As the oxide thickens, the total film thickness *decreases*, indicating that the oxide film is dissolving slowly into the acid (at a rate of somewhat less than  $\sim 1$  Å/h). Dissolution is accompanied by roughening of the oxide/electrolyte interface.

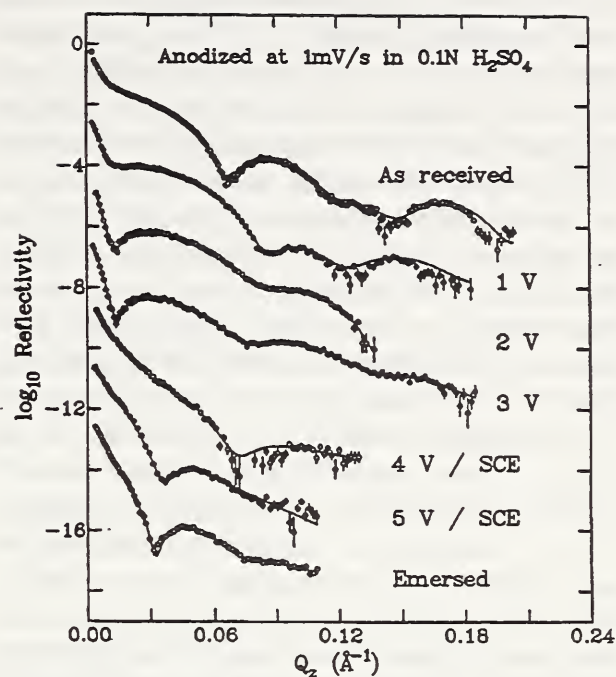


Figure 4. Reflectivity curves of a Ti film in situ for different growth voltages. Neighboring curves are offset by two orders of magnitude for clarity. Solid lines are fits to the data.

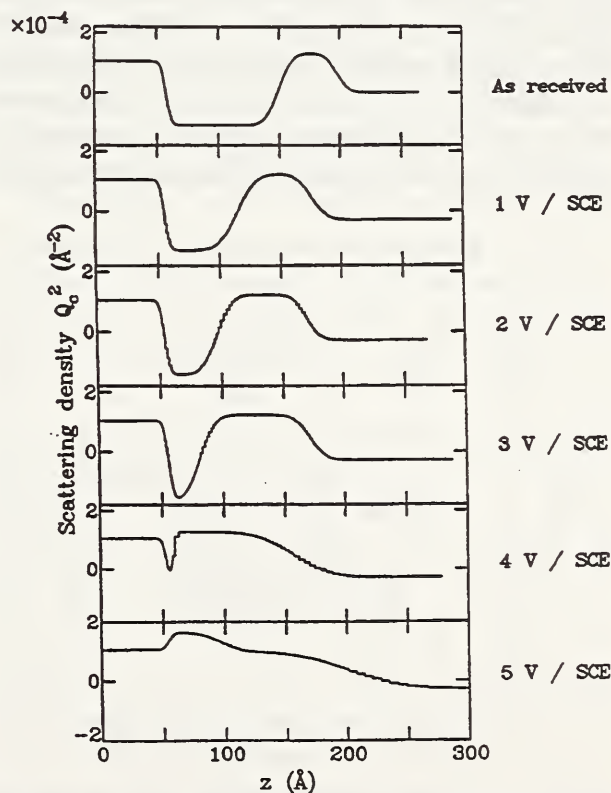


Figure 5. Scattering density profiles for the data shown in figure 4.

To investigate the stability of these anodic oxide films in reducing conditions, an oxide film which had been formed at 3 V was kept under cathodic bias at -2 V while the reflectivity was monitored. Figure 6 shows the time evolution of the fitted layer profile. For the first 30 hours both the oxide and the metal absorb hydrogen, as evidenced by the decrease in  $Q_c^2$  in both regions, and the oxide surface grows substantially rougher. At 30 hours the scattering density of the metal rises suddenly, as hydrogen is evolved and Ti is dissolved. By 39 hours most of the Ti and oxide films have been dissolved away. It is believed that this behavior is driven by the dissolution of the oxide. Under *anodic* bias the oxide is self-healing: dissolution is accompanied by oxidation of the Ti underlayer so that the oxide remains the same thickness. Under *cathodic* bias, however, the metal maintains its thickness as the oxide dissolves. When the oxide is sufficiently thinned, local paths are formed between the electrolyte and the Ti, which at these potentials is oxidized to the soluble  $Ti^{2+}$  [20]. The breakdown of the passivating layer is thus identified in our study as a consequence of a much higher rate of dissolution for Ti over  $TiO_2$ . There are obvious technological ramifications for this result. A common method of protecting certain metals is to bias them cathodically. For Ti this method is not commonly used, and these results suggest a microscopic rationale for this. This study illustrates the utility

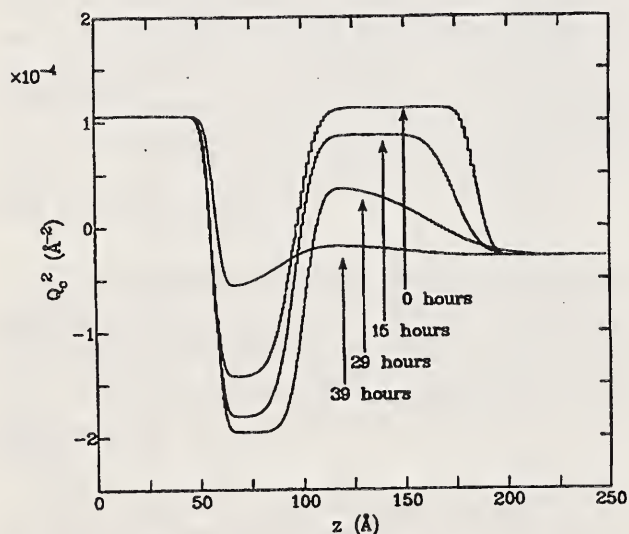


Figure 6. Time evolution of the scattering density profile of an oxide film maintained at -2V.

of *in situ* neutron reflectometry to investigate oxide films or other liquid/solid interfaces.

### Anomalous Critical Scattering in Tb

The critical scattering that is present just above the transition temperature  $T_c$  of a crystalline material arises from finite regions of the crystal which undergo thermally-induced fluctuations into the low-temperature ordered phase. The resulting quasielastic lineshape measured in a neutron-scattering experiment is well described by a single Lorentzian function of  $q$  with a linewidth that is inversely proportional to the average size of these fluctuating regions. In 1986, high  $q$ -resolution x-ray measurements of the critical scattering associated with the cubic-to-tetragonal phase transition in  $SrTiO_3$  were reported which exhibited an unexpected two-component lineshape, with the second component having a much narrower width [21]. A second component implies the existence of a second length scale, and runs counter to our current understanding of second-order phase transitions in which only one divergent length scale is present above  $T_c$ . Much more recently, high  $q$ -resolution neutron-scattering measurements on Ho just above its magnetic-spiral phase transition temperature revealed a similar anomalous two-component lineshape [22]. Taken together, these two seminal results suggest that the narrow component may be a feature common to all phase transitions in condensed matter systems. Indeed, two-component lineshapes have also been documented in both  $RbCaF_3$  and  $KMnF_3$  [23,24]. Studies on other systems are in progress.

Central to all of these investigations has been the question concerning the origin of the narrow component. X-rays, which probe crystal surfaces to a depth of order 1 micron, cannot tell if the narrow component is absent in the crystal bulk. Neutrons, which do probe the bulk, have not yet been able to separate surface and bulk contributions. This question has now been answered [25] through high  $q$ -resolution neutron-scattering measurements of the quasielastic scattering in a cube-shaped single crystal of Tb which, like Ho, exhibits a transition to a magnetically-ordered spiral phase [26]. By use of a 300 micron wide beam, it has been possible to isolate thin slices of the Tb crystal. The finding is that the origin of

the narrow component lies in the near-surface volume or "skin" of the Tb sample, and not in the bulk [25]. In this context the meaning of skin is distinct from that of surface since the narrow component is spread over several hundred microns and not just one or two. Moreover, it is also found that not all skins are equivalent. The intensity of the narrow component scattering is greatest in those faces which are orthogonal to the  $c$ -axis face.

The neutron scattering experiments were performed on the NBSR BT-7 reflectometer [27]. This reflectometer is ideally suited to this study because the incident horizontal beam width can be varied from zero to several mm (with an accuracy of  $\pm .01$  mm) using motorized slits positioned upstream from the sample. By narrowing the width of the incident beam to as little as 300 microns (0.3 mm), the near-surface volume of the Tb crystal can be probed preferentially by translating the crystal face into the beam. In the same fashion, scattering from the bulk can be isolated by translating the center of the crystal into the beam and reducing the spatial extent of the scattered beam with exit slits and appropriate collimation. The experimental scattering geometry is shown schematically in figure 7a. With the Tb [100] axis mounted vertically, the [001] direction was aligned along the translation axis of a motorized goniometer stage so that the neutron beam sampled very narrow regions of the crystal as depicted by the shaded area. Figure 7b shows translation scans below the spiral transition temperature  $T_s = 229.5$  K for two different beam widths of 1.56 mm and 0.30 mm, with the spectrometer fixed at the  $(0,0,\delta)$  satellite peak position. The translation scale was set so that zero corresponds to the front face of the crystal. The intensity scale for the wider beam setting has been normalized to that for the narrower beam setting to better contrast the markedly different profiles at the crystal edge. Because the absorption is constant as the crystal is translated through the beam, the peak intensity remains constant until it drops to zero when the crystal moves out of the beam. This drop-off becomes much sharper with a narrower beam.

Identical scans are shown above  $T_s$  in figure 7c. In this case, as the beam approaches the crystal  $c$ -axis face the intensity does *not* remain

constant. Instead, a truly remarkable enhancement of the intensity is observed, persisting over a limited range of 0.2 K above  $T_s$ . The enhancement is broad and weak for the wider beam setting which is nearly one quarter of the full crystal width. But at the narrowest beam setting, the enhancement becomes sharper and larger. This is an extremely important point because it demonstrates that the quasielastic scattering is concentrated near the face of the crystal rather than in the bulk. The narrower the beam, the greater the enhancement. At the narrowest setting, the width over which this enhancement takes place is of order 0.75 mm. Taking into account the effect of the finite beam width, crystal miscut, and scattering angle leaves an effective enhancement width of order 0.2 mm.

The cause of the enhancement was determined by comparing transverse- $q$  scans at the same temperature taken at two different translations; one slightly displaced from the crystal face where the enhancement was maximum (6.75 mm), and one at the crystal center (3.50 mm) [28]. In both cases the distinctive two-component lineshape is present. Whereas the peak intensity of the broad component differs by only 6% in the two scans, that of the narrow component changes by over 70%. The constant background is the same within 4%. The anomalous enhancement is therefore due to a striking increase in the intensity of the narrow component within the skin of the Tb crystal face.

The reason why a small, but finite, narrow component is still present in the bulk is that the incident beam illuminates square-shaped portions of the skin at those points where the beam enters and exits the crystal on the two faces orthogonal to the  $c$ -axis Tb face. (Exit slits and vertical collimation were used to eliminate the scattering from the top and bottom faces of the crystal.) Therefore these faces contribute a narrow component as well. Indeed, if one assumes that the narrow component is identically zero in the bulk, then a simple geometrical model predicts an anisotropy of order 5 between  $c$ -axis and orthogonal faces, with the latter contributing the most to the narrow component intensity. It is of course still possible that the bulk contributes to the total narrow-component intensity at both translation settings. However, the data presented

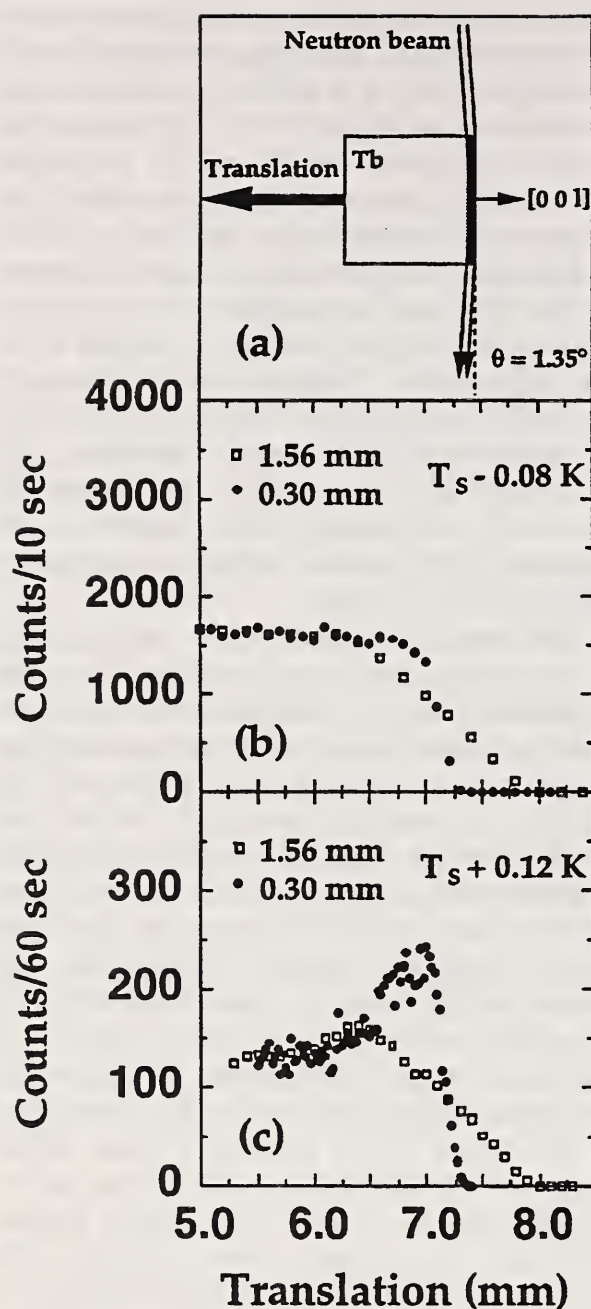


**Figure 7.** (a) Schematic diagram of scattering geometry. The Bragg angle  $\theta_B$  has been slightly exaggerated for clarity. (b) Translation scans below  $T_s$ , at beam widths of 0.30 mm and 1.56 mm. Intensities have been normalized to those for the narrower beam. (c) Identical scans above  $T_s$ , showing the enhancement at the  $c$ -axis face.

in figure 7c show that the skin, and not the bulk, is the predominant source of this feature.

The microscopic explanation for the second length scale is as yet unknown. One model put forth is based on the presence of extended defects

such as dislocations which mediate the large scale fluctuations [23]. Given the present results, these defects would have to be populated most heavily in the skin of the crystal, and in an anisotropic fashion. Another intriguing possibility is that the second length scale results from the boundary condition imposed by the crystal surface on the magnetic interaction driving the phase transition. The fact that the spins in Tb are confined to the basal plane below  $T_s$ , could then easily account for the observed anisotropy between crystal faces.

## Polymer Systems

### • Chain End and Junction Distribution in Ordered Diblock Copolymers

Block copolymers are commonly used for industrial applications such as paints, adhesives and compatibilizers. The area of thin films (thickness  $< 1 \mu\text{m}$ ) of such materials has recently received notable experimental attention at a fundamental thermodynamic level. A key feature of block copolymers is a junction point that prevents the two blocks from macrophase separating, thus only microphase separation is possible between otherwise incompatible polymers. This restriction however leads to a diverse range of observable microstructures such as lamellae, cylinders, spheres etc., and thus it is evident that a thorough characterization of the block junction is necessary to understand block copolymer ordering behavior at a basic level. To this end we have performed several neutron reflection measurements on selectively labelled (deuterated) block copolymers with different amounts of the deuterated block; below we highlight only some of our measurements that shed light on localization of junction points in diblock copolymer thin films.

Figure 1a shows neutron reflection from a well ordered pure diblock copolymer, poly (styrene- $d_8$ - $b$ -2-vinylpyridine) or dPS-P2VP of total molecular weight  $\sim 160 \text{ k}$ . The film was spin cast on a silicon substrate and annealed at  $170^\circ \text{C}$  (well above its ordering temperature) for 24 hours. This diblock copolymer with a polystyrene content of 50% volume fraction forms thermally induced alternating lamellar structure by preferential segregation of dPS to the air surface and P2VP to

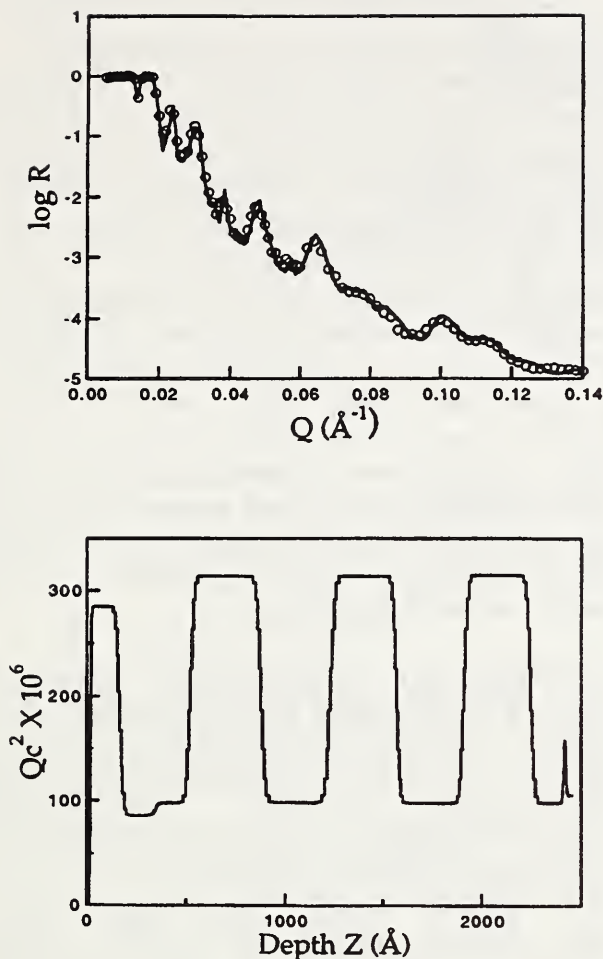


**Figure 8.** (a, upper) Neutron reflectivity profile of P(S-b-2-VP) diblock copolymer. The circles are experimental data and the solid line is the calculated one from scattering length density distribution shown in Figure 8b. (b, lower) Scattering length density profile used in fitting.

the silicon surface. The open circles in figure 8a represent experimental data, while the solid line corresponds to the calculated reflectivity from the model scattering length density profile depicted in figure 8b. The density distribution of the 2500 Å thick layer shows a highly oriented lamellar structure parallel to the silicon substrate. A decrease of scattering length occurs near the air surface due to an incomplete top lamellar layer [29]. The interfacial width is about 30 Å, indicative of very strong segregation between the two blocks. By comparison, Anastasiadis et al. [29] reported interfacial widths of about 50 Å in another strongly segregated system PS-PMMA (polystyrene-methacrylate). Differences in interfacial widths reflect different values of the

Flory-Huggins interaction parameter,  $\chi$ , that characterizes polymer-polymer interaction. A positive value denotes an unfavorable interaction. For dPS-P2VP its value is .08 [30], significantly higher than that for PS-PMMA.

While the above measurements establish that the dPS and P2VP are well segregated in the form of alternating lamellae, they do not unequivocally establish the localization of junction points within the different domains. To this end we have studied a junction labelled block copolymer PS-dPS-P2VP of total molecular  $\sim 90$  k. Deuterated segments constitute about 30 vol % of the polystyrene block. Figure 9a shows neutron reflectivity from a spun cast thin film of the above triblock. The scattering length density profile used for the fit is shown in figure 9b. It is clear that the small labelled block (and consequently the chain junction) exists in a narrow region at the interface between the two incompatible blocks.

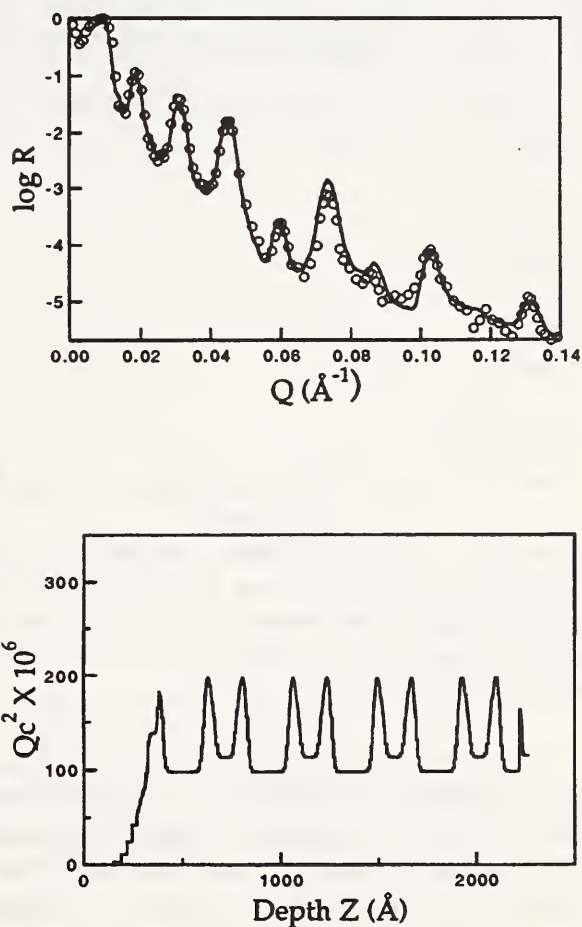


**Figure 9.** (a, upper) Neutron reflectivity profile of junction-labeled diblock copolymer, P(S-b-d<sub>5</sub>-S-b-2-VP). (b, lower) Scattering length density profile used in fitting.

• **Phase Separation in Thin Films of Polystyrene and Polyvinylmethylethene**

Neutron and x-ray reflection were used to investigate phase separation and film confinement effects in thin film blends of deuterated polystyrene (dPS 443 k) and polyvinylmethylether (PVME 84 k). In general two factors are expected to modify the phase diagram from its bulk behavior (Fig. 10). First, depletion of PVME in the bulk of the film caused by its preferential segregation to both air and the silicon surface could shift the phase diagram effectively to higher compositions of dPS, for fixed film thickness. Secondly, entropic confinement by virtue of reduced dimensionality is expected to restrict the length scale of fluctuations responsible for phase separation normal to the plane of the film. Both factors become increasingly important with reduction in film dimensions and proximity to the two phase boundary. Here we report on some preliminary thin film measurements on this classic lower critical solution temperature (LCST) blend system.

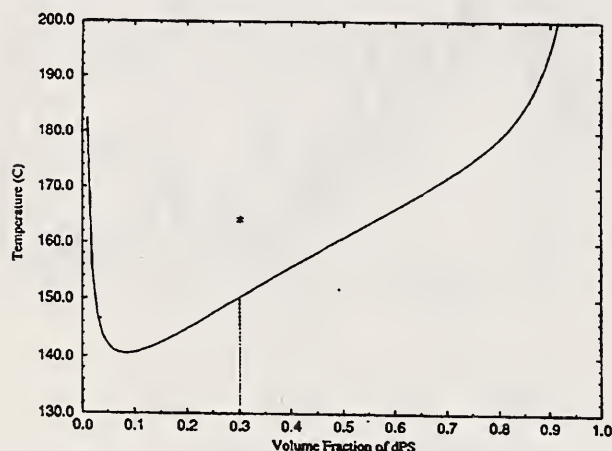


Figure 10. Spinodal phase diagram for bulk dPS(443 k)/PVME(84 k). For a 30% dPS/70% PVME blend, the spinodal temperature is 150 °C. The asterisk marks the temperature at which damping of reflectivity oscillations is observed to occur.

Figure 11 shows neutron reflectivity from a 30% dPS/70% PVME film of approximately 1000 Å heated to different temperatures under high vacuum, allowing several hours for equilibration at each temperature. Figure 11 illustrates that the film thickness oscillations get strongly damped at the higher temperatures. Similarly, x-ray reflection data measured in increments of

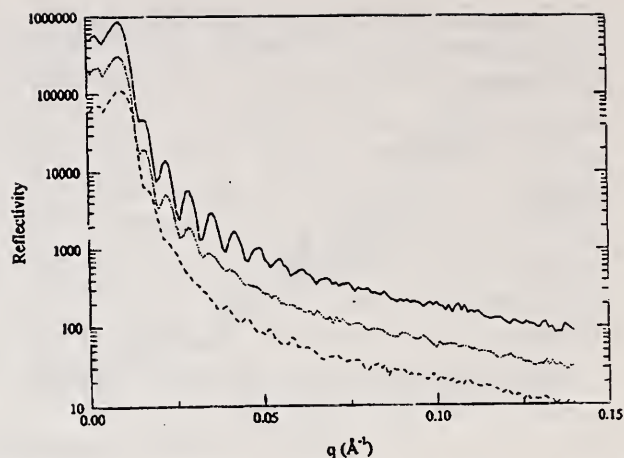


Figure 11. Neutron reflectivity data for a 30% dPS/70% PVME, 1000 Å thick sample. Solid, dotted and dashed lines correspond to measurements taken at 110 °C, 150 °C, and 170 °C, respectively. The sample was heated in vacuum.

5 °C from 130 °C upwards show pronounced damping of oscillations in the temperature range 160 °C - 165 °C for the same sample. Assuming that the damping is associated with transition from mixed state to two phase (binodal or spinodal), we note that the film transition value of ~162.5 °C, as indicated by the asterisk in figure 11, is well above the bulk spinodal (and binodal) value of ~150 °C. When cooled to 130 °C, the oscillation amplitudes came back reversibly within the cooling span of an hour or two, similar to bulk samples. In a thinner sample of ~450 Å similarly heated to 170 °C, the oscillation amplitudes did not come back reversibly at 130 °C in the same time. When cooled under vacuum to room temperature, a frozen spinodal decomposition pattern was clearly visible under a high power microscope. The above measurements are in contrast to a 70% dPS/30% PVME, ~1000 Å thick film that did not show significant damping with increase of temperature as measured up to 175 °C (inside bulk spinodal), and whose surface remained smooth at the end of the heat cycle.

Thus we conclude that reflectivity techniques and surface microscopy are potentially useful tools for mapping the thin film phase diagram. Preliminary results suggest that such a diagram is shifted up in temperature from the bulk dPS/PVME phase diagram. Efforts are currently underway for a more comprehensive study of this system, and to establish generality using other systems.

### • Chemically Grafted Polymer Brushes

Tethered polymeric systems are commercially important for modifying surface and interfacial properties, colloid stabilization, etc. Consequently, they have been the subject of numerous theoretical, experimental, and simulation studies. Most theories have focussed on predicting the shape of the concentration profile of end anchored chains immersed in good and poor solvents in the "brush" (moderately high grafting density) regime. Experimental measurements on such systems is however difficult since typical end adsorbing energies encountered are in the range of 10's of  $k_B T$ , insufficient to retain the strongly solvated polymer molecule. However, this problem can be overcome by chemically grafting (100's  $k_B T$ ), the chains to a substrate. Here we highlight some of our findings on one such system.

Neutron reflection was used to determine the concentration profile of a high molecular weight tri-chlorosilane terminated polystyrene (PS-SiCl<sub>3</sub>, 105 k), chemically end-grafted on to a polished silicon wafer. Figure 12 shows neutron reflectivity from a 105 k end-grafted PS "brush" of moderately high grafting density immersed in a good solvent, pure deuterated toluene. The reflectivity shows a few small amplitude interference kinks (oscillations) that correspond to the brush height in solvent. Due to the diffuse tip of the brush, these oscillations are strongly damped. The solid line in figure 12 is the calculated reflectivity from the model profile depicted by the solid line in figure 14. It takes the form

$$\phi(z) = \phi(0) [1 - (z/d)^n] \quad \text{for } z < d$$

where  $\phi(0)$ ,  $d$ , and  $n$  are fitting parameters corresponding to the polymer volume fraction at the surface, cut-off length of the profile, and the power law exponent. Additionally, the profile was convoluted with a normalized gaussian to yield a tail to the profile. All parameters were allowed to float freely to best fit the data, and cross checked with the polymer coverage measured by x-ray reflectivity on the dry wafer in air. Best fit parameters were  $n = 2.28$  (slightly steeper than a parabola) and  $d = 821 \text{ \AA}$ . Such a profile results from a complex interaction between polymer-polymer (interchain) and polymer-solvent interaction. In contrast, the solid line in figure 13

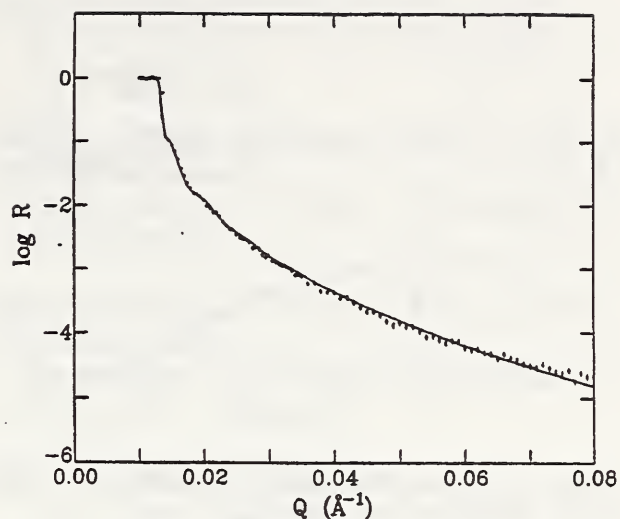


Figure 12. Neutron reflectivity from a 105 k end-grafted PS "brush" of moderately high grafting density in deuterated toluene. The solid line is a fit to the data as described in text.

shows neutron reflectivity from the same wafer in a poor solvent, cyclohexane at 9.5 °C, where intrachain interactions become important as well. The corresponding dashed profile in figure 13 is essentially step like in accordance with predictions of modern theories.

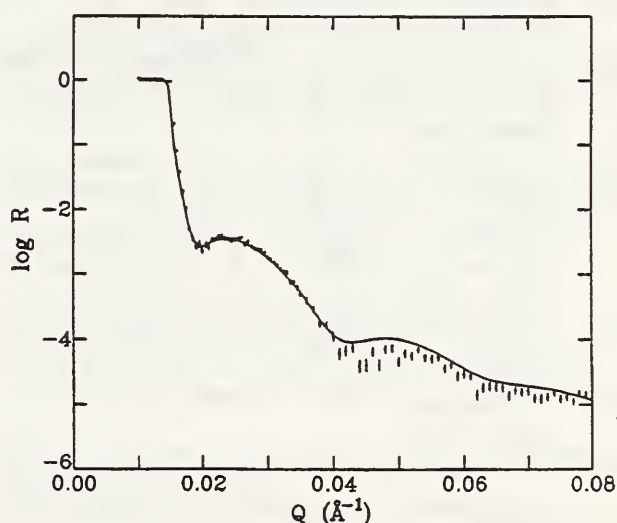


Figure 13. Neutron reflectivity from the same "brush" sample as in figure 12, in a poor solvent, deuterated cyclohexane.

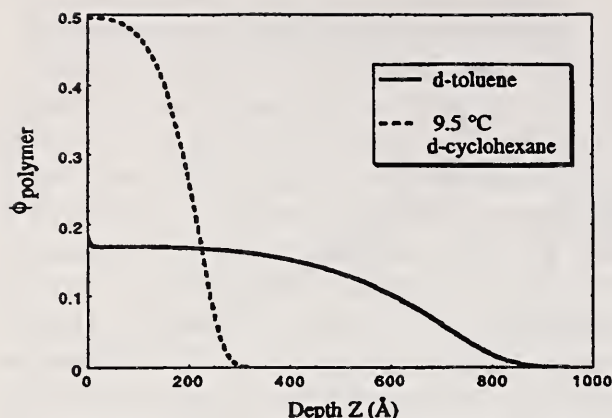


Figure 14. Fitted concentration profile for the 105 K "brush" in toluene and cyclohexane.

## References

- [1] P. F. Carcia, A. D. Meinhardt, and A. Suna, *Appl. Phys. Lett.* **47**, 178 (1985).
- [2] F.J.A. den Broeder, H. C. Donkersloot, H.J.G. Draaisma, and W.J.M. de Jonge, *J. Appl. Phys.* **61**, 4317 (1987).
- [3] B. N. Engel, C. D. England, R. A. Van Leeuwen, M. H. Wiedmann, and C. M. Falco, *Phys. Rev. Lett.* **67**, 1910 (1991).
- [4] G. J. Nieuwenhuys, *Adv. Phys.* **24**, 515 (1975).
- [5] S. Blügel, B. Drittler, R. Zeller, and P. H. Dederichs, *Appl. Phys. A* **49**, 547 (1989).
- [6] J. F. Ankner and C. F. Majkrzak, *Mat. Res. Soc. Conf. Proc.* (in press); J. F. Ankner (in preparation).
- [7] J. F. Ankner, A. Schreyer, Th. Zeidler, C. F. Majkrzak, H. Zabel, J. A. Wolf, and P. Grunberg, in *Neutron Optical Devices and Applications*, edited by C. F. Majkrzak and J. L. Wood, SPIE Conference Proc. **1738**, 260 (1992).
- [8] G. Will, S. J. Pickart, H. A. Alperin, and R. Nathans, *J. Phys. Chem. Sol.* **24** (1963) 1679.
- [9] J. Heremans and D. L. Partin, *Phys. Rev. B* **37** (1988) 6311.
- [10] J. J. Chen, Z. H. Wang, M. S. Dresselhaus, G. Dresselhaus, G. Springholtz, and G. Bauer, *Solid State Electronics*, in print.
- [11] T. M. Giebultowicz, H. Luo, N. Samarth, J. K. Furdyna, V. Nunez, J. J. Rhyne, F. Faschinger, G. Springholtz, G. Bauer, and H. Sitter, *Physica B*, in print.
- [12] P-A. Lindegar, private communication.
- [13] T. M. Giebultowicz, P. Klosowski, N. Samarth, H. Luo, J. K. Furdyna, and J. J. Rhyne, *Phys. Rev. B*, in print in print.
- [14] P. Klosowski et al., *J. Appl. Phys.* **70** (1991) 622.
- [15] N. Samarth et al., *Phys. Rev. B* **44** (1991) 4701.
- [16] T. M. Giebultowicz, N. Samarth, H. Luo, P. Klosowski, and J. K. Furdyna, *Phys. Rev. B* **46** (1992) 12076; *Physica* **180 & 181** (1992) 485.
- [17] T. M. Giebultowicz, W. Fashinger, V. Nunez, P. Klosowski, G. Bauer, H. Sitter, and J. K. Furdyna, *J. Crystal Growth*, in print.
- [18] R. J. Cohen and K. E. Newman, *Phys. Rev. B* **46** (1992) 14282.
- [19] D. G. Wiesler and C. F. Majkrzak, *Physica B*, in press.
- [20] J. Schmets, J. V. Muyllder, and M. Pourbaix, in *Atlas of Electrochemical Equilibria in Aqueous Solutions*, M. Pourbaix, ed., 213 (Pergamon, Oxford, 1966).
- [21] S. R. Andrews, *J. Phys. C* **19**, 3712 (1986).
- [22] T. R. Thurston, G. Helgesen, D. Gibbs, J. P. Hill, B. D. Gaulin, and G. Shirane, *Phys. Rev. Lett.* **70**, 3151 (1993).
- [23] T. W. Ryan, R. J. Nelmes, R. A. Cowley, and A. Gibaud, *Phys. Rev. Lett.* **56**, 2704 (1986).
- [24] U. J. Nicholls and R. A. Cowley, *J. Phys. C* **20**, 3417 (1987); A. Gibaud *et al.*, *Phys. Rev. B* **44**, 2437 (1991).
- [25] P. M. Gehring, K. Hirota, C. F. Majkrzak, and G. Shirane, *Phys. Rev. Lett.* **71**, 1087 (1993).
- [26] W. C. Koehler, *J. Appl. Phys.* **36**, 1078 (1965).
- [27] C. F. Majkrzak, *Physica B* **173**, 75 (1991).
- [28] The absorption at the front face is different from that at the back face. Comparing center and back face scans obviates the need for any absorption correction since then the corrections are identical.
- [29] S. H. Anastasiadis, T. P. Russell, S. K. Satija, C. F. Majkrzak, *J. Chem. Phys.* **92**, 5677 (1990).
- [30] Y. Matsushita, K. Mori, R. Saguchi, I. Noda, M. Nagasawa, *Macromolecules*, **23**, 4313 (1990).

## Research Topics

### Temperature Dependence of the 90° Spin Coupling in Fe/Al/Fe Trilayers

J. F. Ankner<sup>7</sup>, J. A. Borchers<sup>12</sup>, M. E. Filipkowski<sup>9</sup>, C. F. Majkrzak<sup>12</sup>, and G. A. Prinz<sup>9</sup>.

### Polarization of Pd Interlayers in Fe/Pd Superlattices

J. A. Borchers<sup>12</sup>, J. F. Ankner<sup>7</sup>, J. R. Childress<sup>15</sup>, C. F. Majkrzak<sup>12</sup>, and R. W. Erwin<sup>12</sup>.



- Spatial Modulation of the Magnetic Moment in Co/Pd Superlattices**  
J. A. Borchers<sup>12</sup>, J. F. Ankner<sup>7</sup>, B. N. Engel<sup>17</sup>, C. F. Majkrzak<sup>12</sup>, and C. M. Falco<sup>17</sup>.
- Magnetization Profile of Co/Pt Superlattices**  
J. F. Ankner<sup>7</sup>, J. A. Borchers<sup>12</sup>, C. F. Majkrzak<sup>12</sup>, R.F.C. Farrow<sup>5</sup>, and R. F. Marks<sup>5</sup>.
- Polarized Neutron Reflectivity Studies of Fe<sub>3</sub>O<sub>4</sub>/NiO Superlattices**  
J. F. Ankner<sup>7</sup>, J. A. Borchers<sup>12</sup>, S. D. Berry<sup>3</sup>, D. M. Lind<sup>3</sup>, C. F. Majkrzak<sup>12</sup>, and R. W. Erwin<sup>12</sup>.
- X-ray Reflectivity Characterization of YBa<sub>2</sub>Cu<sub>3</sub>O<sub>7</sub>/PrBa<sub>2</sub>Cu<sub>3</sub>O<sub>7</sub> Superlattices**  
M. Z. Cieplak<sup>14</sup>, T. M. Giebultowicz<sup>4</sup>, J. A. Borchers<sup>12</sup>, and J. F. Ankner<sup>7</sup>.
- Antiferromagnetic Spin Ordering, and Interlayer Magnetic Correlations In MnTe/CdTe Superlattices**  
T. M. Giebultowicz<sup>4</sup>, W. Faschinger<sup>18</sup>, G. Bauer<sup>18</sup>, V. Nunez<sup>19,12</sup>, P. Klosowski<sup>12</sup>, and J. K. Furdyna<sup>20</sup>.
- Dynamical Scattering of Polarized Neutrons by Thin Magnetic Films**  
V. Nunez<sup>19,12</sup>, C. F. Majkrzak<sup>12</sup>, and N. F. Berk<sup>12</sup>.
- Onset of Helimagnetism in Weakly Strained Epitaxial FCC Antiferromagnet Cd<sub>1-x</sub>Mn<sub>x</sub>Se**  
T. M. Giebultowicz<sup>4</sup>, V. Nunez<sup>19,12</sup>, N. Samarth<sup>20</sup>, H. Luo<sup>20</sup>, and J. K. Furdyna<sup>20</sup>.
- NiC/Ti Supermirror Coating Reflectivity**  
J. Wood<sup>11</sup> and C. F. Majkrzak<sup>12</sup>.
- In Situ Neutron Reflectivity Studies of Ti Oxidation and Dissolution**  
D. G. Wiesler<sup>12</sup> and C. F. Majkrzak<sup>12</sup>.
- Study of Mitochondrial Outer Membrane Bilayers by Neutron Reflectometry**  
S. Krueger<sup>12</sup>, M. Colombini<sup>19</sup>, S. K. Satija<sup>12</sup>, J. F. Ankner<sup>7</sup>, and C. F. Majkrzak<sup>12</sup>.
- Fe/Si Supermirror Polarizer Efficiency**  
J. Wood<sup>11</sup> and C. F. Majkrzak<sup>12</sup>.
- Co/Cu Superlattices: Polarized Neutron Reflectometry Study**  
A. Schreyer<sup>13</sup>, H. Zabel<sup>13</sup>, J. F. Ankner<sup>7</sup>, and C. F. Majkrzak<sup>12</sup>.
- Magnetic Critical Scattering in Ho Thin Films**  
P. M. Gehring<sup>12</sup>, L. D. Gibbs<sup>1</sup>, and C. F. Majkrzak<sup>12</sup>.
- Magnetic Critical Scattering in Single Crystal Tb: Skin Effects**  
P. M. Gehring<sup>12</sup>, H. Hirota<sup>1</sup>, G. Shirane<sup>1</sup>, and C. F. Majkrzak<sup>12</sup>.
- Fe/Cr Superlattices: Polarized Neutron Study of Interlayer Coupling**  
A. Schreyer<sup>13</sup>, J. F. Ankner<sup>7</sup>, H. Zabel<sup>13</sup>, and C. F. Majkrzak<sup>12</sup>.
- Neutron Channeling in Ti Films**  
Y. P. Feng<sup>2</sup>, S. K. Sinha<sup>2</sup>, H. Zhang<sup>12</sup>, D. G. Wiesler<sup>12</sup>, and C. F. Majkrzak<sup>12</sup>.
- FeCo/Si Supermirror Efficiency**  
J. Wood<sup>11</sup>, H. Mook<sup>10</sup>, and C. F. Majkrzak<sup>12</sup>.
- Neutron Reflectivity Studies of Biological Membrane Films**  
K. Gawrisch<sup>8</sup>, B. Koenig<sup>6</sup>, S. Krueger<sup>12</sup>, C. F. Majkrzak<sup>12</sup>, S. K. Satija<sup>12</sup>, and W. J. Orts<sup>12</sup>.
- Electrochemical Oxidation of Fe Films**  
L. Krebs<sup>6</sup>, J. Kruger<sup>6</sup>, G. C. Long<sup>21</sup>, D. G. Wiesler<sup>12</sup>, J. F. Ankner<sup>7</sup>, and C. F. Majkrzak<sup>12</sup>.
- Proteins in Thin Films**  
A. Liebmann<sup>16</sup>, H. Wu<sup>16</sup>, M. Foster<sup>16</sup>, S. K. Satija<sup>12</sup>, and C. F. Majkrzak<sup>12</sup>.
- Structure and Diffusion in Langmuir-Blodgett Films**  
L. A. Feigin<sup>23</sup>, D. G. Wiesler<sup>12</sup>, J. F. Ankner<sup>7</sup>, C. F. Majkrzak<sup>12</sup>, S. K. Satija<sup>12</sup>, and A. Karim<sup>22</sup>.
- Block Copolymers in Confined Geometries**  
P. Lambooy<sup>5</sup>, T. P. Russell<sup>5</sup>, G. Kellogg<sup>24</sup>, A. Mayes<sup>24</sup>, S. K. Satija<sup>12</sup>, and P. D. Gallagher<sup>12</sup>.
- Interfacial Structures of Electrically Conducting Adsorbed Multilayers**  
G. Kellogg<sup>24</sup>, A. Mayes<sup>24</sup>, W. Stockton<sup>5</sup>, M. Ferreira<sup>24</sup>, M. F. Rubner<sup>24</sup>, and S. K. Satija<sup>12</sup>.
- Mixtures of Symmetric Diblock Copolymers**  
A. M. Mayes<sup>24</sup>, T. P. Russell<sup>5</sup>, and S. K. Satija<sup>12</sup>.
- Influence of Surfaces and Finite Film Thickness on Block Copolymer Morphology**  
N. Singh<sup>25</sup>, M. Sikka<sup>25</sup>, F. S. Bates<sup>25</sup>, S. K. Satija<sup>12</sup>, and P. D. Gallagher<sup>12</sup>.

### **Chemically Adsorbed Polymer Brushes**

A. Karim<sup>22</sup>, S. K. Satija<sup>12</sup>, L. J. Fetters<sup>2</sup>, and C. F. Majkrzak<sup>12</sup>.

### **Block Copolymer Mixtures in Thin Films**

N. Singh<sup>25</sup>, M. Sikka<sup>25</sup>, F. S. Bates<sup>25</sup>, S. K. Satija<sup>12</sup>, and C. F. Majkrzak<sup>12</sup>.

### **Surface Segregation in Thin Polymer Films**

N. Singh<sup>25</sup>, M. Sikka<sup>25</sup>, F. S. Bates<sup>25</sup>, S. K. Satija<sup>12</sup> and P. D. Gallagher<sup>12</sup>.

### **Surface and Phase Behavior of Thin Polymer Blend Films**

T. Slawecki<sup>26</sup>, S. K. Kumar<sup>26</sup>, A. Karim<sup>22</sup>, and S. K. Satija<sup>12</sup>.

### **Effect of Solvent on Surface Induced Diblock Copolymer Ordering**

H. Lin<sup>27</sup>, A. Steyr<sup>127</sup>, A. Karim<sup>22</sup>, T. P. Russell<sup>5</sup>, and S. K. Satija<sup>12</sup>.

### **Water Adsorption at Polyimide/Silicon Wafer Interface**

W.-L. Wu<sup>22</sup>, J. H. VanZanten<sup>22</sup>, and W. J. Orts<sup>12</sup>.

### **Glass Transition Temperature of Polymers Near Surface**

W.-L. Wu<sup>22</sup>, J. H. VanZanten<sup>22</sup>, W. J. Orts<sup>12</sup>, and S. K. Satija<sup>12</sup>.

### **Adsorption of Surfactants at a Hydrophobic Surface Near the Solid-Liquid Interface**

D. C. McDermott<sup>28</sup>, R. Thomas<sup>28</sup>, A. R. Rennie<sup>29</sup>, S. K. Satija<sup>12</sup>, and P. D. Gallagher<sup>12</sup>.

### **Affiliations**

<sup>1</sup>Brookhaven National Laboratory

<sup>2</sup>Exxon Research and Engineering Co.

<sup>3</sup>Florida State University

<sup>4</sup>George Mason University

<sup>5</sup>IBM Almaden

<sup>6</sup>Johns Hopkins University

<sup>7</sup>MURR, Columbia, MO

<sup>8</sup>National Institute of Health

<sup>9</sup>Naval Research Laboratory

<sup>10</sup>Oak Ridge National Laboratory

<sup>11</sup>Ovonics Company

<sup>12</sup>Reactor Radiation Division

<sup>13</sup>Rüth University, Germany

<sup>14</sup>Rutgers University

<sup>15</sup>THOMSON-CSF, France

<sup>16</sup>University of Akron

<sup>17</sup>University of Arizona

<sup>18</sup>University of Linz, Austria

<sup>19</sup>University of Maryland

<sup>20</sup>University of Notre Dame

<sup>21</sup>Ceramics Division

<sup>22</sup>Polymers Division

<sup>23</sup>Inst. Crystallography, Russian Academy of Science

<sup>24</sup>MIT

<sup>25</sup>University of Minnesota

<sup>26</sup>Penn State University

<sup>27</sup>University of Rhode Island

<sup>28</sup>University of Oxford

<sup>29</sup>Cambridge University

## MACROMOLECULAR AND MICROSTRUCTURE STUDIES

During the past year, three small angle neutron scattering (SANS) instruments were in operation at the CNRF for the first time for macromolecular and microstructural studies on a wide range of materials including polymers, colloids and microemulsions, microporous media, biological macromolecules, nanocrystalline metals and ceramics, molecular composites, and liquid crystals among many others. In its first year of operation, approximately 85 experiments were carried out on the new, high resolution, 30-m SANS instrument on guide NG-3 that is partially supported by the NSF through its Center for High Resolution Neutron Scattering (CHRNS) at the CNRF. A comparable number of experiments were performed on both the 30-m SANS instrument at NG-7, an instrument jointly developed by NIST, Exxon Research and Engineering Co., and the University of Minnesota, and the lower resolution, 8-m Reactor/Polymers Divisions' SANS instrument at guide NG-5. Roughly one-half of the total beam time on the 30-m instruments (~75% on the CHRNS SANS and ~25% on the NIST/Exxon/Univ. of Minnesota SANS) was distributed among groups who submitted 71 proposals that were peer reviewed and allocated beam time by the CNRF's Program Advisory Committee. In this section of this report, the results of some of these studies, in which Reactor Division scientists have had a major role, are briefly described.

### Inorganic Materials

#### • Ordered Mesopores in Silica

A new class of mesoporous materials prepared with liquid crystal templates is being studied with scientists from Mobil Research and Development, where the materials were first developed, and the University of California at Santa Barbara. The materials have amorphous, silica-based frameworks with highly regular arrays of uniform sized channels whose diameters can be tailored in the range from 1.5 to over 10 nm through the choice of templating molecules and reaction conditions. The cavity sizes in these materials are larger than have been achieved in crystalline materials such as zeolites, and afford new opportunities for

applications as catalysts and adsorption media. The SANS measurements carried out to date have focused both on characterizing the pore structure and on elucidating the liquid crystal templating mechanism involved in forming the materials.

A typical SANS pattern from a UCSB-prepared material that had been calcined to remove the template from the pores is shown in figure 1. The material has a honeycomb pore structure that gives rise to diffraction peaks that can be indexed on a 2D hexagonal lattice and correspond to a nearest neighbor pore spacing of 44 Å and a pore diameter of about 36 Å. The structureless pattern also shown in figure 1 was obtained after soaking the material in a pore masking solution of 40% H<sub>2</sub>O/60% D<sub>2</sub>O which demonstrates that the pores are fully accessible and that the scattering length density of the pore framework is close to that of bulk amorphous silica.

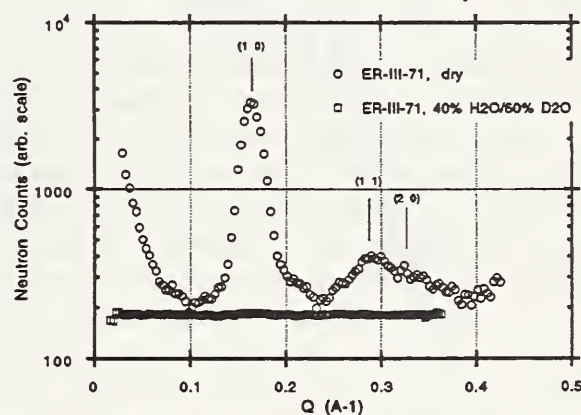
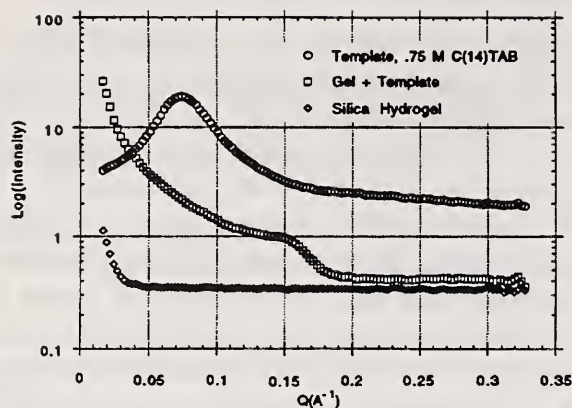


Figure 1. SANS from a powder sample of mesoporous silica with hexagonally ordered cylindrical pores. The diffraction from the pores vanishes when the pores are filled with an H<sub>2</sub>O/D<sub>2</sub>O mixture that has the same scattering density as the silica framework.

Synthesizing these materials involves combining a cationic surfactant solution (e.g. tetradecyltrimethylammonium bromide, or C<sub>14</sub>TAB) with a silica hydrogel under certain pH conditions. The results of SANS measurements on these precursor phases, and their mixture, in which the aqueous medium was 40% H<sub>2</sub>O/60% D<sub>2</sub>O, are shown in figure 2. Under these contrast conditions, the surfactant should dominate the



**Figure 2.** SANS from the concentrated surfactant solution (circles) and silica hydrogel (diamonds) that when combined (squares) begins to form the ordered mesoscopic structure seen in figure 1 for the final product material.

scattering and the mesopore structure should be seen through the organization of the surfactant molecules within the framework structure. The scattering from the surfactant solution (circles in Fig. 2) has a prominent peak at  $Q \sim 0.075 \text{ \AA}^{-1}$  corresponding to an intermicelle spacing of about  $84 \text{ \AA}$ , which is nearly twice the spacing of the pores in the final product material. The scattering from the silica hydrogel (diamonds) is, as expected for this null contrast condition, nearly flat over the  $Q$ -range of interest. The third pattern in figure 2 (squares) is from the slurry that forms when the surfactant and hydrogel are combined. This sample is probably multiphase, with both an aqueous phase and a suspended solid phase, but already shows the emergence of a peak near the  $Q_{10}$  position of the 2D hexagonal structure of the mesopore material. These results clearly show that the templating mechanism is more complex than originally proposed in that the surfactant molecules become organized into long cylindrical micelles with an hexagonal, nearly close-packed arrangement only when a source of silica is present under proper pH conditions. Measurements are continuing that will hopefully further elucidate this process.

#### • Advanced Ceramics

The combination of the multiple small-angle neutron scattering (MSANS) and conventional SANS techniques makes it possible to measure pore sizes from a few nanometers up to  $10 \text{ \mu m}$ .

Thus, the pore evolution during sintering of ceramic compacts, formed from powders which contain particles in the  $0.1 \text{ \mu m}$  to  $1 \text{ \mu m}$  size regime, can be followed from the earliest sintering stages through to the final stage. In collaboration with Southwest Research Institute and NIST's Ceramics Division, MSANS, and SANS are being used to study the effects of non-sinterable additives on the pore size distribution of commercial alumina powder compacts during densification. The results indicated that the addition of large fused alumina particles retards densification but does not appreciably alter the final-stage effective pore size. On the other hand, the addition of small zirconia particles has little effect on densification but greatly accelerates pore coarsening, resulting in a much larger effective pore size in the final sintering stage. Thus, SANS and MSANS are enabling a direct statistically-significant observation of sintering processes in these materials.

In collaboration with Dow Chemical Corporation and NIST's Ceramics Division, a comprehensive study aimed at understanding and controlling the microstructural evolution during processing of silicon nitride is underway. MSANS and SANS measurements of isothermally-sintered silicon nitride doped with  $\sim 6 \text{ wt.}\%$  magnesia have been performed to characterize the porous microstructure from the largest to the smallest pore sizes in the system. The samples were sintered at  $1600 \text{ }^\circ\text{C}$  for hold times between 0 and 180 minutes, providing sample densities ranging from 73% to 93% of theoretical density (TD). The density of the green body is 53% TD. Figure 3 shows the effective pore radii as a function of %TD for both MSANS and conventional SANS (Porod) analyses. The MSANS results show that the largest pores in the system coarsen at densities between 70% and 80% TD before becoming smaller again as densification proceeds. On the other hand, the Porod results show that the effective size of the smallest pores in the system decreases monotonically as the system densifies. Further measurements of samples with hold times between 60 and 180 minutes are planned in order to better understand the abrupt decrease in Porod radius between 96% and 97% TD. A companion study of isothermally-sintered yttria-doped silicon nitride is planned to study the effect of this

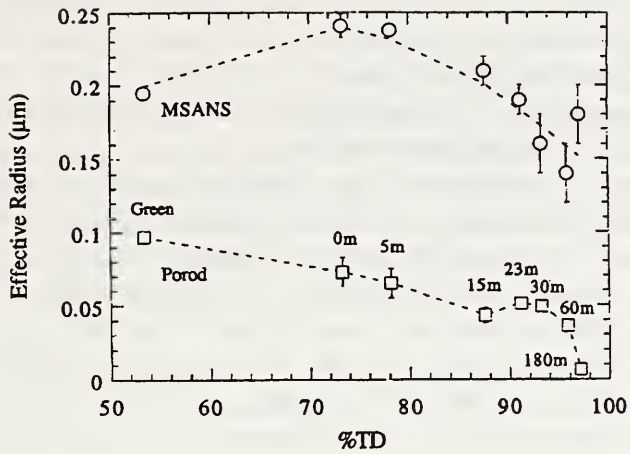


**Figure 3.** Effective pore radius versus %TD from MSANS and Porod analyses for magnesia-doped silicon nitride sintered at 1600 °C for the number of minutes indicated.

sintering aid on the evolution of the pore size distribution during densification.

Preliminary experiments have also been performed in collaboration with Northwestern University on conventionally-reacted as well as microwave-assisted reaction-bonded silicon nitride (RBSN). During fabrication, the nitridation reaction causes the pores in the original compacted silicon powder to become filled with lower density silicon nitride. MSANS studies show that the effective radius of the largest pores in the system decreases during densification for both microwave-assisted and conventional RBSN. The final pore sizes are very similar although there is some suggestion of a more complicated morphology in microwave-assisted RBSN. A Porod analysis shows a larger drop in surface area for microwave-assisted RBSN which would be consistent with a more efficient filling of small pores in this case. Further measurements are planned to investigate the uniformity of microwave-assisted RBSN compared to conventional RBSN and to relate the microstructural variations to strength and fracture toughness studies.

### • Nanostructured Ceramics

Nanostructured ceramics are those compacts which have been formed from powders with nano-sized particles of diameters typically less than 10 nm. Such powders are of interest since there is evidence that superplastic forming can be used

to enable near-net-shape processing of ceramics. This eliminates the need for costly machining. Since nanostructured compacts contain comparatively smaller pores, conventional SANS techniques can be used to measure pore size distributions as a function of densification. Such studies have been performed on both air and vacuum-sintered research-grade nanostructured zirconia in collaboration with Rutgers University and NIST's Ceramics Division. Figure 4 shows the scattering from samples sintered at 850 °C in air and in vacuum. The vacuum-sintered sample density is 95% TD whereas the air-sintered sample density is 58% TD. Thus, the pore volume fraction is much smaller in the vacuum-sintered sample and the data do not exhibit the strong interparticle interference peak seen in the air-sintered sample, which has a much larger pore volume fraction.

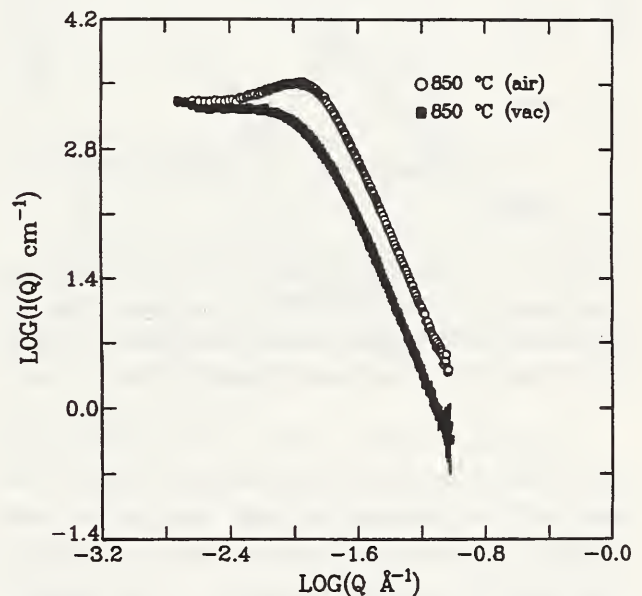


**Figure 4.** Log(I(Q)) versus log(Q) plot of the scattering from nanophase zirconia sintered at 850 °C in air (58% TD) and in vacuum (95% TD).

The availability of samples of sufficient size and uniformity to permit absolute calibration of the scattering data has resulted in the development of a fully quantitative microstructural model for this system. The model assumes ellipsoidal pores in the gaps between globular grains and takes into account interparticle interference effects. A unimodal log-normal pore size distribution with adjustable modal and median size is assumed, consistent with TEM assessments of the grain size

distribution. Figure 5 shows the log-normal volume pore size distributions corresponding to the best fits to the data from nanostructured zirconia vacuum-sintered at 850 °C for three different sintering times. The figure shows that the material exhibits remarkable stability in pore size distribution up to 95% TD. In addition, the mean pore diameter at 95% TD is still less than 20 nm. This is an important achievement since the ultimate objective in fabrication is to obtain nearly full density without major pore and grain coarsening. Future experiments will focus on yttria-stabilized and pressure-sintered nanophase zirconia systems.

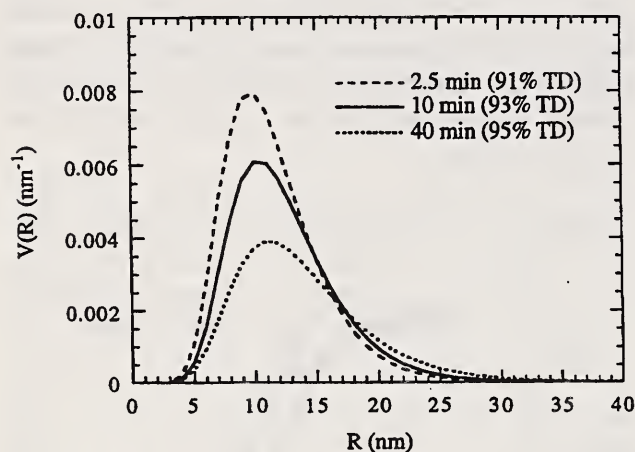


**Figure 5.** Lognormal volume pore size distributions corresponding to the best fits to the data, using the model described in the text, for nanophase zirconia sintered at 850 °C for the times indicated.

Compacts formed from commercial-grade nanostructured zirconia powders have also been measured in collaboration with Nanophase Technologies Corp., a participating company in NIST's Advanced Technology Program. The scattering from these materials sintered in air at different temperatures is qualitatively similar to that observed from the research-grade samples described above.

#### • Nanocrystalline Palladium

Nanocrystalline metals, with average grain size on the order of several nanometers, have a number of interesting properties including exceptional strength. Because of the restriction on dislocation generation and mobility imposed by the small grain size, plastic deformation is inhibited and consequently yield strength is increased. The presence of defects, however, has a strong

influence on the mechanical properties and the quantitative information on the defect structures that SANS can provide is of great value in reaching an understanding of the mechanical behavior of these materials.

A systematic study of the defect structures in nanocrystalline palladium, prepared by the inert gas condensation and compaction technique, is ongoing in collaboration with Northwestern University and Argonne National Laboratory [1]. The scattering from the as-compacted material (Fig. 6), which is typically only 85% of full density, exhibits four changes in slope and is indicative of three distinct defect sizes. The source of scattering for all three sizes is thought to be dominated by voids since the void volume fraction derived from the  $q^2$ -weighted integrated cross section (the scattering invariant) accounts fully for the measured density of the material. The smallest voids (~1 nm), which produce the leveling off in the scattering at the largest  $q$  values, are identified as triple junction voids based on positron life time studies. The next larger voids are about the size of missing grains, and scale with grain size (inferred from the broadening of x ray diffraction peaks) in annealed samples. The largest defects are of near micron size and do not appear to change significantly with annealing conditions. Efforts are continuing toward obtaining more highly compacted material that hopefully would have fewer defects and be sinterable to nearly full density without appreciable grain growth.

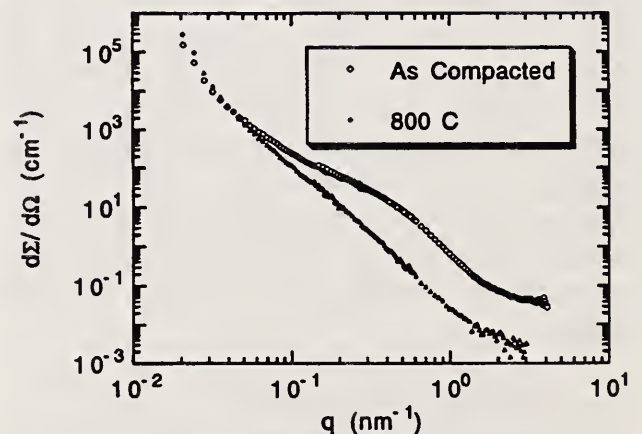


**Figure 6.** Small angle scattering from nanocrystalline palladium before and after annealing at 800 °C for 100 minutes.

## Biology

The use of the 30-m SANS instruments at the CNRF to study biological systems has continued to increase over the past year. The wide  $Q$  range and high flux available make these instruments well-suited for the study of a wide variety of biological systems, from large biopolymer matrices to small macromolecular complexes.

### ● Agarose Gels

Although agarose-based pulsed gel electrophoresis is widely used for the separation and analysis of long DNA fragments, relatively little is known about the microstructure of the agarose gel matrix itself. Such information could be quite useful because characteristics such as void size, strand thickness, gel microheterogeneity and correlations in spatial structure—as well as changes that might occur when electric fields are applied—can be expected to influence the way macromolecules migrate through the gels. In collaboration with the NIH and the College of Wooster, the structure of agarose gels has been studied over a wide range of  $Q$  values from  $0.05 \text{ nm}^{-1}$  to  $3.0 \text{ nm}^{-1}$  spanning a length scale from approximately 2.5 nm to 120 nm. These studies have shown that SANS can be used to probe the properties of the junctions formed between individual agarose strands.

The effects of such factors as concentration, cooling rate and solvent quality have been examined. Subtle changes in gel structure are observed when the pre-gelation agarose concentration or the cooling rate at which the gels are formed is varied. In contrast, dramatic evidence of structural rearrangement is observed when the solvent quality is changed by the addition of dimethyl sulfoxide, or when the temperature of the gel is elevated above  $70^\circ\text{C}$ . Figure 7 shows the measured scattered intensities from 3% agarose in  $\text{D}_2\text{O}$  on a  $\log(I(Q))$  versus  $\log(Q)$  scale as a function of temperature. Below  $70^\circ\text{C}$ , three regions can be delineated: at small  $Q$  values ( $0.05 \text{ nm}^{-1} \leq Q \leq 0.25 \text{ nm}^{-1}$ ) corresponding to length scales between 25 nm and 120 nm, a  $I(Q) \sim Q^{-\alpha}$  power law behavior is observed; at intermediate  $Q$  values ( $0.25 \text{ nm}^{-1} \leq Q \leq 0.8 \text{ nm}^{-1}$ ), an  $I(Q) \sim Q^{-\beta}$  behavior is observed where  $\beta > \alpha$ ; for  $Q > 0.8 \text{ nm}^{-1}$  corresponding to length scales

smaller than 8 nm,  $\log(I(Q))$  is a slowly varying function of  $\log(Q)$  appearing relatively "flat" when compared to the other two regions. The value of  $\alpha$  is close to 2.0 and that of  $\beta$  is close to 2.5. The  $Q^*$  value at which the slope changes from  $\alpha$  to  $\beta$  corresponds to a minimal size of  $\approx 3.5\text{--}4 \text{ nm}$  for the hydrogen-bonded junctions between agarose strands. The flat portion of the data in the high  $Q$  region is due to scattering from structures of the order of a few nanometers and is probably associated with small molecular groups tied to the agarose backbone.

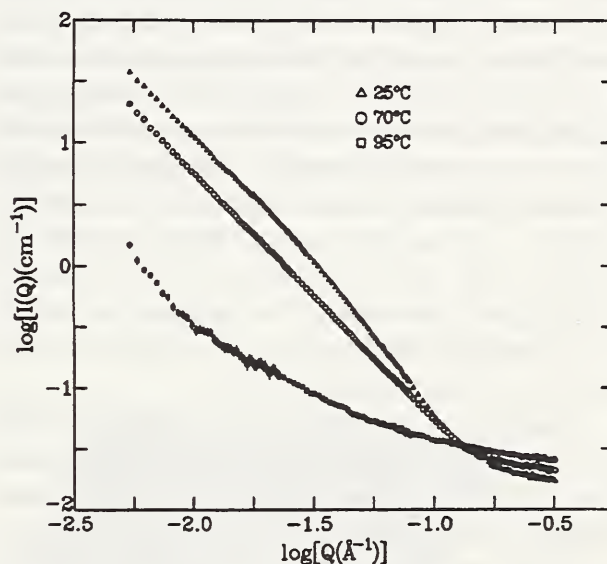


Figure 7.  $\log(I(Q))$  versus  $\log(Q)$  plot of the small angle scattering from 3% agarose in  $\text{D}_2\text{O}$  heated to the temperatures indicated.

As the temperature is increased above  $70^\circ\text{C}$ , hydrogen bonds between strands are disrupted, leading to a thinning of the interstrand junctions. This is manifested by a shift in  $Q^*$  to higher  $Q$  values such that the  $\beta = 2.5$  region seems to disappear. When the temperature reaches  $95^\circ\text{C}$ , the gel is completely melted and the scattered intensity changes dramatically to a smoothly varying curve on a  $\log(I(Q))$  versus  $\log(Q)$  scale. The intensity at the smallest  $Q$  values decreases markedly while that at the largest  $Q$  values increases. This is expected since large correlations between strands are no longer present while, at the same time, the small molecular groups associated with the agarose backbone enjoy enhanced degrees of freedom.

Additional studies of agarose gels in the presence of pulsed and steady-state electric fields

are currently underway. Preliminary studies indicate that pulsed fields result in structural changes at the largest length scales measured while steady-state fields have little or no effect. Thus, these studies may become important in helping to understand why large fragments of DNA can only be separated using pulsed-field gel electrophoresis.

- **Small Protein Complexes**

Structural studies of the Troponin C/Troponin I complex, a 6-nm diameter muscle regulatory protein, have been completed in collaboration with the Los Alamos National Laboratory (LANL). Deuterated TnC was complexed with nondeuterated TnI and measured at low concentration under a variety of solvent conditions. The results indicate that the TnC molecules are more extended in the complex than free TnC dimers and that the centers of mass of the TnC and TnI subunits coincide. Since data were obtained at higher Q values with good statistics, more advanced modeling of the shape of the complex as well as the individual components is possible and such analysis is currently underway.

Studies of the effects of acetylation of the protein core of the nucleosome, a 10-nm diameter protein/DNA complex which forms the basic subunit of chromatin, are continuing in collaboration with LANL and the University of California at Davis. The radius of gyration ( $R_g$ ) has been determined for both the acetylated and non-acetylated complexes in dilute solution under a variety of solvent conditions. In all cases, the  $R_g$  values are found to be higher in the acetylated complex. The results are currently being compared with models for various protein/DNA arrangements. Measurements at higher Q values are planned in order to more accurately determine the particle shape in both the acetylated and non-acetylated conformations.

Measurements of the distance between myosin light chains in myosin and acto-myosin complexes are being performed in collaboration with the University of California at San Francisco. Such measurements require high concentrations of protein since small differences in spectra are being sought. Thus, the samples are measured in pelleted form which has necessitated the design and construction of new demountable sample cells. In addition, the first scattering experiments on

NCD, a 4 nm diameter motor protein involved in chromosome aggregation, have been performed in dilute solution. Future experiments will explore changes in  $R_g$  under different biochemical conditions and in the presence of non-hydrolyzable ATP analogs.

Initial measurements on cyclic AMP receptor proteins have been performed in collaboration with NIST's Center for Advanced Research in Biotechnology. The receptor protein (CRP) and its small molecule ligand (cAMP) provide an important model system for studying protein-ligand interactions essential for the regulation of gene expression in a large number of living systems. Measurements performed in  $D_2O$  solvent showed that the conformational change induced in CRP by cAMP binding resulted in a 20% decrease in its  $R_g$  value. Measurements at higher Q values are planned in order to obtain more detailed shape information of CRP in both its active conformation with cAMP bound and its non-liganded inactive conformation. Since the active complex binds DNA, studies of the CRP/DNA complex and related DNA binding receptor proteins will also be performed.

The CNRF is continuing to provide the necessary support to meet the specialized needs of the biology community. The user's biology laboratory has been upgraded when possible and cooperative arrangements have been made with other biochemistry laboratories at NIST to provide access to more specialized equipment as needed.

## **Polymers**

Recent research efforts have focussed on the morphology and phase separation of polymers and on the rheology of complex fluids such as polymer solutions, liquid crystals and microemulsions.

- **Rheology of Dissolved Diblock Copolymers**

The influence of shear on polymer and copolymer structures has received considerable recent attention due to its importance in polymer processing (injection molding, extrusion, etc). Understanding shear-induced order may lead to improved processing conditions and therefore to superior polymer materials.

A systematic study of the effects of shear on concentrated diblock copolymer solutions is



underway in collaboration with Brooklyn Polytechnic University. The system chosen for the initial measurements is monodisperse polystyrene/polyisoprene (PS/PI) at a concentration of about 65% in dioctylphthalate (DOP). The copolymer has nearly equal block sizes and at this concentration orders with a lamellar morphology below a convenient order disorder transition (ODT) temperature of 39 °C. The solution was sheared using the NIST-Boulder Couette shear cell at temperatures both below and above the quiescent ODT. Two distinct geometries corresponding to a radially or to a tangentially incident neutron beam were used. By monitoring the relative intensities of the diffraction peaks from the lamellae observed with these two geometries, their orientation could be determined unambiguously.

It was found that below the quiescent ODT both steady and oscillatory shear orient the

lamellae predominantly along stream lines (lamellae are parallel to the shear cell wall). Nearly perfect alignment was achieved with oscillatory shear (200% strain), with peaks observed only in the tangential geometry, whereas under couette flow (steady shear) weak peaks were also observed in the radial geometry indicating some degree of misalignment (see Fig. 8).

Above the quiescent ODT, shear was seen to induce ordering of lamellae along streamlines starting at a characteristic shear rate which depends on temperature. The degree of alignment is characterized by a power law behavior with shear rate. When the shear rate is rescaled, a master curve (reminiscent of the time-temperature superposition principle) is found for all temperatures. This means that in order to attain a specific degree of lamellar orientation, one could change either the temperature or the shear rate alone.

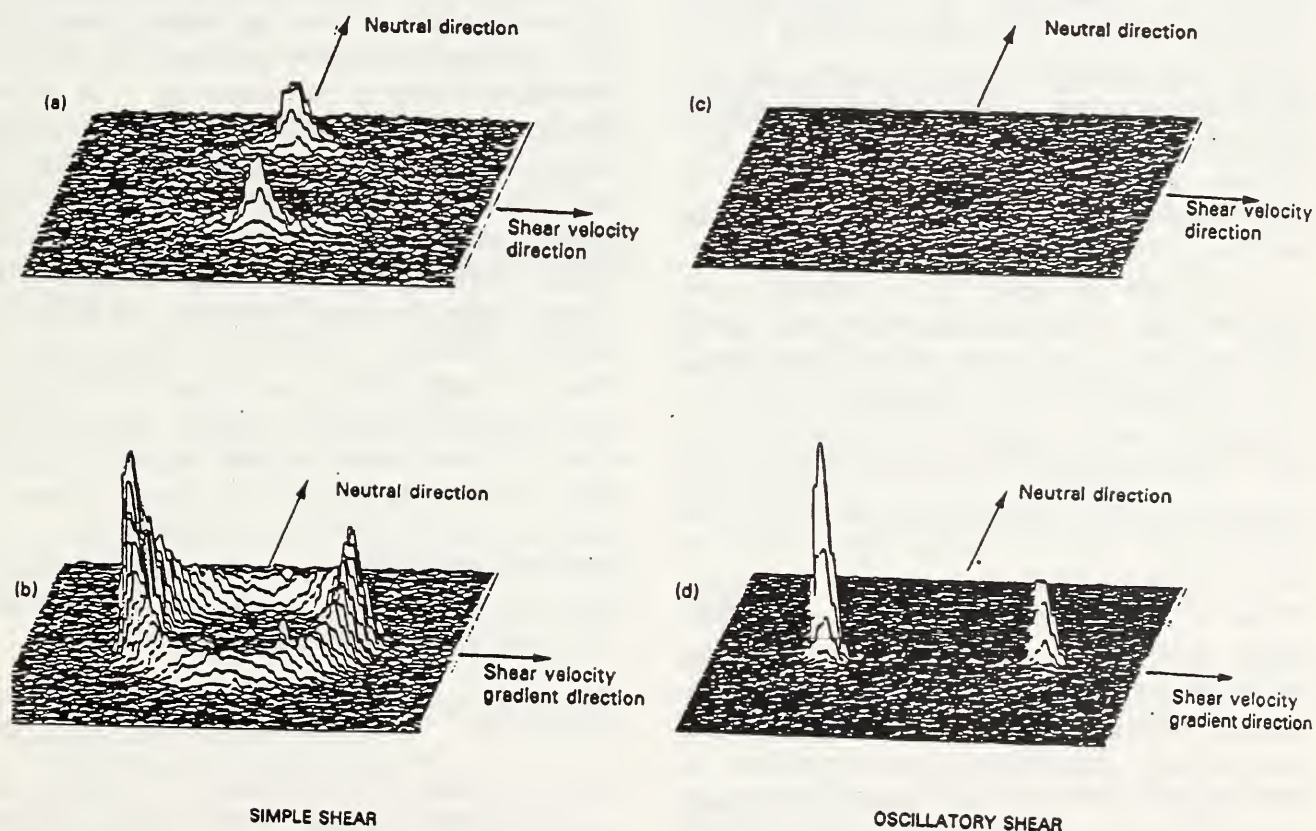


**Figure 8.** SANS from a concentrated solution of PS/PI in DOP with the neutron beam incident either radially (a and c) or tangentially (b and d) to the Couette shear cell. Both steady shear (a and b) and oscillatory shear (c and d) are represented.

- **Kinetics of Phase Separation of Polymer Blends Mediated by Block Copolymers**

Copolymers are often added to polymeric materials in order to enhance compatibilization and improve mechanical properties. Copolymers tend to form interfaces between different materials analogous to surfactants in microemulsions. The goal of our joint investigations with Brooklyn Polytechnic University is to better understand how this local mixing affects the kinetics of phase separation. This will hopefully lead to new methods for controlling polymer microstructures. Blends of polyethylbutylene (PEB) and polymethylbutylene (PMB) and their copolymers have been studied. Deuteration of one of the homopolymers was used to enhance the neutron contrast. A set of three samples containing either no diblock copolymer, 10% or 20% diblock copolymer were first heated to a temperature of 250 °C (well above the order-disorder transition temperature) for a few hours in order to allow for equilibration in the single phase region and then quenched to ambient temperature (kept at 25 °C) just prior to measurements. The scattering was monitored over time. Even though the sample temperature equilibrated to 25 °C within 3 to 4 minutes, sample changes manifested as an evolution of the scattering patterns were observed over long periods of time (many hours).

As shown in figure 9, a spinodal peak appeared after a few minutes, moved to higher scattering wave vector before reaching a maximum and then moved to lower scattering wave vector before disappearing "behind" the instrument beam stop. The intensity at the peak position also showed an unusual time dependence. Increasing the diblock copolymer content slows down the phase separation kinetics as well as keeps the "domains" smaller which enhances compatibilization during the early stages of spinodal decomposition. The initial increase of the peak position with time is not predicted by the linear theory of early-stage spinodal decomposition. At later times, fits of  $Q_{max} \sim t^a$  and  $I_{max} \sim t^b$  gave exponents  $a$  and  $b$  which are higher than predicted for homopolymer blends. Our results show that for up to 300 minutes, there is no clear scaling region for the variation of the peak position with time.

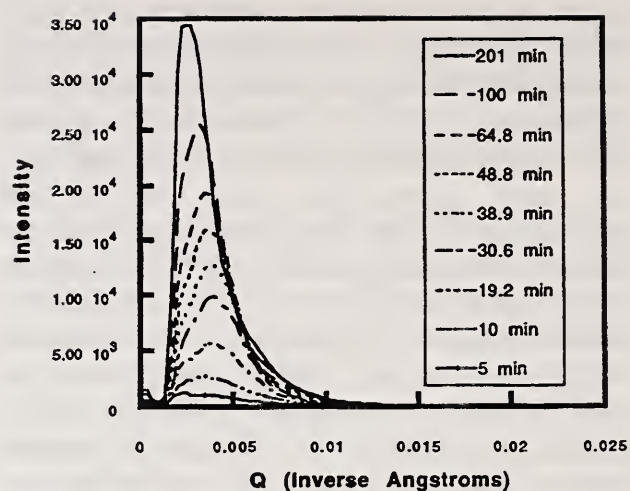


**Figure 9.** SANS spectra from a PEB/PMB blend mixed with 20% PEB-PMB diblock copolymer at various times after the temperature quench from 250 to 25 °C.

- **Modeling of the High-Q Scattering from Polymer Gels and Networks**

Modeling of the scattering function for polymer networks has been a challenge due to the large number of possible pathways to transfer correlations between two segments. In collaboration with H. Benoit (CRM Strasbourg), recent progress has been made in the modeling of high-Q scattering from polymer gels [2] and regular 2D polymer networks [3]. Given a polymer gel with constant functionality  $f$  containing branches of  $n$  segments each, the high-Q scattering can be put in the form (Kratky plot)  $Q^2 S(Q) = A + B/Q^2$ , where the coefficients  $A$  and  $B$  can be expressed as:  $A = 12/b^2$  and  $B = 36[-2 + f(f-1)/2]/nb^4$  where  $b$  is the monomer segment length and where theta solvent conditions have been assumed. Expressions for good solvent conditions have also been obtained. These expressions remain to be tested experimentally on model gels with known functionality and branch sizes.

## References

- [1] P. G. Sanders, J. R. Weertman, J. G. Barker, and R. W. Siegel, *Scripta Metall. et Mat.*, **29**, 91 (1993).
- [2] H. Benoit, F. Joanny, G. Hadzioannou, and B. Hammouda, *Macromolecules* **26**, 7590 (1993)
- [3] B. Hammouda, *J. Chem. Phys.* (in press, 1993).

## Research Topics

### Polymers

#### Microstructure of Conductive Carbon-Loaded Elastomers Under Uniaxial Stress

D. Tomlin<sup>28</sup>.

#### Interface Structure of Semicrystalline Polymer Blends

S. K. Kumar<sup>34</sup>, J. P. Runt<sup>34</sup>, and C. Barron<sup>34</sup>.

#### Structure and Interlayer Forces Between Tethered Polymer Chains

A. P. Gast<sup>43</sup>, M. C. Fair<sup>43</sup>, G. A. McConnell<sup>43</sup>, and J. S. Huang<sup>14</sup>.

#### Conformation of Main Chain Liquid Crystal Polymers as a Function of Temperature and Magnetic Field

S. K. Yarmey<sup>55</sup> and V. Arrighi<sup>17</sup>.

#### Comparison of Polymer Physical Gels before and after Solvent Removal

R. R. Lagasse<sup>40</sup> and G. E. Beaucage<sup>40</sup>.

#### Domain Morphology in Semi-Crystalline, Highly Chlorinated Polyethylene

G. E. Beaucage<sup>40</sup> and D. W. Schaefer<sup>40</sup>.

#### Molecular Interdiffusion in Polystyrene Latex Film Formation

K. D. Kim<sup>21</sup>, A. Klein<sup>21</sup>, L. Sperling<sup>21</sup>, and B. Hammouda<sup>37</sup>.

#### Structure of Polymers Adsorbed in Microporous Silica

W. C. Forsman<sup>65</sup> and P. Dreux<sup>65</sup>.

#### Phase Transformations and Domain Structure in Nylon

N. S. Murthy<sup>1</sup> and W. J. Orts<sup>37</sup>.

#### Domain Morphology of Semicrystalline Biodegradable Polymer Blends

Y. W. Cheung<sup>60</sup> and R. S. Stein<sup>60</sup>.

#### Conformation of Homopolymers Confined within Block Copolymer Domains

X. Quan<sup>3</sup> and G. Venugopal<sup>3</sup>.

#### Chain Conformation in Bimodal Homopolymer Blends

M. R. Landry<sup>12</sup>.

#### Molecular Weight Dependence of the Conformation of Dilute Polymers Near Their Theta Temperature

A. T. Boothroyd<sup>33</sup>, A. R. Rennie<sup>50</sup>, and L. J. Fetters<sup>14</sup>.

#### Structure of Polymer Brushes Extending From Plate-like Polymer Micelles

J. S. Huang<sup>14</sup>, D. Richter<sup>19</sup>, A. P. Gast<sup>43</sup>, and L. J. Fetters<sup>14</sup>.

#### Conformation of Long Chain Polymers Dispersed Among Shorter Chains

A. Zirkel<sup>19</sup>, D. Schneiders<sup>19</sup>, D. Richter<sup>19</sup>, and L. J. Fetters<sup>14</sup>.

#### Low Resolution Structure of Polymer-Virus Complexes

C. W. Lantman<sup>32</sup> and P. Thiyagarajan<sup>2</sup>.

#### Size Scaling of Flexible Diblock Copolymer Coils in Semi-Dilute Solutions

A. M. Mayes<sup>23</sup>, T. P. Russell<sup>16</sup>, and J. G. Barker<sup>37</sup>.

#### Temperature Dependence of the Conformation of Model Telechelic Ionomers in Solution

E. Karayianni<sup>68</sup>.

#### Effects of Shear on Diblock Copolymers in Solution

B. Hammouda<sup>37</sup> and N. P. Balsara<sup>5</sup>.

#### Phase Separation Kinetics of Homopolymer/Copolymer Mixtures

B. Hammouda<sup>37</sup>, J. Lin<sup>5</sup>, and N. P. Balsara<sup>5</sup>.

#### Single Particle and Interparticle Structure of Dendrimers

B. J. Bauer<sup>35</sup>, B. Hammouda<sup>37</sup>, and R. M. Briber<sup>59</sup>.

### Biology.

#### Structural Characterization of Agarose Gels in the Presence of Pulsed and Steady-State Electric Fields

S. Krueger<sup>37</sup>, A. P. Andrews<sup>9</sup>, and R. J. Nossal<sup>27</sup>.

#### Conformational Changes in Cyclic AMP Receptor Proteins

S. Krueger<sup>37</sup>, K. McKenney<sup>6</sup>, and F. Schwarz<sup>6</sup>.

#### Structure of Muscle Regulatory Proteins: Troponin C/Troponin I Complexes

G. Olah<sup>22</sup>, J. Trehwella<sup>22</sup>, S. Rokop<sup>22</sup>, and S. Krueger<sup>37</sup>.

**Effect of Histone Acetylation on the Structure of Chromatin Complexes**

P. Yau<sup>51</sup>, E. M. Bradbury<sup>51</sup>, J. Gatewood<sup>22</sup>, B. Imai<sup>22</sup>, and S. Krueger<sup>37</sup>.

**The Distance Between Myosin Light Chains in Myosin and Acto-Myosin**

R. Mendelson<sup>52</sup>, S. Fujiwara<sup>52</sup>, and D. Stone<sup>52</sup>.

Structured Fluids.

**Shear-Induced Orientation and Ordering of Disk-Like Liquid Crystal Micelles**

S. Kumar<sup>20</sup>, J. Mang<sup>20</sup>, and B. Hammouda<sup>37</sup>.

**Triglyceride Microemulsions**

S. F. Trevino<sup>46</sup> and R. Joubran<sup>49</sup>.

**Microstructure of Silicone-Based Surfactant Microemulsions**

R. Hill<sup>11</sup> and M. T. He<sup>62</sup>.

**Scattering Behavior of Microemulsions near the Lifshitz Line**

E. W. Kaler<sup>56</sup>, K.-V. Schubert<sup>56</sup>, and R. Strey<sup>24</sup>.

**Concentration Dependence of the Structure of Mixed Colloids for Controlled Drug Release**

E. Y. Sheu<sup>45</sup> and M. Polikandritou<sup>64</sup>.

**The Structure and Shear Thinning Behavior of Polymeric Microgels**

N. J. Wagner<sup>56</sup>, J. Bender<sup>56</sup>, and J. Bergenholtz<sup>56</sup>.

**Effects of Shear on 'Hard-Sphere' Colloidal Systems**

R. H. Ottewill<sup>60</sup>, A. R. Rennie<sup>50</sup>, H.J.M. Hanley<sup>29</sup>, and G. C. Straty<sup>29</sup>.

**Particle Morphology of Mixed Colloids of Bile Salts and Triglycerides**

R. P. Hjelm<sup>22</sup>.

**Critical Scattering from Heavy Water**

G. W. Neilson<sup>50</sup>, R. H. Tromp<sup>50</sup>, B. Stockford<sup>50</sup>, and A. Rennie<sup>50</sup>.

**Structure of Micelles in Viscoelastic Solutions**

P. Butler<sup>67</sup>, L. Magid<sup>58</sup>, W. Hamilton<sup>31</sup>, and B. Hammouda<sup>37</sup>.

**Droplet to Bicontinuous Phase Transitions in Microemulsions**

S.-H. Chen<sup>23</sup>, D. Lee<sup>23</sup>, and C.-Y. Ku<sup>23</sup>.

**Microstructure of Shearing Liquid Crystal Polymers**

N. J. Wagner<sup>56</sup>, J. Bergenholtz<sup>56</sup>, J. Bender<sup>56</sup>, L. Walker<sup>56</sup>, and B. Hammouda<sup>37</sup>.

**Micelle-Vesicle Transitions in Mixed Surfactant Colloidal Solutions**

E. W. Kaler<sup>56</sup>, S. Kline<sup>56</sup>, A. P. Full<sup>56</sup>, and R. Koehler<sup>56</sup>.

**Shear Induced Structural Transitions in Dense Colloids**

C. F. Zukoski<sup>57</sup>, M. K. Chow<sup>57</sup>, and C. Rueb<sup>57</sup>.

**Structure of Dense Binary Colloids under Shear Flow**

H.J.M. Hanley<sup>29</sup>, G. C. Straty<sup>29</sup>, C. F. Zukoski<sup>57</sup>, and W. Hunt<sup>57</sup>.

**Suspensions and Gels Formed by Self-Associating Polymer Molecules**

R. H. Ottewill<sup>60</sup> and A. R. Rennie<sup>50</sup>.

**Gelation of Dense Colloidal Silica: Effects of Shear**

H.J.M. Hanley<sup>29</sup>, G. C. Straty<sup>29</sup>, and C. D. Muzny<sup>54</sup>.

Materials Science.

**Pore Structure in De-Alloyed Silver/Gold**

K. Sieradski<sup>18</sup>, S. Corcoran<sup>18</sup>, and D. G. Wiesler<sup>37</sup>.

**Effect of Humidity on the Morphology of Chitosan**

S. F. Trevino<sup>46</sup> and J. Walker<sup>47</sup>.

**Grain Size and Interfacial Surface Area of Solid Propellants**

S. F. Trevino<sup>46</sup> and R. J. Lieb<sup>48</sup>.

**Scattering from Hydrogen Trapped on Edge Dislocations in Palladium**

K. L. Stefanopoulos<sup>66</sup> and J. P. A. Fairclough<sup>66</sup>.

**Defect Structures in Nanocrystalline Palladium**

P. G. Sanders<sup>30</sup>, J. R. Weertman<sup>30</sup>, R. W. Siegel<sup>2</sup>, and J. G. Barker<sup>37</sup>.

**Hydrogen Trapping at Lattice Defects in Palladium**

J. S. King<sup>61</sup> and B. J. Heuser<sup>63</sup>.

**Dislocation Scattering in Deformed Copper**

B. J. Heuser<sup>63</sup> and J. S. King<sup>61</sup>.

**Structure and Magnetic Properties of Iron/Silicon-based Nanocrystalline Materials**

G. E. Fish<sup>1</sup> and J. W. Lynn<sup>37</sup>.

**Structure of Liquid Crystal/Epoxy Molecular Composites**

R. P. Hjelm<sup>22</sup> and E. Douglas<sup>22</sup>.

**Current Fluctuations in High-T<sub>c</sub> Superconductors Near T<sub>c</sub>**

G. L. Squires<sup>7</sup> and C. D. Frost<sup>7</sup>.

**Porosity in Synthetic Reverse-Osmosis Membranes**

S. Kulkarni<sup>38</sup>.

**Irradiation Induced Microstructural Changes in Reactor Pressure Vessel Steels**

G. R. Odette<sup>53</sup>, E. Mader<sup>53</sup>, R. D. Klingensmith<sup>53</sup>, and J. G. Barker<sup>37</sup>.

**Aging Mechanisms in Reactor Pressure Vessel Steels**

J. P. Massoud<sup>13</sup>, M. Akamatsu<sup>13</sup>, and J. G. Barker<sup>37</sup>.

**Pore Structure and Formation Mechanisms of Mesoporous Molecular Sieves Prepared with Liquid Crystal Templates**

C. J. Glinka<sup>37</sup>, J. M. Nicol<sup>37</sup>, G. D. Stucky<sup>53</sup>, and D. Margolese<sup>53</sup>.

**Structure and Correlations in Magnetic Nanocomposite Materials**

J. J. Rhyne<sup>63</sup>, R. W. Erwin<sup>37</sup>, and C. L. Chien<sup>18</sup>.

**Binary Fluid Phase Separation in Silica Aerogel**

B. J. Frisken<sup>41</sup>, D. S. Cannell<sup>53</sup>, and M. Lin<sup>14</sup>.

**Effect of Powder Size Distribution and Non-Sinterable Particulate Addition on the Pore Evolution of Alumina During Densification**

R. A. Page<sup>42</sup>, Y. Pan<sup>42</sup>, S. Krueger<sup>37</sup>, and G. G. Long<sup>8</sup>.

**Microstructure Evolution of Microwave Assisted Reaction Bonded Silicon Nitride as a Function of Nitridation**

A. Allen<sup>8</sup>, G. G. Long<sup>8</sup>, S. Krueger<sup>37</sup>, J. Thomas<sup>30</sup>, and D. L. Johnson<sup>30</sup>.

**Evolution of the Pore Size Distribution During Densification of Silicon Nitride with Different Sintering Additives**

S. Krueger<sup>37</sup>, A. Allen<sup>8</sup>, G. G. Long<sup>8</sup>, and C. J. Hwang<sup>10</sup>.

**Influence of Vacuum on the Densification of Nanostructured Silicon Nitride**

A. Allen<sup>8</sup>, G. G. Long<sup>8</sup>, W. Chen<sup>8</sup>, A. Pechenik<sup>8</sup>, and S. Krueger<sup>37</sup>.

**Kinetic Studies of the Evolution of the Gel Matrix During Nucleation and Growth of Zeolites**

E. Coker<sup>69</sup>, R. Thompson<sup>69</sup>, G. G. Long<sup>8</sup>, and S. Krueger<sup>37</sup>.

**In Situ Characterization of the Pore Evolution in Colloidal Silicate Sol-Gels during Sintering**

H. Kerch<sup>8</sup>, A. Allen<sup>8</sup>, G. G. Long<sup>8</sup>, H. Burdette<sup>8</sup>, and S. Krueger<sup>37</sup>.

**Microstructure Evolution of Air and Vacuum-Sintered Nanostructured Zirconia**

H. Hahn<sup>39</sup>, G. Skandan<sup>39</sup>, S. Krueger<sup>37</sup>, G. G. Long<sup>8</sup>, A. Allen<sup>8</sup>, and H. Kerch<sup>8</sup>.

**Microstructure Evolution of Commercial Grade Nanostructured Zirconia**

J. Parker<sup>26</sup>, S. Krueger<sup>37</sup>, G. G. Long<sup>8</sup>, and A. Allen<sup>8</sup>.

**Porosity in Plasma-Sprayed Alumina as a Function of Chemical Composition and Heat Treatment**

A. Goland<sup>4</sup>, H. Herman<sup>44</sup>, J. Ilavsky<sup>44</sup>, G. G. Long<sup>8</sup>, and S. Krueger<sup>37</sup>.

**Microstructure of Reactive Silica Cements**

A. Allen<sup>8</sup>, R. Livingston<sup>15</sup>, and P. Heaney<sup>36</sup>.

**Affiliations**

<sup>1</sup>Allied-Signal, Inc.

<sup>2</sup>Argonne National Laboratory

<sup>3</sup>AT&T Bell Labs

<sup>4</sup>Brookhaven National Laboratory

<sup>5</sup>Brooklyn Polytechnic University

<sup>6</sup>CARB

<sup>7</sup>Cavendish Laboratory, UK

<sup>8</sup>Ceramics Division, NIST

<sup>9</sup>College of Wooster

<sup>10</sup>Dow Chemical Co.

<sup>11</sup>Dow Corning Corp.

<sup>12</sup>Eastman Kodak

<sup>13</sup>Electricite de France

<sup>14</sup>Exxon Research & Eng. Co.

<sup>15</sup>Federal Highways Administration

<sup>16</sup>IBM Almaden Research Center

<sup>17</sup>Imperial College, UK

<sup>18</sup>Johns Hopkins University

<sup>19</sup>KFA, Jülich, Germany

<sup>20</sup>Kent State University

<sup>21</sup>Lehigh University

<sup>22</sup>Los Alamos National Laboratory

<sup>23</sup>Massachusetts Institute Technology

<sup>24</sup>Max Planck Institute, Germany

- <sup>25</sup>MURR, Columbia, MO  
<sup>26</sup>Nanophase Technologies Corp.  
<sup>27</sup>National Institute of Health  
<sup>28</sup>Naval Research Laboratory  
<sup>29</sup>Thermophysics Division, NIST Boulder  
<sup>30</sup>Northwestern University  
<sup>31</sup>Oak Ridge National Laboratory  
<sup>32</sup>Optical Coating Laboratory, Inc.  
<sup>33</sup>Oxford University, UK  
<sup>34</sup>Penn State University  
<sup>35</sup>Polymers Division, NIST  
<sup>36</sup>Princeton University  
<sup>37</sup>Reactor Radiation Division  
<sup>38</sup>Rensselaer Polytechnic Institute  
<sup>39</sup>Rutgers University  
<sup>40</sup>Sandia National Laboratory  
<sup>41</sup>Simon Fraser University  
<sup>42</sup>Southwest Research Inst.  
<sup>43</sup>Stanford University  
<sup>44</sup>State University of New York, Stonybrook  
<sup>45</sup>Texaco R&D  
<sup>46</sup>U.S. Army RD&E Center  
<sup>47</sup>U.S. Army Natick RD&E Ctr.  
<sup>48</sup>U.S. Army Research Laboratory  
<sup>49</sup>U.S. Dept. of Agriculture  
<sup>50</sup>University of Bristol  
<sup>51</sup>University of California, Davis  
<sup>52</sup>University of California, San Francisco  
<sup>53</sup>University of California, Santa Barbara  
<sup>54</sup>University of Colorado  
<sup>55</sup>University of Connecticut  
<sup>56</sup>University of Delaware  
<sup>57</sup>University of Illinois  
<sup>58</sup>University of Kentucky  
<sup>59</sup>University of Maryland  
<sup>60</sup>University of Massachusetts  
<sup>61</sup>University of Michigan  
<sup>62</sup>University of Minnesota  
<sup>63</sup>University of Missouri (MURR), Columbia, MO  
<sup>64</sup>University of Oklahoma  
<sup>65</sup>University of Pennsylvania  
<sup>66</sup>University of Salford, UK  
<sup>67</sup>University of Tennessee  
<sup>68</sup>University of Wisconsin  
<sup>69</sup>Worcester Polytechnic Inst.

## NEUTRON BEAM APPLICATIONS

### Neutron Diffraction Measurement of Residual Stress

Considerable progress has been made in the last two years at NIST in a number of areas relating to the neutron diffraction measurement of residual stress. This includes the development of new methods of sample alignment ("ALIGN"), the development of a comprehensive data reduction program ("STRESS"), and the design and construction of a new multipurpose double-axis diffractometer with a number of state-of-the-art features specifically for improved residual stress measurement. The basic elements of the first two were discussed in some detail in last year's report; an update of the third will be presented later in this section. The main focus of this section will be on recent applications of the neutron diffraction technique to real problems, the solution of which has been greatly facilitated by our recent advances in methodology.

#### ● Weldments

The fracture safety of welds may be compromised by the residual stress state which is usually unknown, the microstructure which may contain crack nuclei, and compositional gradients, especially that of hydrogen. Neutron techniques can, in principle, provide critical measurements of the above three phenomena and thus guide the development of rational solutions to the associated welding problems. A major portion of our experimental effort in this past year has been devoted to the study of the first of these elements, and has ranged in scope from studies of prototypical geometry weldments (to test finite element models), to specimens relating directly to real-world problems such as leaks in railroad tank cars and bridge failures.

Evolution of Stresses Around a Weld. Utilizing the nondestructive character of neutron diffraction, an ONR-supported study of the evolution of residual stress patterns on a pass-by-pass basis was begun in FY92 for a model system. Because of micro-structural anisotropies in the original bainite sample, studies were begun this year on a new test specimen of high-strength low-alloy steel (HSLA-100) with the same geometry as was shown in last

year's report: a  $15 \times 15 \times 1.9$  cm<sup>3</sup> plate, with a v-notch weld channel. Measurements have been made in the central plane around the notch before welding and after one weld pass. Data collection is in progress for the same specimen after two weld passes.

At each of 25 sampling points in the base metal ( $3 \times 3 \times 3$  mm<sup>3</sup> gauge volume), one or two Bragg peak scans were made in the reflection geometry, and at least four scans were made in transmission. This provided sufficient information to extract, without any assumptions or approximations, three normal stress components and one shear stress component. A few points in the weld metal, which require separate analysis, were also examined. The "stress-free"  $d_0$  was obtained from the unwelded plate, which was confirmed to be essentially stress free by neutron diffraction.

Certain features are noteworthy:

1. A clear, highly-tensile stress field is produced in the base metal in the measurement region nearest the channel (gauge volume centers 3 mm from channel) for both transverse and the longitudinal directions. The tensile stress maximum ( $\sim 700$  MPa) occurs in the longitudinal direction and is approximately twice the maxima in the transverse directions.
2. At gauge volume centers 8 mm away from the channel, measured stresses are near zero or somewhat compressive.

The neutron results for the axial and transverse directions in the central plane of the plate are in good qualitative agreement with results obtained by x-ray diffraction for surface stresses around a bead weld on a steel plate. The results, when complete, will provide unique information not previously available to welding researchers.

Testing models. A very active area in welding science/technology is that of modeling weldments by means of finite element methods (FEM). One output of such modeling is the prediction of the residual stress distribution produced by the welding process. In a coordinated ORNL-NIST, ONR-supported program we have determined the residual stress distribution for a geometry amenable to modeling: a spot-welded disk. The associated ORNL modeling effort is in progress.

A schematic of the HSLA specimen is shown in figure 1, with the measurement region and the 2.0 cm diameter spot weld indicated on the 7.6 cm diameter, 1.86 cm thick disk. The gauge volume in this case was again  $3 \times 3 \times 3 \text{ mm}^3$ , and the (110) Fe reflection was used.

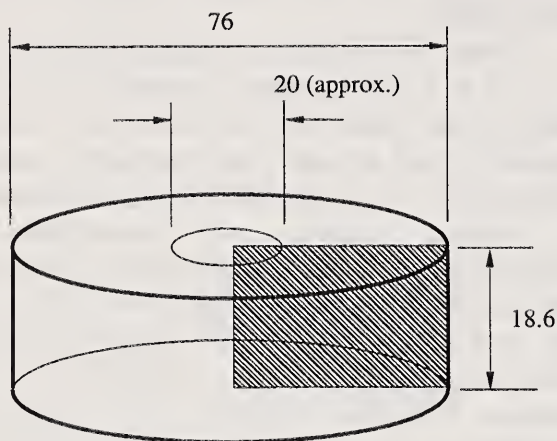


Figure 1. Schematic of the HSLA spot-welded disk. The shaded area is the plane over which the gauge volumes were centered. Dimensions are in millimeters.

The same specimen was examined prior to welding and was found to be essentially stress free so that  $d_0$  was obtainable. The value was confirmed by examining the balance of stresses normal to planes containing gauge-volume centers (shown in Fig. 2), interpolating, and assuming cylindrical symmetry of stresses.

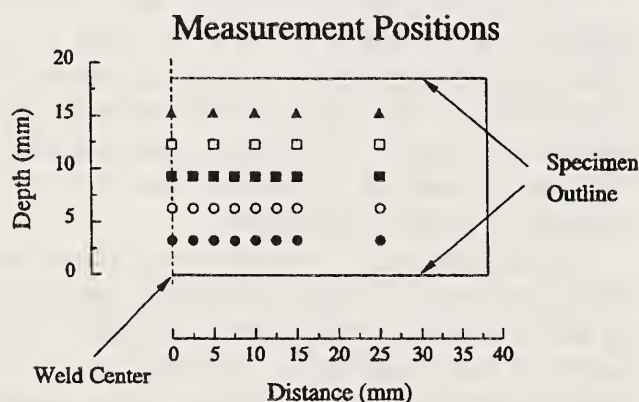


Figure 2. Exact measurement positions of the  $3 \times 3 \times 3 \text{ mm}^3$  gauge volume centers on the shaded plane of figure 1.

One of the notable results of this relatively straightforward experimental study is that all six stress components (i.e., three normal and three shear) were determined at each of the measurement points. This was possible because of the compact geometry of the sample and the full-circle goniometer mounted on the BT-6 instrument which, together, allowed a broader-than-usual range of sample orientations to be studied. To our knowledge, this represents the first such determination using neutron diffraction. The residual stress distributions are shown in figure 3.

Like the v-channel weldment results, all of the normal stresses near the weld-metal/base-metal interface are tensile. In the context of the modeling yet-to-be-done, the fact that the normal stress magnitudes do not change monotonically with axial distance from the weld (e.g. for  $r \leq 5 \text{ mm}$ ) may provide a critical test of the calculations.

Tank-car Weldments. The Federal Railroad Administration of the Department of Transportation (DOT) has a direct responsibility for the safe transport of hazardous materials via tank cars. One aspect of this responsibility has to do with the effectiveness and durability of axial stiffeners welded to older tank cars to increase tank shell buckling strength. Analytical calculations performed some years ago indicated that high tensile stresses, which would promote structural failure, may occur at the start- and end-points of the skip welds used to attach the stiffeners to the tank cars [1].

In a DOT-supported collaborative project with the Metallurgy Division, we have made the first determination of residual stress distributions in skip-weld specimens of the type used for railroad tank car stiffeners. A total of four specimens produced under different welding conditions, and one unwelded specimen, were characterized. The measured residual stress distributions through the thickness around the start and end points of the weldments are not in very good agreement with the analytical-model predictions. We find that only the normal stresses parallel to the bead-on-plate weldment direction are tensile. In addition, although the maximum tensile stress measured is comparable to the predicted value, the measured change in stress with distance from the weld tip is much less than the model calculations.



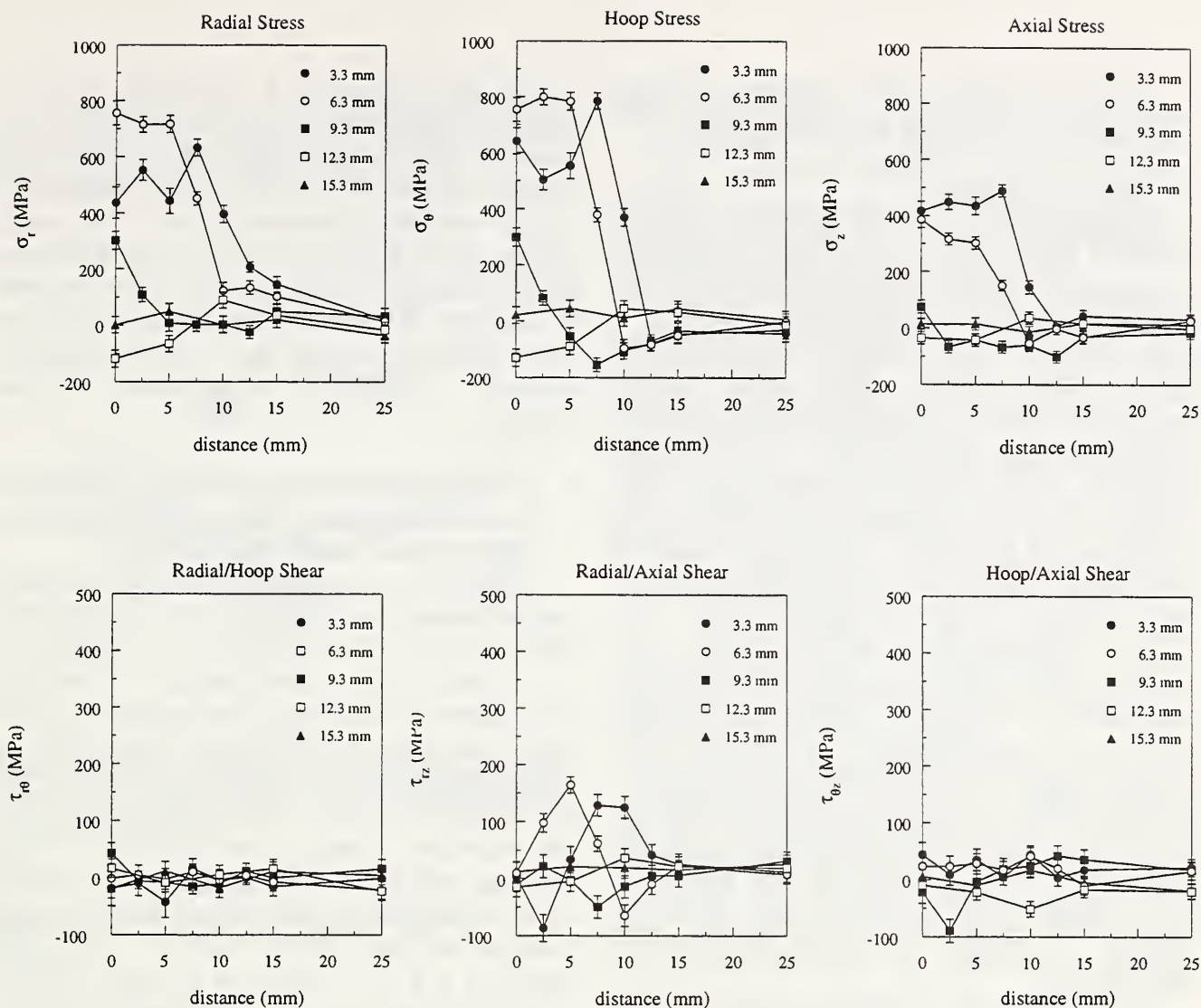


**Figure 3.** Measured residual stresses on the measurement plane of the spot-welded disk. Symbols correspond to those shown in figure 2.

Because of the nondestructive nature of the neutron measurements, these same samples will be characterized by x-ray diffraction so that complete surface and subsurface residual stress distributions will be available in the regions of interest.

**Infrastructure Application.** Although only a few catastrophic bridge failures have occurred (compared to the large number of bridge structures in service), any failure is expensive to repair and can result in loss of life. Of the failures, undesirable residual stresses have caused or contributed in many cases. Because of this the Federal Highway Administration of DOT has, for many years, sought a practical and reliable NDE method for measuring residual stresses in bridge structures, with particular interest in weldments. Several candidate techniques have shown promise, but only to a limited degree even in the laboratory.

A major difficulty has been that no primary standard was available to confirm the correctness of the results obtained with the candidate methods.

Very recently we have completed a preliminary study of strains in a laboratory specimen of a T-shaped full-penetration-welded stiffener for a bridge girder. Strains transverse to the weld direction were measured as a function of distance from the weldment for an array of points encompassing the thickness and width of the region of interest. Very clear strain gradients, asymmetric with respect to specimen morphology, were present in the region examined. These results indicate that great care must be taken in interpreting measurements performed with field-portable techniques which average over large regions of the specimen.

It is expected that a more comprehensive study will be begun in this area in the near future.

- **Other Applications**

Powder Metallurgy. Near net-shape manufacturing of metal components by low temperature compaction of metal powders offers substantial cost savings in materials and machining. However, a major limitation of this technology results from the fact that even relatively small tensile residual stresses cause fractures because of the low cohesive strength of interparticle bonds. It is therefore critical to model fabrication processes and the residual stresses they produce, and to measure the stresses to test the models. The fragile nature of the compacts makes neutron diffraction the only viable method for evaluating these stresses.

In a collaboration with researchers from M.I.T., initial studies have been completed on a compacted iron powder. Although the measurements are straightforward, in principle, the predicted strains are on the order of 100  $\mu$ strain, which is at about the limit of sensitivity of the BT-6 instrument. At this level, such factors as density gradients in the sample become very important. This because of an effect of path length on apparent d-spacing in wavelength-dispersive measurements.

The first set of measurements, although very encouraging, could not provide unambiguous results because the density profile in the compact (which is analogous to path length) had not been measured. New specimens are being prepared at M.I.T. for neutron diffraction study which will be fully characterized as to density, and which will test a number of different aspects of the processing technique.

- Squeeze-cast Metal-ceramic Composites.

Ceramic-fiber reinforced metal-matrix composites (MCCs) are beginning to be used in applications requiring good strength at high temperatures, good structural rigidity and dimensional stability, light weight, and good fabricability. One place that automotive engineers see enormous potential value for MCCs is as piston head reinforcements in automobile engines. At present, questions relating to residual stresses in the piston body, the squeeze cast reinforced top of the piston, and the effect of residual stresses on the performance of the squeeze-cast component must be answered.

We have performed a preliminary study of GM-provided aluminum-alloy matrix metal and the alumina/silicate reinforcement fiber preform to determine if neutron diffraction could characterize residual stresses in these materials. The results suggest that it should be possible in the aluminum matrix, but unlikely in the ceramic fibers (because of relatively low intensity and the complexity of the overlapping alumina and silicate diffraction patterns). Definitive measurements are in progress.

- **A New Double-Axis Spectrometer for Single-Crystal Diffraction, Texture, and Residual Stress Measurement (DASSATS)**

DASSATS is a multipurpose neutron diffraction instrument that is projected to be installed in 1994 on BT-8. The current status is as follows:

A basic US-1 (BNL-design: Universal Spectrometer 1) drum has been modified to allow take-off angles up to 120° ( $2\theta_M$ ) for residual stress measurements (Fig. 4). Texture and single-crystal diffraction will utilize a take-off angle of  $\sim 25^\circ$ . An extensive primary and secondary beam handling system has been designed for residual stress measurements, that allows the choice of potential sampling volumes from  $25 \times 25 \times 25$  mm<sup>3</sup> to  $1 \times 1 \times 1$  mm<sup>3</sup>, with a beam limiter to reduce the size of the reactor beam before it enters the monochromator drum. The primary system will slide in and out of the plug that is placed in the monochromator drum. The diffracted beam system will slide between the counter and the sample table. The sliding action is meant to allow for objects on the sample table to freely move in space, while going from one scan to another or even while performing some classes of scans. When required, the slides will accommodate a set of Soller slit blades.

An automated monochromator system with remote controlled rocking, translation, etc., and four different monochromators (on an elevator system) has been designed. An elevator device to shift a pyrolytic graphite filter in and out of the beam will be incorporated. Its purpose is to suppress the higher orders in the monochromatized beam for single crystal and texture measurements. Candidate position sensitive detector systems, including one with a radial collimator option, continue to be evaluated.

On completion it is expected that DASSATS will increase throughput for residual stress measurements by at least a factor of five.

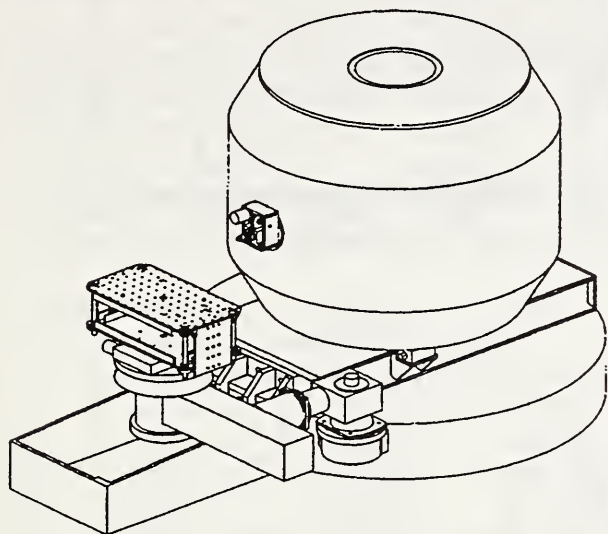


Figure 4. Partial schematic of "DASSATS", the new residual stress, texture, and single-crystal diffractometer to be installed on BT-8.

## Neutron Diffraction Measurement of Texture

### • Continuing Studies of Shaped-Charge Liners

It is well known that the textures of polycrystalline metals play a significant role in plasticity and other important physical properties of materials. However, the utilization of texture information for the improvement of specific materials properties or for the tailoring of fabrication processes is not a common practice yet, partly because of the difficulty of obtaining quantitative three-dimensional orientation distribution functions (ODF). Very recently, a comprehensive ODF analysis program package, called popLA, has been developed by Kallend, et al. [2], which is designed to make modern ODF analysis methods available to the general materials science community. This is now incorporated for routine use in our analysis software.

As a continuing project for DOD, complete three-dimensional ODFs of several heavy-metal shaped-charge liners, such as of tungsten, molybdenum and tantalum, and fabricated with different thermo-mechanical treatments, were

determined to find the correlations between the measured textures and the macroscopic properties.

The orientation distributions determined from the ODFs were so accurate that the texture-effect corrections, based on the ODF, could be utilized in the Rietveld profile refinement procedure.

**Tungsten Shaped-charge Liners.** The texture of a tungsten shaped-charge liner, fabricated by the HERF process from arc-cast ingots, was investigated by neutron diffraction and three-dimensional ODF analysis. Two  $\sim 12 \times 12 \text{ mm}^2$  plates, were obtained from each liner, one from 25 mm below the apex (labeled WTOP), and the other from 25 mm above the liner base (labeled WBOT). Four pole figures, (110) (200) (211) and (310), were measured with  $1.50 \text{ \AA}$  neutrons at the NIST research reactor for each sample. The orientation distribution functions (ODF) of the samples were obtained by the WIMV method with orthorhombic sample symmetry.

The major texture components found in the liner are summarized in Table 1. There are three dominant texture components in the liner, i.e.,  $(111)\langle 101 \rangle$ ,  $(100)\langle 011 \rangle$ , and  $(112)\langle 110 \rangle$ . The section near the apex exhibited primarily an  $(hkl)[110]$ -type texture, but the section near the base showed not only the sheet-type but also a strong fiber-type texture. The  $(112)\langle 110 \rangle$  component was strong near the apex of the liner, but was considerably weaker near the base of the liner. The part closer to the base had a higher degree of texture (texture index of 2.0), than the part closer to the apex (texture index of 1.9).

The orientation distributions determined from the ODFs were used for the calculation of the texture effect on the diffraction profiles. The details of the application of ODF to the Rietveld refinement is reported in the Crystallography Section of this report.

Table 1. The intensities (mrd units) of the major texture components, obtained from the two different parts of the liner.

Textures	W-BOT	W-TOP
(100)[011]	14	12
[100]-fiber	7	2
(111)[101]	11	10
[111]-fiber	6	1
(112)[110]	3	9
(115)[110]	1	8

**Molybdenum Shaped-charge Liners.** The crystallites orientation distributions of three different conical molybdenum shaped-charge liners, labeled C00, C20 and C40, fabricated with different thermomechanical treatment processes, were investigated by using neutron diffraction measurements and three-dimensional ODF analysis. Two specimens were obtained from each liner, one from 25 mm below the apex and the other from 25 mm above the liner base. The pole figure data of the four reflections, (110) (200) (211) and (222), were measured from each specimen, using 1.25 Å neutrons. The ODFs of all the samples were obtained by the WIMV method with triclinic sample symmetry. The agreement between the experimental and the recalculated pole figures was excellent for all the samples.

Several distinct pole density peaks were typically found from the sample orientation distribution (SOD) maps of all six samples. They are (111) $\langle uvw \rangle$ , (100) $\langle uvw \rangle$ , and intensity ridges extending from these peaks to (112) $\langle uvw \rangle$  and (115) $\langle uvw \rangle$ . The pole density distributions of the (111) $\langle uvw \rangle$ , (100) $\langle uvw \rangle$  and (112) $\langle uvw \rangle$ , as a function of the  $\psi$ -angles, were obtained from the three-dimensional SODs, and are presented in figure 5. The solid lines in the figures represent the distributions at the sections near the apex, and the dotted lines represent those at the sections near the liner base. The dotted curves have generally higher base-line intensities than the solid curves, which indicates that the bottom part of a liner tends to have stronger fiber-type texture than the part near the apex.

**Plastic Anisotropy of Molybdenum Liners.** The plastic strain ratio, commonly called the R-value, is defined by  $R(\alpha) = \epsilon_{yy}/\epsilon_{zz}$ , where  $\alpha$  is the angle of the stress direction measured from the rolling direction (RD) of the sample, and  $\epsilon_{yy}$  and  $\epsilon_{zz}$  are the width strain and thickness strain, respectively. The R-value is a parameter that indicates the anisotropy characteristics of sheet metals, and is related to the limit strains attainable in fabrication processes, such as stretching or deep-drawing. The R-values of the samples were calculated from the coefficients of the Harmonic ODF, using two different slip models: the restricted glide model and the pencil-glide model. The two sets of calculated R-values of the six samples are given in Table 2. It is known that

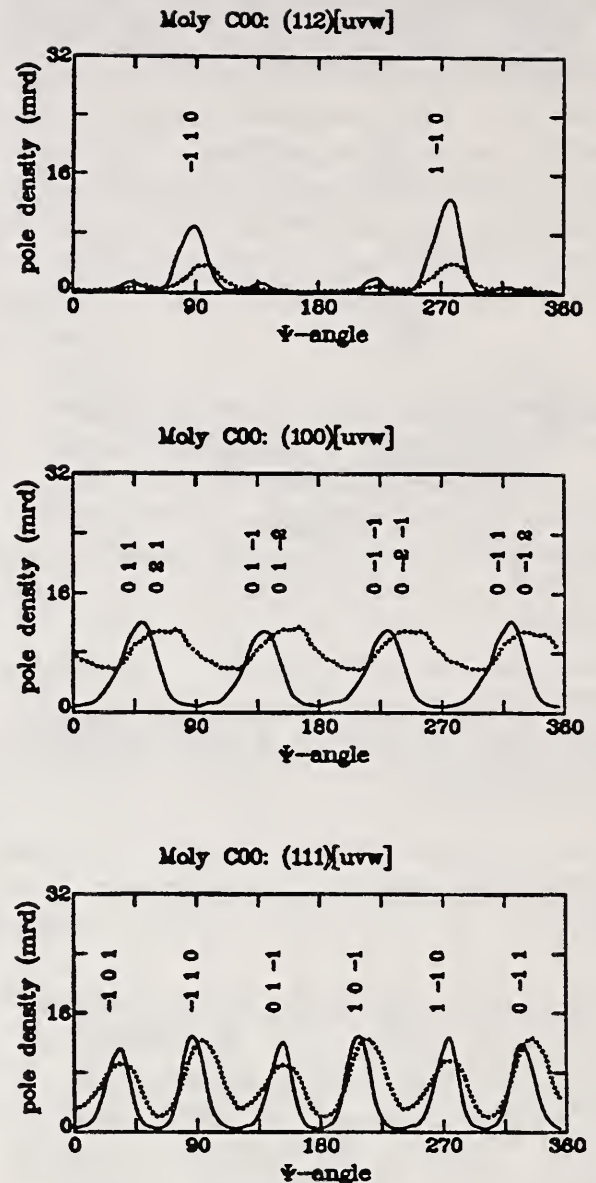


Figure 5. The (112) $\langle uvw \rangle$ , (100) $\langle uvw \rangle$  and (111) $\langle uvw \rangle$  distributions of the C00-A sample as a function of the  $\psi$ -angle. The solid lines indicate the distributions near the apex, and the dotted lines indicate those near the base of the liners.

the drawability of a sheet metal is closely related to the average strain ratio:  $R(\alpha) = (R(0) + R(45) + R(90))/4$ , and the directional variation in the plane of the sheet, commonly called the plane strain ratio:  $\Delta R = (R(0) + R(90) - 2R(45))/2$ . The desirable values for deep-drawing are a larger R (larger than 1) and smaller  $\Delta R$ . The R-values of the liners in Table 2 are less than 1 on average, and hence predict a poor drawability. The small values of the R are attributed to the presence of the strong (100) $\langle hkl \rangle$  component in the samples.

The criteria of the R values for the deep-drawing of sheet metals are not necessarily valid for the jet ductility performance of the liners. However, the R-values are a simple 1-d parameter, and hence may be easy to correlate with other plastic properties, such as the lengths of the shaped charge jets produced by the liners. Such correlations should be investigated.

**Table 2.** The R-values as a function of the directions, obtained from the Harmonic ODF using the restricted glide model (R) and the pencil-glide model (P). The R and the WR are also given.

Angles	C00-A	C00-B	C20-A	C20-B	C40-A	C40-B
	R / P	R / P	R / P	R / P	R / P	R / P
0.	0.54/0.49	0.73/0.61	0.63/0.57	0.86/0.72	0.43/0.46	0.66/0.59
15.	0.81/0.67	0.69/0.62	0.64/0.60	0.75/0.67	0.50/0.51	0.63/0.58
30.	0.95/0.88	0.63/0.62	0.61/0.62	0.55/0.55	0.59/0.60	0.59/0.56
45.	1.17/1.17	0.60/0.59	0.59/0.62	0.49/0.52	0.64/0.66	0.59/0.58
60.	1.08/1.24	0.69/0.62	0.66/0.67	0.62/0.63	0.67/0.67	0.65/0.63
75.	0.85/0.83	0.82/0.75	0.73/0.74	0.87/0.84	0.64/0.67	0.72/0.69
90.	0.75/0.78	0.87/0.82	0.77/0.78	1.00/0.98	0.64/0.67	0.75/0.71
R	0.91/0.90	0.70/0.65	0.65/0.65	0.71/0.69	0.59/0.61	0.65/0.62
$\Delta R$	-0.53/-0.54	0.20/0.13	0.11/0.06	0.44/0.33	-0.11/-0.10	0.12/0.07

## Neutron Autoradiography of Paintings

The Smithsonian Conservation Analytical Lab (CAL)-NIST autoradiography research program has concentrated in three areas: the continuing study of paintings by 19th century American artists, methodology development to improve the efficiency of the autoradiography process, and the renovation of a second laboratory.

The paintings studied by the Smithsonian this year were attributed to Thomas W. Dewing and included Landscape with Figures and The Reading. Changes in the position of the heads of figures in both paintings revealed an effort to create a feeling of psychological distance between the figures. These observations are important and were presented in a special seminar to a group of Smithsonian and University of Maryland staff and students [3].

In addition to the Smithsonian's program, two paintings from the Kimbell Art Museum in Fort Worth, Texas were studied. These included St. Sebastian Tended by Irene (Circle of Georges de La Tour) and Cheat with the Ace of Clubs by Georges de La Tour. This work was carried out

with the participation of paintings conservator, Michael Gallagher of the Kimbell Art Museum and other members of the museum staff.

In the area of methodology development, the feasibility study of using scintillation screens for improving the efficiency of registering the painting autoradiographic signatures on films, and for direct capturing of images via video/electronic means showed good potential. Film speed enhancement of more than 10 was confirmed with actual painting study with no discernable loss in image quality. The use of cold neutrons for painting activation was also investigated with very good results. Utilizing a scintillation screen for film speed enhancement and a glancing-angle geometry for activation by cold neutrons could give a painting adequate radioactivity for autoradiography study in an amount of time comparable to that which would be required at a thermal column. A cold neutron guide has a much lower level of undesirable gamma rays and high energy neutrons and offers further advantages in greater activation sensitivity and easier accessibility.

A collaborative program to investigate the use of cold neutron guide and digital autoradiography techniques was carried out in Berlin at Hahn-Meitner-Institut (HMI). A 17th century Dutch painting from the Picture Gallery in Berlin was autoradiographed at the HMI cold neutron facility. A portion of the autoradiographs were recorded using FUJI photostimulable phosphor imaging plates. A great increase in sensitivity was observed over the standard film system. The images were preserved in digital form and could be readily processed.

In summary, methodology developments provide opportunities:

1. To reduce the total exposure to the paintings under study while maintaining autoradiography quality.
2. To reduce painting activation requirements through more efficient use of neutrons and improved detection/imaging systems, thus making possible autoradiography studies of paintings at many other reactor facilities. Traditionally, a minimum physical size and neutron intensity are required before a successful activation can be carried out for autoradiography study of paintings. These requirements are considerably relaxed by:
  - a) Using neutron guides where instead of placing a painting perpendicular to the incoming neutrons, the painting is placed almost parallel to the beam, significantly increasing the exposed area.
  - b) Improved efficiency of the imaging system requiring lower radioactivity in the painting.
3. To improve the painting pigment identification process by increasing the time resolution in the autoradiography exposure sequence—possible because of the improved efficiency of the activation and imaging procedures.
4. To incorporate computer image processing enhancement in the filmless approach for dissemination of autoradiography information.
5. To make autoradiography information more accessible for distribution and comparison with other painting analysis techniques.

Use of the second laboratory during the exposure of film following irradiation was implemented this year with its use for the Dewing painting, Landscape with Figures. The environ-

ment is tightly controlled and the area is secured. This additional space was also especially important for the housing of paintings during the various stages involved in preparation for the autoradiography study of Cheat with the Ace of Clubs.

CAL's facility for neutron induced autoradiography at the NBSR has been operated under the direction of Jacqueline S. Olin, Assistant Director for Archaeometric Research, Conservation Analytical Laboratory, Smithsonian.

## References

- [1] O. Orringer, J. E. Gordon, Y. H. Tang and A. B. Periman, Proceedings of the 1988 Applied Mechanics Rail Transportation Symposium, AMD-Vol. 96/RTD-Vol. 2, pp. 87-94.
- [2] J. S. Kallend, U. F. Kocks, A. D. Rollett, and H.-R. Wenk, Operational texture analysis, Mat. Sci. Eng., A132:1 (1991).
- [3] S. Hobbs, Conservation Analytical Lab Special Seminar, Nov. 1992.

## Research Topics

### Evaluation of New Neutron Area-Detectors for NDE Applications

P. C. Brand<sup>23</sup>, Y. T. Cheng<sup>18</sup>, and H. J. Prask<sup>17</sup>.

### Design and Construction of a New Neutron Diffractometer for Single-Crystal Diffraction, Texture Determination, and Residual Stress Measurement

P. C. Brand<sup>23</sup>, C. S. Choi<sup>17</sup>, J. W. Lynn<sup>17</sup>, L. P. Robeson<sup>17</sup>, E. Prince<sup>17</sup>, and H. J. Prask<sup>17</sup>.

### 'STRESS': A Comprehensive Code for Data Reduction in Neutron Diffraction Residual Stress Measurements

P. C. Brand<sup>23</sup>.

### New Methods for Aperture and Specimen Alignment for Neutron Diffraction Residual Stress Studies

P. C. Brand<sup>23</sup> and H. J. Prask<sup>17</sup>.

### A New Approach to the Determination of $d_0$ for Neutron Diffraction Residual Stress Measurements

P. C. Brand<sup>23</sup> and H. J. Prask<sup>17</sup>.

### Evolution of Residual Stresses Around a V-notch Multipass Weld in a Steel Plate

J. Blackburn<sup>21</sup>, P. C. Brand<sup>23</sup>, R. J. Fields<sup>14</sup>, and H. J. Prask<sup>17</sup>.

**Determination of Subsurface Residual Stresses in a 150 mm Steel Shell Base**

P. C. Brand<sup>23</sup>, H. J. Prask<sup>17</sup>, W. Sharpe<sup>1</sup>, and C. S. Choi<sup>1,17</sup>.

**Fabrication and Characterization of Standard Reference Specimens for Residual Stress Measurement Techniques**

H. J. Prask<sup>17</sup>, P. C. Brand<sup>23</sup>, T. M. Proctor<sup>19</sup>, and E. Drescher-Krasicka<sup>14</sup>.

**The Effect of Whisker Size and Concentration on Residual Microstresses in SiC-Whisker-Reinforced Alumina**

E. Fuller<sup>5</sup>, A. Krawitz<sup>24</sup>, and H. J. Prask<sup>17</sup>.

**Texture Study of Tantalum for Shaped-Charge Liners**

C. S. Choi<sup>1,17</sup> and J. Orosz<sup>1</sup>.

**The Effect of Texture and Sample Geometry on the r-Value of Heavy Gauge Tantalum Plate**

C. Michaluk<sup>4</sup>, C. S. Choi<sup>1,17</sup>, and J. Bingert<sup>12</sup>.

**Examination of the Paintings of Thomas Wilmer Dewing\***

S. Hobbs<sup>18</sup>, R. Cunningham<sup>18</sup>, and Y.-T. Cheng<sup>18</sup>.

\*[Paintings on loan from the National Museum of American Art].

**Examination and Authentication of the Paintings of Albert Pinkham Ryder\***

I. Alexander<sup>18</sup>, R. Cunningham<sup>18</sup>, Y.-T. Cheng<sup>18</sup>, E. Broun<sup>15</sup>, B. Heller<sup>6</sup>, M. Quick<sup>11</sup>.

†[Source of studied paintings—National Museum of American Art, Detroit Institute of Art, and Los Angeles County Museum of Art]

**The Use of Scintillation Screens and Cold Neutron Guide in Autoradiography of Paintings**

Y.-T. Cheng<sup>18</sup>, W. Leuther<sup>8</sup>, and C. Fischer<sup>8</sup>.

**Filmless Autoradiography and Image Processing**

Y.-T. Cheng<sup>18</sup>, W. Leuther<sup>8</sup>, C. Fischer<sup>8</sup>, I. Alexander<sup>18</sup>, A. Calmes<sup>16</sup>, and M. Ormsby<sup>16</sup>.

**Microstructure Study of Molybdenum Liners by Neutron Diffraction**

C. S. Choi<sup>1,17</sup>, E. L. Baker<sup>1</sup>, and J. Orosz<sup>1</sup>.

**Application of O.D.F to the Rietveld Profile Refinement of Polycrystalline Solids**

C. S. Choi<sup>1,17</sup>, E. L. Baker<sup>1</sup>, and J. Orosz<sup>1</sup>.

**Texture Study of Tungsten Liners.**

C. S. Choi<sup>1,17</sup>, T. Fuesting<sup>2</sup>, and E. L. Baker<sup>1</sup>.

**ALIGN: A Comprehensive Code Facilitating the Alignment of a Spectrometer and Slits for Residual Stress Measurements by Means of Neutron Diffraction**

P. C. Brand<sup>23</sup>.

**The Effect of the Attenuation Coefficient ( $\mu$ ) on  $d$ -Spacing Determinations in Neutron Residual Stress Measurements**

P. C. Brand<sup>23</sup> and H. J. Prask<sup>17</sup>.

**Residual Stress Analysis of Bent Steel Pipes**

P. C. Brand<sup>23</sup>, J. Goff<sup>9</sup>, M. T. Hutchings<sup>9</sup>, and H. J. Prask<sup>17</sup>

**The Effect of Beam Divergence on  $d$ -Spacing Determinations in Neutron Residual Stress Measurements by Means of  $2\theta$ -scans**

P. C. Brand<sup>23</sup> and H. J. Prask<sup>17</sup>.

**Residual Stress Measurements on Spot Welded High-Strength Low Alloy Steel**

P. C. Brand<sup>23</sup>, J. Blackburn<sup>21</sup>, R. J. Fields<sup>14</sup>, and H. J. Prask<sup>17</sup>.

**The Effect of the Total Neutron-Through-Specimen-Flight-Path on  $d$ -Spacing Determinations in Neutron Residual Stress Measurements by Means of  $k$ -scans**

P. C. Brand<sup>23</sup> and H. J. Prask<sup>17</sup>.

**Characterization of a Kaowool-Reinforced Aluminum-Silicon Squeeze Casting Alloy for the Fabrication of Wear Resistant Automobile Pistons**

P. C. Brand<sup>23</sup>, C. G. Tibbetts<sup>7</sup>, and H. J. Prask<sup>17</sup>.

**Residual Stress Measurements on Bead on Plate Repair Welds for Railroad Tank Cars**

P. C. Brand<sup>23</sup>, O. Orringer<sup>22</sup>, G. M. Hitcho<sup>14</sup>, and H. J. Prask<sup>17</sup>.

**Residual Stress Measurements Feasibility Study on a Non-magnetized Nd<sub>2</sub>Fe<sub>14</sub>B Magnet Material**

P. C. Brand<sup>23</sup>, C. Fuerst<sup>7</sup>, and H. J. Prask<sup>17</sup>.

**Residual Strain Measurements on a Compacted Iron Powder Specimen**

P. C. Brand<sup>23</sup>, S. Brown<sup>13</sup>, J. Wlassich<sup>13</sup>, and H. J. Prask<sup>17</sup>.

## **Texture Development in Deformed Ice II Polycrystals: A Study of Neutron Diffraction**

C. S. Choi<sup>1,17</sup>, S. F. Trevino<sup>1,17</sup>, K. Bennet<sup>20</sup>, H. W.  
Wenk<sup>20</sup>, W. B. Durhan<sup>25</sup>, and L.-A. Stu<sup>26</sup>.

### **Affiliations**

<sup>1</sup>Army Armament RD&E Ctr.

<sup>2</sup>Babcock & Wilcox, VA

<sup>3</sup>Boeing Corp.

<sup>4</sup>Cabot Corp., PA

<sup>5</sup>Ceramics Division

<sup>6</sup>Detroit Institute of Art

<sup>7</sup>General Motors

<sup>8</sup>Hahn-Meitner Institut, Germany

<sup>9</sup>Harwell, U.K.

<sup>10</sup>Honeywell

<sup>11</sup>LA County Museum of Art

<sup>12</sup>Los Alamos National Laboratory

<sup>13</sup>M.I.T.

<sup>14</sup>Metallurgy Division

<sup>15</sup>National Museum of Art

<sup>16</sup>National Archives

<sup>17</sup>Reactor Radiation Division

<sup>18</sup>Smithsonian Institution

<sup>19</sup>T-Prosci Co.

<sup>20</sup>U.C. Berkeley, CA

<sup>21</sup>U.S. Navy David Taylor Research Center

<sup>22</sup>U.S. Department of Transportation

<sup>23</sup>University of Maryland

<sup>24</sup>University of Missouri

<sup>25</sup>Lawrence Livermore

<sup>26</sup>U.S. Geological Survey



## ANALYTICAL CHEMISTRY

### Nuclear Methods Group

The development and application of nuclear analytical techniques for elemental compositional analysis of greater accuracy, higher sensitivity and better selectivity are the goals of the Nuclear Methods Group. A high level of competence has been developed in both instrumental and radiochemical neutron activation analysis (INAA and RNAA). In addition, the group has the capability of using neutron beams as analytical probes with both prompt gamma activation analysis (PGAA) and neutron depth profiling (NDP). PGAA measures the total amount of an analyte present throughout a sample by the analysis of the prompt gamma-rays emitted during neutron capture. NDP, on the other hand, determines concentrations of several important elements (isotopes) as a function of depth within the first few micrometers of a surface by energy analysis of the prompt charged-particles emitted during neutron bombardment. These techniques (INAA, RNAA, PGAA, and NDP) provide a powerful combination of complementary tools to address a wide variety of analytical problems of great importance in science and technology.

During the past few years, a large part of the group's efforts has been directed at the exploitation of the analytical applications of cold neutrons. These efforts are needed to take full advantage of the guided cold-neutron beams now available at the new Cold Neutron Research Facility (CNRF). The group's involvement has been to design and construct state-of-the-art instruments for both PGAA and NDP using cold neutrons.

#### • SRM Analysis and Certification

The nuclear analytical methods has continued to contribute to the Standard Reference Material (SRM) certification effort; this year's efforts include measurements performed on a number of SRMs including: Domestic Sludge, Automobile Catalyst, Spinach Leaves, Fused Zirconia, Zircon Sand, five Lubricating Oils, and a Fuel Oil. Group members are serving as Technical Champions for several of these new SRMs, and as such are responsible for scientific decisions made

throughout the production and certification processes of these materials. Several highlights of the Group's SRM work this year are described below. Three nuclear analytical techniques (INAA, RNAA, and PGAA) have been used to determine 30 different elements in the food reference material SRM 1570a, Spinach Leaves. These techniques provided 66% of the NIST data for this SRM. Twenty-one elements have been determined by INAA, 7 elements by RNAA, and 9 elements by PGAA, with some overlap between techniques. Of the 37 elemental determinations made by these techniques, 43% have total overall analytical uncertainties of 2.5% (relative) or less at the 95% confidence level, and over 70% have uncertainties of 5% or less. It should also be noted that 11 of the 30 elements are at the ultratrace concentration level (i.e., less than 1 mg/kg). In addition, the INAA analyses were made on samples of only 150 mg each, and thus provided homogeneity information important for certification.

Another SRM that has been studied extensively this year is the Estuarine Sediment, SRM 1646a. Both the INAA and RNAA techniques have analyzed this material, with a total of 14 elements determined. Ten elements have been determined by INAA and 5 by RNAA, with one element determined by both techniques. One element, antimony, appears to be inhomogeneous in this matrix. Of the rest, the INAA data have average uncertainties of 2.3%. The RNAA results have average uncertainties of 5.5%, but three of the five elements determined are at the ultratrace concentration level.

Cold Neutron Depth Profiling (CNDP) has been used to certify the concentration of  $^{10}\text{B}$  in SRM 2137, the new Boron Implant in Silicon. The SRM has been certified to contain  $1.018 \times 10^{15}$  atoms/cm<sup>2</sup> of  $^{10}\text{B}$  with an uncertainty of  $0.035 \times 10^{15}$  atoms/cm<sup>2</sup>. The 1 cm<sup>2</sup> silicon pieces of this SRM are intended for the calibration of secondary ion mass spectrometry (SIMS) instruments, and is particularly important in semiconductor research and development applications. The depth distribution of the boron implant has also been studied by the Microanalysis Group of NIST using SIMS, and this information is provided on the certificate.

- **Neutron Activation Analysis Method Development**

Although NAA has been in use for many years, new developments continue to provide improvements in detection sensitivities, elemental specificity, precision, and overall accuracy. Particularly in the last few years, the NAA technique has become one of the primary analytical techniques for the certification of elemental concentrations in biological SRMs. One important reason is that NAA has unique quality assurance characteristics which provide accurate analyses and which often allow the analytical values obtained to be internally evaluated and cross checked. In addition, the capability of INAA for nondestructive analyses (eliminating dissolution errors) and for homogeneity determinations of ng/g level concentrations for samples whose sizes are as low as 100 mg has made this technique an important contributor to trace element analyses at NIST. Furthermore, the relative matrix independence of NAA has resulted in applications to many other materials as well, including high temperature superconductors, soils, and fly ash, rocks and ores, etc.

Optimizing the gamma-ray counting conditions for the various forms of NAA can generally improve precision, increase sample throughput, or both. This is especially important when counting the very small amount of radioactivity from the analysis of ultratrace quantities of impurities, for example in semiconductor silicon or (after radiochemistry) noble metals in human tissue. Sensitivity can be gained by using high-efficiency, low-background detectors; a subsidiary benefit is that less radioactive material needs to be generated, handled, and discarded. The sources of background in gamma-ray detectors have been reexamined at NIST and elsewhere in recent years, with improved understanding. It is now clear that with care in the selection of the materials from which the detector and the shielding are constructed, the only important source of gamma-ray background is the interaction of cosmic ray particles with the shield and the detector itself. Experiments are underway to reduce this component by active, anti-cosmic ray shielding.

The computer-controlled robotic sample changer (RSC) which was obtained last year has been extensively evaluated and optimized during

the current year. This system provides the capability for continuous utilization of a detector system and is capable of precisely positioning eight different types of sample containers, ranging from a 100 ml polyethylene screw-top bottle (used for radiochemically separated samples) to a "2/5 dram" polyethylene snapcap vial, or a 54 mm diameter disposable plastic Petri dish. After an extensive evaluation and optimization process, the system will now provide a reliable and repeatable positioning uncertainty of  $\pm 0.51\%$  (1s; n=12) at 3 mm distance from the detector, and 0.25% (1s) for a 5 cm counting geometry. This system has been used to provide certification data for two Standard Reference Materials, SRM 1570a, Spinach Leaves, and SRM 1646a, Estuarine Sediment.

- **Specimen Bank Research**

The Biomonitoring Specimen Bank Research Project has continued to support other agencies' monitoring programs. These programs include the EPA Human Liver Project (HLP), the NOAA National Status and Trends (NS&T) program, the NCI Micronutrient Program, the IAEA/NIST/FDA/USDA Total Diet Study, the NOAA Alaska Marine Mammal Tissue Archival Project (AMMTAP), and the National Marine Mammal Tissue Bank (NMMTB). Research has centered on specimen banking protocols and improved analytical methodology. The group uses instrumental and radiochemical neutron activation analysis to determine element compositions of tissues included in the National Biomonitoring Specimen Bank (NBSB). In addition, participation in intercalibration exercises with the project participants and the development of QA materials for various marine analyses has helped to enhance the quality of the analytical results used in the assessment of the environmental health of the nation. During the past year samples have been collected, processed, and archived in the NBSB for the NMMTB and AMMTAP. Concentrations (or upper limit values) for approximately 35 elements have been determined using INAA for 29 marine mammal livers. Mercury has also been determined separately in fourteen of these livers.

### • Dietary Studies

A world-wide research program was initiated by the International Atomic Energy Agency (IAEA) in 1985 to obtain reliable data on the average daily dietary intake of nutritionally important elements in various developed and developing countries. The United States is represented in this project by three agencies with multidisciplinary expertise: FDA (sampling strategy), NIST/Nuclear Methods Group (analytical methodology), and the USDA (planning dietary studies). All three agencies are providing specialized knowledge for a meaningful interpretation of data. This international diet study is unique in that all samples have been collected and analyzed by identical, or strictly comparable, procedures in each country, and with appropriate QA to ensure data comparability. The measurement program was completed at the end of 1992, by which time approximately 450 samples have been analyzed.

For this study, typical total diets have been collected in 15 countries and analyzed for more than 20 elements. After sample collection, the diets were prepared and freeze-dried locally and then transferred to the IAEA laboratory at Seibersdorf (Austria) for homogenization, division into smaller aliquots and distribution to a network of experienced analytical laboratories which use a wide variety of analytical techniques. The analytes of interest include practically all the minor and trace elements considered to be essential or of interest as possible food contaminants, viz. Al, As, Ca, Cd, Cl, Cr, Cu, F, Fe, Hg, I, K, Mg, Mn, Mo, Na, Ni, P, Pb, Se, Sn, V, and Zn. The Nuclear Methods Group has used INAA and RNAA to determine Cr, Fe, Hg, Mo, Se, and Zn in all the samples, and Cd in selected groups of samples. A preliminary evaluation of the results has yielded a number of interesting observations. For example, the variability of the intakes of essential elements among countries is relatively small (factor of 2 or less between highest and lowest) for Cr, Cu, K, Mg and Zn, and relatively large (around a factor of 4 or more) for I, Mn and Se. Three countries (Japan, Norway, and Spain) appear to exceed the Provisional Tolerance Intakes (PTIs) for As. However, this may be due to a high consumption of organically-bound As in fish where the toxic

effect is minimal and the PTI does not apply. The apparent high intake of Hg in the Iranian and Turkish diets may indicate a cause for concern and an extended study (followed by remedial measures) may be warranted.

Presently, evaluation of the entire data set is in progress, and a final report is anticipated by the end of 1994. A portion of the results from this investigation has already been extensively used by the World Health Organization in formulating a revised set of global recommendations for daily dietary intakes of essential elements. This set of recommendations is expected to be released by March of 1994 as a monograph entitled, "Trace Elements in Human Nutrition."

### • Neutron Activation—Mass Spectrometry

The collaboration with Brian Clarke and colleagues at McMaster University on neutron activation-mass spectrometry (NA-MS) has continued to provide valuable information on ultratrace levels of boron and lithium. NA-MS couples nuclear activation to generate  $^4\text{He}$  and  $^3\text{He}$  (from  $^{10}\text{B}$  and  $^6\text{Li}$ , respectively) with the high precision of mass spectrometry. Under ideal conditions the detection limits are in the ng/g for boron and in the pg/g range for lithium. It is therefore well suited to an investigation of the natural concentration levels of boron and lithium in biomaterials; both elements present difficult analytical problems for other methods. This is especially true for the determination of sub-ppb levels of lithium where other analytical techniques face serious analytical difficulties, mainly caused by contamination control and, in some cases, by insufficiently low detection limits.

Over the past year we have determined B and Li concentrations in a wide variety of biological materials, including more than one hundred individual food items, as well as several different protein components of blood. Blood Li levels may be both genetically and environmentally regulated. An environmental contribution is deduced from the relationship between the blood Li level and the amount of the element ingested. No such information is available for B, another element present in ultratrace amounts in human blood. Unusually high levels of Li and B in the waters off northern Chile offer an opportunity to study the

genetic and environmental regulation of these elements in the blood of healthy subjects.

- **Superconductivity Research**

The group has undertaken an active role in the NIST program on high-temperature superconductivity research. In cooperation with materials scientists at NIST and elsewhere, we are measuring impurities in superconductor starting materials and final products, as well as determining the stoichiometry of the major constituents. The needs of the superconductivity program have stimulated the development of methods for accurate, rapid analysis of these materials by both NAA and PGAA. In particular, an effort is underway to establish an accurate monitor-activation analysis technique at NIST. Conventional NAA requires the irradiation and counting of a standard for each element to be determined in a given sample. Preparing numerous standard solutions requires much labor, and the accurate quantitation of unanticipated activities in the gamma spectrum is not possible. An elegant solution has been pioneered in Europe, which uses a dimensionless compound nuclear constant called  $k_0$ , which can be measured much more accurately than the cross sections and other constants that comprise it. We have begun to apply this approach to cold-neutron PGAA, which is especially subject to systematic errors from neutron scattering effects, and have found that the  $k_0$  approach for determining element ratios offers all the advantages of internal standards in other methods. We intend to apply the  $k_0$  formalism to delayed NAA as well.

- **Neutron Depth Profiling**

Incremental improvements in the NDP instrument are continually being pursued. One of the major parameters in determining the reaction depth in NDP is the accurate determination of the residual energy of the charged particles. Silicon surface barrier detectors used at room temperature are limited to about 10 keV FWHM resolution at the charged particle energies of interest. Presently we are working in collaboration with Texas A&M University to improve the depth resolution by using time-of-flight (TOF) techniques. The residual energy of the heavy recoil particle are determined by TOF via microchannel plate

detectors. Initial efforts are focused towards profiling nitrogen distributions in semiconductor materials with resolutions of a few nanometers. Proof-of-principle experiments are nearly complete, and an application paper will follow shortly.

A major application of the NDP facility in 1993 has been the characterization of a variety of diamond-like films. The work has resulted in three or more publications during the last year. Analyses have been performed to determine the boron dopant distribution in a single layer, and in alternately doped multilayer deposits. Diamond-like substrates are often used as the precursors for electronic circuits that require efficient heat transfer, such as for devices operated in a vacuum or with high-current components. Boron nitride is one diamond-like material ideally suited for analysis using NDP. NDP is currently being used to establish the stoichiometry of the nitrogen and boron in the matrix and reveal non-uniformities in the film deposition profile.

- **Prompt-Gamma Activation Analysis**

A permanent, full-time instrument for cold-neutron prompt-gamma activation analysis (PGAA) has been constructed as part of the NIST Cold Neutron Research Facility. This instrument allows accurate nondestructive measurements of a number of elements, including H, B, C, N, S and Cd. Hydrogen has been particularly emphasized. Detection limits, constrained by background, of less than 10 micrograms have been achieved for some samples. This capability is of value in numerous applications where quantitative, nondestructive analysis of small quantities of hydrogen in materials is necessary. Further background reduction by one to two orders of magnitude is probable in the near future. Sensitivities (counting rate per gram of analyte) for a number of elements have been compared using the new cold-neutron instrument to those obtained with the thermal University of Maryland-NIST PGAA instrument. Sensitivities for most elements are a factor of four better with the cold-neutron apparatus, as a result of the increased capture cross sections for cold neutrons, and the systems compact sample-detector geometry. Installation of a Compton suppression system and an evacuated

sample chamber will greatly lower background and substantially improve measurements.

The PGAA system has been used for the analysis of hydrogen and other elements in a number of samples originating from NIST programs and from the academic and industrial laboratories with whom NIST collaborates. We give below a series of examples to demonstrate the utility of the method.

PGAA has found great utility in multielement analysis, particularly of geological samples. The method has been used to measure the concentrations of 14 elements in the Allende meteorite (with good agreement with literature values), and chlorine and other elements in a number of terrestrial basalts used in  $^{36}\text{Cl}$  studies. We have also used PGAA to measure concentrations of 7 elements in glass capillaries used in neutron focusing, element ratios in a number of substituted yttrium-barium-nickel oxides, and Si/Al ratios in mesoporous zeolites used as catalysts.

Numerous specimens of pure and substituted  $\text{C}_{60}$  fullerenes have been analyzed for hydrogen (and simultaneously for other elements such as C, S, K, and Rb) in support of neutron scattering and chemical experiments. Many of these measurements have been performed with the sample sealed inside the aluminum container intended for the scattering spectrometer. Early samples of  $\text{C}_{60}$  had been found to contain large amounts of contaminant hydrocarbon, so high (0.9 wt% H) as to vitiate the neutron scattering measurements that were planned; repurification gave a satisfactory product with about 600 mg/kg. Later samples of  $\text{C}_{60}$  analyzed have been found to be vastly superior in quality, some containing as little as 0.025 wt % H. With substituted fullerenes we have often been able to measure other elements. We have measured the H/S ratio in a sample of  $\text{C}_{60}(\text{SO}_4\text{H})_8$  ( $1.0 \pm 0.1$ , as expected), both major alkali and impurity hydrogen in superconducting  $\text{K}_3\text{C}_{60}$  and its  $\text{K}_6$  and  $\text{Rb}_n$  analogs, C and halogen in  $\text{C}_{60}\text{Br}_{24}$  and  $\text{C}_{60}\text{I}_4$ , and argon in a sample of amorphous carbon sputtered using an argon plasma.

Attempts to measure hydrogen in semiconductors and related materials have met with limited success because the amount of hydrogen present has usually been much less than expected. Hydrogen has been measured in 1-g and 4-g specimens of hydrothermally grown single-crystal

quartz, with fused quartz used as a blank. The concentrations determined were found to be less than 10 mg/kg, in agreement with infrared measurements. In another application, hydrogen was sought for in a 1.0- $\mu\text{m}$  phosphosilicate glass film deposited on a quarter of a 15-cm silicon wafer; the effective sample mass was 1 mg. The net hydrogen content in this sample was  $< 5 \mu\text{g}/\text{cm}^2$ . Hydrogen has also been measured in 1-g samples of semiconductor-grade germanium, in order to determine whether etching the crystal increases the susceptibility for hydrogen absorption. Hydrogen concentrations determined in the crystals ranged from 50 - 80 mg/kg Ge; surprisingly, no differences were observed between the etched and unetched crystals.

An important application of cold-neutron PGAA has been the determination of hydrogen in metals, due to the possibility of hydrogen embrittlement. A 2.6 hour irradiation of a 234-mg sample of NIST SRM 354 (unalloyed titanium) yielded a hydrogen concentration of  $235 \pm 30$  mg/kg; the certified concentration is  $215 \pm 6$  mg/kg. Hydrogen concentrations have also been measured in two titanium-alloy jet-engine turbine blades. Both blades were taken from an engine in which another blade had failed during service. A hydrogen profile of each blade was created by measuring hydrogen at numerous locations. Hydrogen concentrations measured in the first blade ranged from  $140 \pm 40$  to  $210 \pm 40$  mg H/kg Ti, with an average concentration of  $190 \pm 40$  mg H/kg Ti. The second blade exhibited higher hydrogen concentrations as well as a larger concentration gradient; H concentrations ranged from  $140 \pm 40$  to  $750 \pm 50$  mg H/kg Ti, with an average concentration of  $480 \pm 190$ . Higher hydrogen concentrations were measured on the tip and edges of the blade than at the base and in the interior. The addition of Compton suppression will greatly decrease the uncertainties for H measurements in metals.

An important area of PGAA research this year has involved the effects of neutron scattering. Neutron scattering by hydrogen causes changes in the analytical sensitivities (cps/mg) of both thermal and cold neutron PGAA. The effects of thermal neutron (TN) scattering on analytical sensitivities can be quantitatively accounted for by elastic scattering, i.e. scattering in which the average

energy of the neutrons does not change. Effects of neutron scattering on analytical sensitivities of cold neutron (CN) PGAA are different from those of TNPAA. Results of initial studies indicate that cold neutrons interacting within a room temperature target, on average, gain energy upon scattering, resulting in decreased sensitivities. Experiments have been designed to determine whether cooling the target alleviates the part of the CNPGAA sensitivity decrease that is due to neutron warming. If the temperature of the target and the "effective temperature" of the neutron beam were similar, there would be little or no change in the average energy of the neutrons.

CNPGAA sensitivities for H have been measured for spherical and disk-shaped targets of tris-hydroxymethyl-aminomethane (9.15% H) at room temperature and after cooling to liquid nitrogen temperature (77 K) under vacuum. Relative to sensitivities for the 298 K targets, sensitivities for the cooled targets were enhanced. Sensitivities for cooled disks showed the same qualitative trends as those at 298 K, i.e., decreasing sensitivity with increasing targets thickness, but with less decrease for the cooled targets. Sensitivities for H in the room-temperature spheres decrease with sample size, but those at low temperatures are constant within the uncertainties associated with counting statistics (0.5% to 2.5%) and target positioning in the beam (1 - 4%). Constant sensitivity for spherical targets of varying diameters indicates that there is no measurable change in the average energy of the neutrons. Cooling these targets appears to eliminate the sensitivity decreases that are caused by an increase in the average energy of the neutrons. Neutron scattering, even without energy change, alters the path length of the neutron within the target, so that the entire effect for disks is not eliminated by controlling sample temperature. However, that part of the sensitivity decrease that is due to neutron warming is at the very least mitigated and the remainder of the effect that is due to inelastic scattering can be studied using Monte Carlo methods.

#### ● Focused Neutron Research

A long-range program to explore and develop the analytical applications of focused beams of cold neutrons has been initiated within the group.

The ultimate goal of this research is to produce beams of neutrons which have intensities several orders of magnitude greater than previously available. Such beams will greatly enhance the capabilities of both PGAA and NDP, and may ultimately lead to a neutron probe for micro-analysis. Glancing-angle reflective optics can be used to transport soft x-rays and thermal neutron beams through narrow channels, which act as miniature versions of neutron guides commonly used at research reactors. The advantage of the narrow ( $\approx 10 \mu\text{m}$ ) channels is that the neutron beam can be bent more sharply than for the wide ( $\approx 50 \text{ mm}$ ) guides. Recent developments in the manufacture of polycapillary fibers, with thousands of channels having sizes of a few micrometers, have enabled cold neutrons to be guided and focused on a scale suitable for laboratory needs. A high intensity beam on a small sample area can be useful for improving both the detection limits of individual elements and the spatial resolution of neutron absorption measurements in analytical research.

The NIST neutron focusing team has tested a prototype focusing lens constructed at the Kurchatov Institute in Moscow. This lens uses 721 lead-silica polycapillary fibers of 0.36 mm outer diameter, each containing 1261 parallel channels of  $6 \mu\text{m}$ , and with 36% open area. This 220 mm long lens has been examined with thermal and cold neutrons of various spectral and spatial dimensions. The lens compresses a beam of 29 mm diameter at its entrance to about 1 mm at the focus, a distance of 104 mm from the exit. The actual gain in intensity varies strongly with the incident beam divergence.

More recently, we have tested a second focusing lens consisting of 919 borosilicate glass fibers. Each 0.44 mm diameter fiber contains 547 parallel channels of  $14 \mu\text{m}$ , with 55% open area. This lens has a total length of 100 mm and a focal distance of 57 mm from the lens exit. The size and intensity of the transmitted neutron beam has been determined using a high resolution video radiation detector. The intensity distribution of the beam at the focus is approximately conical with a full-width at half-maximum of 0.49 mm, and with an average gain in intensity of about 20. These experimental results agree well with those obtained by computer simulation. This research is being

performed in collaboration with X-Ray Optical Systems, Inc. of Albany, New York, which has an Advanced Technology Program award to develop focusing systems for both x-rays and neutrons using capillary optics.

- **Detector Imaging Research**

The Nuclear Methods Group, working through a CRADA with CID Technologies Inc. and the Surface and Microanalysis Science Division, has developed a video radiation detector (VRD) based upon a charge injection device (CID) camera and image processing system. This system allows live-time high resolution imaging of neutron and charged particle fields. The VRD system is essentially 100% efficient for the detection of alpha particles above a few MeV energy and emission rates as small as  $10^{-5}$  Bq have been localized. The system allows discrimination between tritons, alpha particles, and fission fragments. Spatial resolution of less than  $12\mu\text{m}$  is achieved by interpolating between pixels. Also the charge injection device (CID) is sensitive to visible, x-ray and UV photons, so that charged-particle images can be correlated with optical images of the sample.

We have used the VRD for characterizing neutron focusing components for neutron intensity, determination of the focal plane, and analyzing individual elements in the focusing device. Neutron field maps produced by the VRD have been indispensable for the project. The location and size of the focus can be determined much more quickly with the VRD than by using a series of photographic films. It has also been used for detecting spontaneous emission of naturally radioactive materials from minerals or contaminants in the analysis of environmental samples.

- **Group Interactions**

The strong interaction with industrial scientists using NDP, PGAA, and NAA has continued during the year with a growing number of guest workers, research associates, and joint publications. For example, working this year with researchers from SEMATECH, we have used NDP to study various aspects of quality control using CVD (chemical vapor deposition) reactors. These measurements will be useful in optimizing process yield and reliability as well as establishing

confidence for the industrial in-house analytical techniques.

## **Smithsonian Institution**

The Conservation Analytical Laboratory of the Smithsonian Institution has maintained an INAA research facility within the Nuclear Methods Group at NIST for over 15 years. This facility, which consists of two automated sample changers and three gamma detectors with associated electronics, provides high precision multi-element chemical analysis for use in a wide range of Smithsonian and Nuclear Methods Group research projects. In the past year over 2500 archaeological samples have been analyzed in support of Smithsonian research projects.

One of the more intensive studies using INAA concerns Classic Maya pictorial polychrome pottery. Created in what is now southern Mexico, Guatemala, and Belize during A.D. 600-900, these elaborate vessels represent one of the great ceramic traditions of the world. By combining traditional art historical methods and the instrumental neutron activation analysis of the ceramic pastes, the products of centers of Maya ceramic production are identified and located. More than 8,000 chemical analyses of excavated Maya pottery permit a compositional characterization of the Maya Lowlands and provide a database against which the analyses of nonprovenienced museum objects of "matching" compositions can be attributed to particular subregions in the Maya area.

In the course of research being conducted to meet a given set of objectives, new and significant possibilities can emerge—ones that were completely unforeseen at the beginning of the project. This is the case with the emerging potential for linguistic and dialectical mapping of the Maya region. While some of the glyphs found on Maya vases once were described as primarily "decorative" in nature, they have been found recently to have a strong syntactic integrity that permitted various substitutions and elaborations, one frequently repeated glyphic phrase is recognized as primarily derived from the Cholan Maya language family, but often incorporates loans of non-Cholan forms of glyphs or dialectical variations in the glyphic elements. Previously the

nonprovenienced vessels in museums, the majority looted from their resting places, were regarded only as isolated, aesthetic curiosities of Maya creativity. Using the chemically-derived compositional attributions of the pottery we are beginning to map the distributional pattern of dialectical variation. As we merged linguistically reflected social distances with economic or political information obtained in our study of the trade in pottery, we move increasingly forward in our interpretation of the archaeological record.

### Food and Drug Administration

(D. L. Anderson, W. C. Cunningham,  
S. G. Capar, and T. R. Lindstrom)

The Food and Drug Administration (FDA) maintains a neutron activation analysis (NAA) facility in the reactor building of the National Institute of Standards and Technology (NIST). This facility is directed by FDA's Center for Food Safety and Applied Nutrition and provides agencywide analytical support for special investigations and applications research. NAA complements other analytical techniques used at FDA and serves as a reference technique and confirmatory quality assurance (QA) tool. Instrumental, neutron-capture prompt- $\gamma$ , and radiochemical NAA procedures (INAA, PGAA, and RNAA, respectively) continue as the prime nuclear analytical approaches. A radioisotope-induced X-ray emission (RIXE) spectrometer provides support for FDA programs which monitor toxic elements in housewares (especially Pb), and the low-level  $\gamma$ -ray counting facility developed by the Nuclear Methods Group of the NIST Inorganic Analytical Research Division is used to determine the radionuclide content in various matrices. This combination of analytical techniques enables diverse multielement and radiological information to be obtained for foods and related materials.

The continued development and production of biological standard reference materials (SRMs) is vital to FDA's analytical programs. FDA's NAA laboratory provided analytical assistance leading to the element concentrations listed for ten reference materials, developed by Agriculture Canada and now available from the NIST Office of Standard Reference Materials. Both INAA and

PGAA techniques were used. The reference materials are—

- NIST RM 8414 (bovine muscle powder),
- NIST RM 8415 (whole egg powder),
- NIST RM 8416 (microcrystalline cellulose),
- NIST RM 8418 (wheat gluten),
- NIST RM 8432 (corn starch),
- NIST RM 8433 (corn bran),
- NIST RM 8435 (whole milk powder),
- NIST RM 8436 (durum wheat flour),
- NIST RM 8437 (hard red spring wheat flour), and
- NIST RM 8438 (soft winter wheat flour).

QA is a continuing effort in FDA's analytical laboratories. The NIST ultralow-level gamma-ray counting system was used to verify the  $^{137}\text{Cs}$  activity concentrations in several maple syrup test portions. Four syrups were also analyzed by the Winchester Engineering and Analytical Center (WEAC), FDA's radioanalytical field laboratory. The  $^{137}\text{Cs}$  activity concentrations ranged above and below WEAC's limit of detection (LOD, approximately 1.5 Bq/kg). The results (listed below) agreed very well.

Syrup ID	Bq $^{137}\text{Cs}$ /kg	
	FDA/NIST	WEAC
A	2.92 $\pm$ 0.17	2.8 $\pm$ 0.5
B	4.94 $\pm$ 0.28	5.0 $\pm$ 0.6
C	0.15 $\pm$ 0.01	<LOD
D	0.25 $\pm$ 0.02	<LOD

In another QA exercise, general analytical support was provided to FDA's National Center for Toxicological Research. A series of calcium supplements were analyzed using INAA as a reference for verification of independent analytical results for calcium.

Dietary intakes based on PGAA data were calculated for H, B, Na, S, Cl, and K in 234 foods from FDA Total Diet Study (TDS) collection K11 (November, 1990 to January, 1991) [1]. Fruits, vegetables, and nuts had the highest B concentrations and supplied over 50% of the dietary intake for B in eight age/sex groups. Higher B concentrations in drinking water and greater fruit and vegetable consumption could significantly increase B intakes. Added NaCl (*i.e.*, that introduced during processing or



preparation) was estimated to account for about half the dietary Na and Cl for 6-11 month-old children and ~75% of Na and ~80% of Cl for all other age/sex groups. An estimated 10% of dietary Na was contributed by other additives, *e.g.*, baking powder in grain products, emulsifying agents in processed cheese, and a variety of preservatives. Sulfur concentrations in food and S intakes were dominated by protein-related cysteine, with relatively little contribution from food additives. Potassium and Na concentrations and intakes determined for collection K11 agreed very well with the 1982-1989 TDS averages.

Thirty-six commercial houseware items and 87 ceramic test tiles (85 fired with hobby glazes and 2 blank bisques) were examined qualitatively for the presence of Pb by using  $^{109}\text{Cd}$ -induced L X-ray emission [2]. For the housewares, the technique provided fast, nondestructive analysis of areas ranging from about 10 cm diameter (general regions) to about 4 mm diameter (*e.g.*, isolated design regions). Lead was found in 25 of 28 ceramicware items and in all 8 other housewares, and in all the test tile glazes above the limit of detection of 1 count per second (cps) for the Pb  $L_{\beta}$  X-ray. For housewares, Pb response did not always correspond to Pb leachability. For 68 test tile glazes labeled as containing Pb (39 of which were also labeled as dinnerware safe), count rates ranged from 290 to 730 cps, while for the other 17, labeled (with one exception) as "non-toxic," much lower count rates (5-61 cps) were observed. Other elements found in the housewares or test glazes were As, Au, Ca, Co, Cr, Cu, Fe, Mn, Nb, Ni, Rb, Sr, Y, Zn, and Zr.

## University of Maryland

The University of Maryland (at College Park, UMCP) aerosol chemistry group has used the NBSR reactor for instrumental neutron activation analysis to characterize atmospheric aerosol particles and gases for more than 20 years. Detailed and accurate multielement analyses are routinely achieved, nondestructively, for up to 40 elements in samples collected for periods of several hours to a few days on various types of filters and in cascade impactors which size fractionate the aerosol into as many as 10 size domains. Some of the elements measured, *e.g.*,

As, Se, and Hg, are highly toxic and are, therefore, of epidemiological interest, especially in the Chesapeake Bay and Coastal Marine environments. Equally important is that information on elemental constituents remains a powerful, fundamental tool with which atmospheric sources, transport, and processes may be elucidated. Current projects are discussed below.

### • Characterization of Submicrometer Aerosol Particles

Detailed investigations of the size-distribution and composition of urban aerosols are important to the scientific community because they contain information about the formation, sources, transport, and atmospheric behavior of particles containing toxic and nutrient substances, and respiratory irritants. This work extends measurement to very small (often  $<100 \mu\text{g}$ ) samples of submicrometer aerosol particles size-fractionated with low-pressure-drop Micro-Orifice Impactors (MOI). In a recently completed study, size-segregated aerosol samples were collected at three sites near Washington, DC, an area influenced largely by emissions from motor vehicles, utility coal and oil combustion, and municipal incineration; and at two sites in the heavily industrialized Philadelphia area, to determine the spatial variability in elemental size spectra and relationships between modal diameter and atmospheric aerosol origin and age, including hygroscopic growth functions.

Samples were collected daily from 7 am to 6 pm EST at the three Washington sites in mid August to late September, 1990; and at the Philadelphia area sites from mid October to mid November using 10-stage MOI which provided 7 size fractions in the range  $<0.06$  to  $3 \mu\text{m}$ . INAA have now been completed for up to 40 elements on 74 MOI sets, representing  $>600$  individual samples, laboratory blanks, and field blanks.

The results of this study confirm the existence of fine structure in submicrometer aerosol and suggests that particles from various sources remain separated, *i.e.*, unmixed over urban transport scales. In the heavily industrialized Philadelphia area, the size spectra show individual accumulation aerosol peaks for elements such as Zn, Ti, and V at modal diameters of approximately  $0.1 \mu\text{m}$ .

These clearly represent the influence of plumes from a municipal incinerator, titanium pigment plant, and residual oil combustion, i.e., sources in close proximity to the sampling sites. Elements such as As, Se, and S, which have strong components from distant sources and occur in much wider peaks with modal diameters near 0.5  $\mu\text{m}$  and represent what receptor modelers have termed "regional" sulfate. Whereas classical receptor modeling employs statistical techniques to resolve the contributions of generic source types from ambient measurements of unfractionated fine particles, our results demonstrate the resolution of individual sources. This is a degree of resolution not previously attained by statistical analysis of unfractionated fine aerosol particles.

In addition, by fitting spectra containing single peaks and correlating the fitted mass median aerodynamic diameters against water activity, we have developed the first hygroscopic growth function for V in ambient aerosol particles. As discussed below, growth functions for various elements are sorely needed to predict their dry deposition fluxes, especially to natural waters.

#### • Chesapeake Bay Atmospheric Deposition Study

Atmospheric deposition by wet and dry processes is known to be an important source of several anthropogenic, particulate-bound metals in critically important waters such as the north atlantic Ocean, the coastal mid-Atlantic waters, and the Great Lakes. The Chesapeake Bay, perhaps the world's most productive bay, is especially subject to deposition of anthropogenic air pollutants as it lies in close proximity to heavily polluted urban areas, e.g., Baltimore, MD, Washington, DC, Norfolk, VA, and receives polluted air masses from the heavily industrialized Ohio Valley.

We are now in the third year of a project to characterize the spatial and temporal variations in the concentrations of various elements in aerosol particles depositing on the Chesapeake Bay. Aerosol particles with diameters smaller than 10  $\mu\text{m}$  are sampled weekly at three rural shoreline sites, one at the Wye Research Institute in the northern Bay, a second near the Elms educational institute in the middle Bay, and the third at Haven

Beach located near Gloucester Point in the south Bay.

Analyses have been completed for more than 450 samples, field blanks, and laboratory blanks. In addition to INAA, inductively-coupled plasma-atomic emission spectrometry (ICP-AES), and graphite furnace atomic absorption spectrometry with Zeeman background correction (GFAAS) were also used. Analyses for Al, As, Cd, Cr, Cu, Fe, Ni, Ni, Pb, S, Se, and Zn have been used to estimate aerial dry deposition fluxes to Bay surface waters as the product of the annual average concentrations and deposition velocities ( $V_d$ ) determined from limited experimental measurements on other waters reported in the literature. The results indicate that dry deposition fluxes for many elements emitted from high-temperature combustion sources are comparable to wet fluxes. The dry deposition fluxes of elements associated with large particles of coal or crustal materials typically exceed the wet fluxes for these elements.

Deposition models suggest that particle size is extremely important in determining deposition velocities. Size is governed by the nature of the source, coagulation, cloud processing, and hygroscopic growth. Over large distances, atmospheric processes tend to homogenize separate particle populations. However, on the urban scale, our submicrometer aerosol studies have shown that aerosol particle populations from individual sources remain discrete, i.e., unmixed. Thus, particle size, hygroscopic growth, and deposition of various elements will differ for particles emitted from different sources. To investigate the importance of these effects, we have collected size segregated aerosol samples with micro-orifice impactors on the pier at the Matapeake Police Station on Kent Island, and on the Pier at the Chesapeake Biological Laboratory in Solomons, MD. INAA of 15 sets of these samples are in progress. Preliminary results show that most of the deposition occurring under neutral conditions at wind speeds of 5 m/s (the mean Bay wind speed) is accounted for by the fraction of the elemental mass associated with large particles, i.e., particles  $> 5 \mu\text{m}$ , aerodynamic diameter. For example, at Matapeak, particles collected on stages 0 and 1 (diameters 21 and 7  $\mu\text{m}$ ) accounted for 85% of the deposition of S and V, despite the fact

that only 10% of their mass resides in these particles.

### Federal Bureau of Investigation

The Elemental and Metals Analysis Unit (EMAU) of the Federal Bureau of Investigation (FBI) Laboratory irradiates samples for neutron activation analysis (NAA) at the NIST reactor facility. These samples are evidence in criminal cases being investigated by the FBI, state, and local jurisdictions throughout the United States. The primary analysis is of lead projectiles (bullets and shotshell pellets). In a typical case bullets from a crime scene are compared with the bullets from cartridges found in the possession of a suspect. The samples are irradiated at NIST along with an appropriate standard (SRM 2416, or SRM 2417) and then transported to FBI Laboratory facilities for gamma-ray spectroscopy. By NAA, samples are quantitatively analyzed for trace amounts of copper, antimony, and arsenic. The quantities of these trace elements found thus characterizes each bullet and allows bullets to be compositionally compared within a specific case. Further, the lead data from approximately the last ten years has been stored in a database. With this database new samples can be compared to each other and to all samples the FBI has analyzed to give an idea of how common their composition is. When appropriate, Special Agent Examiners provided expert court testimony in these cases.

The FBI also occasionally irradiates copper and steel samples at NIST. These analyses are also quantitative determinations for the trace elements present, and ultimately inter-sample comparison.

In addition to using NAA to analyze samples from criminal cases, several projects of note are being worked on this year. Using NIST facilities EMAU has analyzed bullet lead which was used as a testing standard in a collaborative crime laboratory testing program. EMAU is also participating in a study of the effects of bullet fragments on brain tissue by analyzing bullet lead before and after implantation in the brain tissue of mice. On-going research concerning the quantitative trace analysis of bullet and shotshell pellet lead continues as questions arise in criminal cases.

### References

- [1] D. L. Anderson, W. C. Cunningham, and T. R. Lindstrom, Concentrations and Intakes for H, B, S, K, Na, Cl and NaCl in Foods. Submitted to Journal of Food Composition and Analysis.
- [2] D. L. Anderson, W. C. Cunningham, T. R. Lindstrom, and I. Olmez, Identification of Lead and Other Elements in Ceramic Glazes and Housewares, Using  $^{109}\text{Cd}$ -Induced X-Ray Emission. Submitted to Journal of AOAC International.

### Research Topics

#### Use of INAA, PGAA, and RNAA to Determine 30 Elements for Certification of an SRM: Spinach Leaves, 1570a

D. A. Becker<sup>16</sup>, K. M. Garrity<sup>16</sup>, R. R. Greenberg<sup>16</sup>, and E. A. Mackey<sup>16</sup>

#### The $k_\alpha$ Approach in Cold-Neutron Prompt Gamma Activation Analysis

R. M. Lindstrom<sup>16</sup> and R. F. Fleming<sup>31</sup>.

#### Boron and Nitrogen Profiling in Diamond and Boron Nitride Films

L. Pilione<sup>18</sup>, A. Badzian<sup>18</sup>, T. Badzian<sup>18</sup>, H. Hofsäss<sup>29</sup>, G. P. Lamaze<sup>16</sup>, and R. G. Downing<sup>16</sup>.

#### Nondestructive Determination of Weight Percent Boron in Dielectric Films

R. G. Downing<sup>16</sup> and G. P. Lamaze<sup>16</sup>.

#### IAEA-NIST-FDA-USDA Joint Project on Dietary Intake of Minor and Trace Elements in Different Countries

G. V. Iyengar<sup>16</sup> and R. R. Greenberg<sup>16</sup>.

#### Development of Fresh-Frozen, Biological Standard Reference Materials

R. Demiralp<sup>16</sup>, B. J. Koster<sup>16</sup>, and S. A. Wise<sup>17</sup>.

#### Regional and Indigenous Sources of Pollutants From Coal Combustion in Maryland

J. M. Ondov<sup>30</sup>.

#### Neutron Capture Prompt-Gamma Emission Measurement of Hydrogen and Dopants in $\text{KTiPO}_4$ and $\text{KTiAsPO}_4$

M. Crawford<sup>8</sup>, K. Cheng<sup>8</sup>, A. Ferretti<sup>8</sup>, W. Bindloss<sup>8</sup>, J. M. Nicol<sup>19</sup>, and R. M. Lindstrom<sup>16</sup>.

**Certification of Standard Reference Materials by Neutron Activation Analysis**

R. R. Greenberg<sup>16</sup>, D. A. Becker<sup>16</sup>, R. Demiralp<sup>16</sup>, K. M. Garrity<sup>16</sup>, R. M. Lindstrom<sup>16</sup>, E. A. Mackey<sup>16</sup>, and B. R. Norman<sup>16</sup>.

**Improvements to INAA Methodology**

R. R. Greenberg<sup>16</sup>, D. A. Becker<sup>16</sup>, R. Demiralp<sup>16</sup>, R. M. Lindstrom<sup>16</sup>, and E. A. Mackey<sup>16</sup>.

**Quality Assurance Improvements for NAA**

R. R. Greenberg<sup>16</sup>, D. A. Becker<sup>16</sup>, R. Demiralp<sup>16</sup>, R. M. Lindstrom<sup>16</sup>, E. A. Mackey<sup>16</sup>, and P. Bode<sup>41</sup>.

**Development of Radiochemical Separations for NAA**

D. A. Becker<sup>16</sup>, K. M. Garrity<sup>16</sup>, R. R. Greenberg<sup>16</sup>, E. A. Mackey<sup>16</sup>, and B. R. Norman<sup>16</sup>.

**Evaluation of Errors and Interferences in NAA**

D. A. Becker<sup>16</sup>, M. J. Blackman<sup>22</sup>, R. R. Greenberg<sup>16</sup>, and R. M. Lindstrom<sup>16</sup>.

**Lithium Distribution in Protonated Optical Waveguide Materials**

N. A. Sanford<sup>9</sup>, J. A. Aust<sup>9</sup>, J. M. Zavada<sup>4</sup>, G. P. Lamaze<sup>16</sup>, and R. G. Downing<sup>16</sup>.

**Trace Elemental Characterization of Silicon Semiconductor Materials**

D. A. Becker<sup>16</sup> and R. M. Lindstrom<sup>16</sup>.

**Improvements to PGAA Methodology**

R. M. Lindstrom<sup>16</sup>, D. L. Anderson<sup>11</sup>, E. A. Mackey<sup>16</sup>, R. L. Paul<sup>16</sup>, and D. H. Vincent<sup>31</sup>.

**Oxygen-17 Profiling in Semiconductor Materials**

J. N. Cox<sup>12</sup>, G. P. Lamaze<sup>16</sup>, and R. G. Downing<sup>16</sup>.

**Evaluation of Accuracy and Precision in INAA of Botanical Materials**

D. A. Becker<sup>16</sup>.

**Neutron Scattering Effects in PGAA**

R. M. Lindstrom<sup>16</sup>, E. A. Mackey<sup>16</sup>, R. L. Paul<sup>16</sup>, D. H. Vincent<sup>31</sup>, and M. Blaauw<sup>41</sup>.

**New Developments in Monitor Activation Analysis**

R. F. Fleming<sup>31</sup>, G. P. Lamaze<sup>16</sup>, R. M. Lindstrom<sup>16</sup>, E. A. Mackey<sup>16</sup>, and R. L. Paul<sup>16</sup>.

**Oxygen-17 Profiling for the Determination of Reaction Constants in Stellar Burn-up**

J. Blackmon<sup>28</sup>, G. P. Lamaze<sup>16</sup>, and R. G. Downing<sup>16</sup>.

**Determination of Boron and Lithium using Neutron Activation - Mass Spectrometry**

R. G. Downing<sup>16</sup>, G. V. Iyengar<sup>16</sup>, and B. Clarke<sup>36</sup>.

**Boron Profiling in Semiconductor Dielectric Films by NDP**

J. N. Cox<sup>12</sup>, B. Sun<sup>12</sup>, J. Gigante<sup>34</sup>, R. Carpio<sup>21</sup>, T. Z. Hossain<sup>7</sup>, G. P. Lamaze<sup>16</sup>, and R. G. Downing<sup>16</sup>.

**Bio Analytical and Specimen Bank Research**

R. G. Downing<sup>16</sup>, R. Demiralp<sup>16</sup>, K. A. Fitzpatrick<sup>16</sup>, K. M. Garrity<sup>16</sup>, R. R. Greenberg<sup>16</sup>, G. V. Iyengar<sup>16</sup>, B. J. Koster<sup>16</sup>, J. K. Langland<sup>16</sup>, and E. A. Mackey<sup>16</sup>.

**Intercalibration of NDP Facilities,**

K. Ünlü<sup>32</sup>, B. Werhring<sup>32</sup>, G. P. Lamaze<sup>16</sup>, R. G. Downing<sup>16</sup>.

**Studies in Elemental Speciation**

D. A. Becker<sup>16</sup> and K. M. Garrity<sup>16</sup>.

**Determination of Bromate in Bread Products using HPLC and RNAA**

C. R. Warner<sup>11</sup> and W. C. Cunningham<sup>11</sup>.

**Determination of <sup>137</sup>Cs and <sup>40</sup>K in Foods using Low-Level Counting Techniques**

D. L. Anderson<sup>11</sup> and W. C. Cunningham<sup>11</sup>.

**Multielement Analysis of Foods and Related Materials by NAA and PGAA**

D. L. Anderson<sup>11</sup> and W. C. Cunningham<sup>11</sup>.

**Boron Profiles of Thermionic Materials (ZrBC)**

P. Davis<sup>14</sup>, G. P. Lamaze<sup>16</sup>, and R. G. Downing<sup>16</sup>.

**High Sensitivity Gamma-Ray Spectrometry**

R. M. Lindstrom<sup>16</sup>.

**Application of Radioisotope-Induced X-Ray Emission to the Identification of Lead and Other Elements in Ceramic Glazes and Housewares**

D. L. Anderson<sup>11</sup> and W. C. Cunningham<sup>11</sup>.

**Elemental Characterization of High Temperature Superconductors**

D. A. Becker<sup>16</sup>, K. M. Garrity<sup>16</sup>, R. M. Lindstrom<sup>16</sup>, E. A. Mackey<sup>16</sup>, R. L. Paul<sup>16</sup>, and D. H. Vincent<sup>31</sup>.

**Boron Depth Profiling Standard Reference Material for Secondary Ion Mass Spectrometry**

G. P. Lamaze<sup>16</sup>, R. G. Downing<sup>16</sup>, and D. Simons<sup>25</sup>.

### Comparison of Nuclear Reactors for Analytical Chemistry

D. A. Becker<sup>16</sup>.

### Determination of Hydrogen by PGAA

D. L. Anderson<sup>11</sup>, R. R. Greenberg<sup>16</sup>, R. M. Lindstrom<sup>16</sup>, E. A. Mackey<sup>16</sup>, R. L. Paul<sup>16</sup>, and D. H. Vincent<sup>31</sup>.

### Analytical Applications of Cold Neutrons

H. Chen<sup>16</sup>, R. Demiralp<sup>16</sup>, R. G. Downing<sup>16</sup>, R. R. Greenberg<sup>16</sup>, G. P. Lamaze<sup>16</sup>, J. K. Langland<sup>16</sup>, R. M. Lindstrom<sup>16</sup>, E. A. Mackey<sup>16</sup>, D.F.R. Mildner<sup>16</sup>, R. L. Paul<sup>16</sup>, V. A. Sharov<sup>13</sup>, D. H. Vincent<sup>31</sup>, G. Molnár<sup>42</sup>, and Z. Reváy.

### Research and Development of Focusing Neutron Optics

R. E. Benenson<sup>23</sup>, H. Chen<sup>16</sup>, R. G. Downing<sup>16</sup>, N. Gao<sup>35</sup>, D. M. Gibson<sup>35</sup>, C. A. MacDonald<sup>35</sup>, D.F.R. Mildner<sup>16</sup>, V. A. Sharov<sup>13</sup>, W. P. Siegmund<sup>20</sup>, J. W. Swider<sup>30</sup>, and Q. F. Xiao<sup>35</sup>.

### Development of High Resolution Position Sensitive Charged Particle and Neutron Detectors

J. Carbone<sup>6</sup>, D. Carta<sup>6</sup>, R. Wentink<sup>6</sup>, H. Chen<sup>16</sup>, C. Zeissler<sup>25</sup>, and R. G. Downing<sup>16</sup>.

### Focusing Neutrons for Small-Angle Scattering

R. E. Benenson<sup>23</sup>, H. Chen<sup>16</sup>, R. G. Downing<sup>16</sup>, C. J. Glinka<sup>19</sup>, and D.F.R. Mildner<sup>16</sup>.

### Chesapeake Bay Atmospheric Deposition Study

Z. C. Lin<sup>30</sup>, J. M. Ondov<sup>30</sup>, and Z. Y. Wu<sup>30</sup>.

### Characterization of Submicrometer Aerosol Particles

F. Divita<sup>30</sup> and J. M. Ondov<sup>30</sup>.

### Boron Profiling of Nickel-Boron Bilayers,

S. Baker<sup>15</sup>, G. Smith<sup>15</sup>, G. P. Lamaze<sup>16</sup>, and R. G. Downing<sup>16</sup>.

### Forensic Applications of NAA

E. R. Peele<sup>10</sup>, R. F. Rebbert<sup>10</sup>, R. Aaron<sup>10</sup>, R. Bilko<sup>10</sup>, K. Bryan<sup>10</sup>, K. Lundy<sup>10</sup>, R. Rebbert<sup>10</sup>, J. Riley<sup>10</sup>, and D. Thompson<sup>10</sup>.

### Archeological Applications of NAA

R. Bishop<sup>22</sup>, M. James Blackman<sup>22</sup> and J. E. Myers<sup>22</sup>.

### Analytical Study of the Geological Obsidian Sources and Archaeological Artifacts From the Northern Caucasus and Transcaucasia

R. Bishop<sup>22</sup>, M. James Blackman<sup>22</sup>, J. E. Myers<sup>22</sup>, R. C. Badaljan<sup>1</sup>, Z. K. Kikodze<sup>2</sup>, I. G. Narimanov<sup>1</sup>, and P. Kohl<sup>33</sup>.

### Development of Time-of-Flight CNDP for Improved Depth Resolution

J. Welsh<sup>26</sup>, E. Schweikert<sup>26</sup>, G. P. Lamaze<sup>16</sup>, R. G. Downing<sup>16</sup>.

### Trace Hydrogen Determination in Metals and Other Materials

R. M. Lindstrom<sup>16</sup> and R. L. Paul<sup>16</sup>.

### Coincidence Measurements of Gamma Cascades in <sup>128</sup>Te(n,gamma)<sup>129</sup>Te

L. F. Conticchio<sup>30</sup>, R. M. Lindstrom<sup>16</sup>, R. L. Paul<sup>16</sup>, D. M. Mustillo<sup>30</sup>, J. W. Swider<sup>30</sup>, and W. B. Walters<sup>30</sup>.

### Maya Ceramic Production and Exchange.

R. Bishop<sup>22</sup> and A. Foias<sup>37</sup>.

### Pre-Columbian Peruvian Ceramic Production and Exchange.

R. Bishop<sup>22</sup> and M. Glowacki<sup>38</sup>.

### The Production and Exchange of Spanish Colonial Tin-Lead Glazed Ceramics from Peru and Panama.

J. S. Olin<sup>22</sup>, M. J. Blackman<sup>22</sup>, P. Rice<sup>40</sup>, and D. Mustillo<sup>30</sup>.

### Phrygian Ceramic Production at Gordian.

M. J. Blackman<sup>22</sup> and R. C. Henrickson<sup>22</sup>.

### The Production and Distribution of Medieval Islamic Tin-Lead Glazed Ceramics and Frit Ware.

M. J. Blackman<sup>22</sup>, S. Redford<sup>39</sup>, and J. Hallett<sup>43</sup>.

### Affiliations

<sup>1</sup>Acad. of Science (Azerbaijan, FUSSR)

<sup>2</sup>Acad. of Sci. (Georgia, FUSSR)

<sup>3</sup>Acad. of Sci. (Armenia, FUSSR)

<sup>4</sup>Army Research Office, Research Triangle Park

<sup>5</sup>Budapest Neutron Center

<sup>6</sup>CID Technologies

<sup>7</sup>Cornell University

<sup>8</sup>DuPont

<sup>9</sup>Electromagnetic Technology Division

<sup>10</sup>Federal Bureau of Investigation

<sup>11</sup>Food and Drug Admin.

<sup>12</sup>INTEL

- <sup>13</sup>Kurchatov Institute, Russia
- <sup>14</sup>Linnfield State College
- <sup>15</sup>Los Alamos National Laboratory
- <sup>16</sup>Nuclear Methods Group
- <sup>17</sup>Organic Analytical Res. Div.
- <sup>18</sup>Pennsylvania State University
- <sup>19</sup>Reactor Radiation Division
- <sup>20</sup>Schott Optical Glass
- <sup>21</sup>Sematech
- <sup>22</sup>Smithsonian Institution
- <sup>23</sup>State Univ. of New York at Albany
- <sup>24</sup>Statistical Engineering Div.
- <sup>25</sup>Surface and Microanalysis Div.
- <sup>26</sup>Texas A&M University
- <sup>27</sup>Texas Instruments
- <sup>28</sup>Triangle Universities Nuclear Laboratory
- <sup>29</sup>University of Konstanz
- <sup>30</sup>University of Maryland
- <sup>31</sup>University of Michigan
- <sup>32</sup>University of Texas - Austin
- <sup>33</sup>Wellesley College
- <sup>34</sup>Westinghouse
- <sup>35</sup>X-Ray Optical Systems
- <sup>36</sup>McMaster University
- <sup>37</sup>Vanderbilt University
- <sup>38</sup>Brandeis University
- <sup>39</sup>Georgetown University
- <sup>40</sup>Southern Illinois University
- <sup>41</sup>Technical University Delft, The Netherlands
- <sup>42</sup>Budapest Neutron Centre, Hungary
- <sup>43</sup>Oxford University, UK

## NEUTRON METROLOGY AND DOSIMETRY

This project provides measurement services, standards, and fundamental research in support of national industrial competitiveness in areas related to neutron physics. The industrial fields served include materials development, scientific instrument manufacturing, electric power production, radiation protection, radiation therapy, and radiation hardness testing.

This project maintains, develops, and applies well-characterized neutron fields for detector development, methods evaluation, and standardization as needed for materials dosimetry in nuclear reactor applications and for personnel dosimetry in radiation protection. These neutron fields include thermal neutron beams, "white" and monochromatic cold neutron beams, a thermal-column-cavity fission neutron field, and  $^{252}\text{Cf}$  fission neutron fields, both moderated and unmoderated. The calibration of these neutron fields is derived from related artifacts, facilities, and capabilities maintained by the project: the national standard neutron source NBS-I, a manganous sulfate bath for neutron source comparisons, a collection of fissionable isotope mass standards (FIMS), a collection of boron and lithium isotopic standards, and spectroscopy facilities for both gamma rays and alpha particles. In addition a larger volume, higher fluence-rate fission neutron field, the Materials Dosimetry Reference Facility (MDRF) is maintained collaboratively at the University of Michigan's Phoenix Memorial Laboratory.

The group also carries out forefront research at the CNRF in weak interaction physics and tests of fundamental symmetry principles, develops advanced measurement techniques in neutron interferometry, and performs experimental tests of critical neutron transport data and computational methods. The work in fundamental neutron physics is reported in a separate section of this volume. Highlights of other activities are given below.

### Neutron Fields and Standards

#### • Fission-Spectrum Neutron Fields for Calibrations

NIST has developed and maintains both  $^{252}\text{Cf}$  and  $^{235}\text{U}$  neutron fission-spectrum fields for

customer calibration work. The  $^{235}\text{U}$  fission spectrum is produced in a 30-cm diameter cavity in the graphite of the NIST reactor's thermal column. This facility is called the Cavity Fission Source. Its sample exposure position is the small volume inside a cadmium pill box, between two fissioning disks of  $^{235}\text{U}$ .

Customers' dosimeters are irradiated to certified fluences of fast neutrons and then returned to the customers for their analysis. By basing the fluence certification upon calibration transfer from  $^{252}\text{Cf}$  sources calibrated in the NIST MnSO<sub>4</sub> Bath Facility, traceable certifications are available at an uncertainty level of about 2.5%.

Certified Neutron Fluence Standards for HFIR. A timely example of the use of fission spectrum neutrons to calibrate neutron dosimeters for a customer is the recent assistance provided to Oak Ridge National Laboratory (ORNL) in examining the fast neutron dosimetry of the High Flux Isotope Reactor (HFIR). In 1992, ORNL dosimetry foil sets were irradiated at the pressure vessel embrittlement surveillance positions of HFIR to confirm calculated neutron exposure histories. The results showed large discrepancies between fluences derived from threshold reactions, such as  $^{58}\text{Ni}(n,p)$  or  $^{54}\text{Fe}(n,p)$ , and fast fission reactions, such as  $^{237}\text{Np}(n,f)$ , and helium accumulation fluence monitors, such as  $^9\text{Be}(n,\text{He})$ . Because fission product counting and helium accumulation measurements are more complicated than gamma counting single-isotope (n,p) products, NIST was asked by the Nuclear Regulatory Commission (NRC) to irradiate dosimeters of each type to certified fluences in the Cavity Fission Source. These fluence standards were provided to ORNL who verified that their readings agreed with NIST certified values within the stated uncertainties.

NIST was also asked to provide a measure of the gamma-ray exposure at the dosimetry locations at the HFIR pressure vessel wall, separated from the core by 20 cm of beryllium and 70 cm of water. At this depth of penetration, ORNL calculations suggested a large gamma-to-neutron ratio. Dr. William McLaughlin of the Radiation Interactions and Dosimetry Group (NIST Div. 846) provided assistance and measured the gamma

dosimeters contain 70% carbon, 25% chlorine, and just 5% hydrogen, to reduce their sensitivity to neutrons. The gamma measurement confirmed ORNL calculations, which explain the neutron dosimeter discrepancies in terms of photonuclear response of the fission dosimeters and the beryllium ( $^9\text{Be} + \text{gamma} \rightarrow \text{neutron} + ^8\text{Be} \rightarrow \text{neutron} + 2 \text{alpha}$ ). This quality assurance check on neutron dosimetry was helpful in obtaining authorization for HFIR's return to operation after a lengthy shutdown to study unexplained high levels of embrittlement in test specimens which are representative of the condition of the reactor pressure vessel.

The Materials Dosimetry Reference Facility (MDRF). A new, high-intensity reference neutron field for reactor dosimetry has been placed into operation at the Ford Nuclear Reactor (FNR) at the University of Michigan in collaboration with NIST. Initial neutron spectrum characterization has been accomplished and the fast neutron population ( $E > 1 \text{ MeV}$ ) is referenced to both the  $^{235}\text{U}$  fission spectrum in the Cavity Fission Source at the thermal column of the NIST Reactor and a known  $^{252}\text{Cf}$  neutron source strength. MDRF certified neutron fluences are established with  $^{58}\text{Ni}(n,p)^{58}\text{Co}$  activation monitors. Further refinement of the spectrum and fluence rate uncertainties will continue in FY 94.

Designed and constructed by NIST, the MDRF hosts calibration and validation experiments in support of materials neutron dosimetry for the nuclear power industry and for the metallurgical community engaged in estimating radiation damage in steel. This reference field is a natural extension of a long-term NIST program to develop standard and reference neutron fields for measurement assurance applications and for testing new detectors and techniques. Field characterization and user operation of the facility is a joint effort by the NIST and the Phoenix Memorial Laboratory of the University of Michigan.

The MDRF complements the Cavity Fission Source at the NIST reactor by providing a tenfold increase in the fast-neutron fluence rate, a much larger irradiation volume with modest gradients, and a neutron spectrum similar to that at the inner surface of a PWR pressure vessel. An option to alter the intermediate-energy neutron rate is

afforded by installation of a  $^{10}\text{B}$  filter liner. The fluence rate ( $E > 1 \text{ MeV}$ ) is  $2.7e^{11} \text{ cm}^{-2} \text{ s}^{-1}$  and the neutron-to-gamma dose ratio is about 1.0.

#### ● Thermal Column Irradiations and Experiments

Superheated drop detectors mounted inside our environmental chamber were irradiated in a beam from the thermal column, to test a theory of bubble production as a function of temperature. This work was part of a Master's thesis for a student at the U.S. Naval Academy.

$\text{BF}_3$  detectors were calibrated in a thermal neutron beam for the DOE Environmental Measurements Laboratory and for the Army Pulsed Reactor Facility.

Certified fluence irradiations of gold wire dosimeters were carried out for the Armed Forces Radiobiology Research Institute.

Further testing was done on development of a new  $^{10}\text{B}$  ionization chamber. Isobutane gas was tested as a substitute for the P-10 argon-methane mixture used previously. The higher stopping power of the isobutane did improve the sharpness of the alpha particle peak in the pulse height distribution, but a much higher operating voltage was required. In some applications, the flammability of isobutane can impose restrictions on its use. Further testing will be carried out to see if the same improvement in pulse height distribution can be obtained by just increasing the anode-to-target spacing in the chamber while using the more widely available P-10 gas.

#### ● Filtered Beam Measurements

As part of an international comparison of fast neutron fluence measurements under the auspices of the International Bureau of Weights and Measures (BIPM), NIST  $^3\text{He}$  detector measurements of the 24.5 keV iron-filtered beam were compared with the readings of a Bonner Sphere transfer instrument which is being circulated among various national standards laboratories. The NIST  $^3\text{He}$  detector was calibrated by transmission measurements at both the thermal column and at the monochromatic beam at the neutron interferometer facility in the cold neutron guide hall.



- **Neutron Flux Measurements at CNRF Instrument Positions**

Neutron flux (fluence rate) measurements were made at five positions between the sample cryostat and the filter of the SPINS instrument on NG-5. The measurements were made with a small fission chamber having a heavy  $^{235}\text{U}$  deposit from the NIST collection of Fissionable Isotope Mass Standards.

## **Fundamental Neutron Physics**

A number of major programmatic milestones in the fundamental neutron physics were reached in the last year. This program consists of a number of collaborative experimental programs involving NIST staff as well as researchers from U.S. and foreign universities and laboratories. The research efforts concern investigations in the precise measurement of neutron properties, development of new neutron optical techniques and tests of fundamental physical laws. Among the highlights of the past year was the first decay data taken with the NIST neutron lifetime apparatus on the end guide position NG-6. A detailed inter-comparison of accurate neutron flux monitors was carried out at the monochromatic beam at NG-7. An additional milestone was reached with the first successful operation of the multidegree of freedom vibration isolation system at the neutron interferometer position. Other highlights include the installation of the new laser system for the polarized  $^3\text{He}$  neutron spin filter developmental program and the successful completion of the first "user" experiment at the monochromatic beam position at NG-7.

- **Determination of the Neutron Lifetime**

The NIST program aimed at the determination of the neutron lifetime reached a major milestone this year with the detection of decay protons at end position NG-6. The new NIST neutron decay detector (based upon earlier collaborative efforts carried out at the Institut Laue Langevin in Grenoble) incorporates a number of novel features. The new multiparametric data acquisition system allows a detailed study of background and a far better identification of spurious events. A new magnet with substantially improved homogeneity and an active proton extraction system essentially

eliminates a potentially important class of systematic effects.

Data collection with the new apparatus will continue until the spring reactor shut-down. A significant improvement on the previous measurement is anticipated.

- **Neutron Interferometry Installation**

The past year has seen marked progress toward the completion of the neutron interferometry installation on NG-7. A novel, in-guide, pyrolytic graphite monochromator has been installed and is now operational. This design provides highly efficient extraction of wavelength selected neutrons with very low background. Two experiments were carried out this year using this beam.

The first experiment involved the inter-comparison of two highly accurate neutron flux monitors. The first of these is a "self-calibrating" device based upon coincident detection of alpha particles and gamma rays following neutron capture on  $^{10}\text{B}$ . A detailed description of this work is given elsewhere in this report.

The second experiment took advantage of a novel feature of neutron diffraction in single crystals to observe the Coriolis acceleration. According to the dynamical theory of diffraction, the behavior of a neutron undergoing diffraction very near the Bragg condition in a nearly perfect single crystal will behave as though it has an "effective mass" substantially less than its free mass. In silicon, this effective mass is nearly six orders of magnitude less than the free neutron mass. Such a small effective mass implies that a very small force applied to a neutron undergoing diffraction will cause a greatly enhanced deflection.

In this measurement, the diffracting crystal was harmonically "rocked" with amplitudes in the range of  $10^{-4}$  radian per second (comparable to the earth's angular rotational velocity). A neutron undergoing diffraction in such a rocking crystal will experience a Coriolis acceleration which will be enhanced by the neutrons small effective mass. Thus while the scale for the deflection of a free neutron might be (an unobservably small) several angstroms, the enhanced deflection is several millimeters.

This deflection was measured in several configurations in late 1993 and data reduction is in progress. We anticipate that this project will continue in the future with a series of additional measurements using the small "effective" neutron mass to explore other effects including the gravitational deflection of neutrons.

## Research Topics

### Utilization of the Materials Dosimetry Reference Facility—and Further Neutron and Gamma Field Characterization

J. A. Grundl<sup>6</sup>, C. M. Eisenhauer<sup>6</sup>, E. D. McGarry<sup>6</sup>, D. M. Gilliam<sup>6</sup>; A. I. Hawari<sup>13</sup>, P. A. Simpson<sup>13</sup>, and R. Venkatoraman<sup>13</sup>.

### Fast Neutron Transport Through Lead

E. D. McGarry<sup>6</sup> and C. Heimbach<sup>2</sup>.

### Benchmark Measurements and Calculations for Criticality Safety

D. M. Gilliam<sup>6</sup> and J. F. Briesmeister<sup>7</sup>.

### Neutron Fluence Rate Measurements at the CNRF

D. M. Gilliam<sup>6</sup>.

### Defined-Geometry Alpha Counting

D. M. Gilliam<sup>6</sup> and J. Lerman<sup>16</sup>.

### Certified Neutron Fluence Standards from the Cavity Fission Source

E. D. McGarry<sup>6</sup> and J. A. Grundl<sup>6</sup>.

### Quality Assurance Checks on Masses and Impurities in Neutron Dosimeters for NRC Reactor Pressure Vessel Embrittlement Surveillance

E. D. McGarry<sup>6</sup> and J. A. Grundl<sup>6</sup>.

### Measurement of LET Spectra

R. B. Schwartz<sup>6</sup>, H. Gerstenberg<sup>1</sup>, and P. Lamperti<sup>6</sup>.

### Response of Albedo Neutron Dosimeters as a Function of Angle

R. B. Schwartz<sup>6</sup>, B. A. Torres<sup>1</sup>, and E. Boswell<sup>6</sup>.

### Neutron Irradiations for other Government Agencies

R. B. Schwartz<sup>6</sup>, D. M. Gilliam<sup>6</sup>, C. Heimbach<sup>2</sup>, F. Hajnal<sup>3</sup>, and M. J. Harper<sup>9</sup>.

### Neutron Transport Calculations

C. M. Eisenhauer<sup>6</sup>.

### Determination of the Neutron Lifetime

M. S. Dewey<sup>6</sup>, D. M. Gilliam<sup>6</sup>, G. L. Greene<sup>6</sup>, J. M. Richardson<sup>6</sup>, and W. M. Snow<sup>11</sup>.

### Accurate Determination of Neutron Capture Flux

M. Arif<sup>6</sup>, M. S. Dewey<sup>6</sup>, D. Gilliam<sup>6</sup>, G. L. Greene<sup>6</sup>, J. M. Richardson<sup>6</sup>, W. M. Snow<sup>11</sup>, J. Pauwels<sup>3</sup>, and R. Scott<sup>8</sup>.

### Search for Time Reversal Invariance in Neutron Beta Decay

J. F. Wilkerson<sup>7</sup>, E. Wasserman<sup>7</sup>, J. Nico<sup>7</sup>, R.G.H. Robertson<sup>7</sup>, S. Freedman<sup>10</sup>, A. Garcia<sup>10</sup>, T. Chupp<sup>13</sup>, K. Coulter<sup>13</sup>, M. S. Dewey<sup>6</sup>, G. L. Greene<sup>6</sup>, and A. Thompson<sup>6</sup>.

### Observation of the Coriolus Acceleration Neutron in a Rotating Crystal

A. Zeilinger<sup>12</sup>, M. Arif<sup>6</sup>, D. Brown<sup>6</sup>, K. Raum<sup>14</sup>, and M. Kollner<sup>14</sup>.

### Parity Non-Conserving Neutron Spin Rotation

B. Heckel<sup>15</sup>, D. Markoff<sup>15</sup>, E. Adelberger<sup>15</sup>, G. L. Greene<sup>6</sup>, and W. M. Snow<sup>13</sup>.

### Highly Accurate Neutron Wavelength Measurements

M. S. Dewey<sup>6</sup>, K. J. Coakley<sup>17</sup>, W. M. Snow<sup>11</sup>, J. M. Richardson<sup>6</sup>, M. Arif<sup>6</sup>, and G. L. Greene<sup>6</sup>.

### LASER Polarization of <sup>3</sup>He for Neutron Spin Filters

A. Thompson<sup>6</sup>, G. Greene<sup>6</sup>, and M. S. Dewey<sup>6</sup>.

## Affiliations

<sup>1</sup>Armed Forces Radiobiology Research Institute

<sup>2</sup>Army Pulsed Reactor Facility

<sup>3</sup>Central Bureau for Nuclear Measurement, Belgium

<sup>4</sup>DOE Environmental Measurements Laboratory

<sup>5</sup>Inst. for Ref. Materials & Measurements (CEC)

<sup>6</sup>Ionizing Radiation Division

<sup>7</sup>Los Alamos National Laboratory

<sup>8</sup>Scottish Universities Research and Reactor Center

<sup>9</sup>United States Naval Academy

<sup>10</sup>University of California, Berkeley

<sup>11</sup>University of Indiana

<sup>12</sup>University of Innsbruck

<sup>13</sup>University of Michigan

<sup>14</sup>University of Munich

<sup>15</sup>University of Washington

<sup>16</sup>Washington University of St. Louis

<sup>17</sup>Statistical Engineering Division

## POLYMERS DIVISION PROGRAMS

Single chain characterization of polymers in solutions as well as in bulk states has continuously been an important area for neutron scattering measurements. Small-angle neutron scattering (SANS) and neutron reflectivity have also opened new research opportunities in multiphase systems and interfacial structures, especially with in-situ flow rate dependence and time resolved measurements. These studies have provided not only fundamental understandings in multicomponent polymeric systems but also technologically important information in polymer blends/alloys applications. A few of our projects are summarized below.

### Equilibrium Phase Behavior

- **Thermodynamic Interactions in Model Polyolefin Blends Obtained by SANS**

The dependence of the Flory-Huggins interaction parameter,  $\chi$ , on temperature, composition, and chain length was investigated for binary blends of amorphous model polyolefins, materials which are structurally analogous to copolymers of ethylene and 1-butene. The components were prepared by saturating the double bonds of nearly monodisperse polybutadienes (78%, 88%, and 97% vinyl content) with  $H_2$  and  $D_2$ , the latter to provide contrast for SANS experiments. Values of  $\chi$  were extracted from SANS data in the single-phase region for two series of blends, H97/D88 and H88/D78, using the random-phase approximation and the Flory-Huggins expression for free energy of mixing. These values were found to be insensitive to chain length (one test only) and to the component volume fractions for  $\phi = 0.25, 0.50, \text{ and } 0.75$ . Their temperature dependence (27-170 °C) obeys the form  $\chi(T) = A/T + B$  with coefficients that connote upper critical solution behavior, yielding  $T_c \sim 40$  °C for one blend series (H97A/D88) and  $T_c \sim 60$  °C for the other (H88/D78). These estimates are consistent with SANS pattern changes and supplemental light scattering results that indicate two-phase morphologies at lower temperatures. The  $\chi(T)$  coefficients for the two series are also consistent with the random copolymer theory.

- **Thermodynamic Interactions and Correlations in Mixtures of Two Homopolymers and a Block Copolymer by SANS**

Thermodynamic interactions in mixtures of two homopolymers and a block copolymer were obtained from SANS measurements. Experimental SANS profiles from homogeneous, ternary mixtures of model polyolefins-poly(ethyl butylene)/poly(methyl butylene)/poly(methyl butylene)-b-poly(ethyl butylene)—were compared with theoretical predictions based on the multicomponent random phase approximation (RPA). The polymers were nearly monodisperse, and were synthesized by saturating the double bonds in anionically synthesized polydienes with  $H_2$  and  $D_2$ , thus yielding polyolefins with neutron scattering contrast. The theoretical scattering profiles depend on 16 structural parameters and 6 Flory-Huggins interaction parameters,  $\chi$ , all of which were obtained independently. The  $\chi$  parameters were obtained from SANS measurements on binary poly(ethyl butylene)/poly(methyl butylene) blends. The SANS profiles obtained from the ternary blends were in quantitative agreement with the theoretical predictions over the observable  $q$ -range (0.008 to 0.04  $\text{\AA}^{-1}$ ), and over a wide range of block copolymer concentrations (from 10 to 80 volume % copolymer). This suggests that the measured  $\chi$  parameters are consistent with the original ideas of Flory and Huggins, that  $\chi$  is a measure of monomer-monomer interactions, and is thus independent of block copolymer concentration. Partial structure factors, related to correlations in the concentration of individual components, were examined by selective labeling, and were also found to be in quantitative agreement with the predictions of the multicomponent RPA.

- **Localization of a Homopolymer Dissolved in a Lamellar Structure of a Block Copolymer Studied by SANS**

The localization of deuterated styrene homopolymer dissolved in a lamellar structure of a styrene-2-vinylpyridine diblock copolymer was studied in comparison with that of the end-part of the block copolymer by observing diffraction from the styrene and 2-vinylpyridine microdomains of

deuterated styrene homopolymer/styrene-2-vinylpyridine diblock copolymer blends by SANS. Even when the average scattering lengths of both domains were equal, that is, "phase contrast matching" was theoretically achieved, diffraction was definitely observed. From the diffraction profiles in SANS and the dependence of domain spacing on the volume fraction of styrene homopolymer, it is found that the homopolymers are isolated in the middle of polystyrene domains, though they are less concentrated in the middle than the end-parts of the block chains.

- **Molecular Weight Dependence of Lamellar Domain Spacing of ABC Triblock Copolymers and Their Chain Conformations in Lamellar Domains**

The molecular weight dependence of the lamellar domain spacing of isoprene-styrene-2-vinylpyridine triblock copolymers in bulk was studied over the molecular weight range from 40k to 280k by using small-angle X-ray scattering (SAXS). It was found that the lamellar domain spacings of the triblock copolymers are larger than those of styrene-2-vinylpyridine diblock copolymers with the same molecular volumes. This result can be interpreted by theories of microphase separation at the strong segregation limit, taking into account the fact that the number of boundaries in the repeating structure of triblock copolymers is twice that of diblock copolymers. Moreover, SANS studies imply that the middle block chain of triblock copolymers is contracted along the direction parallel to lamellae in the almost same manner as the block chain of the diblock copolymers.

- **SANS from Dilute Blends of Deuterated Polystyrene in Poly (vinylmethylether) and Protonated Polystyrene**

SANS has been used to study the radius of gyration and thermo-dynamics of dilute blends of deuterated poly-styrene (PSD) in a strongly interacting matrix of poly(vinylmethylether)(PVME) and in a weakly interacting matrix of protonated polystyrene (PSH). The PSD chain is found to be slightly expanded in the PVME matrix over the PSH matrix with the statistical segment length for PSD being 7.3 Å in PVME versus 6.8 Å in PSH. The Flory interaction

parameter,  $\chi/v_0$ , for the PSD/PVME blend is found to be in approximate agreement with an extrapolation of data from studies of  $\chi/v_0$  for PSD/PVME at high concentration to the dilute concentrations studied in this work. The concentration dependence of  $\chi/v_0$  is close to linear and shows no strong change in slope down to  $\phi=0.02$ , the lowest concentration studied in this work. Analysis of the temperature dependence of  $\chi/v_0$  and the second virial coefficient,  $A_2$ , indicates that phase separation should occur for PSD/PVME in the range of 200 °C for a sample with  $\phi_{\text{PSD}} \sim 5\%$ .

- **SANS of Independently Crosslinked Blends of Deuterated Polystyrene and Poly (vinylmethylether)**

Blends of polystyrene (PSD) and poly (vinylmethylether) (PVME) have been synthesized where the PVME is crosslinked by an electron beam in the presence of isopropanol (50% concentration). Then the isopropanol is replaced by deuterated styrene monomer and divinylbenzene which is polymerized. This forms a second PSD network which is crosslinked independent of the PVME network. By producing samples by this method it may be possible to synthesize independently crosslinked blends which are thermodynamically miscible. Previous attempts at producing independently crosslinked blends of PVME and PS have resulted in phase separated blends, even in the temperature range where the uncrosslinked blend is single phase. This is due to the loss of entropy from the crosslinking reaction and elastic energy contributions from the swollen network driving the system into the two-phase region.

- **SANS Studies of Dendrimer Solutions**

Dendrimer molecules are polymers formed by a stepwise synthesis in which each additional layer doubles the terminal functionality causing a highly branched and densely packed structure. Work was done in collaboration with Donald Tomalia of Michigan Molecular Institute, who supplied poly-amidoamine dendrimers of various sizes. Dendrimers were obtained of ninth and tenth generations having molecular weights of  $3.5 \times 10^5$  and  $7.0 \times 10^5$  Daltons, respectively.

Single-chain scattering was measured by extrapolation to zero concentration and both of

these dendrimers showed higher order features. Such features have been seen previously in scattering from small objects such as latex spheres, but have not been seen in dissolved single molecules before. This indicates that these large dendrimers are quite uniform.

The size and location of these features is similar to that of either a sphere of uniform density with an abrupt transition at the outside, or a distribution that has a maximum segment density away from the center and a zone of transition at the outside.

## Kinetics of Phase Separation

### ● SANS Studies of Space-Time Organization of Structure in Polymer Blends

Self-organization of structure in polymer blends via spinodal decomposition (SD) was studied over a wide spatial-scale and time-scale (both covering over 4 orders of magnitude) by using a combined time-resolved SANS and light scattering method. The system studied was a binary critical fluid of deuterated polybutadiene and protonated poly-isoprene having a narrow molecular weight distribution in a weak segregation limit. The scattering analyses made it possible to study space-time organization of various elements of the structure: (i) the global structure; (ii) the interfacial structure such as the mean curvature of the tangled interface, the interfacial area density, and the interfacial thickness; (iii) the "interphase", i.e., the interfacial region with characteristic thermal concentration fluctuations; and (iv) the local structure characterized by the thermal concentration fluctuations within each domain. In the late stage SD, the form factor from the "interphase" was found to be time-independent, having the  $q$ -dependence of  $q^{-2.5}$ .

### ● Effect of Initial Thermal Fluctuations on the Time-Resolved SANS Study of the Self-Assembly Processes of DPB/HPB Blends

Time-resolved SANS experiments have been performed on the self-assembling process of a mixture of deuterated polybutadiene (DPB) and protonated polybutadiene (HPB) at the critical composition. This mixture has an upper critical solution temperature (UCST) type phase diagram

with the spinodal temperature at 99.2 °C. Specimens held in the single-phase state (at  $T=T_i$ ) were quenched to a point inside the spinodal phase boundary (at  $T=T_f$ ) to induce phase separation via spinodal decomposition (SD). In order to examine the effect that thermal concentration fluctuations present in the single-phase region have on SD, three different  $T_i = 102.3, 123.9, \text{ and } 171.6$  °C were chosen while  $T_f$  was fixed at -7.5 °C. The time-dependent SANS structure factor,  $S(q,t;T_i)$ , showed clear scattering peaks corresponding to the early and intermediate stages of SD. The time changes in the wavenumber  $q_m(t;T_i)$  and the intensity  $S_m(t;T_i)$  at the peak of  $S(q,t;T_i)$  followed different paths depending on the sample temperature before quenching. This fact evidences a definite effect of thermal-concentration fluctuations on SD (i.e., a significant "memory" effect). A critical test of the linearized Cahn-Hilliard-Cook theory led to the conclusion that this theory can describe satisfactorily the early stage SD in the deep-quench region.

## Effect of Flow Field

### ● Shear-Induced Morphological Structures in Triblock Copolymers

In-situ measurements of the SANS behavior of a styrene-butadiene-styrene triblock copolymer in a steady shear field were made as a function of shear rate and temperature. The kinetics of the scattering behavior after cessation of shear were also examined. In the quiescent state, before shear, an isotropic scattering pattern (in the  $x$ - $z$  plane) was observed due to randomly oriented grains of a rod-like microstructure. At low shear rates, the scattering becomes anisotropic, with a set of peaks observed at low scattering angle, normal to flow ( $z$ -direction). Above a critical shear rate, a second set of peaks appeared at a higher scattering angle. The peak positions appeared to be consistent with reflections from the 100 and 110 Bragg planes of a hexagonally packed cylindrical array; however, a more detailed analysis indicated the two sets of peaks were related to two different structures. Upon cessation of shear, the rate of change in the azimuthal broadening of the first set of peaks was faster than the broadening of the second set of peaks. The ratio of intensities of the two sets of peaks also

varied. Two possibilities for the new state have been proposed which are consistent with the scattering results. Transmission electron microscopy (TEM) was the method chosen to try and distinguish between these two models. TEM on samples quenched after shear flow shows two distinct types of grains, with different sizes and packing of cylinders. The morphology of this specimen, made at  $0.585 \text{ s}^{-1}$  and  $100 \text{ }^\circ\text{C}$ , in the "side-view" and "end-view" conditions confirm that the primary structure is a hexagonally packed array of cylinders, with an approximate 100 Bragg plane spacing,  $d_{100} = 22 \pm 3 \text{ nm}$ . A preferred orientation of cylinders is seen, with the 110 planes parallel to the xy-plane of the shear gradient. A secondary structure of small cylinders is also evident, with approximate 100 Bragg plane spacings of  $d_{100} = 12 \pm 2 \text{ nm}$ . This second structure is oriented with the 100 planes parallel to the xy-plane of the shear gradient. To our knowledge, this is the first direct image of a new morphology excited by shear and we believe it is the first observation of two morphologies of this type coexisting.

- **SANS Behavior of Polystyrene/DOP Solutions at High Shear Rates**

A careful examination of the prior SANS data obtained on mixtures of deuterated and protonated polystyrenes in dioctyl phthalate was conducted. In the direction parallel to flow, the scattering at low  $q$  is depressed at low shear rates, relative to the quiescent scattering, then becomes enhanced at higher shear rates. In contrast, the scattering normal to flow remains fairly constant at low shear rates, then becomes enhanced at higher shear rates.

We believe that the near-isotropic increase in the scattering intensity reflects a true shift in the critical temperature instead of an effect due to deformation of concentration fluctuations. Values of the critical temperature,  $T_c$ , were obtained as function of shear rate. The data may be fit to a power law which is different than what has been previously observed in other systems.

To obtain a clearer representation of the degree of anisotropy in the scattering, we examine the quantity,  $1/S_{\parallel}(q) - 1/S_{\perp}(q)$ , where  $S_{\parallel}(q)$  and  $S_{\perp}(q)$  are the sector averaged structure factors parallel and normal to flow respectively. From the

predictions of Onuki and Kawasaki [1],  $1/S_{\parallel}(q) - 1/S_{\perp}(q)$  should scale as  $q^{2/5}$  as  $q$  approaches zero. We observe that the limiting slopes of  $1/S_{\parallel}(q) - 1/S_{\perp}(q)$  plotted versus  $q$  scale as  $q^{\sigma}$ , where the exponent,  $\sigma$ , is a function of shear rate. The value of  $\sigma$  appears to vary between the mode coupling value of  $2/5$  and  $2$ . The shear rate dependence of  $\sigma$  may be fit to the empirical relation:

$$\sigma = 2/5 + 8/5[\dot{\gamma}\tau/(1 + \dot{\gamma}\tau)]$$

where  $\tau$  is a characteristic relaxation time.

For the direction normal to flow, we see that  $S(q, \dot{\gamma}=0) - S_{\perp}(q, \dot{\gamma})$  is invariant for lengths greater than  $1/q^*$ . This result is in contrast to prior results obtained on high molecular weight polymer blends, where  $q^* \propto \dot{\gamma}^{1/3}$ . The observed length scale compares favorably to the so-called Debye length,  $\lambda_D$ , for the polymer molecular weight of our solutions. Using this length and the Stokes relation, a characteristic relaxation time can be calculated, which is consistent with our results.

- **Response of a Liquid Crystalline Polymer to Shear as Studied by Neutron Scattering**

The in-situ scattering profile and rheology of a liquid crystalline polymer under shear flow has been measured at various temperatures and shear rates. A 21 wt% solution of poly( $\gamma$ -benzyl L-glutamate) (PBLG) in deuterated benzyl alcohol (DBA) was sheared at shear rates ranging from  $0.07 \text{ s}^{-1}$  to  $90 \text{ s}^{-1}$  at  $55 \text{ }^\circ\text{C}$ ,  $65 \text{ }^\circ\text{C}$ , and  $75 \text{ }^\circ\text{C}$ . The neutron scattering pattern was collected at  $\lambda=5 \text{ \AA}$  and  $9 \text{ \AA}$  to view the sample on different length scales. Viscosity results demonstrate the shear rate regime that was studied includes the plateau and shear thinning regions (regions II and III in the Onogi and Asada [2] scheme).  $55 \text{ }^\circ\text{C}$  is near the gelation temperature of this system and results demonstrate that at low shear ( $\dot{\gamma} < 0.03 \text{ s}^{-1}$ ) there is an alignment perpendicular to the flow for this temperature. This may be explained by the theoretically predicted mechanism of "log rolling." Further analysis has allowed the correlation of molecular response (alignment) to the shear flow and macroscopic response. We have determined the existence of three regimes. At low shear rates, there is a gradual increase of the alignment of the molecule by the shear field. At intermediate shear rates, the molecule is

generally aligned by the shear with no shear rate dependence on its alignment. Within this regime, the viscosity is Newtonian. At higher shear rates, there is an increase in molecular alignment found with increasing shear rate. This is also the regime where shear thinning is observed in the viscosity. The transition between these three regimes has been correlated to the first two relaxation times of a rodlike polymer in concentrated solution.

## Interfacial Characterization, Modification and Phase Separation with Reaction

### • Structural Stabilization of Phase Separating PC/Polyester Blends Through Interfacial Modification by Transesterification Reaction

Competition between phase separation and transesterification in immiscible polymer blends of polycarbonate (PC) and a copolyester (PET) is studied as a function of time and temperature by DSC and SANS. We found that 1) Global structure coarsens at  $T \leq 200$  °C due to the dominance of phase separation over transesterification and melts at  $T \geq 220$  °C due to the dominance of transesterification at the domain interface. However, transesterification is slow but still significant even at  $T \leq 200$  °C. 2) An intricate balance of transesterification and phase separation rates controls global and interfacial structures. 3) Interfacial structures become measurable under certain conditions, and the interfacial thickness between PC or PET and the copolymers generated by transesterification increases with time. 4) DSC results are consistent with results obtained by SANS, but the latter is more sensitive than the former and differentiates the structural changes at different length scales caused by phase separation and transesterification.

### • Chain Ends and Junction Point Distributions in Ordered Block Copolymer Thin Films

Lamellar ordering in nearly symmetric polystyrene—poly 2 vinyl pyridine (PS-P2VP) block copolymers was examined by neutron reflectivity in thin film geometry. The PS blocks were selectively deuterated at the junction points or at the chain ends to determine their spatial distribution within the lamellar domains. The reflectivity analysis showed the PS-P2VP interface

to be extremely narrow ( $\sim 25$  Å), with the junction points confined to the interfacial region. In contrast, the chain ends exhibit a broader maximum in the center of the domains. Molecular weight dependence of the chain end and junction point distribution, and compatibilizing effects with homopolymers are being investigated.

### • Silica Filled In-Situ Composites

Organic-inorganic interpenetrating networks were synthesized and characterized in an effort to make silica-filled polymeric materials. The samples were made by forming  $\text{SiO}_2$  by hydrolysis of tetraethylorthosilicate and by forming organic polymer by the free radical polymerization of 2-hydroxyethyl acrylate. No solvent was necessary, but the loss of the hydrolysis product, ethanol, caused some shrinkage. Hydrogen fluoride and benzoyl peroxide were used to catalyze the inorganic and organic polymerizations respectively, and samples were made with a range of relative rates of polymerization of the two components.

SANS, SAXS, and TEM were used to characterize the resultant morphology. When the vinyl polymerization was more rapid than the sol-gel reaction, macroscopic phase separation occurred producing a very heterogeneous sample. When the sol-gel polymerization occurred first a very uniform two phase morphology resulted with a characteristic size less than 10 nm. At relative rates between these two extremes, dendritic structures resulted. SANS results were consistent with microscopy, giving power law scattering for the dendritic structures.

## References

- [1] A. Onuki and K. Kawasaki, *Phys.*, **121**, 456 (1979).
- [2] S. Onogi and T. Asada in *Rheology*; G. Asarita, G. Marrucci, and L. Nicolais, eds.; Plenum: New York, 1980, Vol. 3.

## Research Topics

### Thermodynamic Interactions in Model Polyolefin Blends Obtained by Small-Angle Neutron Scattering

N. P. Balsara<sup>1</sup>, D. J. Lohse<sup>1</sup>, W. W. Graessley<sup>9</sup>, and C. C. Han<sup>8</sup>.

**Thermodynamic Interactions and Correlations in Mixtures of Two Homopolymers and a Block Copolymer by Small Angle Neutron Scattering**

N. P. Balsara<sup>1</sup> and C. C. Han<sup>8</sup>.

**Localization of a Homopolymer Dissolved in a Lamellar Structure of a Block Copolymer Studied by Small-Angle Neutron Scattering**

Y. Matsushita<sup>6</sup>, H. Torikai<sup>6</sup>, I. Noda<sup>6</sup>, and C. C. Han<sup>8</sup>.

**Molecular Weight Dependence of Lamellar Domain Spacing of ABC Triblock Copolymers and Their Chain Conformations in Lamellar Domains**

Y. Matsushita<sup>6</sup>, Y. Mogi<sup>6</sup>, I. Noda<sup>6</sup> and C. C. Han<sup>8</sup>.

**Compatibilization Effects of Block Copolymers on Polymer Blends**

A. I. Nakatani<sup>8</sup>, P. Fauvarque<sup>2</sup>, and C. C. Han<sup>8</sup>.

**Conformational Analysis of Cyclic Oligomers**

W. L. Nachlis<sup>8</sup> and C. C. Han<sup>8</sup>.

**Molecular Composites Through Hydrogen Bonding: Rod-like Polymers in Blends**

M. D. Dadmun<sup>8</sup> and C. C. Han<sup>8</sup>.

**Small Angle Neutron Scattering from Dilute Blends of Deuterated Polystyrene in Poly(vinylmethylether) and Protonated Polystyrene**

R. M. Briber<sup>13</sup>, B. J. Bauer<sup>8</sup>, and B. Hammouda<sup>10</sup>.

**Small Angle Neutron Scattering of Independently Crosslinked Blends of Deuterated Polystyrene and Poly(vinylmethylether)**

R. M. Briber<sup>13</sup> and B. J. Bauer<sup>8</sup>.

**Small Angle Neutron Scattering Studies of Dendrimer Solutions**

B. J. Bauer<sup>8</sup>, R. M. Briber<sup>13</sup> and B. Hammouda<sup>10</sup>.

**SANS Studies of Space-Time Organization of Structure in Polymer Blends**

H. Jinnai<sup>3</sup>, T. Hashimoto<sup>3</sup>, H. Hasegawa<sup>3</sup>, and C. C. Han<sup>8</sup>.

**Effect of Initial Thermal Fluctuations on the Time-Resolved SANS Study of the Self-Assembly Processes of DPB/HPB Blends**

H. Jinnai<sup>3</sup>, H. Hasegawa<sup>3</sup>, T. Hashimoto<sup>6</sup>, and C. C. Han<sup>8</sup>.

**Shear-Induced Morphological Structures in Triblock Copolymers**

F. A. Morrison<sup>5</sup>, J. A. Mays<sup>12</sup>, M. Muthukumar<sup>14</sup>, A. I. Nakatani<sup>8</sup>, C. L. Jackson<sup>8</sup>, and C. C. Han<sup>8</sup>.

**SANS Behavior of Polystyrene/DOP Solutions at High Shear Rates**

A. I. Nakatani<sup>8</sup>, J. F. Douglas<sup>8</sup>, and C. C. Han<sup>8</sup>.

**Response of a Liquid Crystalline Polymer to Shear as Studied by Neutron Scattering**

M. D. Dadmun<sup>8</sup> and C. C. Han<sup>8</sup>.

**Structural Stabilization of Phase-Separating PC/Polyester Blends Through Interfacial Modification by Transesterification Reaction**

H. Yoon<sup>8</sup>, Y. Feng<sup>12</sup>, and C. C. Han<sup>8</sup>.

**Phase Separation and Surface Segregation in Binary Polymer Thin Film Blends**

A. Karim<sup>8</sup>, S. K. Kumar<sup>7</sup>, and C. C. Han<sup>8</sup>.

**Chain Ends and Junction Point Distributions in Ordered Block Copolymer Thin Films**

A. Karim<sup>8</sup>, N. Torikai<sup>6</sup>, Y. Matsushita<sup>6</sup>, I. Noda<sup>6</sup>, and C. C. Han<sup>8</sup>.

**Silica Filled In-Situ Composites**

B. J. Bauer<sup>8</sup>, C. L. Jackson<sup>8</sup>, A. I. Nakatani<sup>8</sup>, and C. C. Han<sup>8</sup>, T. Ulibarri<sup>15</sup>.

**Copolymer Effects on the Phase Behavior of Polybutadiene/Polyisoprene Blends**

R. Thudium<sup>16</sup>, A. Haksa<sup>16</sup>, H. Yoon<sup>8</sup>, and C. C. Han<sup>8</sup>.

**Phase Behavior Study of Polystyrene/Polybutadiene/Polystyrene-Polybutadiene Mixtures by SANS**

L. P. Sung<sup>8</sup>, A. I. Nakatani<sup>8</sup>, C. C. Han<sup>8</sup>, G. S. Allen<sup>17</sup>, M. Fair<sup>18</sup>, D. Marr<sup>19</sup>, S. Pearson<sup>20</sup>, and R. Thudium<sup>16</sup>.

**Gelation of Polyvinylchloride in Bulk and in Solution**

M. Fair<sup>18</sup> and C. C. Han<sup>8</sup>.

**Affiliations**

<sup>1</sup>Exxon Research and Engineering Co

<sup>2</sup>G.R.L. Elf Aquitaine, Artix, France

<sup>3</sup>Kyoto University, Japan

<sup>4</sup>Kyoto Institute of Technology, Japan

<sup>5</sup>Michigan Technical University

<sup>6</sup>Nagoya University, Japan



<sup>7</sup>Penn State University

<sup>8</sup>Polymers Division

<sup>9</sup>Princeton University

<sup>10</sup>Reactor Radiation Division

<sup>11</sup>University of Alabama

<sup>12</sup>University of Connecticut

<sup>13</sup>University of Maryland

<sup>14</sup>University of Massachusetts

<sup>15</sup>Sandia National Laboratories

<sup>16</sup>Goodyear Tire and Rubber Corp.

<sup>17</sup>Rohm & Haas

<sup>18</sup>Aristech Chemical Corp. (PA)

<sup>19</sup>Raychem Company (CA)

<sup>20</sup>3M Company (MN)

---

## EXXON SANS RESEARCH AT THE CNRF

Exxon scientists have actively participated in the research at the CNRF during the past year. The NIST/Exxon/University of Minnesota SANS instrument has been fully operational, giving researchers the opportunities to perform many fruitful experiments. Exxon scientists performed experiments studying the microstructures of systems which are both scientifically important and relevant to the corporation's technology needs. Included in this section are short reports describing some of these programs involving systems such as polymer blends, polymer solutions, block copolymers, polymer/surfactant assemblies, polymer micro-emulsion interactions, binary fluids in porous media and their phase behavior, surfactant/micelle/emulsion systems, and asphaltene solutions. Most of them utilized the SANS instrument at the CNRF, some of them are neutron reflectivity (NR) experiments. Exxon scientists have also started exploratory experiments on neutron radiography/tomography involving hydrocarbon systems.

### Polymers

#### • Structure of Diblock Copolymer Aggregates in Solution

The aggregation phenomena and the structure of the aggregates of a series of anionically prepared diblock copolymers in selective solvents were studied by SANS. The diblock copolymers of interest were poly(ethylene-ethylene propylene) (PE-PEP) as well as poly(styrene-isoprene) (PS-PI) with various ratios of diblock molecular weights. Combinations of deuterium labeling were synthesized to aid proper index matching for structure determination. The solvents were composed of a mixture of decane and deuterated decane to achieve the desired contrast conditions. For the PS-PI in

decane system, we found spherical aggregates with very narrow size distributions. The aggregation number depends on the temperature and composition. The minimum polymer concentration for which micelle can be formed (CMC) is about 10 ppm at room temperature for the 10 K/7.5 K molecular weight PS/PI system. At higher concentrations (> 1% wt/wt), the aggregation number (as determined by the low angle extrapolation) is a strong function of the temperature. It was found that the aggregation number reaches an apparent plateau of 125 below 15 °C, and decreases almost linearly towards the dissociation temperature of 65 °C. At higher concentrations, an ordered phase was observed. At concentrations above the over-lap concentration, a crystalline phase was also seen. The type of crystal structure depends on the core-to-corona ratio. We also found by SANS that these polymeric micelles are capable of solubilizing PS homopolymers (the nonsoluble phase in decane) in the core similar to the way surfactant micelles form microemulsions. The swollen polymeric micelles appear to retain the micellar aggregation number of the diblock copolymers. This allows us to vary the "grafting density" of PI on the PS droplet in a continuous way. Our neutron spin echo study of the PI dynamics using de Gennes' elastic model can now be further tested as the predicted cubic dependence of the relaxation time as a function of the grafting density.

Systematic study of PE-PEP system yield the PE platelet thickness as a function of the PE molecular weight (weak dependence) and the molecular weight ratio of PE/PEP (strong dependence). It has also been found that the PE-PEP platelet aggregate (formed in decane at room temperature) could solubilize a limited amount of

PE (the nonsoluble phase). The thickness of the platelet (the PE) phase does not seem to be much affected by the addition of homopolymer.

- **Thermodynamics of Random Copolymer Mixtures**

Blends of polyolefins are important items of commerce. Despite this commercial importance, very little work has been done to directly determine the thermodynamics of mixing in such blends. There has been some neutron scattering on polyolefin blends, including those of polypropylene and polyethylene, those of various forms of polyethylene, and those of polypropylene and ethylene-propylene copolymer. The lack of basic data on the thermodynamics of polyolefin mixtures proceeds from two basic causes: the complications due to crystallization for blends in the solid state, and the similarities in physical properties (density, refractive index) between these materials in the melt. Both factors make it difficult to determine miscibility and interactions at any temperature. This is an unfortunate state of affairs, as one might expect that many polyolefin blends of commercial interest are near phase transitions as they are commonly used. Since there are no strong, specific interactions between these saturated hydrocarbon polymers, they will not be completely miscible over all ranges of temperature, composition, molecular weight, etc. On the other hand, since the dispersive forces between them are so weak (very small unfavorable enthalpy of mixing), it should be possible to find regions of composition and temperature where the blends of high molecular weight polyolefins are single phase, that is, where even the small entropy of mixing is enough to offset the enthalpy of mixing. From a scientific point of view, the simplicity of their interactions means that polyolefin blends are also of interest as models for polymer blends in general. Developing such an understanding of the miscibility of the polyolefins should have a number of technological implications in terms of the processability and properties of these materials.

In the work described here, the miscibility of random copolymers of ethylene and butene with each other has been examined. These polymers have been made by the hydrogenation of polybutadienes with a range of vinyl content. Since the saturation can be done with either hydrogen or

deuterium, we have been able to obtain precisely matched versions of each polymer in the study, differing only in labeling. The availability of these polymers also allows for a test of the theory of random copolymer miscibility. It was found that the standard random copolymer theory does not describe the data in that the interaction parameters were not proportional to the square of the difference in the compositions of the component copolymers. Rather, blends of ethylene rich copolymers had lower  $\chi$  values than corresponding butene rich blends. From this work a catalogue of solubility parameters ( $\delta$ ) can be derived by using the Hildebrand formulation of the interaction parameters and a knowledge of how deuteration affects the solubility parameter.

- **Microphase Separation in a Model Graft Copolymer**

The interfacial properties of block copolymers are of great interest because of their widespread use as compatibilizers in the production of polymer blends. In this application, their presence at the interface between incompatible polymers lowers the surface energy and thus stabilizes the mixture against phase separation. Random copolymers and graft copolymers are the most often used copolymer structures. While fundamental experimental studies have almost exclusively focused on the more tractable diblock copolymers, we expect that a study of the interfacial and phase behavior of the more complicated, yet technologically more important, graft copolymer would yield new and useful information.

The model graft copolymer we study consists of an elastomeric backbone of poly(ethyl acrylate) (PEA) with pendant monodisperse thermoplastic grafts of polystyrene (PS). Both SANS and neutron reflectivity (NR) experiments were performed to study the bulk and interfacial properties of the graft copolymer with different grafting ratio. In both studies, the PEA molecules were partially deuterated to increase the contrast between the two components of the graft copolymer. For the SANS study, 0.5 mm thick films of the copolymers were used. The films were formed in a conventional press and heated to 130 °C for 3 min. They were then either quickly quenched to room temperature, or annealed at 100 °C for 24 hr. All three samples (9%, 28%, and 48% PS

contents by weight) showed some degree of microphase separation of the PS grafts from the PEA backbones, evidenced by a broad peak in the scattering curve. The effect of annealing was to increase the apparent microphase ordering. As uniaxial strain is applied to the film samples by stretching them using a stretching device, the samples showed either conventional (i.e., affine deformation, for 9% and 48% samples) or anomalous ("butterfly" isointensity patterns, for 28% sample). In NR experiments, we observed evidence for periodic structure in all three samples (about 1500 Å thick) spin coated on silicon substrates, but it is exhibited most strongly in the 28% PS sample, which we believe to have a lamellar structure and is confirmed by transmission electron microscopy. This periodicity also perfected itself as the samples were annealed.

### ● Conducting Polymers

A series of neutron scattering measurements were performed on solutions of metallic and semi-conducting forms of polyaniline in three different organic solvents: dimethylsulfoxide (DMSO), N-methylpyrrolidinone (NMP), and p-cresol. The solubility of polyaniline in these solvents is greatly enhanced by the addition of protonic surfactants such as camphor sulfonic acid (CSA); the surfactant dopes the semiconductor to a metal by protonating the backbone and the aliphatic counterion associates with the charged chains via Coulomb attraction. The goal of the measurements was to determine the molecular weight of polyaniline in solution and to study the conformation of the polymer as a function of solvent properties and concentration of the solubilizing side-chains. Since the solutions are polyelectrolytes, the effects of passive salts on the conformation of the chains were also studied. The data can be fit to a Debye function to obtain an estimate of the radius of gyration; from these data we obtain  $R_g = 215 \text{ \AA}$ . Somewhat larger estimates of  $R_g$  were obtained from scattering measurements on undoped polyaniline in NMP. The effect of adding salt to the solutions of polyaniline was also studied. In DMSO, the addition of salt greatly increased the apparent radius of gyration. This may indicate that adding salt causes aggregation in these solutions. By contrast, in NMP, adding salt

seemed to cause a partial collapse of the polymer chains.

### ● Blends of Amorphous-Crystalline Block Copolymers with Amorphous Homopolymers

We have recently been examining polymers with an amorphous polypropylene (PP) block and a semicrystalline polyethylene-like (PE) block, as well as blends of these with PP homopolymer. The amount and molecular weight of the added homopolymer has been shown to have a large effect on the crystallization kinetics and room-temperature morphology of the mixtures, and by rheology it has been seen that these are microphase separated well into the melt region. In this work we performed SANS experiments to study the structure of the block polymer both below and above the melting point, and to see how this is modified by the addition of homopolymer.

The polymers studied here have been made by the hydrogenation of anionically polymerized polydienes. Saturation of low vinyl polybutadienes results in an analog of an ethylene-butene copolymer with around 3 mole % butene. This is close to the composition of linear low density polyethylene, and we will designate this as PE. Similarly, hydrogenation of poly(2-methyl-1,3-pentadiene) gives an atactic polypropylene (PP). The PE-PP diblock copolymers used here (DEP) were made by hydrogenating a block polymer of butadiene (PBd) and methyl pentadiene. The characteristics of the polymers used are listed in the following table:

Sample	wt%	M <sub>n</sub> (x10 <sup>3</sup> )	M <sub>w</sub> (x10 <sup>3</sup> )
dDEP65	51.5	60.6	64.8
hDEP61	50.3	58.4	61.3
APP15	0	14.4	15.1

where  $M_n$  and  $M_w$  are number-averaged and weight-averaged molecular weights, respectively. The first diblock, dDEP65, has a partially deuterated PE block in that perdeutero butadiene was used as the monomer for its synthesis. The last polymer in the list is a PP homopolymer with a low enough molecular weight to mix well with the PP block of the DEPs. These blends were made by dissolving both the block polymer and the homopolymer in xylene, followed by precipitation into methanol.

Since the diblocks are nearly symmetric in composition, lamellar morphology was expected and indeed seen by microscopy. In order to measure the lamellar spacing and other morphological parameters by scattering, it is important to produce samples with a preferred orientation of the lamellae. We produced well oriented samples, which we examined perpendicular to the lamellar planes as well as parallel to them.

The SANS results gave a lamellar spacing at room temperature of about 52 nm for dDEP65. The values of the spacing as well as those of other morphological variables can be found by fitting the data with a model. Three orders of peaks could be distinguished in the scattering patterns. Addition of APP15 increased this value slightly in line with the amount added. With the SANS we could watch how this changed with heating. Up to 75 °C (still below  $T_m$ ), there was very little change in the spacing. At 110 °C, however, the peaks moved to higher angles, indicating a shrinkage of the spacing to around 47 nm. Moreover, five orders could be seen, indicating a more uniform distribution of the spacing. The perpendicular-view scattering can be used to determine the interfacial thickness between the lamellae. Just as in the parallel-view results discussed above, the most dramatic change occurred when the samples melted. At this point the thickness dropped from 6.0 to 1.8 nm. This is in line with the observation of more orders described above.

## Fluids and Microemulsions

### ● Phase Separation of Binary Fluids in Confined Geometry

SANS experiments were performed to measure the structure factor for a binary fluid, water/lutidine, imbibed inside porous Vycor glass (porosity 31%, average pore size 70 Å). Previous results have been reported that random field Ising behavior was observed in such a system, as proposed by the random field Ising model (RFIM). However, our measurements performed at concentrations both near and away from the critical point showed similar results, which do not agree with the RFIM.

The experiments were performed under the condition that the global concentration inside Vycor is such that the scattering length density of the

fluid mixture matches that of the solid part of Vycor. In the one phase region below the critical temperature, the scattering was about two orders of magnitude lower than that from a dry Vycor. However, a small peak existed at a  $Q$  (scattering wavevector) value larger than the Vycor peak position. This small peak is due to a lutidine-rich wetting layer coated on the internal surfaces of the porous Vycor, and it is confirmed by an independent experiment in which we purposely coated the internal surfaces with alkylsiloxane molecules having contrast with Vycor, and filled the rest of the pore spaces with hexane/deuterated hexane mixture matching the scattering density of Vycor.

The scattering above the bulk critical temperature into the two phase region can be fitted with two major components: one describes random one-phase rich domains, the other describes (lutidine-rich) wetting layers on the internal surfaces of the porous glass. Both components grow with increasing temperature. However, the size of the domains stops growing at a value close to the average size of the pores. As a result, the phase separation never becomes macroscopic. This result seems to agree well with a model based on pore confinement of the imbibed fluid mixture. The experimental results suggest that in a porous medium such as Vycor, where the pore size is relatively narrowly distributed, the main effect on the fluid mixture is confinement. The fact that the size of the random domains never exceeds the size of an average pore suggests that the fluid mixture does not sense the randomness of the porous medium, therefore, the random field Ising behavior is not expected.

### ● Polymers in Microemulsion

SANS has been used to study the structure of a complex system of a polymer in a microemulsion cavity and the interaction between the various components in the system. Microemulsion polymerization is used to obtain monodispersed high molecular weight colloidal polymer particles with the smallest possible radius, which are of significant technological importance. The interaction between the polymer and the microemulsion droplets determines the physical properties of the system which may differ from those of the microemulsion itself. The properties of the polymer may be also affected by the confinement in the

droplet. Acryl amid is synthesized in a radical polymerization by irradiating the monomers ( $\gamma$ -Cs<sup>137</sup> at 600 rad/min 5-20 min) in a matrix of water in oil/AOT (surfactant) microemulsion system. Both heptane and toluene are used as oil. Two types of polymers are formed, linear and crosslinked. Specific labeling of the various components allows selective study of the polymer itself, the AOT shell of the microemulsion droplet and the water-polymer core. We found that the microemulsion-polymer complex is very different from the parent microemulsion. Basically, without the monomer present, the system phase separates to oil and water phases. When adding acryl amide monomers small micelles of about 20 Å diameter are formed. Polymerization of the monomer leads to stable microemulsion droplets with a radius varying from 100 to 200 Å depending on the composition of the system. Both the linear polymer and the crosslinked one are inside the microemulsion droplets; however there is an exchange process of the water and the polymer between different droplets. During the polymerization process the droplets increase in size to accommodate the polymer.

### Neutron Tomography/Radiography

The 3D study of fluid transport in porous media with ~20 micron spatial resolution is the goal of this exploratory effort. We had previously constructed an x-ray microtomography/radiography system to study the 1-30 micron scales, i.e., large pore geometry and pore connectivity. Our current plan is to use cold neutron radiography/tomography to measure 3D fluid distributions with 20-100 micron resolution in 1-2 cm sized specimens. The contrast mechanism makes neutrons well suited to this application. Results reported by other workers show promise but did not demonstrate sufficient spatial or opacity resolution for our work. We have constructed a 2D CCD-based position-sensitive neutron detector, and have tested it at both CT-W and at the NG7-30M SANS instrument positions. The detector is a modification of the x-ray detector that has demonstrated ~1 micron resolution at Brookhaven National Laboratory's National Synchrotron Light Source. Background radiation levels at CT-W inside the Reactor Building would require extensive

shielding of the detector for successful tomographic reconstruction. The much lower background in the guide hall combined with coincidence filtering of the radiography data has allowed the detector to operate unshielded. A 1 cm diameter test specimen has been scanned and reconstructed at ~60 micron spatial resolution (see Fig. 1). In the configuration tested the statistical accuracy of the detector is neutron flux limited, and it takes about 12 hr to complete a full scan for such a tomography reconstruction at current neutron flux conditions. Flux improvement after the reactor shutdown in 1994 is expected to shorten the time considerably. Continued development will address the maximum spatial resolution of the detector and the rejection of isotropic scattering from specimens.



**Figure 1.** The image shown in the picture is a volume raytrace of a 3D (200 x 200 x 150) map of the neutron cross section of a regular BNC connector using our neutron tomography scanner. The scan was obtained at the NG7-SANS sample position with a wavelength of 5 Å, 30% resolution and all 8 guides in.

### Research Topics

#### Diblock Copolymer Aggregates in Solution

J. S. Huang<sup>4</sup>, L. J. Fetters<sup>4</sup>, S.-L. Chang<sup>13</sup>, D. Perahia<sup>4</sup>, M. Y. Lin<sup>4</sup>, A. P. Gast<sup>13</sup>, G. McConnell<sup>13</sup>, E. Lin<sup>13</sup>, D. Richter<sup>6</sup>, L. Willner<sup>6</sup>, and D. Schneiders<sup>6</sup>.

#### Graft Copolymers

D. G. Peiffer<sup>4</sup>, W. Dozier<sup>1</sup>, and M. Y. Lin<sup>4</sup>.

#### Polymers in Microemulsion

J. S. Huang<sup>4</sup>, D. Perahia<sup>4</sup>, M. Y. Lin<sup>4</sup>, R. G. Wilk<sup>3</sup>, R. E. Stefandl<sup>3</sup>, and C. Gryte<sup>3</sup>.

### Emulsion Interfacial Structure

X.-Z. Wu<sup>4</sup>, M. Y. Lin<sup>4</sup>, D. A. Weitz<sup>4</sup>, and S. K. Sinha<sup>4</sup>.

### Worm-like Micelles Under Shear

M. Y. Lin<sup>4</sup>, M.-W. Kim<sup>4</sup>, S. K. Sinha<sup>4</sup>, D. G. Peiffer<sup>4</sup>, H. Hanley<sup>8</sup>, and G. Straty<sup>8</sup>.

### Self-associating Polymers

D. G. Peiffer<sup>4</sup>, M. Y. Lin<sup>4</sup>, A. Timbo<sup>5</sup>, J. S. Higgins<sup>5</sup>.

### Surface-derivatized Porous Vycor

M. Y. Lin<sup>4</sup>, J. M. Drake<sup>4</sup>, and S. K. Sinha<sup>4</sup>.

### Crystalline-amorphous Diblock Copolymers

D. J. Lohse<sup>4</sup>, K. Sakurai<sup>17</sup>, M. Agamalyan<sup>2</sup>, and M. Y. Lin<sup>4</sup>.

### Polyaniline Solutions

D. J. Pine<sup>4</sup>, C. Gettinger<sup>16</sup>, and J. S. Huang<sup>4</sup>.

### Asphatene Solutions

M. Y. Lin<sup>4</sup>, S. K. Sinha<sup>4</sup>, and E. Herbolzheimer<sup>4</sup>.

### Binary Fluids in Silica Gel

B. J. Frisken<sup>12</sup>, M. Y. Lin<sup>4</sup>, D. S. Cannell<sup>16</sup>, and S. K. Sinha<sup>4</sup>.

### Thermodynamics of Random Copolymer Mixtures

D. J. Lohse<sup>4</sup>, N. P. Balsara<sup>9</sup>, L. J. Fetters<sup>4</sup>, D. N. Schulz<sup>4</sup>, J. A. Sissano<sup>4</sup>, W. W. Graessley<sup>10</sup>, and R. Krishnamoorti<sup>10</sup>.

### Proprietary Polymer Research

A. Hanyu<sup>4</sup>, and F. Stehling<sup>4</sup>.

### Neutron Tomography/Radiography

J. H. Dunsmuir<sup>4</sup>, M. Y. Lin<sup>4</sup>, and S. K. Sinha<sup>4</sup>.

### Polymer/Surfactant Layers Near a Liquid Surface

S. K. Sinha<sup>4</sup>, K. Chari<sup>7</sup>, S. K. Satija<sup>11</sup>, M. Y. Lin<sup>4</sup>, P. D. Gallagher<sup>11</sup>, and A. Karim<sup>11</sup>.

### Neutron Reflectivity From Polymer on Surfaces

D. Perahia<sup>4</sup>, L. J. Fetters<sup>4</sup>, S. K. Sinha<sup>4</sup>, S. K. Satija<sup>11</sup>, and D. G. Wiesler<sup>11</sup>.

### Neutron Waveguides

Y.-P. Feng<sup>4</sup>, S. K. Sinha<sup>4</sup>, H. Zhang<sup>15</sup>, and C. F. Majkrzak<sup>11</sup>.

### Affiliations

<sup>1</sup>Argonne National Laboratory

<sup>2</sup>Brookhaven National Laboratory

<sup>3</sup>Columbia University

<sup>4</sup>Exxon Research & Engineering Co.  
and other Exxon affiliates

<sup>5</sup>Imperial College, U.K.

<sup>6</sup>KFA, Germany

<sup>7</sup>Kodak

<sup>8</sup>Thermophysics Division, NIST Boulder

<sup>9</sup>Polytechnic University

<sup>10</sup>Princeton University

<sup>11</sup>Reactor Radiation Division

<sup>12</sup>Simon Fraser University

<sup>13</sup>Stanford University

<sup>14</sup>Tsinghua University, Taiwan

<sup>15</sup>University of Maryland

<sup>16</sup>University of California (S.B.)

<sup>17</sup>University of Massachusetts (Amherst)

---

## UNIVERSITY OF MINNESOTA PROGRAMS

The University of Minnesota, through its Center for Interfacial Engineering, is a member of the CNRF's participating research teams (PRT) in small angle neutron scattering (SANS) (with NIST and the Exxon Research and Engineering Co.) and reflectometry (with NIST and IBM).

### SANS

- **Block Copolymer Phase Behavior Near the Order-Disorder Transition**

A comprehensive program has been established to investigate the equilibrium phase behavior of block copolymers in the vicinity of the order-disorder transition. This program combines three areas of experimentation: synthesis of model materials, rheological testing, and small angle neutron scattering. During the past year we have expanded the materials base in this effort to

include eight chemically distinct compounds. In each case, the polymers are prepared by anionic polymerization, and where applicable, catalytic hydrogenation. This affords us control over the location and amount of deuteration, which provides the necessary neutron contrast. Overall, we have prepared more than 70 polyolefin diblock copolymers (PEP-PEE, PE-PEP, PE-PEE, PE-VCH, PEE-PVCH, PEP-PVCH where PE, PEP, PEE and PVCH refer to poly(ethylene), poly ethylenepylene), poly(ethylethylene), and poly(vinylcyclohexane), respectively), and 10 poly(styrene)-poly(vinylpyridine) (PS-PVP) specimens. A cohesive picture has emerged from extensive SANS experimentation on these materials. Two new factors, fluctuations and conformational asymmetry, that are not included in the mean-field theories, have been shown to be critically important in this class of amphiphilic compounds. Our studies have led to the identification of two new complex layered phases, hexagonally modulated lamellae (HML) and hexagonally perforated lamellae (HPL), and we have shown that the occurrence of these states is coupled to the conformational properties of each block. Fluctuation effects have been demonstrated to drive the development of cubic phases, notably the ordered bicontinuous double diamond (OBDD) phase. By increasing the molecular weight of the block copolymer, we have been able to eliminate the occurrence of cubic phases in the phase diagram. Overall, this work has led to a qualitatively different understanding of block copolymer phase behavior, and has demonstrated the gross deficiencies of the classical mean-field theories near the order-disorder transition.

- **Influence of Shear on Block Copolymer Melts**

During the past year we have finished development of a general purpose solids shearing device, and placed it in operation at the 30 meter SANS instrument. This machine allows the user to perform reciprocating steady shear deformation on polymer specimens (or other soft solids) that can range in thickness from about 0.1 to 5 mm, and with strain amplitudes that extend from roughly 50 to 1000%. The shear rate can be adjusted over four-orders of magnitude while maintaining the sample temperature between 20

and 250 °C with a precision of about 1 °C. Primary use of this instrument by the Minnesota group has been with block copolymer melts. A variety of experiments have been conducted on model polyolefins that explore the shear-rate dependence of the order-disorder transition temperature, and the response of different ordered microstructures to a hydrodynamic field. Lamellae, cylinders, spheres, modulated layered, and bicontinuous microstructures have been subjected to shear deformation while concurrently being examined by SANS. Each of these microstructures exhibits a unique frequency dependent behavior, leading to domain orientation in some cases, and shear induced phase transitions in others. This knowledge will provide the basis for developing processing schemes that exploit the unique, and potentially anisotropic, properties of block copolymers. The shear device has also been used to prepare and characterize specimens of poly(styrene)-poly(isoprene) diblock copolymers with specific domain orientations that were then used in a study of polymer diffusion in ordered media.

- **Microstructure and Aggregation Behavior of Novel Glycerol-based Surfactants in Dilute Aqueous Solutions**

Surfactants in water at low concentration form micelles, vesicles, and other dispersion aggregates. The parameters that control the shape and size of these aggregates are sometimes poorly understood. In this program we are exploring the aqueous microstructures of several novel glycerol-based surfactants with polyoxyethylene head groups ( $E_n$ ) of different sizes ( $E_5$ ,  $E_8$ ,  $E_{18}$ ). Experiments have focused on exploiting the scattering form factor of dilute surfactant solutions, which relates directly to the size and shape of surfactant aggregates. Although these surfactants have a branched conformation, the SANS result reveals that in dilute aqueous solutions, the surfactant with  $E_5$  head group forms bilayers or vesicles while those with  $E_8$  or  $E_{18}$  head groups form rod-like micelles and spherical micelles, respectively.

- **Microstructure of Siloxane 'Superspreader' Surfactants in Dilute Aqueous Solutions**

Some siloxane surfactants can facilitate water spreading on certain hydrophobic surfaces such as

polyethylene film, which other types of surfactants do not wet. Our experimental evidence has shown that the surfactant microstructure in dilute aqueous solution is related to this unique 'superspreading' ability of these siloxane surfactants. SANS results show that these siloxane 'superspreaders' surfactants form planar microstructures such as vesicles and bilayer pieces. One of the surfactants formed a lamellar liquid crystal with a large inter-bilayer distance on the order of  $10^3$  Å concentration below 1 wt%. The derived surfactant bilayer thickness for this surfactant is consistent with the molecular dimensions. The bilayer dispersion formed by these siloxane 'superspreaders' surfactants may play an important role in facilitating spreading. Siloxane surfactants that form micelles in dilute solutions do not perform as 'superspreaders'.

## Reflectometry

- **Surface Segregation**

Recent synthetic efforts in our laboratory have dealt with the hydrogenation of polystyrene (PS) to produce poly(vinylcyclohexane) (PVCH), a saturated polyolefin with a glass transition 40 degrees higher than PS. This methodology has been successfully used to hydrogenate poly(styrene)-1,2 poly(butadiene) to poly(vinylcyclohexane)-poly(ethylene)(PVCH-PEE) and Poly(styrene)-1,4 poly(butadiene) to poly(vinylcyclohexane)-poly(ethylene) (PVCH-PE). These materials are important from the perspective of examining the relative importance of enthalpic and entropic forces for surface segregation, since PVCH has a higher cohesive energy density than other saturated dienes but has a coil size (for equal molecular weight) similar to PEE and significantly smaller than PE. For a symmetric 50 k PVCH-PEE diblock, neutron reflection shows us that PEE is the surface active component, while for a symmetric 14 k PVCH-PE diblock, PVCH is the surface active species. We interpret this result as segregation driven by local packing entropy for the PVCH-PEE system and by long range conformational entropy for the PVCH-PE system.

- **Influence of Surfaces and Finite Film Thickness on Block Copolymer Morphology**

The focus of this project is to determine the influence of film thickness on block copolymer morphologies (e.g., lamellae, hexagonal rods and BCC spheres) and to assess the capability of the surface to induce uniform order inside the film. The symmetric polymers readily self-assemble (above  $T_g$ ) into lamellar structures driven by the preferential segregation of one of the components to the two surfaces. On the other hand asymmetric copolymers with non-lamellar morphologies do not easily order. Rod forming systems that are hexagonally packed in the bulk, require annealing above the order-disorder transition to create registry between the surfaces and the ordered microstructure. In a preliminary investigation of a system that forms BCC spheres in bulk, coordination of the cubic structure with the surfaces was never observed. This result indicates the limitation of the surface field in uniformly ordering morphologies that do not conform with the surfaces. At certain compositions bulk polyolefin diblock copolymers exhibit order-order transitions. In order to evaluate the influence of finite film thickness on these transitions we have examined films with ~25 bilayers, 5 bilayers, and 3 bilayers. In the thickest film we managed to reproduce the bulk phase behavior. The same transitions could be obtained in the intermediate thickness film during the heating cycle, but on cooling the system did not revert back to the initial state. However, the thinnest film did not show any phase transitions. This study is a classic example of the influence of reduced dimensionality on phase transitions. Analogous examples of the influence of film thickness can be found in the liquid crystal literature. Confinement effects have also been studied by depositing a thick Ge layer on top of a block copolymer film that resided on a Si wafer.

- **Block Copolymer Mixtures in Thin Films**

The main goals of this project are to understand the influence of polydispersity on block copolymer morphology and to obtain individual chain density profiles of the short and the long chains in a bimodal mixture. Blends of symmetric copolymers ( $f = 0.55$ ) which form lamellar micro-



structures have been studied. The first important question is whether these copolymers are mixed at a microscopic level or whether macroscopic phase separation occurs. Our results indicate microscopic mixing. This has been concluded from the results of a mixture containing 10% deuterated polymer blended with 90% protonated polymer. The presence of Bragg peaks in the reflectivity clearly indicates an equal distribution of the deuterated component in all the layers. Furthermore, by selective deuteration we have managed to extract individual segment density profiles for bimodal mixtures. Our results show that the longer chains stretch into the center of the domain while the shorter chains are confined close to the interface. Preliminary analysis indicates a complex variation of the domain spacing with volume fraction.

## Research Topics

### Phase Behavior of Poly(ethylene)-Poly (ethylene-propylene) Diblock Copolymers

J. H. Rosedale<sup>5</sup>, K. Almdal<sup>4</sup>, K. Mortensen<sup>4</sup>, and F. S. Bates<sup>5</sup>.

### Structure of Hexagonal Mesophases between Lamellae and Cylinders

I. W. Hamley<sup>5</sup>, J. H. Rosedale<sup>5</sup>, K. A. Koppi<sup>5</sup>, F. S. Bates<sup>5</sup>, K. Almdal<sup>4</sup>, K. Mortensen<sup>4</sup>, M. F. Schulz<sup>5</sup>, and A. K. Khandpur<sup>5</sup>.

### Influence of Dynamic Shear on the BCC Sphere Phase in a Block Copolymer Melt

K. A. Koppi<sup>5</sup>, F. S. Bates<sup>5</sup>, K. Almdal<sup>4</sup>, and K. Mortensen<sup>4</sup>.

### Ordered Phase Structure of Poly(vinylcyclohexane) Based Diblock Copolymers

M. D. Gehlsen<sup>5</sup> and F. S. Bates<sup>5</sup>.

### Shear-rate Dependence of the Lamellar-to-Disorder Transition in Model Polyolefin Diblock Copolymers

K. A. Koppi<sup>5</sup>, T. Tepe<sup>5</sup>, M. Tirrell<sup>5</sup>, and F. S. Bates<sup>5</sup>.

### Solution Structure of Hydrophobically Modified Polyelectrolytes

P. Guenoun<sup>5</sup> and M. Tirrell<sup>5</sup>.

### Shear Orientation of PS-PI Diblock Copolymers for Diffusion Measurements

M. Hamersky<sup>5</sup>, T. Lodge<sup>5</sup>, and M. Tirrell<sup>5</sup>.

### SANS from Polyoxyethylene-trisiloxane Surfactants in Aqueous Solution

M. He<sup>5</sup>, R. M. Hill<sup>1</sup>, L. E. Scriven<sup>5</sup>, and H. T. Davis<sup>5</sup>.

### Aggregation in Glycerol Based Surfactants with Varying Head Group Size

M. He<sup>5</sup>, X. Li<sup>5</sup>, H. T. Davis<sup>5</sup>, and L. E. Scriven<sup>5</sup>.

### Entropy-Driven Surface Segregation in Block Copolymer Melts

M. Sikka<sup>5</sup>, N. Singh<sup>5</sup>, N. Koneripalli<sup>5</sup>, A. Karim<sup>2</sup>, F. S. Bates<sup>5</sup>, and S. K. Satija<sup>3</sup>.

### Influence of Proximity to Surfaces on Classical Block Copolymer Morphologies

N. Singh<sup>5</sup>, M. Sikka<sup>5</sup>, N. Koneripalli<sup>5</sup>, A. Kudrle<sup>5</sup>, F. S. Bates<sup>5</sup>, S. K. Satija<sup>3</sup>, and A. Karim<sup>2</sup>.

### Influence of Finite Film Thickness on Phase Transitions in Block Copolymer Films

N. Singh<sup>5</sup>, I. W. Hamley<sup>5</sup>, M. Sikka<sup>5</sup>, F. S. Bates<sup>5</sup>, A. Karim<sup>2</sup>, S. K. Satija<sup>3</sup>, and C. F. Majkrzak<sup>3</sup>.

### Block Copolymer Mixtures in Thin Films

N. Singh<sup>5</sup>, N. Koneripalli<sup>5</sup>, M. Tirrell<sup>5</sup>, F. S. Bates<sup>5</sup>, S. K. Satija<sup>3</sup>, and A. Karim<sup>2</sup>.

### Confined Block Copolymers

N. Koneripalli<sup>5</sup>, N. Singh<sup>5</sup>, M. Sikka<sup>5</sup>, F. S. Bates<sup>5</sup>, and S. K. Satija<sup>3</sup>.

## Affiliations

<sup>1</sup>Dow Corning

<sup>2</sup>Polymers Division, NIST

<sup>3</sup>Reactor Radiation Division, NIST

<sup>4</sup>Risø National Lab., Denmark

<sup>5</sup>University of Minnesota

## CNRF INSTRUMENTATION DEVELOPMENT

FY93 saw very significant progress made in a broad spectrum of CNRF instrumentation. This includes the commencement of full operation of the cold neutron reflectometer and medium resolution time-of-flight spectrometer (TOF), and installation and testing of parts of the high-resolution TOF spectrometer. Significant progress in the development of neutron capillary guides has continued along with important developments in a number of other areas.

Instrumentation related to Fundamental Neutron Physics and to prompt-gamma activation analysis and cold neutron depth profiling is described elsewhere in this report.

### New Instruments

- **The NIST/IBM/U. Minn Neutron Reflectometer**

A neutron reflectivity program using the BT-7 thermal neutron reflectometer has already been highly successful. From this, methods and techniques were developed to be used in the new cold neutron reflectometer installation of which has been completed in the guide hall. In terms of measuring absolute reflectivity the performance of the instrument is already comparable to the BT-7 reflectometer, with additional improvements yet to come. The horizontal sample geometry of the new instrument has, as planned, been successfully utilized for studying liquid-air interfaces, which is not practical on the BT-7 instrument. The low background of the guide hall has permitted the use of a position-sensitive detector for grazing-angle neutron diffraction measurements.

- **The Medium-Resolution Time-of-Flight Spectrometer**

The medium-resolution Time-of-Flight (TOF) Spectrometer on the NG-6 guide is fully operational. The allocation of beam time through the Program Advisory Committee officially commenced in March 1993. During the past year, progress has been made in several areas. Improvements in shielding have resulted in a further reduction of the detector background count-rates. Design and construction of a new 128-input TOF interface between the data acquisition system

and the detectors is nearing completion. This will allow full separation of the signals from the 107 TOF detectors, thus eliminating the present necessity of detector pairing. Also, we have been able to match better the enlarged horizontal mosaics (~50') afforded by the double-layered monochromators by constructing and utilizing a new Fermi chopper, operational in the 0.4-0.6 nm wavelength range, with 80' collimation instead of the 40' collimation previously available. Using the new chopper without the 60' collimator between the monochromators results in intensity gains of 3-3.5 over the 40' choppers for the same resolution. In the coming year, we anticipate making further improvements in both detector background and beam intensity.

- **Multiple-Disk Chopper Time-of-Flight Spectrometer**

This instrument will use a set of chopper disks, and a partitioned guide, to produce pulses of neutrons of a single wavelength at the sample position. The first and last chopper pairs determine the incident wavelength and the three intermediate choppers remove contaminant wavelengths and unwanted pulses [1]. There are three slots in each of the disks belonging to the first and last counter-rotating chopper pairs. By appropriately phasing these disks the resolution of the instrument can be changed, without having to change the incident wavelength or the speed of the choppers. The sample chamber will accept a variety of cryostats or furnaces, providing the capability to locate the sample at the correct position and in the desired orientation. Detectors will be placed 4 meters from the sample, in three parallel banks. Their total active area will be about 10 m<sup>2</sup>.

The complete chopper system was delivered in May. It comprises four vacuum housings, seven motor/bearing assemblies and disks, a VME-based chopper control system, and a PC. Installation and detailed acceptance tests were successfully completed in June. At 20,000 rpm the measured phase stability of the choppers, under several different phasing conditions, was consistently < 83 ns (i.e. < 0.01°) standard deviation. A VAX 4000 has been programmed to control the

choppers via the PC. A number of safety features have been incorporated into the control system. In particular, pressures in the chopper housings are continuously monitored, and a high pressure condition in any housing initiates a complete shutdown, either through software or directly through the chopper control hardware if the VAX is not operating.

The guide, including an optical filter to remove high energy radiation, will be delivered in early 1994. There has been progress in the design of shielding, the sample chamber, the flight chamber, and an oscillating radial collimator (ORC). The ORC spans  $170^\circ$  of arc with blades at  $2^\circ$  intervals, and it will probably be made using 0.1 mm polyester blades coated with  $Gd_2O_3$ . We have developed theoretical analyses and performed numerical calculations of the transmission properties of (i) neutron optical filters and (ii) oscillating radial collimators; this work has been written up for publication.

As of October 1993 we received 119 detectors and 112 amplifiers from the manufacturer; we expect to receive 50 detectors and 50 amplifiers each month until the order (presently 740 detectors and 740 amplifiers) is complete. Following delivery all units are extensively tested for compliance with specifications. An 8-input multiplexer is used for intrinsic background measurements. This device is a prototype front end multiplexer for the data acquisition system.

#### ● "SPINS" Spectrometer

The SPINS (Spin Polarized Inelastic Neutron Scattering) spectrometer was installed this year and operated at fixed incident energies of 15 and 5 meV. However, it was determined that additional shielding would be required, especially given the increased intensities expected with conversion from the  $D_2O$  ice to liquid hydrogen cold source. The shielding modifications were successfully made during one of the scheduled reactor shutdowns.

The first 100 Fe/Si supermirror plates from which broad band and wide-angle transmission polarizers are to be constructed were received. Testing of the composite stack is planned as soon as the construction of the bending device is completed. The energy-dependent Drabkin flipper construction was finished at Brookhaven National

Laboratory and is also scheduled for testing in the near future.

Meanwhile, the Johns Hopkins University condensed matter physics team, led by Collin Broholm, has designed and built a special horizontally focusing analyzer to be installed on the triple-axis spectrometer as another option. It is anticipated that the Johns Hopkins analyzer, the Drabkin flipper, and the transmission polarizer devices will be tested before the extended reactor shutdown beginning in the spring of 1994.

#### ● Neutron-Backscattering Spectrometer

The CNRF backscattering spectrometer is currently under development and will be installed on guide NG-2. The design of this instrument incorporates several flux-enhancing elements including a straight converging-guide section and a phase-space-transform (PST) chopper. The converging guide will increase the flux incident on the PST chopper by a factor of 3 at the expense of an increase in beam divergence. The PST chopper then Doppler-shifts neutron energies up or down depending on whether they are less than or greater than 2.08 meV. This energy is set by the  $d$ -spacing between the (111) lattice planes of silicon which cover both monochromator and analyzer. Monte Carlo simulations suggest that the PST chopper should enhance the flux incident on the monochromator by a factor of 5 to 6 over that from a stationary deflecting crystal. The target energy resolution for the backscattering spectrometer is about  $0.7 \mu\text{eV}$  FWHM with a  $Q$ -range from 0.3 to  $1.8 \text{ \AA}^{-1}$ . A Doppler-driven monochromator, operating at top speed, will give a maximum neutron energy transfer of  $\pm 50 \mu\text{eV}$ .

Several major components of this instrument have now been ordered. These include a 20-ton steel vacuum chamber which will eliminate air-scattering, a spherically focusing analyzer array which will stand 2 meters tall and span  $165^\circ$  in angle, the PST chopper, and several elements of the monochromator Doppler drive. The vacuum chamber, designed by Christoph Brocker, has been delivered. The analyzer array is scheduled for completion by October of 1994. Other major components of the backscattering spectrometer which will be ordered by March 1994 include a neutron velocity selector, which will limit the bandwidth  $\Delta\lambda/\lambda$  at a wavelength of  $6.27 \text{ \AA}$  to

12%, and the supermirror sections needed to form the converging guide. A schematic diagram of the spectrometer layout is given in figure 1.

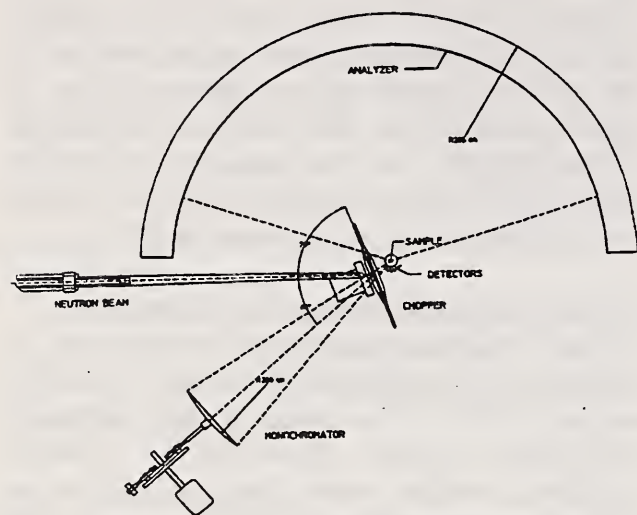


Figure 1. A schematic diagram of the neutron-backscattering spectrometer.

#### • Spin Echo Spectrometer

The neutron spin echo (NSE) spectrometer is being built and will be operated as a PRT facility involving NIST, KFA-Jülich, and Exxon Research and Engineering. The KFA-Jülich has recently finished construction of a similar spectrometer. The CNRF NSE spectrometer will be installed in the end position on guide NG-5. The instrument is optimized to maximize the neutron flux on the sample (by keeping the length as short as possible), while achieving as high a resolution as practicable. The maximum Fourier time is expected to be at least  $9.2 \times 10^{19} \lambda^3 \text{ s/m}^3$  (*i.e.* 47 ns for 8 Å neutrons, which corresponds to an energy resolution of 14 neV). The design attempts to reduce the magnetic field coupling between the two main coils in order to allow access to large momentum transfers (up to  $2 \text{ \AA}^{-1}$ ).

The incident beam will be monochromatized to  $\sim 10\%$  by a mechanical velocity selector (to be delivered in 1994 by Dornier), and polarized by a transmission cavity similar to the one described below for SANS use. Provisions have been made for the possible use of a reflection polarizer at longer wavelengths or a Drabkin flipper for better monochromatization of the beam.

The main coils and carriers are presently under construction and delivery is expected near the end of 1994.

## Other Instrumentation

#### • Capillary Neutron Optics

The principle of multiple mirror reflection from smooth surfaces at small grazing angles enables the transport of neutron beams through polycapillary fibers of narrow hollow channels of diameter of  $\sim 10 \mu\text{m}$ . These miniature neutron guides can be used to construct focusing lens for neutron absorption techniques in analytical and materials research for increasing the spatial resolution of the measurement and improving the detection limits for individual elements. The transmission properties of the polycapillary fibers depend critically on the glass composition, the bending radius, the surface smoothness and the internal diameter. These properties need to be understood if the capillaries are to be used efficiently to construct a high gain focusing device [2]. We have performed experimental measurements, computer simulations and analytic calculations to support the design of neutron focusing lenses.

We have studied the properties of individual polycapillary fibers of various compositions [3], and performed cold neutron transmission measurements on both straight and bent fibers of different lengths using a high-resolution position-sensitive video radiation detector. The transmission efficiencies depend strongly on the divergence of the incident beam. Provided that the reflectivity of the inner surface is close to unity, the transmission loss is linearly proportional to the average number of reflections that neutrons make travelling along the channel. The transmission through bent polycapillaries is important because the bending of the fibers makes the redirecting of neutron beams possible. We have also performed divergence measurements on the transmitted beam for both straight and bent polycapillaries.

These experimental results have been compared with a ray-tracing simulation [4]. Good agreement between the two has been obtained by considering in the simulation only reflectivity losses caused by absorption. We conclude that the influence of other loss mechanisms on reflectivity, such as surface roughness and waviness, are not significant compared with the absorption loss for the borosilicate fibers. This program has enabled us to characterize the expected performance of a neutron

focusing lens placed at the end of a  $^{58}\text{Ni}$  guide tube. An order of magnitude increase in neutron intensity within a submillimeter focal spot is predicted.

The size of the beam at the focus for a given wavelength depends on the focal length of the lens, the critical angle of the fibers, the radius of the polycapillary fibers, and numerical aperture of the lens. We obtain an optimum focal length of the lens by maximizing the current density at the focus for a given size of the focal spot. This length depends on the critical angle averaged over the spectrum transmitted by the lens [5]. We have also calculated the distribution of polar angles for trajectories which may be propagated through a cylindrical channel. We can then determine the transmission and the beam profile at a given distance from the end of the channel as a function of polar angle [6].

We have studied a prototype neutron focusing lens with a focal length of 104 mm, and shown that a cold neutron beam can be focused to a size of 1 mm with a gain of order three. The actual characteristics depend on the divergence and spectrum of the incident beam. The neutron transmission of the fibers, and consequently the gain of the lens, depends on the neutron wave-length. In addition the gain depends on the compatibility of the angular divergence of the beam with the angular acceptance of the fibers. A second lens of focal length 57 mm has also been tested [7]. The intensity distribution of the images taken by the detector at different distances around the focus indicates (see Fig. 2) the focused intensity with a conical distribution rising up from the surrounding background. The full-width at half-maximum is 0.49 mm, with an average gain in intensity of about 20. These experimental results agree well with those obtained by computer simulation.



Figure 2. Intensity distribution of images at different distances around the focus.

### • A Transmission Polarizing Cavity for SANS

A transmission polarizing cavity, similar to that developed for use at the ILL [8], is currently under development for the NG-3 SANS spectrometer. Shown schematically in figure 3, the cavity consists of silicon plates with an Fe/Si supermirror coating that form a V inside a section of Ni-coated neutron guide. The cavity is designed to polarize a wide beam ( $5 \times 5 \text{ cm}^2$ ) over a range of wavelengths ( $5\text{-}15 \text{ \AA}$ ) by preferentially reflecting neutrons of one spin state out of the beam.

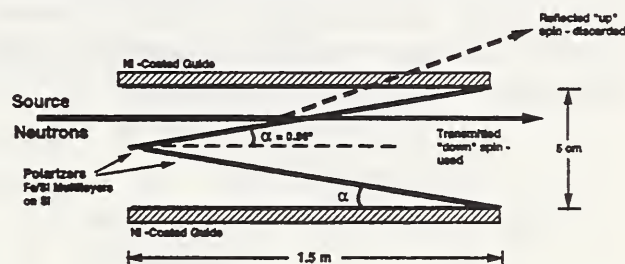
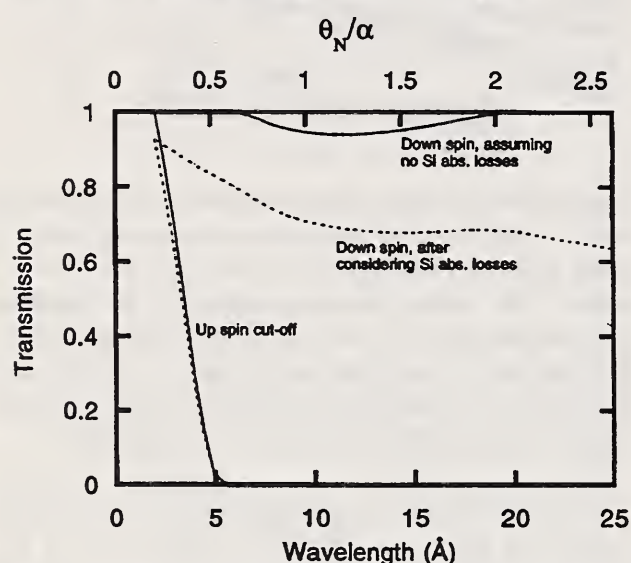


Figure 3. A schematic representation of a polarizing cavity. The incident beam enters the cavity between guide walls and impinges on a polarizing Fe/Si supermirror. The setting angle,  $\alpha$ , is fixed so that up spin neutrons are reflected and exit through the guide walls (perhaps after multiple reflections). Down spin neutrons are transmitted through the polarizer to be used for the polarized-neutron SANS experiments.

The performance expected from the polarizing cavity has been investigated by Monte Carlo ray tracing. Figure 4 shows the transmission of both the up and down spin neutrons through the cavity as a function of wavelength. The solid lines show the ideal transmissions assuming (i) that reflectivities are 100%, (ii) that there are no losses due to diffuse scattering, and (iii) that Si absorption is negligible. Under such conditions, there would be no transmission of up spin neutrons through the cavity beyond a wavelength,  $\lambda$ , of  $\sim 5 \text{ \AA}$ . Ideally, the transmission of down-spin neutrons is 100% except between  $\lambda = 9\text{-}20 \text{ \AA}$  (or  $\theta_{\text{Ni}}/\alpha = 0.75\text{-}2$ ). Over this range a  $\leq 7\%$  loss occurs as a result of down spin neutrons which "glance" off the supermirror and have enough increased divergence to escape through the guide wall. When absorption losses due to the 1.5 mm thick Si substrate are considered, up-spin neutrons are still completely removed, as shown by the dashed curves in figure 4. Transmission of down spin neutrons, however, is reduced to  $\sim 75\%$  over the useful range of wavelengths.

Prototype supermirrors for the SANS polarizer have been obtained that have a polarizing efficiency greater than 90% when the angle of incidence is between  $1/2$  and 3 times the critical angle of Ni ( $\theta_{Ni}$ ). The Fe/Si multilayers are coated on 1.5 mm thick Si wafers that are flat when free-standing which simplifies the construction of the device. The large difference in the critical angles for the two spin states— $\sim 1/2 \theta_{Ni}$  and  $3 \theta_{Ni}$  for the "down" and "up" spin states respectively—enables a relatively large convergence angle  $\alpha$  to be used ( $\alpha = 2 \theta_{Ni}$  for a wavelength of 4.7 Å in the present case) which facilitates polarizing a wide beam over a broad range of wavelengths.



**Figure 4.** The calculated transmission of up and down spin neutrons for the polarizing cavity shown in figure 3 obtained using Monte Carlo ray tracing. The solid lines are calculated assuming that the supermirrors are ideal—i.e. they reflect perfectly and exhibit no losses due to either diffuse scattering or absorption. The dashed lines better reflect the expected performance of the polarizer by considering losses due to Si absorption. Further details are as follows:  $\Delta\lambda/\lambda = 0.15$ ; Si substrate thickness = 0.15 cm; and  $\alpha = 0.96^\circ$ .

## The Hydrogen Cold Source

The design of a new liquid hydrogen cold source for the NBSR was described in last year's annual report. The design and safety reviews for this source are now complete, and fabrication and assembly are now well underway, in preparation for installation in the reactor during the scheduled shutdown for heat exchanger replacement in

March 1994. During this shutdown, which is estimated to last 6-9 months, the old D<sub>2</sub>O source and the bismuth/lead tip will be removed, and replaced with the new source. The LH<sub>2</sub> source is a 2-cm thick spherical annulus with an outside diameter of 32 cm, a volume of 5 liters, and a 20-cm diameter exit hole to fully illuminate the neutron guides (see Fig. 5)

During the past year, the Monte Carlo simulations (using MCNP) related to source neutronics and heating have been substantially extended. A complete model of the core of the NBSR, including detailed modelling of the fuel, has been developed and used to derive both source heating ( $\gamma$ -ray and neutron) and a surface source for neutronic calculations. With the new results, we have confirmed that source heating will be less than 1 kW, and were able to make design changes to ease fabrication with confidence that the heating effects were allowable. The neutronic calculations have confirmed our earlier estimates of performance which were based on an empirical surface source. The predictions of these calculations indicate that for neutrons with energies less than 5 meV the new source will provide gains of more than five over the present source.

In order to test the thermal hydraulic behavior of the new source, which incorporates a novel geometry, a full scale glass model of the cryostat and associated hydrogen transfer lines was built by the NIST Chemical Sciences and Technology Laboratory at Boulder. As noted above, refined MCNP calculations indicate that less than 1 kW will be deposited in the LH<sub>2</sub> and the Al chamber by neutrons and gamma rays during normal operation. The tests demonstrated that at least 2200 W can be removed by the proposed natural circulation loop. They also demonstrated that the system is very stable when operated with two phase flow in the return line, and that the response to sudden changes in power dissipated is rapid and smooth, with a new equilibrium established virtually instantaneously. From measurements of system mass, the void fraction in the hydrogen cold source will vary from 12% to 8% as the pressure changes from 0.8 bar to 1.5 bar. In addition to verifying the overall thermal hydraulic performance of our proposed system configuration, the measurements revealed a number of potential

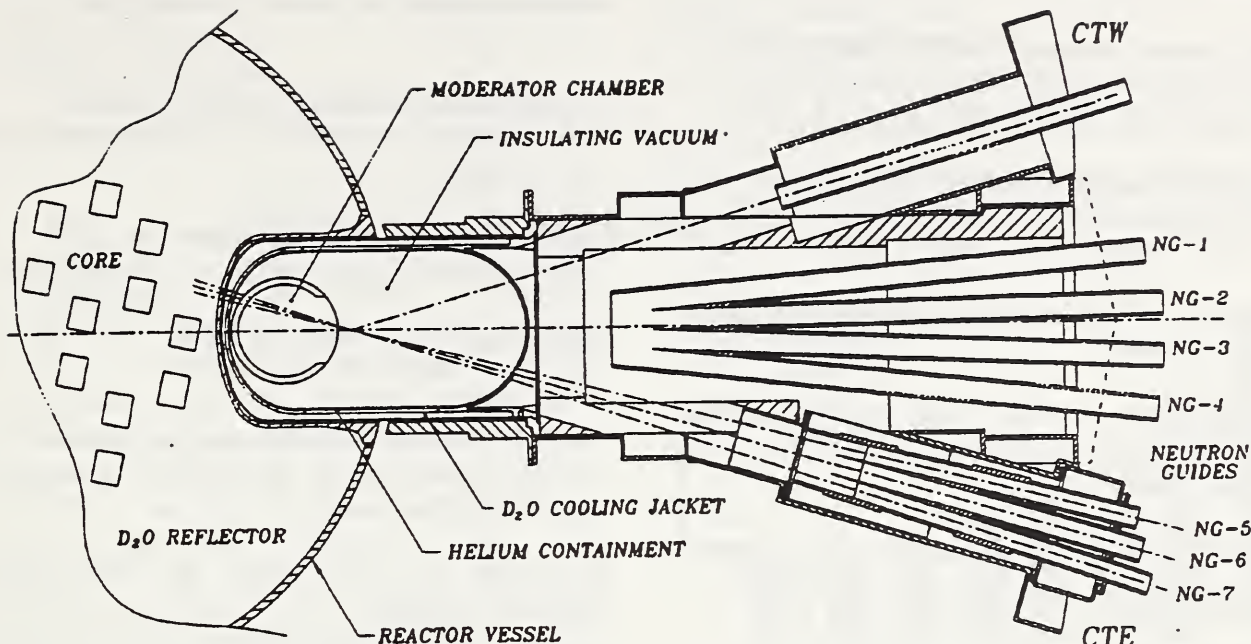


Figure 5. Plan view of the hydrogen cold source in the cryogenic beam port of the NBSR.

problems, which led to revisions of the moderator chamber detailed design.

The proposed hydrogen cold source was the subject of two outside reviews in the past year. An analysis of the nature of the hazards related to the new source was submitted to the Nuclear Regulatory Commission (NRC), who in turn had the analysis reviewed externally. The NRC ruled in May that the liquid hydrogen cold source "does not present an unreviewed safety question", and can therefore be installed under the provisions of 10 CFR Part 50.59, subject to the approval of the NBSR Safety Evaluation Committee. In March, a panel of outside experts on cold neutron sources, cryogenics, and reactor safety was brought to Gaithersburg for a two-day technical review of all aspects of the design, safety, installation and operation of the LH<sub>2</sub> source. They concluded "the design of this cold source is technically sound and introduces no unresolved safety issues."

Another milestone in the project was passed in May when the acceptance test of the new helium refrigerator was successfully completed. The refrigerator can operate at 3.5 kW, with a helium discharge temperature of 14 K. It ran 40 days without a failure, but was twice shutdown by AC power interruptions due to thunderstorms.

Modifications to the control system are now being designed which will reduce the susceptibility of the refrigerator to the most common electrical failures (which are of extremely short duration). In cases in which the refrigerator is shut down by power interruptions, an automatic restart capability is incorporated to minimize down time.

## References

- [1] J.R.D. Copley and T. J. Udovic, *J. Res. NIST* **98**, 71 (1993).
- [2] D.F.R. Mildner, H. Chen, R. G. Downing, and V. A. Sharov, *J. Neutron Research* **1**, 1-11 (1993).
- [3] H. Chen, D.F.R. Mildner, R. G. Downing, R. E. Benenson, Q. F. Xiao, and V. A. Sharov, *Nucl. Instrum. & Meth. B*, in press (1994).
- [4] Q. F. Xiao, H. Chen, D.F.R. Mildner, R. G. Downing, and R. E. Benenson, *Rev. Sci. Instrum.* **64**, 3252-3257 (1993).
- [5] D.F.R. Mildner, *J. Appl. Cryst.* **26**, 721-727 (1993).
- [6] D.F.R. Mildner and H. Chen, *J. Appl. Cryst.*, in press (1993).
- [7] H. Chen, D.F.R. Mildner, and Q. F. Xiao, *Appl. Phys. Lett.*, in press (1994).
- [8] F. Mezei, *SPIE Vol. 983 Thin-Film Neutron Optical Devices* (1988) 10.

## Research Topics

### Cold Neutron Focusing Using Capillary Optics

H. Chen<sup>4</sup>, R. G. Downing<sup>4</sup>, D.F.R. Mildner<sup>4</sup>, V. A. Sharov<sup>6,14</sup>, R. E. Benenson<sup>11</sup>, and Q. F. Xiao<sup>14</sup>.

### The High-Resolution Multiple-Disk Chopper Time-of-Flight Spectrometer

J.R.D. Copley<sup>10</sup>, J. C. Cook<sup>5,12</sup>, and D. J. Pierce<sup>10</sup>.

### The Medium-Resolution Time-of-Flight Spectrometer

T. J. Udovic<sup>10</sup>.

### The NSF/NIST (CHRNS) Triple-Axis Spectrometer

V. Nunez<sup>12</sup>, C. F. Majkrzak<sup>10</sup>, S. F. Trevino<sup>1,10</sup>, and C. L. Broholm<sup>7</sup>.

### The NIST/IBM/U. of Minn. Cold Neutron Reflectometer

S. K. Satija<sup>10</sup> and A. Karim<sup>9</sup>.

### A Liquid Hydrogen Cold Neutron Source

R. E. Williams<sup>10</sup>, J. M. Rowe<sup>10</sup>, and P. A. Kopetka<sup>10</sup>.

### Fe-Si Supermirror Polarizers

C. F. Majkrzak<sup>10</sup>, J. F. Ankner<sup>15</sup>, and V. Nunez<sup>12</sup>.

### NiC-TiMn Supermirror Reflectivity Measurements

C. F. Majkrzak<sup>10</sup> and J. F. Ankner<sup>15</sup>.

### Drabkin Energy-Dependent Spin Flipper Fabrication

C. F. Majkrzak<sup>10</sup>, L. Passell<sup>2</sup>, V. Nunez<sup>12</sup>, H. P. Layer<sup>10</sup>, W. E. Dickerson<sup>10</sup>.

### Composite Pyrolytic Graphite Crystal Monochromator Reflectivity Measurements

D. A. Neumann<sup>10</sup>, C. W. Bocker<sup>12</sup>, and C. F. Majkrzak<sup>10</sup>.

### Full Scale Tests of the Thermal Performance of a Hydrogen Cold Source for the NBSR

J. Seegworth<sup>3</sup>, D. Olson<sup>3</sup>, J. M. Rowe<sup>10</sup>, M. Jones<sup>3</sup>, P. A. Kopetka<sup>10</sup>, R. E. Williams<sup>10</sup>.

### Analysis of the Transmission Properties of Neutron Optical Filters

J.R.D. Copley<sup>10</sup>.

### Analysis and Simulation of the Performance of Oscillating Radial Collimators

J.R.D. Copley<sup>10</sup> and J. C. Cook<sup>1,12</sup>.

### Resolution Properties of Counter-rotating Chopper Monochromators for Neutron Spectroscopy

J. C. Cook<sup>1,12</sup>.

### A Transmission Polarizing Cavity for SANS

W. J. Orts<sup>10</sup>, J. G. Barker<sup>10</sup>, C. F. Majkrzak<sup>10</sup>, and C. J. Glinka<sup>10</sup>.

### High Field Superconducting Magnet for SANS

R. W. Erwin<sup>10</sup>, J. W. Lynn<sup>10</sup>, and L. Santodonato<sup>10</sup>.

### Sliding Plate Shear Device for SANS

K. Koppi<sup>13</sup> and F. S. Bates<sup>13</sup>.

### The Cold Neutron Backscattering Spectrometer

P. M. Gehring<sup>10</sup>, C. W. Bocker<sup>12</sup>, R. Christman<sup>16</sup>, and D. A. Neumann<sup>10</sup>.

### Stress Test of Graphite for the Phase Space Transform Chopper

C. W. Bocker<sup>12</sup>, P. M. Gehring<sup>10</sup>, D. H. Fravel<sup>10</sup>, and D. A. Neumann<sup>10</sup>.

### Test of Analyzer Crystals for the Backscattering Spectrometer

B. Frick<sup>5</sup>, P. M. Gehring<sup>10</sup>, D. A. Neumann<sup>10</sup>, and C. W. Bocker<sup>12</sup>.

### Graphite Mosaic for the Phase Space Transform

P. M. Gehring<sup>10</sup>, D. A. Neumann<sup>10</sup>, and C. W. Bocker<sup>12</sup>.

### Modeling of Neutron Focusing Lenses

D.F.R. Mildner<sup>4</sup>, H. Chen<sup>4</sup>, R. G. Downing<sup>4</sup>, Q. F. Xiao<sup>14</sup>, and J. W. Swider<sup>12</sup>.

### Neutron Transmission of Polycapillary Fibers

H. Chen<sup>4</sup>, D.F.R. Mildner<sup>4</sup>, R. E. Benenson<sup>11</sup>, Q. F. Xiao<sup>14</sup>, and V. A. Sharov<sup>6,14</sup>.

### The Neutron Spin Echo Spectrometer

N. Rosov<sup>10</sup>, J. M. Rowe<sup>10</sup>, and M. Monkenbusch<sup>8</sup>.

## Affiliations

<sup>1</sup>Army RD&E Center

<sup>2</sup>Brookhaven National Lab

<sup>3</sup>CSTL, NIST Boulder

<sup>4</sup>Inorganic Analytical Res. Div.

<sup>5</sup>Institut Laue-Langevin

<sup>6</sup>Inst. of Roentgen Optical Sys.

<sup>7</sup>Johns Hopkins University

<sup>8</sup>KFA Jülich

<sup>9</sup>Polymers Division



<sup>10</sup>Reactor Radiation Division

<sup>11</sup>SUNY (Albany)

<sup>12</sup>University of Maryland

<sup>13</sup>University of Minnesota

<sup>14</sup>X-ray Optical Systems, Inc.

<sup>15</sup>MURR, Columbia, MO

<sup>16</sup>NESCO Service Company

## GUEST RESEARCHERS AND COLLABORATIONS

Experimenters from outside the Reactor Radiation Division have played a most important role in the scientific programs at the NBSR since its earliest days. In fact, the great majority of the experiments carried out on its neutron beam instruments involve the active participation of users from industry, universities, other federal agencies, and other divisions of NIST. The construction and operation of the CNRF, a national user facility, has meant that, in recent years, the user involvement has greatly increased, making the NBSR user program the most extensive at any U.S. research reactor. This trend is likely to continue for a number of years, not only while the CNRF instrumentation rises to its full potential, but also as modernization of equipment in the reactor confinement building permits more experiments to be carried out on each instrument.

The increasing number of external research participants, i.e., non-division scientists who have been directly engaged in research projects based on the NBSR, is evident in figure 1, which also indicates that the RRD staff are a small, although essential, component of the total number of researchers who have performed experiments at the reactor. External participants are often involved in more than one experiment in any one year, but are counted only once per year in figure 1. The rightmost column of figure 1 represents participants from 46 U.S industrial laboratories, 72 universities, 29 other government institutions, and 78 foreign institutions.

The growth in user participation has occurred through several modes of access, the most important of which is one that offers the CNRF instruments to all qualified researchers through a process of proposal submission and peer review. In this formal proposal system, which is now entering its third year of operation, calls for proposals are issued twice yearly to a mailing list of more than 1500 scientists, with proposal forms and detailed information about the available

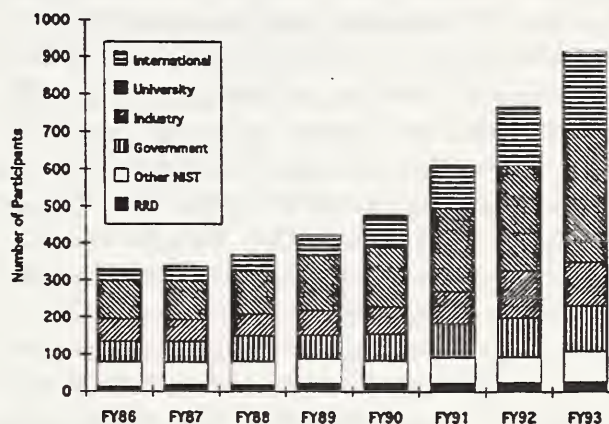
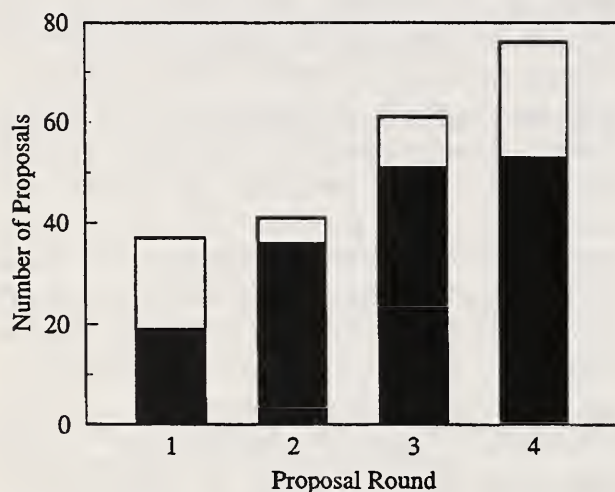


Figure 1. Research participants at the NBSR.

instrumentation. Soon after the proposal deadline, the proposals received in response to a call are mailed out for external peer review. The final decisions for beam time allocations are made by a Program Advisory Committee (PAC), which compares the proposals on the basis of the written reviews. The third and fourth calls for proposals, issued during fiscal year 1993, the period being reported on here, attracted 155 proposals, as compared with 90 in the previous year, which was the first year of operation of the system. The NSF-funded Center for High Resolution Neutron Scattering (CHRNS), which comprises one of the two 30-m SANS diffractometers and the SPINS cold-neutron triple-axis spectrometer, is now approaching its full capacity to serve users in terms of number of available instrument-days, but the major NBSR upgrades scheduled for 1994 will mean a qualitative improvement in performance in 1995. The fraction of total beam time reserved for general users is 75% on the CHRNS 30-m SANS, and 67% for other CNRF neutron scattering instruments, except for PRT instruments (see below), on which 25% is set aside for general users.

Figure 2 shows the growth in the number of proposals for the neutron scattering instruments in

the CNRF for the first four proposal cycles. Proposals for chemical analysis stations (Cold Neutron Depth Profiling and Prompt Gamma Activation Analysis) are not included here since they are now being handled on a different basis, as discussed below. SANS proposals accounted for all of the first round proposals shown in this chart, and 55% of those in the fourth round. In future proposal rounds, one can expect the SANS machines to remain the most popular instruments, but the number of SANS proposals compared to the total will decline as time goes on. The approval rate for proposals submitted was fairly high, about 70% for the last round, but the number of instrument-days allocated as a fraction of those requested was less than 60%. The proposals show a good distribution among scientific disciplines, and are becoming increasingly diverse in succeeding proposal rounds. Polymer Science is the most heavily represented area, especially for SANS and reflectometry, but numerous proposals were also received for experiments on other areas of materials science, biology, condensed matter physics, chemistry, and complex fluids.



**Figure 2.** Neutron scattering proposals submitted to the CNRF in FY 1992 (rounds 1 and 2) and FY 1993 (rounds 3 and 4). Solid portions of the bars indicate accepted proposals.

The 30-m SANS diffractometers were the only neutron scattering instruments offered for proposals in the first two rounds, while the last two have also offered the cold neutron reflectometer, the medium-resolution time-of-flight spectrometer, and the SPINS triple-axis spectro-

meter. The reflectometer has shown very good performance since its initial operation, and has immediately stimulated an oversubscription in terms of proposals and beam time requests. Since the reflectometer is a PRT instrument with only 25% of the time reserved for the proposal system, other means are being considered to accommodate more applicants interested in this increasingly popular technique. Another instrument which has immediately experienced heavy demand from users is the new high-resolution powder diffractometer. Because it is not a CNRF instrument, it is not at present part of the proposal system, but has been accessed through collaborations on an individual basis and through more formal cooperative agreements with two university groups.

The past year marked the introduction of inelastic scattering capabilities in the CNRF guide hall, with the commissioning of the medium-resolution time-of-flight and the SPINS triple-axis spectrometers. Two other major inelastic instruments, the back-scattering spectrometer and the high-resolution time-of-flight spectrometer, will begin operation in 1995. Finally, a contract has now been signed with German suppliers to fabricate major components of the neutron spin-echo spectrometer, which is an ultra-high resolution inelastic scattering instrument.

Two of the CNRF instruments—the cold neutron reflectometer and one of the 30-m SANS diffractometers—were built by participating research teams (PRTs), consortia of several institutions which shared the cost of instrument development and construction. On these instruments, 75% of the beam time is reserved for PRT members, and 25% for general users through the CNRF proposal system. The PRT research programs are discussed in other sections of this report.

Access to the analytical chemistry stations is handled somewhat differently from the CNRF neutron scattering instruments because the duration of experiments can vary from a few hours to several weeks, depending on the nature of the proposed project. Proposals can be submitted on the standard CNRF proposal form, but use of the forms is not required, and less formal proposals submitted directly to the instrument scientists (G. Downing, (301) 975-6286; R. Lindstrom, (301) 975-6281) are considered immediately and are not

presently sent out for external peer review. The CNDP station carried out user experiments with 16 external groups in the period October 1992 through September 1993, and has made formal Cooperative Research and Development Agreements (CRDAs) with four organizations, Intel Corp., Linfield College, X-ray Optical Systems, and Schott Glass, with another CRDA under discussion with Nuclear Analytical Associates. The project with X-Ray Optical Systems has the potential for bringing an entirely new technology, i.e., glass-fiber-based neutron focussing optics, to the marketplace.

The fundamental neutron physics stations in the guide hall operate in yet another mode. The experiments at these two stations, a dedicated cold neutron beam at the end of the NG-6 guide, and the neutron interferometry station on NG-7, are typically of much longer duration than for other CNRF instruments, and involve highly specialized equipment. For example, the first experiment on the NG-6 end station is a two-year project to measure the neutron lifetime, in which most of the time is spent in equipment development, testing and calibration. External participation in such experiments requires long-term and costly commitments and a more thorough and inevitably slower review than offered by the formal user proposal system becomes necessary. An advisory committee separate from the PAC has been established to review the use of the fundamental physics stations, in order to ensure that they properly serve the needs of their research community.

Although the NBSR instruments outside the CNRF are not part of the formal proposal system, they are made widely accessible in several other ways. The most common of these, and the usual way prior the operation of the CNRF, is through direct collaboration with NIST staff. This does not imply that the NIST staff must take a leading role in the measurements, but that there must be enough common scientific interest to justify the use of NIST beam time and the efforts of local scientists and technicians. Three triple-axis spectrometers, a high-resolution powder diffractometer, a polarized beam reflectometer, a residual stress and texture facility, and a station for neutron optics, are extensively used for such collaborative research. In some cases, the involvement of non-NIST groups is through more formal arrangements

resembling the PRT agreements of the CNRF. A group from the U.S. Army participated in the development of the BT-4 and BT-6 spectrometers, and has been stationed at the NBSR for more than 20 years. Other long-term cooperative programs with the University of Maryland, Johns Hopkins University, the University of California at Santa Barbara, and MIT are currently active. Similar arrangements with other university and industrial research groups are being considered.

The Division makes a special effort to accommodate experimenters who can make a case for immediate access based on clear scientific urgency. If the planned experiment is to be carried out on a CNRF instrument, a short proposal can be submitted which is quickly reviewed and assigned beam time if approved by the PAC. Alternatively, NIST staff members can be contacted to arrange collaboration for use of a non-CNRF instrument, or for employing NIST beam time on a CNRF instrument.

Several non-NIST programs are also served by the NBSR through the provision of services such as irradiation, radiography, and materials characterization. Examples include a program with various art galleries for autoradiography of paintings, a program with the FDA for characterization of food and drugs, and activation analysis services for the FBI. Shorter-term projects receive use of NBSR facilities on an as-needed, case-by-case basis. Depending on its nature, a project may be arranged as a collaboration with NIST or as an independent study by the outside agency. In some cases, non-NIST researchers perform proprietary research using NBSR facilities. In such cases, the researchers' institutions are assessed charges on a full-cost recovery basis.

The trends to increasing guest researcher activity, and to increasing diversity in user experiments, will undoubtedly continue for a number of years. The improvements that will be made during the extended shutdown in 1994 will have a major effect on future prospects. The operation of the NBSR at 20 MW, and the installation of the new cold source and the last three neutron guides, means that the NBSR will come back on line in late 1994 with markedly enhanced capabilities for neutron beam experiments, and a greater number and variety of user experiments will become practicable. Encouraging use of the

NBSR and the CNRF by the broadest possible community, and fostering the development of new applications for neutron beams, will remain primary missions of the Division.

For further information on the use of the instrumentation at the NBSR, contact Bill Kamitakahara at (301) 975-6878, or any RRD staff member.

---

## REACTOR OPERATIONS AND ENGINEERING

In spite of several operational problems, reactor on-line time reached 75% which was higher than the previous year. This corresponds to more than 95% of scheduled operating time.

Operating staff proficiency continues to be high. Five senior operators passed their NRC conducted operating requalification examinations with perfect scores. A new staff member successfully obtained his initial senior operator license.

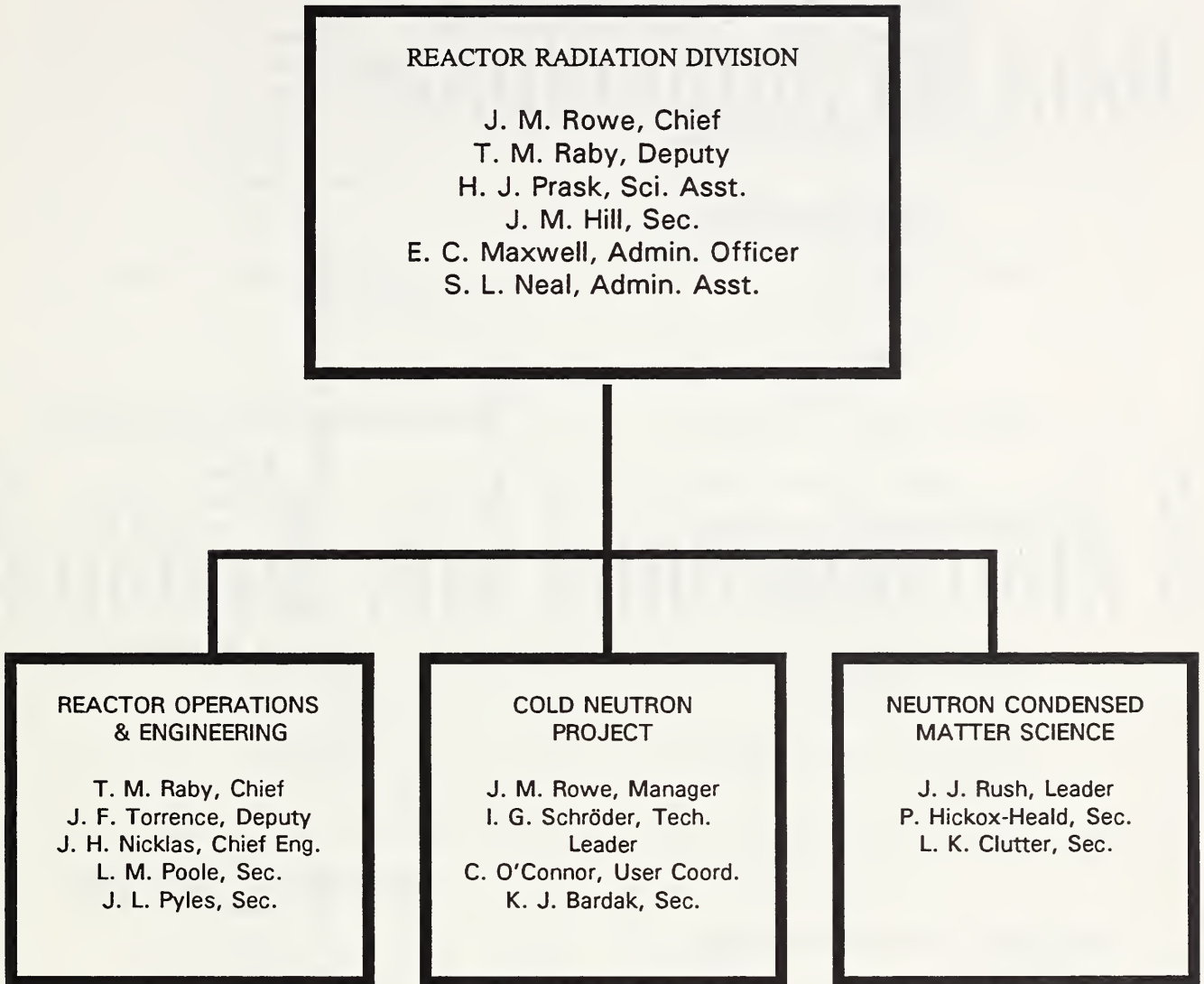
Fuel utilization is still the best in the United States. The fifth generation of fuel has extended the operating cycle by 25% to more than five weeks compared to an equivalent of less than one week when the reactor first operated. Aside from the significant financial savings, this will result in fewer refueling operations and shutdowns.

A major reactor upgrade program is scheduled to begin this spring to coincide with the installation of the new liquid hydrogen cold source which is expected to last 6-9 months. Included in the upgrade are:

- Replacement of the main heat exchangers
- Replacement of two auxiliary heat exchangers
- Major modifications to the primary, secondary, and auxiliary cooling systems
- Installation of cooling water filtration system
- New primary ion-exchange columns with associated piping and custom shielding
- Disposal of radioactive waste
- Replacement of the control rods
- Replacement of the heavy water
- Refueling system upgrade
- Reactor control room upgrade

In this regard, 70 metric tons of heavy water has been purchased from the Italian Government at very favorable rates. This will assure long term availability of heavy water for the reactor. Upgrade of reactor instrumentation has already been initiated with installation of a new advanced 267-unit annunciator system.

## PERSONNEL ROSTER



### Staffing

The Division staff is organized formally into three groups, as shown in Table 1; however, staff are utilized where necessary, irrespective of group. Below the group level of organization, personnel are grouped into research teams according to their predominant interest. Once again, these groupings are not hard and fast—there are many overlapping interests. These teams, including long-term guest researchers, are shown in Table 2. A number of "non-resident" Ph.D. students and continuing collaborators from universities and industry are not listed.

It should be noted that members of the Cold Neutron Project are included in the teams by scientific interest, even though in most cases, their predominant responsibility is for CNRF instrument building and/or operation. In fact, they have only 30% of their time given to the conduct of research, while 70% is dedicated to the facility. Likewise, many members of the Neutron Condensed Matter Science Group have sizable CNRF responsibilities, which may amount for as much as 1/2 time when needed.

HEALTH PHYSICS - DIVISION 354

Slaback, L., Ldr.  
Thomas, C., Sec.

Brown, D.  
Campbell, C.  
Cassells, L.  
Clark, J.  
Deardorff, G.  
Jensen, I.  
Mengers, T.  
Shubiak, J.

NUCLEAR METHODS GROUP -

DIVISION 834

Greenberg, R. R., Ldr.  
Wilson, J., Sec.

Becker, D.  
Blackman, M. J.  
Chen, H.  
Demiralp, R.  
Downing, R. G.  
Fitzpatrick, K.  
Garrity, K. M.  
Iyengar, G. V.  
Koster, B.  
Lamaze, G. P.  
Langland, J. K.  
Lindstrom, R. M.  
Mackey, E. A.  
Mildner, D.F.R.  
Myers, E.  
Norman, B. R.  
Paul, R. L.  
Sharov, V. A.  
Truncer, J. J.

COLD NEUTRON PROJECT

Rowe, J. M., Ldr.  
O'Connor, C. L., User Coord.  
Hill, J. M., Sec.  
Bardiak, K., Ck. Typ.

Barker, J.  
Dickerson, W. E.  
Gallagher, P. D.  
Gehring, P. M.  
Gorman, W.  
Graham, P. H.  
Greene, G. C.  
Hamimouda, B.  
Kamitakahara W. A.  
Heald, A. E.  
Klosowski, P.  
Kopetka, P. H.  
Krueger, S.  
Kulp, D.  
LaRock, J. G.  
Layer, H. P.  
Pierce, D. J.  
Robeson, L.  
Rosov, N.  
Schroder, I. G.  
Thai, T. T.  
Tobin, P. L.  
Williams, R. E.

Guest Scientists & Engineers

Allen, A. J.  
Brocker, C. W.  
Christman, R.  
Lin, M. Y.  
Moyer, J. J.

NEUTRON INTERACTIONS & DOSIMETRY -

DIVISION 846

Grundl, J. A., Ldr.  
Mattiello, R., Sec.

Arif, M.  
Boswell, E.  
Dewey, M. S.  
Eisenhauer, C. M.  
Gilliam, D. M.  
Greene, G. L.  
Littrel K.  
McGarry, E. D.  
Richardson, J. M.  
Schwartz, R. B.  
Thompson, A.

NEUTRON CONDENSED MATTER SCIENCE

Rush, J. J., Group Ldr.  
Hickox-Heald, P., Sec.  
Clutter, L. K., Sec.

Baltic, G. M.  
Berk, N. F.  
Borchers, J. A.  
Bostian, D.  
Casella, R. C.  
Clem, D.  
Clow, W.  
Copley, J.R.D.  
Dura, J. A.  
Erwin, R. W.  
Fravel, D. H.  
Glinka, C. J.  
Green, T. A.  
Karen, V. L.  
Knill, W. C.  
Lynn, J. W.  
Majkrzak, C. F.  
Mighell, A. D.  
Neumann, D. A.  
Orts, W. J.  
Prince, E.  
Reznik, D.  
Rinehart, M. J.  
Rymes, W. H.  
Santodonato, L.  
Santoro, A.  
Satija, S. K.  
Stalick, J. K.  
Udovic, T. J.  
Wiesler, D. G.  
Williams, R. H.

Guest Scientists & Engineers

Broholm, C.  
Choi, C. S.  
Chmaissem, O.  
Cook, J.  
Giebutowicz, T.  
Grigereit, T.  
Huang, Q. Z.  
Karim, A.  
Kim, S.  
Morris, R.  
Mrose, M.  
Nunez, V.  
Sumarlin, I.  
Trevino, S. F.  
Zhang, H.

ADMINISTRATIVE - DIVISION 856

J. M. Rowe, Chief  
E. C. Maxwell, Admin. Off.  
S. L. Neal, Admin. Asst.  
J. M. Hill, Secretary  
H. J. Prask, Physicist  
D. E. Brady, Elect. Eng.  
J. M. Nicol, Res.Chemist

REACTOR OPERATIONS & ENGINEERING

Raby, T. M., Chief  
Poole, L. M., Sec.

Operations

Torrence, J. F., Deputy  
Beasley, R.D.  
Bickford, N. A.  
Cassells, M. G.  
Clark, F. C.  
Dilks, H. W.  
Flynn, D. J.  
Guarin, E. L.  
Lindstrom, L. T.  
McDonald, M. J.  
Mueller, M. W.  
Myers, T. J.  
Ring, J. H.  
Sprow, R. P.  
Stiber, R. F.  
Thompson, R. G.  
Toth, A. L.  
Wilkinson, D. P.  
Wright, K. D.

Engineering

Nicklas, J. H., Chief  
Pyles, J. L., Sec.

Beatty, J. A.  
Hall, K.  
Heine, C. J.  
Liposky, P. J.  
Shuman, L.  
Suthar, M.A.

Research Associates

Anderson, D. A. (FDA)  
Billos, J.  
Boneh, Z.  
Cheng, T.(Smithsonian)  
Cunningham, R.  
Cunningham, W. C. (FDA)  
Olin, J.(Smithsonian)

**Table 2. RRD Research Staffing**

Chemical Physics of Materials

Staff: N. F. Berk  
 J.R.D. Copley  
 P. M. Gehring\*  
 W. A. Kamitakahara\*  
 D. A. Neumann  
 J. M. Nicol\*  
 D. Reznik<sup>5</sup>  
 J. J. Rush (Leader)  
 T. J. Udovic

Long Term Visitors: J. Cook\*  
 S. F. Trevino<sup>8</sup>

Microstructure and Macromolecules

Staff: J. G. Barker\*  
 C. J. Glinka (Leader)  
 B. Hammouda\*  
 S. Krueger\*  
 W. Orts\*

Long Term Visitor: M. Y. Lin<sup>2,\*</sup>

Surfaces and Interfaces

Staff: P. D. Gallagher\*  
 C. F. Majkrzak (Leader)  
 S. K. Satija  
 D. G. Wiesler\*  
 J. A. Dura<sup>5</sup>

Long Term Visitor: H. Zhang<sup>1</sup>

Crystallography and Diffraction Applications

Staff: V. L. Karen  
 A. D. Mighell  
 H. J. Prask  
 E. Prince  
 A. Santoro  
 J. K. Stalick

Long Term Visitors: P. Brand<sup>1</sup>  
 C. S. Choi<sup>8</sup>  
 Q. Z. Huang<sup>1</sup>  
 M. Mrose  
 R. Morris<sup>9</sup>

Engineering and Instrument Development:

Staff: A. E. Heald\*  
 P. Kopetka\*  
 J. G. LaRock\*  
 D. J. Pierce\*  
 I. G. Schröder\* (Leader)  
 R. E. Williams\*

Long Term Visitors: C. Brocker<sup>1\*</sup>  
 R. Christman<sup>4,\*</sup>  
 J. J. Moyer<sup>4,\*</sup>

Magnetism and Superconductivity

Staff: J. A. Borchers  
 R. C. Casella  
 R. W. Erwin  
 J. W. Lynn (Leader)  
 N. Rosov\*

Long Term Visitors: C. Broholm<sup>6</sup>  
 T. Giebultowicz<sup>7</sup>  
 T. Grigereit<sup>1</sup>  
 V. Nunez<sup>1\*</sup>  
 I. Sumarlin<sup>1</sup>

Scientific Assistance and Technical Support

G. Baltic*	W. C. Knill
D. Bostian*	D. Kulp*
D. Clem*	H. P. Layer*
W. Clow	M. J. Rinehart*
W. E. Dickerson*	L. Robeson*
D. H. Fravel*	W. H. Rymes
W. Gorman*	L. Santodonato
P. H. Graham*	R. H. Williams
T. A. Green*	T. Thai*
G. C. Greene*	P. Tobin*
P. Klosowski*	

\*Primarily associated with CNRF

<sup>1</sup>University of Maryland

<sup>2</sup>Exxon Res.& Eng. Co.

<sup>3</sup>Institute Laue-Langevin

<sup>4</sup>Nesco Design Co.

<sup>5</sup>NRC Post-Doc

<sup>6</sup>Johns Hopkins University

<sup>7</sup>George Mason University

<sup>8</sup>Army RD&E Center

<sup>9</sup>University of California, Santa Barbara

## RESEARCH AND ENGINEERING STAFF

- J. G. Barker           o SANS instrumentation and research
- N. F. Berk             o Condensed matter theory  
                          o Scattering theory for microstructure analysis  
                          o Computer software for graphics and data analysis
- N. A. Bickford         o Reactor operations  
                          o Reactor irradiations  
                          o Reactor utilization
- J. A. Borchers         o Thin-film analysis  
                          o Artificially modulated materials  
                          o Magnetism
- D. E. Brady            o Electrical/electronic engineering  
                          o Nuclear reactor instrumentation
- R. C. Casella          o Condensed matter theory, including high  $T_c$   
                          o Group theory analyses of neutron scattering from condensed matter  
                          o Fundamental physics, especially as related to reactor experiments
- J.R.D. Copley          o Time-of-flight spectrometer development  
                          o Neutron instrumentation conceptual design  
                          o Condensed matter physics
- W. E. Dickerson       o Neutron scattering instrumentation  
                          o Microcomputer interfacing  
                          o Nuclear and engineering physics
- J. A. Dura             o Combined molecular beam epitaxy and neutron  
                                  reflectivity/diffraction instrumentation  
                          o Surface, interfacial, and epitaxial physics  
                          o Metastable phases in artificial materials
- R. W. Erwin            o Magnetic materials  
                          o Phase transformations  
                          o Spin echo techniques  
                          o Cryogenics
- P. D. Gallagher        o Neutron reflectometry instrumentation  
                          o Interfacial phenomena in polymer systems and complex fluids
- P. M. Gehring          o Neutron backscattering instrumentation  
                          o Magnetic and structural phase transitions in disordered systems  
                          o Dynamics of high  $T_c$  materials



- C. J. Glinka
  - o SANS microstructure of metals and porous media
  - o Magnetic materials
  - o Cold neutron instrument development
- P. H. Graham
  - o Engineering design
- G. C. Greene
  - o System and user software for cold neutron instrumentation
  - o Spectrometer and data acquisition systems interfaces
- B. Hammouda
  - o SANS from polymers, liquid crystals, and colloids
  - o Dynamics of polymers in solution
  - o Scattering from sheared fluids
- W. A. Kamitakahara
  - o The CNRF guest researcher program
  - o Dynamics of disordered solids
  - o Condensed matter physics
- V. L. Karen
  - o Crystallographic database development
  - o Theory of lattices and symmetry
  - o Neutron and x-ray diffraction
- P. Klosowski
  - o Scientific data visualization
  - o Numerical computer modeling
  - o Data acquisition software and hardware
- P. A. Kopetka
  - o Mechanical engineering
  - o Cold source design
  - o Electro-mechanical systems
- S. Krueger
  - o Small angle neutron scattering instrumentation
  - o Microstructure of materials
  - o Biological problems
- J. G. LaRock
  - o Mechanical engineering
  - o Neutron instrumentation design
- H. P. Layer
  - o Electronics and data processing
  - o Advanced instrumentation
  - o Fundamental physics
- P. J. Liposky
  - o Design engineering
  - o Nuclear systems and components
- J. W. Lynn
  - o Condensed matter physics
  - o Magnetic and superconducting materials
  - o Neutron scattering methods
- C. F. Majkrzak
  - o Condensed matter physics
  - o Polarized neutron scattering and instrumentation development
  - o Neutron reflectivity measurements

- A. D. Mighell
  - o Crystallographic database development
  - o Single crystal and powder diffraction
  - o Theory of lattices
  
- D. A. Neumann
  - o Molecular and layered materials
  - o Condensed matter physics
  - o Neutron and x-ray scattering instrumentation
  
- J. M. Nicol
  - o Properties of catalysts and adsorbates
  - o Molecular materials
  - o Division safety
  
- J. H. Nicklas
  - o Mechanical engineering
  - o Reactor fuel design
  - o Reactor engineering support
  
- W. J. Orts
  - o SANS instrumentation
  - o Neutron scattering and reflectivity from polymers
  - o Polarized neutron small angle scattering
  
- D. J. Pierce
  - o Mechanical engineering
  - o Neutron instrumentation design
  
- H. J. Prask
  - o Residual stress measurement
  - o Neutron NDE of hardware
  - o Neutron NDE instrumentation
  
- E. Prince
  - o Structural properties of alloys, catalysts and minerals
  - o Advanced crystallographic refinement methods
  - o Software for materials structure analyses
  
- T. M. Raby
  - o Reactor operations
  - o Nuclear engineering
  - o Reactor standards
  
- D. Reznik
  - o Condensed matter physics
  - o Dynamics of High  $T_c$  materials
  - o Dynamics of fullerenes
  
- N. Rosov
  - o Spin echo techniques
  - o Phase transformations
  - o Magnetic materials
  
- J. M. Rowe
  - o Orientationally disordered solids
  - o Hydrogen in metals
  - o Cold neutron research and instrumentation
  
- J. J. Rush
  - o Catalysts and molecular materials
  - o Hydrogen in metals
  - o Inelastic scattering methods

- L. Santodonato
  - o Condensed matter physics
  - o Cryogenics
  
- A. Santoro
  - o Structure of electronic and structured ceramics
  - o Theory of crystal lattices
  - o Powder diffraction methods
  
- S. K. Satija
  - o Low-dimensional molecular systems
  - o Fractal aspects of microporous media
  - o Neutron reflectometry
  
- I. G. Schröder
  - o Cold neutron instrumentation development
  - o Nuclear and engineering physics
  - o Optical devices for neutron transport
  
- J. K. Stalick
  - o Neutron and x-ray diffraction
  - o Inorganic chemistry
  - o Crystal database development
  
- M. A. Suthar
  - o Design engineering
  - o Nuclear systems and components
  
- J. F. Torrence
  - o Reactor supervision
  - o Reactor maintenance
  - o Nuclear engineering
  
- T. J. Udovic
  - o Neutron time-of-flight instrumentation
  - o Properties of catalysts and adsorbates
  - o Hydrogen in metals
  
- D. G. Wiesler
  - o Neutron and x-ray reflectometry
  - o Condensed matter physics
  - o Electrochemistry
  
- R. E. Williams
  - o Cold neutron source development
  - o Nuclear engineering

## TECHNICAL STAFF

### **Reactor Operations**

Richard D. Beasley  
Mark G. Cassells  
Forrest C. Clark  
Howard W. Dilks  
Daniel J. Flynn  
Enrique L. Guarin  
Larry T. Lindstrom  
Michael J. McDonald

William W. Mueller  
Thomas J. Myers  
John H. Ring  
Ricky P. Sprow  
Robert F. Stiber  
Attila L. Toth  
Daniel P. Wilkison  
Kevin D. Wright

### **Reactor Engineering**

James A. Beatty  
Keith Hall  
Lynn A. Shuman

### **Neutron Condensed Matter Research**

George M. Baltic  
C. Douglas Bostian  
David Clem  
William R. Clow, Jr.  
Donald H. Fravel  
William T. Gorman  
Thomas A. Green  
Wayne C. Knill

Doris Kulp  
Michael J. Rinehart  
Lewis P. Robeson  
William H. Rymes  
Thuan T. Thai  
Patrick J. Tobin  
Robert H. Williams (Leader)

## PUBLICATIONS

- Adler, S., Rustic, S., Reimer, J., Fendorf, M., Stacy, A., Huang, Q., Santoro, A., Lynn, J.W., Baltisberger, J., Werner, U., "Local Structure, Vacancy Ordering, and Oxide-ion Motion in Defective Perovskites," *Solid State Ionics*, in press.
- Akcasu, A.Z., Klein, R., Hammouda, B., "Dynamics of Multi-Component Polymer Mixtures Via the Random Phase Approximation Including Hydrodynamic Interactions," *Macromol.* 26, 4136 (1993).
- Allen, A.J., Berk, N.F., "Analysis of SAS Data Dominated by Multiple Scattering for Systems Containing Eccentrically-Shaped Particles or Pores," *J. Appl. Cryst.*, in press.
- Anastasiadis, S.H., Menelle, A., Russell, T.P., Satija, S.K., Majkrzak, C.F., "Very Thin Films of Symmetric Diblock Copolymers," *Prog. Colloid. Polym. Sci.* 91, 88 (1993).
- Anderson, R., Mighell, A.D., Karen, V.L., Jenkins, R., Carr, M.J., "Electron Diffraction Databases," *MSA Bull. Micros. Soc. Am.* 23, 128 (1993).
- Ankner, J.F., "Profile Refinement in Neutron Reflectivity and Grazing Angle Diffraction," in Surface X-ray and Neutron Scattering, Springer Proceedings in Physics, edited by H. Zabel and I. E. Robinson, (Springer-Verlag, New York, Berlin Heidelberg, 1992), pp. 105.
- Ankner, J.F., Majkrzak, C.F., Satija, S.K., "Neutron Reflectivity and Grazing Angle Diffraction," *J. Res. Natl. Inst. Stand. Technol.* 98, 47 (1993).
- Ankner, J.F., Borchers, J.A., Farrow, R.F.C., Marks, R.F., "Combined Low- and High-Angle X-ray Structural Refinement of a Co/Pt(III) Multilayer Exhibiting Perpendicular Magnetic Anisotropy," *J. Appl. Phys.* 73, 6427 (1993).
- Ankner, J.F., Majkrzak, C.F., "Subsurface Profile Refinement for Neutron Specular Reflectivity," in Neutron Optical Devices and Applications, edited by C. F. Majkrzak and J. L. Wood, (SPIE, Bellingham, WA, 1993), pp. 260.
- Ankner, J.F., Majkrzak, C.F., Homma, H., "Magnetic Dead Layer in Fe/Si Multilayer: Profile Refinement of Polarized Neutron Reflectivity Data," *J. Appl. Phys.* 73 6436 (1993).
- Ankner, J.F., Schreyer, A., Zeidler, Th., Majkrzak, C.F., Zabel, H., Wolf, J.A., Grunberg, P., "Polarized Neutron Reflectivity Measurements of Collinear and Noncollinear Magnetic Structures in Fe/Cr (100) Superlattices," *Mat. Res. Soc. Symp. Proc.* (MRS, San Francisco), Spring 1993.
- Ankner, J.F., Schreyer, A., Majkrzak, C. F., Brohl, K., Zeidler, Th., Bodeker, P., Zabel, H., "Quantitative Analysis of Polarized Neutron Specular Reflectivity from a Co/Cu (111) Superlattice at the Second Antiferromagnetic Maximum," *Mat. Res. Soc. Symp. Proc.*, (MRS, San Francisco) Spring 1993, in press.

- Antipov, E.V., Capponi, J.J., Chaillout, C., Chmaissem, O., Loureiro, S.M., Marezio, M., Putilin, S.N., Santoro, A., Tholence, J.L., "Synthesis and Neutron Powder Diffraction Study of Superconductor  $\text{HgBa}_2\text{CaCu}_2\text{O}_{6+\delta}$  Before and After Heat Treatment," *Physica C*, in press.
- Axe, J. D., Moss, S. C., Neumann, D. A., "Structure and Dynamics of Crystalline  $\text{C}_{60}$ ," In Fullerenes, edited by Ehrenreich & Spaepen, Academic Press, in press.
- Banfi, G.P., Degiorgio, V., Rennie, A.R., Barker, J.G., "Small-Angle Neutron Scattering Study of Crystal Growth in Semiconductor-Doped Glasses," *Phys. Rev. Lett.* 69, 3401 (1992).
- Balsara, N., Hammouda, B., "Shear Effects on Block Copolymer Lamellae", *Phys. Rev. Lett.*, in press.
- Bao, W., Broholm, C., Carter, S.A., Rosenbaum, T.F., Aeppli, G., Trevino, S.F., Metcalf, P., Honig, J.M., Spalek, J., "Incommensurate Spin Density Wave in Metallic  $\text{V}_{2-y}\text{O}_3$ ," *Phys. Rev. Lett.* 71, 766 (1993).
- Barker, J.G., Glinka, C.J., "Development of a Focusing Mirror for SANS," in Neutron Optical Devices and Applications, edited by Majkrzak, C.F., Wood, J.L. (Bellingham, WA, 1993), pp. 386.
- Beach, R.S., Matheny, A., Salamon, M.B., Flynn, C.P. Borchers, J.A., Erwin, R.W., Rhyne, J.J., "Magnetism and Epitaxy in Lu/Dy/Lu Tri-layers," *J. Appl. Phys.* 73, 690 (1993).
- Beach, R.S., Borchers, J.A., Matheny, A., Erwin, R.W., Salamon, M.B., Everitt, B., Pettit, K., Rhyne, J.J., Flynn, C.P., "Enhanced Curie Temperatures and Magnetoelastic Domains in Dy/Lu Superlattices and Films," *Phys. Rev. Lett.* 70, 3502 (1993).
- Benoit, H., Joanny, J.F., Hadzisionnou, G., Hammouda, B., "Scattering by Linear, Branched and Copolymer Chain Molecules for Large Scattering Vectors," *Macromol.* 26, 7590 (1993).
- Berk, N.F., "Outline of Neutron Scattering Formalism," *J. Res. Natl. Inst. Stand. Technol.* 98, 15 (1993).
- Berliner, R., Smith, H.G., Copley, J.R.D., Trivisonno, J., "Structures of Sodium Metal," *Phys. Rev. B* 46, 14 436 (1992).
- Berry, S. D., Lind, D. M., Lochner, E., Shaw, K.A., Hilton, D., Erwin, R.W., Borchers, J. A., "Interfacial Exchange Coupling and the Magnetization of Iron Oxide/ Nickel Oxide Superlattices," *Mat. Res. Soc. Symp. Proc.*, (MRS, San Francisco), Spring 1993, in press.
- Blau, M., Rowe, J. M., Williams, R. E., "Nuclear Heat Load Calculations for the NBSR Cold Neutron Source Using MCNP," *Trans. Am. Nucl. Soc.* 69, 404 (1993).

- Borchers, J.A., Carey, M.J., Erwin, R.W., Berkowitz, A.E., Majkrzak, C.F., "Propagation of Antiferromagnetic Order Across Paramagnetic Layers in CoO/NiO Superlattices," *J. Appl. Phys.* 73, 6427 (1993).
- Borchers, J. A., Erwin, R., "Comment on 'Phase Transitions in Antiferromagnetic Superlattices'," *Phys Rev B* 48, 6711 (1993).
- Borchers, J.A., Carey, M.J., Erwin, R.W., Majkrzak, C.F., Berkowitz, A.E., "Spatially Modulated Antiferromagnetic Order in CoO/NiO Superlattices," *Phys. Rev. Lett.*, 70, 1878 (1993).
- Borchers, J.A., Erwin, R.W., Berry, S.D., Lind, D.M., Lochner, E., Shaw, K.A., "Magnetic Structure Determination for Fe<sub>3</sub>O<sub>4</sub>/NiO Superlattices", *Appl. Phys. Lett.*, in press.
- Borchers, J.A., Ankner, J.F., Majkrzak, C.F., Engel, B.N., Wiedmann, M.H., Van Leeuwen, Falco, C.M., "Spatial Modulation of the Magnetic Moment in Co/Pd Superlattices Observed by Polarized Neutron Reflectivity," *J. Appl. Phys.*, in press.
- Borchers, J.A., Erwin, R.W., "Structural and Magnetic Ordering in Iron Oxide/Nickel Oxide Multilayers by X-Ray and Neutron Diffraction," *J. Appl. Phys.*, 73, 6886 (1993).
- Brand, P.C., Prask, H.J., "New Methods for the Alignment of Instrumentation for Residual Stress Measurements by Means of Neutron Diffraction," *J. Appl. Cryst.*, in press.
- Carey, M.J., Berkowitz, A.E., Borchers, J.A., Erwin, R.W., "Strong Interlayer Coupling in CoO/NiO Antiferromagnetic Superlattices", *Phys. Rev.* B47, 9952 (1993).
- Casella, R.C. and Werner, S.A., "Electromagnetic Acceleration of Neutrons," *Phys. Rev. Lett.* 69 1625 (1992).
- Casella, R.C., Werner, S.A., "Casella and Werner Reply to the Comment of Wagh and Rakhecha," *Phys. Rev. Lett.* 69, 3590 (1992).
- Chaillout, C., Huan, Q., Cava, R.J., Chenavas, J., Santoro, A., Bordet, P., Hodeau, J.L., Krajewski, J.J., "Synthesis and Crystal Structure of BaSrCuO<sub>2+x</sub> · CO<sub>3</sub>," *Physica C* 195, 335 (1992).
- Chattopadhyay, T., Lynn, J.W., Rosov, N., Grigereit, T.E., Barilo, S.N., Zhigunov, D.I., "Magnetic Ordering in Eu<sub>2</sub>CuO<sub>4</sub>," *Phys. Rev. B*, in press.
- Chmaissem, O., Huang, Q., Putilin, S., Marezio, M., Santoro, A., "Neutron Powder Diffraction Study of the Crystal Structures of HgBa<sub>2</sub>CuO<sub>4+δ</sub> and HgBaO<sub>2</sub>," *Physica C* 212, 259 (1993).

- Chmaissem, O., Huang, Q., Antipov, E.V., Putilin, S.N., Marezio, M., Loureiro, S.M., Capponi, J.J., Tholence, J.L., and Santoro, A., "Neutron Powder Diffraction Study at Room Temperature and at 10K of the Crystal Structure of the 133K Superconductor  $\text{HgBa}_2\text{Ca}_2\text{Cu}_3\text{O}_{8+\delta}$ ," *Physica C* 217, 265 (1993).
- Choi, C.S., Prask, H.J., Orosz, J., "Texture Study of Two Molybdenum Shaped Charge Liners by Neutron Diffraction," *J. Mat. Sci.* 28, 3557 (1993).
- Choi, C.S., Prask, H.J., Orosz, J., "Textures of Tantalum Metal Sheets by Neutron Diffraction," *J. Mat. Sci.* 28, 3283 (1993).
- Choi, C. S., Baker, E. L., Orosz, J., "Microstructure Study of Molybdenum Liners by Neutron Diffraction," in Proc. of Nondestructive Characterization of Materials VI, edited by R. E. Green and C. O. Ruud, (Plenum Press), New York, in press.
- Christides, C., Neumann, D.A., Prassides, K., Copley, J.R.D., Rush, J.J., Rosseinsky, M.J., Murphy, D.W., Haddon, R.C., "Neutron Scattering Study of  $\text{C}_{60}^n$  ( $n=3,6$ ) Librations in Alkali-Metal Fullerides," *Phys. Rev. B* 46, 12 088 (1992).
- Christides, C., Dennis, T.J.S., Prassides, K., Cappelletti, R.L., Neumann, D.A., Copley, J.R.D., "Rotational Dynamics of Solid  $\text{C}_{70}$ : A Neutron Scattering Study," *Phys Rev B.*, in press.
- Christides, C., Prassides, K., Neumann, D.A., Copley, J.R.D., Mizuki, J., Tanigaki, K., Hirose, I., Ebbesen, T.W., "Rotational Dynamics of  $\text{C}_{60}$  in  $\text{Na}_2\text{RbC}_{60}$ ," *Europhys. Letts.*, in press.
- Clinton, T.W., Lynn, J.W., Lee, B.W., Buchgeister, M., Maple, M.B., "Oxygen Dependence of the Magnetic Order of Nd in  $\text{NdBa}_2\text{Cu}_3\text{O}_{6+x}$ ," *J. Appl. Phys.* 73 6320 (1993).
- Clinton, T.W., Lynn, J.W., Liu, J.Z., Jia, Y.X., Shelton, R.N., "Two- and Three-Dimensional Magnetic Order of Er in Superconductivity  $\text{ErBa}_2\text{Cu}_3\text{O}_7$ ," *Physica C*, in press.
- Cole, M., Finch, A. N., Prince, E., "Low Temperature Structure of  $\text{KUO}_2\text{PO}_4\cdot 3\text{D}_2\text{O}$  Determined from Combined Synchrotron Radiation and Neutron Powder Diffraction Measurements," *J. Mater. Chem.* 3, 519 (1993).
- Composto, R.J., Mansfield, T., Beaucage, G., Stein, R.S., Iyengar, D.R., McCarthy, T.J., Satija, S.K., Ankner, J.F., Majkrzak, C.F., "The Volume Fraction Profile of Terminally Adsorbed Polymers," in Complex Fluids, Mat. Res. Soc. Symp. Proc. (MRS, San Francisco), Spring 1993, in press.
- Copley, J.R.D., "The Joy of Acceptance Diagrams," *J. Neut. Res.* 1, 21 (1993).
- Copley, J.R.D., "Acceptance Diagram Analysis of the Performance of Multidisk Neutron Velocity Selectors," *Nucl. Inst. Meth.* A332, 511 (1993).



- Copley, J.R.D., Michel, K.H., "Neutron and X-Ray Scattering Cross Sections of Orientationally Disordered Solid C<sub>60</sub>," *J. Phys. B: Condens. Matter* 5, 4353 (1993).
- Copley, J.R.D., Mildner, D.F.R., "Simulation and Analysis of the Transmission Properties of Curved-Straight Neutron Guide Systems," *Nucl. Sci. & Eng.* 110, 1 (1992).
- Copley, J.R.D., Udovic, T.J., "Neutron Time-of-Flight Spectroscopy," *J. Res. Natl. Inst. Stand. Technol.* 98, 71 (1993).
- Copley, J.R.D., David, W.I.F., Neumann, D.A., "Structure and Dynamics of Buckyballs," *Neutron News.*, in press.
- Depondt, P., Neumann, D.A., Trevino, S.F., "Maximum Entropy as a Tool for the Determination of the c-axis Profile of Layered Compounds," *Acta Cryst.* B49, 153 (1993).
- Everitt, B.A., Salamon, M.B., Flynn, C.F., Park, B.J., Borchers, J.A., Erwin, R.W., Tsui, F., "Magnetic Properties of Dy-Lu Alloys", *J. Appl. Phys.*, in press.
- Gehring, P.M., Hirota, K., Majkrzak, C.F., Shirane, G., "Origin of the Second Length Scale above the Magnetic Spiral Phase of Tb," *Phys. Rev. Lett.* 71, 1087 (1993).
- Gehring, P.M. Chou, H., Shapiro, S.M., Hriljac, J., Chen, D.H., Toulouse, J., Rytz, D., Boatner, L. A., "Anomalous Dispersion and Thermal Expansion in Lightly Doped KTa<sub>1-x</sub>Nb<sub>x</sub>O<sub>3</sub>," *Ferroelectrics*, in press.
- Giebultowicz, T.M., Faschinger, W., Bauer, G., Nunez, V., Klosowski, P., Furdyna, J.K., "Antiferromagnetic Spin Ordering and Interlayer Magnetic Correlations in MnTe/CdTe Superlattices, 6th International Conf. on II-VI Semiconductors and Related Devices, (Newport, RI, Sept. 1993), *J. Cryst. Growth*, in press.
- Giebultowicz, T.M., Furdyna, J.K., Luo, Hong, Samarth, N., Rhyne, J.J., "Strain-Engineered Magnetic Phenomena in MnSe/ZeSe, MnTe/ZnTe, and MnSe/ZnTe Superlattices", *INTERMAG '93 Conf. Proc., IEEE Trans. on Magnetism*, (April 1993), in press.
- Giebultowicz, T.M., Klosowski, P., Samarth, N., Luo, H., Furdyna, J.K., Rhyne, J.J., "Neutron Diffraction Studies of ZincBlende MnTe Epilayers and MnTe/ZnTe: The Effects of Strain and Dilution in a in a Strongly Frustrated FCC Antiferromagnet", *Phys. Rev. B* 48, 12817 (1993).
- Giebultowicz, T.M., Samarth, N., Luo, H., Furdyna, J.K. Klosowski, P., "Strain-Engineered Incommensurability in Epitaxial Heisenberg Antiferromagnets," *Phys. Rev. B* 46, 12070 (1992).
- Giebultowicz, T.M., Luo, H., Samarth, N., Furdyna, J.K., Nunez, V., Rhyne, J.J., Faschinger, W., Springholtz, G., Bauer, G., Sitter, H., "Strain-induced Helimagnetism, Finite Thickness effects and Interlayer Coupling in Magneti Semiconductor Multilayer," *Physica B*, in press.

- Gygax, F.N., Amato, A., Anderson, I.S., Rush, J.J., Schenck, A., "Study of Localization and Diffusion in Scandium and Yttrium," *Zeitschrift für Physikalische Chemie*, in press.
- Hammouda, B., Krueger, S., Glinka, C.J., "Small Angle Neutron Scattering at the National Institute of Standards and Technology," *J. Res. Natl. Inst. Stand. Technol.* 98, 31 (1993).
- Hammouda, B., "SANS from Homogenous Polymer Mixtures: A Unifield Overview," *Adv. Poly. Sci.* 106, 87 (1993).
- Hammouda, B., "Scattering From Mixtures of Flexible and Stiff Polymers," *J. Chem. Phys.*, 98, 3439 (1993).
- Hammouda, B., "Random Phase Approximations for Compressible Polymer Blends," *J. Non-Crystal. Solids*, in press.
- Hammouda, B., "Structure Factors for Regular Polymer Gels and Networks," *J. Chem. Phys.*, in press.
- Hammouda, B., "Dynamics of Ternary Polymer Solutions," *Macromol.* 26, 4800 (1993).
- Harrison, W.T.A., Liang, C.S., Nicol, J.M., Stucky, G.D., "Microporous, Noncentrosymmetric, Octahedral/Tetrahedral-Framework Phases:  $K_{2/3}Li_{1/3}Nb_2PO_8$ ,  $K_{2/3}Li_{1/3}Ta_2PO_8$  and  $K_{2/3}Ag_{1/3}Nb_2PO_8$ ," *Inorg. Chem.*, in press.
- Heremans, C., Wuensch, B.J., Stalick, J.K., Prince, E., "Fast-Ion Conduction and Disorder in Cation and Anion Arrays in  $Y_2(Zr_yTi_{1-y})$ ," *Mat. Res. Soc. Symp. Proc.* 293, 349 (1993).
- Huang, Q., Sunshine, S.A., Cava, R.J., Santoro, A., "Neutron Powder Diffraction Study of the Crystal Structure of  $YSr_2CoCu_2O_7$ ," *J. Solid State Chem.* 102, 534 (1993).
- Huang, Q., Lynn, J.W., Meng, R.L., Chu, C. W., "Crystal Structure of Annealed and As-prepared  $HgBa_2CaCu_2O_{6+\delta}$ ," *Physica C*, in press.
- Huang, Q., Karen, P., Karen, V.L., Kjekshus, A., Lynn, J.W., Mighell, A.D., Natali, Sora, I., Rosov, N., Santoro, A., "Neutron Powder Diffraction Study of the Nuclear and Magnetic Structures of the Oxygen-Deficient Perovskite  $YBaCuCoO_5$ ," *J. Solid State Chem.*, in press.
- Karim, A., Satija, S.K., Orts, W., Ankner, J.F., Majkrzak, C.F., Fetters, L.J., "Chemical Grafting of Silane End-Functionalized Polymer on Silicone Surfaces," *Proc. Mat. Res. Soc. Symp. (MRS, San Francisco)*, Spring, 1993.
- Keimer, B., Aksay, I., Dogan, F., Erwin, R. W., Lynn, J. W., Sarikaya, M., "Inclined-Field Structure, Morphology and Pinning of the Vortex Lattice in Microtwinned  $YBa_2Cu_3O_7$ ," *Science*, in press.

- Knell, U., Heid, C., Wipf, H., Udovic, T.J., Rush, J.J., Lauter, H.J., "Hydrogen in  $\text{YBa}_2\text{Cu}_3\text{O}_x$ : A Neutron Spectroscopy and a Nuclear Magnetic Resonance Study," *Z. Phys. Chem.*, in press.
- Knell, U., Wipf, H., Lauter, H.J., Udovic, T.J., Rush, J.J., "A Neutron-Spectroscopy Study of the Hydrogen Vibrations in Hydrogen-doped  $\text{Yba}_2\text{Cu}_3\text{O}_x$ ", *J. Phys.: Condens. Matter* 5, 7607 (1993).
- Krueger, S., Olson, G.J., Johnsonbaugh, D., Beveridge, T. J., "Characterization of the Binding of Gallium, Platinum and Uranium to Pseudomonas Fluorescents using Small Angle X-ray Scattering and Transmission Electron Microscopy , " *Appl. Environ. Microbiol.*, in press.
- Lee, D.D., Chen, S.H., Satija, S.K., Majkrzak, "Investigation of Surface Ordering in a Microemulsion near the Lamellar Transition by Neutron Reflectivity," *Proc. of 2nd Liquid State Conference (EPS) in Florence, Italy (Sept. 1993)*, in press.
- Lee, W.T., Kaiser, H., Rhyne, J.J., Dumesnil, K., Dufour, C., Mangin, Ph., Marchal, G., Erwin, R.W., Borchers, J.A., "Exchange Coupling in Dy/Er Metallic Superlattices," *J. Appl. Phys.*, in press.
- Li, W-H., Chang, K.J., Hsieh, W.T., Lee, K.C., Lynn, J.W., Yang, H.D., "Magnetic Ordering of Pr in  $\text{PrBa}_2\text{Cu}_{2.7}\text{Zn}_{0.3}\text{O}_{7-y}$ ," *Phys. Rev.* B48, 519 (1993).
- Lieb, R.J., Trevino, S.F., "A Small Angle Neutron and X-Ray Scattering Study of the Onset and Nature of Fracture of Uniaxially Compressed Gun Propellants," *Proc. of U.S. Army Science Conference*, in press.
- Lind, D.M., Tay, S.-P., Berry, S.D., Borchers, J.A., Erwin, R.W., "Structural and Magnetic Ordering in Iron Oxide/Nickel Oxide Multilayers by X-Ray and Neutron Diffraction," *J. Appl. Phys.* 73, 6886 (1993).
- Lynn, J.W., "Magnetic Ordering in Oxide Superconductors," High Temperature Superconductivity, edited by S. K. Malik and S. S. Shah (Nova Science Publishers, Inc., New York, 1993).
- Lynn, J. W., Rosov, N., Fish, G., "Polarization of the Magnetic Excitations in Invar and Non-Invar Amorphous Alloys," *J. Appl. Phys.* 73, 5369 (1993).
- Lynn, J.W., Rosov, N., Barilo, A.N., Zhigurov, D.I., "Magnetic Ordering in  $\text{Eu}_2\text{CuO}_4$ ", *Phys. Rev. B*, in press.
- Lynn, J.W., Rosov, N., Acet, M., Bach, H., "Polarization Analysis of the Magnetic Excitations in  $\text{Fe}_{65}\text{Ni}_{35}$  Invar", *J. Appl. Phys.*, in press.
- Lynn, J.W., "Magnetic Neutron Scattering," *J. Appl. Phys.*, in press.

- Majkrzak, C.F., Berk, N.F., Ankner, J.F., Satija, S.K., Russell, T.P., "Determination of Non-Magnetic Density Profiles Using Polarized Neutron Reflectivity," in Neutron Optical Devices and Applications, edited by Majkrzak, C.F., Wood, J.L. (SPIE, Bellingham, WA, 1993), pp. 282.
- Majkrzak, C.F., Nunez, V., Copley, J.R.D., Ankner, J.F., Greene, G.C., "Supermirror Transmission Polarizers for Neutrons," in Neutron Optical Devices and Applications, edited by Majkrzak, C.F., Wood, J.L. (SPIE, Bellingham, WA, 1993), pp. 90.
- Majkrzak, C.F., "Chapter XIII: Polarized Neutrons," in Handbook of Neutron Scattering, edited by W. Glaser, in press.
- Majkrzak, C.F., Ankner, J.F., Berk, N.F., Gibbs, D., "Neutron and X-ray Diffraction Studies of Magnetic Multilayers," in Magnetic Multilayer, edited by Watson, R., and Bennett, L. (World Scientific Publishers), in press.
- Majkrzak, C.F., Ankner, J.F., "Supermirror Neutron Guide Coatings," in Neutron Optical Devices and Applications, edited by Majkrzak, C.F., Wood, J.L. (SPIE, Bellingham, WA, 1993), pp. 150.
- Mayes, A.M., Russell, T.P., Satija, S.K., Majkrzak, C.F., "Homopolymer Distributions in Ordered Block Copolymers," *Macromol.* 25, 6523 (1993).
- Mayes, A.M., Johnson, R.D., Russell, T.P., Smith, S.D., Satija, S.K., Majkrzak, C.F., "Distributions of Chain Ends and Junction Points in Ordered Block Copolymers," *Macromolecules* 26, 1047 (1993).
- McDermott, D.C., Kanelleas, D.K., Thomas, R.K., Rennie, A.R., Satija, S.K., Majkrzak, C.F., "Study of the Adsorption from Aqueous Solution of Mixtures of Non-Ionic and Cationic Surfactants on Crystalline Quartz Using the Technique of Neutron Reflection," *Langmuir* 9, 2406 (1993).
- Menelle, A., Russell, T.P., Anastasiadis, S.H., Satija, S.K., Majkrzak, C.F., "The Ordering of Thin Diblock Copolymer Films," *Phys. Rev. Lett.* 68, 67 (1992).
- Michel, K.H., Copley, J.R.D., Neumann, D.A., "Reply to the Comment by Burgos et al. on 'Microscopic Theory of Orientational Disorder and the Orientational Phase Transitions in Solid C<sub>60</sub>'," *Phys. Rev. Lett.* 69, 3590 (1992).
- Mighell, A.D., Rodgers, J.R., Karen, V.L., "Protein Symmetry: Metric and Crystal," *J. Appl. Cryst.* 26, 68 (1993).
- Morris, R.E., Harrison, W.T.A., Nicol, J.M., Wilkinson, A.P., Cheetham, A.K., "Determination of Complex Structures by Combined Neutron and Synchrotron X-Ray Powder Diffraction," *Nature* 359, 519 (1992).

- Natali Sora, I., Wong-Ng, W., Huang, Q., Roth, R.S., Rawn, C.J., Burton, B.P., Santoro, A., "X-Ray and Neutron Diffraction Study of  $\text{CaBi}_2\text{O}_4$ ," J. Solid State Chem., in press.
- Natali Sora, I., Huang, Q., Lynn, J.W., Rosov, N., Karen, P., Kjekshus, A., Karen, V.L., Mighell, A.D., Santoro, A., "Neutron Powder Diffraction Study of the Nuclear Magnetic Structures of the Substitutional Compounds  $(\text{Y}_{1-x}\text{Ca}_x)\text{Ba}_2\text{Fe}_3\text{O}_{8+\delta}$ ," Phys. Rev. B, in press.
- Nakotte, H., Robinson, R.A., Lynn, J.W., Bruck, E., deBoer, F.R., "Field-Induced Transition in UPdSn at 3T," Phys. Rev. B47, 831 (1993).
- Nakotte, H., Bruck, E., Brabers, J. H. V. J., Prokes, K., de Boer, F. R., Sechovsky, V., Buschow, K. H. J., Andreev, A.V., Robinson, R.A., Purwanto, A., Lynn, J. W., "Magnetic Properties of Single-Crystalline  $\text{UCu}_3\text{Al}_2$ ," J. Appl. Phys., in press.
- Nenoff, T.M., Harrison, W.T.A., Nicol, J.M., Stucky, G.D., Newsam, J.M., "The Crystal Structure of a New Sodium Zinc Arsenate Phase Solved by Simulated Annealing," Zeolites, 13, 506 (1993).
- Nenoff, T.M., Harrison, W.T.A., Gier, T.E., Nicol, J.M., Stucky, G.D., "Structural Characterization of a Dehydrated Magnesium/Sodium Beryllphosphate-X Phase," Zeolites 12, 770 (1992).
- Nenoff, T.M., Harrison, W.T.A., Gier, T.E., Keder, N.L., Zaremba, C.M., Srdanov, V.I., Nicol, J.M., Stucky, G.D., "Structural Chemical Investigation of  $\text{Na}_3(\text{ABO}_3)_4\text{H}_2\text{O}$  - Type Sodalite Phases," Inorg. Chem., in press.
- Neumann, D.A., Hammouda, B., "Ultra-High Resolution Inelastic Neutron Scattering," J. Res. Natl. Inst. Stand. Technol. 98, 89 (1993).
- Neumann, D. A., Copley, J. R. D., Reznik, D., Kamitakahara, W. A., Rush, J. J., Paul, R. L., Lindstrom, R. M., "Inelastic Neutron Scattering Studies of Rotational Excitations and the Orientational Potential in  $\text{C}_{60}$  and  $\text{A}_3\text{C}_{60}$  Compounds," J. Phys. Chem. Solids, in press.
- Nunez, V., Majkrzak, C.F., Berk, N.F., "Dynamical Scattering of Polarized Neutrons by Thin Magnetic Films," Proc. Materials Research Society Meeting, 313 (1993), pp. 431.
- Olivier, B.J., Schaefer, D.W., Frick, B., Richter, D., Farago, B., Ashley, C.S., Kamitakahara, W.A., "Low-energy Dynamics of Colloidal Versus Polymeric Silica Aerogel," Trans. ACA 27, 1991, Am. Crystal. Assoc. 1993.
- Overhauser, A.W., Giebultowicz, T.M., "Polarization of Spin Density Waves in Lead", Phys. Rev. B 48, 14338 (1993).

- Perahia, D., Wiesler, D.G., Satija, S.K., Fetters, L.J., Sinha, S.K., Milner, S.T., "Neutron Reflectivity of End Grafted Polymers: Concentration and Solvent Quality Dependence in Equilibrium Conditions," *Phys. Rev. Letts.*, in press.
- Prask, H. J., "Materials Characterization with Cold Neutrons", in *Proc. of Nondestruction Characterization of Materials VI*, edited by R.E. Green and C.O. Ruud, (Plenum Press), New York, in press.
- Prask, H.J., Choi, C.S., "Texture: Nondestructive Characterization", in *Concise Encyclopedia of Materials Characterization*, edited by R.W. Cahn and E. Lifshin (Pergammon Press, Oxford, Jan. 1993), pp. 497.
- Prask, H.J., Rowe, J.M., Rush, J.J., Schröder, I.G., "The NIST Cold Neutron Research Facility," *J. Res. Natl. Inst. Stand. Technol.* 98, 1 (1993).
- Prask, H.J., Rowe, J.M., "The Reactor and Cold Neutron Research Facility at NIST," *Proc. of the 3rd International Group on Research Reactors (IGORR-III)*, in press.
- Prask, H.J., "NIST Reactor: Summary of Activities," NISTIR 5120, 1993.
- Price, D.L., Rush, J.J., "Neutron Sources and Applications, "Report of a Review held at Oak Brook, IL, September 8-10, 1992, DOE/ER-0607 p.
- Prince, E., "Construction of Maximum Entropy Density Maps, and Their Use in Phase Determination and Extension," *Acta Crystallg.* D49, 61 (1993).
- Prince, E., Stalick, J.K., editors *Accuracy in Powder Diffraction II Proceedings of the International Conference*, May 26-29, 1992, NIST Spec. Publ. 846.
- Prince, Edward, "Mathematical Aspects of Rietveld Refinement," in *The Rietveld Method*, edited by R.A. Young (International Union of Crystallography, The Netherlands, 1993), pp. 43.
- Reis, K.P., Prince, E., Whittingham, S.M., "Rietveld Analysis of  $\text{Na}_{x/2} \cdot y\text{H}_2\text{O}$  Which has the Hexagonal Tungsten Bronze Structure," *Solid State Ionics* 4, 307 (1992).
- Reis, K.P., Jacobson, A.J., Nicol, J.M., "A Powder Neutron Diffraction Investigation of Structure and Cation Ordering in  $\text{Ba}_{2+x}\text{Bi}_{2-x}\text{O}_{6-y}$ ," *J. Solid State Chem.*, in press.
- Reznik, D., Kamitakahara, W.A., Neumann, D.A., Copley, J.R.D., Fischer, J.E., Strongin, R.M., Cichy, M.A., Smith III, A.B., "A Neutron Scattering Study of Librations and Intramolecular Phonons in  $\text{Rb}_{2.6}\text{K}_{0.4}\text{C}_{60}$ ," *Phys. Rev. B*, in press.
- Rhyne, J. J., Salamon, M. B., Flynn, C. P., Erwin, R. W., Borchers, J. A., "Magnetic Structures of Superlattices," *J. Mag. Magn. Mats.*, in press.

- Robinson, R.A., Lawson, A.C., Lynn, J.W., Buschow, K.H.J., "Incommensurate Magnetic Order in UPtGe," Phys. Rev. B 47, 6138 (1993).
- Robinson, R.A., Lynn, J.W., Nunez, V., Buschow, K.H.J., Nakotte, H., Lawson, A.C., "Crystallographic and Magnetic Properties of UAuSn," Phys. Rev. B 47, 5090 (1993).
- Robinson, R.A., Lynn, J.W., Lawson, A.C., Nakotte, H., "Temperature Dependence of Magnetic Order in Single-crystalline UPdSn", J. Appl. Phys., in press.
- Rosov, N., Lynn, J.W., Williams, J.J.M., Landee, C.P., "Quasi-Elastic and Inelastic Neutron Scattering Studies of  $[(CD_3)ND]FeCl_3 \cdot 2D_2O$ : A One-Dimensional Ising Ferromagnet," J. Appl. Phys. 73, 6081 (1993).
- Rosov, N., Lynn, J.W., Gao, G., O'Reilly, J.W., Pernambuco-Wise, P., Crow, J.E., "Magnetic Ordering of the Cu Spins in  $PrBa_2Cu_3O_{6+x}$ ," Physica C 204, 171 (1992).
- Rosov, N., Lynn, J.W., Erwin, R.W., "Resolution Considerations for Polarized Triple-Axis Spectrometry," Physica B 180 & 181, 1003 (1992).
- Rosov, N., Lynn, J.W., Radousky, H.B., Bennahias, M., Goodwin, T.J., Klavins, P., Shelton, R.N., "Crystal Structure and Magnetic Ordering of the Rare Earth and Cu Moments in  $RBa_2Cu_2NbO_8$  (R = Nd, Pr)," Phys. Lett. B47, 15256 (1993).
- Rosov, N., Lynn, J.W., Kästner, J., Wassermann, E.F., Bach, H., "Temperature Dependence of the Magnetic Excitations in Ordered and Disordered  $Fe_3Pt$ ," J. Appl. Phys., in press.
- Russell, T.P., Menelle, A., Anastasiadis, S.H., Satija, S.K., Majkrzak, C.F., "Ordering of Thin Films of Symmetric Diblock Copolymers," Prog. Colloid. Poly. Sci. 91 97 (1993).
- Russell, T.P., Menelle, A., Anastasiadis, S.H., Satija, S.K., Majkrzak, C.F., "Unconventional Morphologies of Symmetric, Diblock Copolymers Due to Film Thickness Constraints," Prog. Colloid. Poly. Sci. 91, 101 (1993).
- Sanders, P.G., Weertman, J.R., Barker, J.G., Siegel, R.W., "The Effect of Annealing on Small Angle Neutron Scattering From Nanocrystalline Palladium," Scripta Metallurgica. 29, 91 (1993).
- Santoro, A., "Description of Layered Structures--Applications to High  $T_c$  Superconductors", J. Alloys and Compounds 197, 153 (1993).
- Saslow, W.M., Erwin, R., "Normal Modes and Structure Factor for a Canted Spin System: The Generalized Villain Model," Phys. Rev. B 45, 4759 (1993).
- Schober, T., Hempelmann, R., Udovic, T.J., "Hydrogen Sites in  $ZrCoH_3$  by Neutron Vibrational Spectroscopy," Z. Phys. Chem., in press.

- Schreyer, A., Ankner, J.F., Schafer, M., Zeidler, Th., Grübery, P., Majkrzak, C.F., Zabel, H., "Direct Observation of Non Collinear Spin Structures in Fe/Cr (100) Superlattices Using Spin Polarized Neutron Reflectometry, Proc. Conference on Surface X-Ray and Neutron Scattering (Dubna, Russia) June, 1993.
- Schreyer, A., Metoki, N., Zeidler, Th., Bödeker, P., Abromeit, A., Morawe, Ch., Romahn, U., Sonntag, P., Bröhl, K., Zabel, H., Ankner, J.F., Majkrzak, C.F., "Exchange Coupling in Single Crystalline Co/Cu (111) Superlattices," J. Magnet. and Magnet. Mater, in press.
- Schreyer, A., Brohl, D., Ankner, J.F., Zeidler, Th., Bodeker, P., Metoki, N., Majkrzak, C.F., Zabel, H., "Oscillatory Exchange Coupling in Co/Cu(111) Superlattices," Phys. Rev. B47, 15334 (1993).
- Schreyer, A., Zeidler, T., Morawe, Ch., Metoki, N., Zabel, H., Ankner, J.F., Majkrzak, C.F., "Spin Polarized Neutron Reflectivity Study of a Co/Cu Superlattice," J. Appl. Phys. 73, 7616 (1993).
- Schröder, A., Lynn, J. W., Erwin, R. W., Loewenhaupt, M., Lohneysen, H. V., "Magnetic Structure of the Heavy Fermion Alloy CeCu<sub>5.5</sub>Au<sub>0.5</sub>," Physica B, in press.
- Sikka, M., Singh, N., Karim, A., Bates, F.S., Satija, S.K., Majkrzak, C.F., "Entropy Driven Surface Segregation in Block Copolymer Melts," Phys. Rev. Lett, in press.
- Skanthakumar, S., Lynn, J.W., Peng, J.L., Li, Z.Y., "Observation of Noncollinear Magnetic Structure for the Cu Spins in Nd<sub>2</sub>CuO<sub>4</sub> Type Systems," Phys. Rev. B47 (Rapid Communications) 6173 (1993).
- Skanthankumar, S., Lynn, J.W., Peng, J.L., Li, Z.Y., "Field Dependence of the Magnetic Ordering of Cu in R<sub>2</sub>CuO<sub>4</sub>," J. Appl. Phys. 73, 6326 (1993).
- Stalick, J.K., "Quantitative Phase Analysis with the Rietveld Method," in Proc. on Accuracy in Powder Diffraction II (NIST, Gaithersburg, MD, May 26-29, 1992), NIST Spec. Publ. 846, pp. 34.
- Stalick, J.K., Santoro, A., "Crystal Chemistry of the Substitution Compounds of YBa<sub>2</sub>Cu<sub>3</sub>O<sub>7</sub>," in Current Status and Future Directions in Condensed Matter Physics, edited by S.K. Maikl, in press.
- Stewart, J.M., Collins, D.M., Watenpugh, K.D., Prince, E., "Programs for Phasing by Entropy Maximization as Implemented in Xtal 3.2: a Crystallographic Software System," Acta Cryst. D49, 100 (1993).
- Sumarlin, I.W., Lynn, J.W., Neumann, D.A., Rush, J.J., Loong, C-K, Peng, J.L., Lin, Z. Y., "Phonon Density-of-States in R<sub>2</sub>CuO<sub>4</sub> and Superconducting R<sub>1.85</sub>Ce<sub>0.15</sub>CuO<sub>4</sub> (R = Nd, Pr)," Phys. Rev. B48, 473 (1993).



- Sumarlin, I. W., Lynn, J. W., Chattopadhyay, T., "Dispersion of Magnetic Excitations of the Pr Ions in Pr<sub>2</sub>CuO<sub>4</sub>," *Physica C*, in press.
- Toney, M.F., Wiesler, D.G., "Instrumental Effects on Measurements of Surface X-Ray Diffraction Rods: Resolution and Active Sample Area," *Acta Cryst. A* 49, 624 (1993).
- Trevino, S.F., Choi, C.S., Neumann, D.A., "The Methyl Torsional Levels of Solid Acetonitrile (CH<sub>3</sub>CN)-A Neutron Scattering Study," *J. Chem. Phys.* 98, 78 (1993).
- Trevino, S.F., "The Triple Axis and SPINS Spectrometer," *J. Res. Natl. Inst. Stand. Technol.* 98, 59 (1993).
- Tsui, F., Flynn, C.P., Beach, R.S., Borchers, J.A., Erwin, R.W., Rhyne, J.J., "Magnetic Structure in Dy/Sc Superlattices," *J. Appl. Phys.* 73, 6904 (1993).
- Tun, Z., Lussier, J-G., Erwin, R.W., Lynn, J.W., Harrison, A., "A Polarization Analysis of Magnetic Excitations in CsMnI<sub>3</sub>," *Phys. Rev.* B48, 6152 (1993).
- Udovic, T.J., Rush, J.J., Berk, N.F., Anderson, I.S., Daou, J.N., Vajda, P., Blaschko, O., "Neutron Spectroscopic Comparison of Rare-Earth/Hydrogen  $\alpha$ -Phase Systems," *Z. Phys. Chem.* 179, 349 (1993).
- Wiesler, D. G., Majkrzak, C. F., "Neutron Reflectometry Studies of Surface Oxidation," *Proc. Conference on Surface X-Ray and Neutron Scattering*, (Dubna, Russia) June, 1993, in press.
- Wiesler, D. G., Toney, M. F., Melroy, O. R., McMillan, C. S., Smyrl, W. H., "X-ray Diffraction from Anodic TiO<sub>2</sub> Films: In Situ and Ex Situ Comparison of the Ti(0001) Face," *Surf. Sci*, in press.
- Williams, R. E., Blau, M., Rowe, J. M., "Cold Neutron Gain Calculations for the NBSR Using MCNP," *Trans. Am. Nucl. Soc.* 69, 401 (1993).
- Wu, W., Majkrzak, C.F., Satija, S.K., Ankner, J.F., Orts, W.J., Satkowski, M., Smith, S.D., "The Density Profile at a Polymer/Solid Interface," *Polymer Comm.* 33, 5081 (1992).
- Wu, S.Y., Hsieh, W.T., Li, W-H, Lee, K.C., Lynn, J.W., Yang, H.D., "Two-Dimensional Magnetic Order in Pb<sub>2</sub>Sr<sub>2</sub>TbCu<sub>3</sub>O<sub>8</sub>," *J. Appl. Phys.*, in press.
- Yu, S-C., Lynn, J.W., Fish, G.E., "Spin Wave Stiffness Constants of the Amorphous Fe<sub>90-x</sub>Ni<sub>x</sub>Zr<sub>10</sub> (x = 5,10) Alloys", *Jpn. J. Appl. Phys.* 32, 67 (1993).
- Zhang, H., Lynn, J.W., "New Exact Solution of the One-Dimensional Schrodinger Equation and its Application to Polarized Neutron Reflectometry," *Phys. Rev. Lett* 70, 77 (1993).
- Zhang, H., Lynn, J., "Analytic Calculation of Polarized Neutron Reflectivity from Superconductors," *Phys. Rev. B*, in press.

## Patents

Apparatus for Identifying and Comparing Lattice Structures and Determining Lattice Structure Symmetries

Patent No. 5168457 - issue date 12/01/92

Vicky Lynn Karen and Alan D. Mighell

Apparatus and Methods for Identifying and Comparing Lattice Structures and Determining Lattice Structure Symmetries

Patent No. 5235523 - issue date 08/10/93

Vicky Lynn Karen and Alan D. Mighell

## Independent Programs

Aeppli, G., Broholm, C., "Magnetic Correlations in Heavy Fermion Systems: Single Crystal Neutron Scattering," Chapter in Handbook on the Physics and Chemistry of Rare Earths Lanthanide/Actinide Special Volumes, in press.

Allen, A.J., Gavillet, D., Weertman, J.R., "SANS and TEM Studies of Isothermal M<sub>2</sub>C Carbide Precipitation in Ultrahigh Strength AF1410 Steels," *Acta. Metall. Mater.* 41, 1869 (1993).

Almdal, K., Koppi, K.A., Bates, F.S., "Dynamically Sheared Body-Centered-Cubic Ordered Diblock Copolymer Melt," *Macromol.* 26, 4058 (1993).

Anderson, D.L., Cunningham, W.C., Alvarez, G.H., "Multielement Analysis of Foods by Neutron Capture Prompt  $\gamma$ -Ray Activation Analysis, *J. Radioanal. Nucl. Chem.* 167, 139-144 (1993).

Anderson, D.L., Cunningham, W.C., Lindstrom, T.R., "Concentrations and Intakes of H, S, K, Na, Cl and NaCl in Foods," *J. Food Comp. and Anal.*, in press.

Anderson, D.L., Mackey, E.A., "Neutron Scattering-Induced Background Enhancement Prompt-gamma Activation Analysis," *J. Radioanal. and Nucl. Chem. Articles* 167. 127-137 (1993).

Anderson, D.L., Kitto, M.E., McCarthy, L., Zoller, W.H., "Sources and Atmospheric Distribution of Particulate and Gas-Phase Boron," in press.

Axe, J., Broholm, C., Harshman, D.R., Hayden, S.M. Mook, H., Nagler, S., Osborn, R., Sokol, P., "Report from Condensed Matter Physics Working Group," in *Proc. of the Workshop on Scientific Opportunities at Future Spallation Neutron Sources*, Argonne National Lab., May 1993.

Balsara, N.P. Fetters, L.J., Hadjichristidis, N., Lohse, D.J., Han, C.C., Graessley, W.W., Krishnamoorti, R., "Thermodynamic Interactions in Model Polyolefin Blends Obtained by Small Angle Neutron Scattering," *Macromol.* 25, 6137 (1992).

- Balsara, N.P., Jonnalagadda, S.V., Lin, C.C., Han, C.C., Krishnamoorti, R., "Thermodynamic Interactions and Correlations in Mixtures of Two Homopolymers and a Block Copolymer by Small Angle Neutron Scattering," *J. Chem. Phys.*, in press.
- Barr, R.M., Clark, W.B., Clarke, R.M., Venturelli, J., Norman, G.R., Downing, R.G., "Regulation of Lithium and Boron Levels in Normal Human Blood-Environmental and Genetic Considerations," *J. Laboratory and Clinical Medicine* 121, 614-619 (1993).
- Becker, D.A., "Results of the ASTM Nuclear Methods Intercomparison on NIST Apple and Peach Leaves SRMs," *J. Radioanal. and Nucl. Chem. Articles* 168, 169-183 (1993).
- Becker, D.A., "Unique Quality Assurance Aspects of INAA for Reference Material Homogeneity and Certification," *Fresenius J. Anal. Chem.* 345, 298-301 (1993).
- Becker, D.A., Anderson, D.L., Lindstrom, R.M., Greenberg, R.R., Garrity, K.M., Mackey, E.A., "Use of INAA, PGAA and RNAA to Determine 30 Elements for Certification of an SRM: Tomato Leaves, 1573a," *J. Radioanal. and Nucl. Chem. Articles*, in press.
- Becker, D.A., "Errors and Interferences in the Determination of Chromium in Biological Materials by INAA," *Transactions of the American Nuclear Society* 67, 6-7 (1993).
- Becker, D.A., "Quality Assurance in NAA Intercomparisons: Effectiveness vs. Effort," *Transactions of the American Nuclear Society* 67, 10-11, (1993).
- Becker, D.A., "Determination of Platinum and Palladium in NIST Automobile Catalyst SRMs by INAA," *Transactions of the American Nuclear Society* 67, 169-170 (1993).
- Becker, D.A., "Use of a Robotic Sample Changer in Certification of Several Biological Reference Materials by INAA," Proc. of the International Conference on Nuclear Analytical Methods in the Life Sciences, in press.
- Bishop, R.L., "Compositional Analysis of Pre-Columbian Pottery: Research In The Maya Region," Archeometry of Pre-Columbian Sites and Artifacts, D. Scott and P. Mayers, Eds., Getty Research Institute, in press.
- Blaauw, M., Lindstrom, R.M., "Local Area Networks for Use In Neutron Activation Analysis: Advantages and Pitfalls," *J. Radioanal. and Nucl. Chem. Articles*, in press.
- Blackman, M.J., Stein, G.S., Vandiver, P.B., "The Standardization Hypothesis and Ceramic Mass Production: Technological, Compositional, and Metric Indices of Craft Specialization at Tell Leilan, Syria," *American Antiquity*, V. 58, 60-79, (1993).
- Blackman, M.J., "The Effect of Human Size Sorting on the Mineralogy and Chemistry of Ceramic Clays in Chemical Characterization of Ceramic Pastes in Archaeology," *Prehistory Press*, Madison, WI, edited by H. Neff, 113-124, (1992).

- Blackman, M.J., Vidale, M., "The Production and Distribution of Stoneware Bangles at Mohenjo-Daro and Harappa as Monitored by Chemical Characterization Studies in South Asian Archaeology," Prehistory Press, Madison, WI, edited by C. Jarrige, 37-43, (1992).
- Bode, P., Lindstrom, R.M., "Advanced Detector Systems: What Do They Have to Offer for Activation Analysis," J. Radioanal. and Nucl. Chem. 65 187-195 (1993).
- Carpenter, J.M., Cline, D.B., Lanza, R., Mildner, D. F. R. (editors), "Neutrons, X- Rays, and Gamma Rays: Imaging Detectors, Material Characterization Techniques, and Applications", SPIE Conference 1737 (1993).
- Carpenter, J. M., Mildner, D.F.R., "Improving the Resolution of Chopper Spectrometers at Pulsed Neutron Sources", Nucl. Instrum. & Meth. A325, 255 (1993).
- Carpio, R., Lamaze, G.P., Downing, R.G., "Advances in the Analytical Methodology Characterization of BPSG Films," J. of the Electrochem. Soc., in press.
- Chari, K., Antalek, B., Lin, M.Y., Sinha, S.K., "The Viscosity of Polymer-surfactant Mixtures in Water," J. Chem. Phys., in press.
- Chen, H., Heald, S. M., "Comparison of Grazing Angle Extended X-ray Absorption Fine Structure Obtained from Fluorescence and Reflectivity Measurements", J. Appl. Phys. 73, 2467 (1993).
- Chen, H., Mildner, D.F.R., Downing, R.G., Benenson, R.E., Xiao, Q.F, Sharov, V.A. "Neutron Focusing Using Capillary Optics", III European Conference on Accelerators in Applied Research and Technology, Orleans, France, August, 1993, Nucl. Instrum. Meth. B, in press.
- Chen, H., Downing, R.G., Mildner, D.F.R., Sharov, V.A., "Characterization of a Neutron Lens: Study of Capillary Optics," in SPIE Conf. Proc. 1738, C.F. Majkrzak and J. L. Woods, Eds., 395-404 (1992).
- Cheng, Yu-Tarng, "Autoradiographs of Paintings of Albert Pinkham Ryder" in Art Systems, a CD-ROM created by NARCISSE, the Network of Art Research Computer Image Systems, (EURITIS, Montigny, France), 1993.
- Chiba, M., Iyengar, G.V., Greenberg, R.R., Gills, T.E., "Determination of Tin in Biological Materials by Atomic Absorption Spectrophotometry and Neutron Activation Analysis," Sci. Total Environ., in press.
- Clarke, S.M., Melrose, J., Rennie, A.R., Ottewill, R.H., Heyes, R.H., Mitchell, D., Hanley, H.J.M., Straty, G.C., "The Structure and Rheology of Hard Sphere Systems," J. Phys. C, in press.

- Cox, J.N., Hwang, K., Kwok, K.W., Downing, R.G., Lamaze, G.P., "The Spatial Resolution of Water Diffusion and Trapping in Silicate-Glass Thin Films by Micro-FTIR and Neutron Depth Profiling," in Proc. of the 183rd Meeting of the Electrochemical Society, Honolulu, HI, in press.
- Crown, P.L., Bishop, R.L., "The Question Of Source. In Salado Polychrome Pottery: Ceramics and the Ideology of the Southwestern Cult, University of New Mexico Press, Albuquerque, in press.
- Cunningham, W. C., Anderson, D.L., Baratta, E.J., "Radionuclides in Domestic and Imported Foods in the United States 1987-1992, J. AOAC International, in press.
- Dadmum, M.D., Han, C.C., "A Neutron Scattering Study of a Lyotropic Polymer Under Shear near the Gel-point," ACS Polymer preprint 34, 733 (1993).
- Dadmun, M.D., Han, C.C., "The Behavior of a Hydrogen Bonding Molecular Composite," MRS Symposium 1993, in press.
- Dadmun, M.D., Muthukumar, M., Han, C.C., Hempelmann, R., Schwahn, D., Springer, T., "An Investigation of the Gelation of Poly( $\gamma$ -butyl L-glutamate) in Benzyl Alcohol Using Scattering Methods", Macromol., in press.
- Dewey, M. S., Kessler, E. G., Delattes, R. D., Sachetti, F., Petrillo, C., Freund, A., Borner, H. G., Robinson, S., Schillebeeck, P., "Structure Factors in Germanium at 0.342 MeV and 1.382 MeV," Phys. Rev. B, in press.
- Dewey, M. S., Gilliam, D. M., Snow, W. M., "Measurement of the Neutron Lifetime," in Weak and Electromagnetic Interactions in Nuclei, edited by Ts. D. Vylov, World Scientific, (1993), p. 44.
- Ditusa, J.F., Cheong, S.-W., Broholm, C., Aeppli, G., Rupp, Jr., L.W., Batlogg, B., "One Dimensional Spin Fluctuations in a Transition Metal Oxide," Proceedings of the LT20 meeting, Eugene, Oregon, August 1993, Physica B, in press.
- Douglas, C.B., Kaler, E.W., "Bilayer Phases in Aqueous Mixtures of n-Dodecylpenta-oxyethylene Glycol Monoether ( $C_{12}D_5$ ) and Sodium Decyl Sulfonate ( $C_{10}SO_3Na$ )," Trans. Faraday Soc., in press.
- Downing, R.G., Lamaze, G.P., "Neutron Depth Profiling Technique and Facilities," Neutron News 4, 15 (1993).
- Downing, R.G., Lamaze, G.P., Languard, J. K., Hwang, S.T., "Neutron Depth Profiling: Overview and Description of NIST Facilities," J. Res. Natl. Inst. Stand. Technol. 98, 1, 109-126 (1993).
- Downing, R.G., Iyengar, G.V., "Methodological Issues In The Analytical Determination of Boron," Environ. Health Perspect., in press.

- Downing, R.G., Zeissler, C.J., Chen, H., "High Resolution Charged Particle and Neutron Imaging Using Charge Injection Devices", in Neutrons, X Rays and Gamma Rays: Imaging Detectors, Materials Characterization Techniques and Applications edited by J.M. Carpenter, D.B. Cline, R. Lanza and D.F.R. Mildner, SPIE Conference 1737, (San Diego, July 1992), p. 308.
- Gilliam, D.M., Briesmeister, J.F., "Neutron Leakage Benchmarks for Water Moderators," in Reactor Dosimetry, ASTM STP 1228, American Society for Testing and Materials, Philadelphia, PA, in press.
- Gilliam, D.M., Lamaze, G. P., Dewey, M. S., Greene, G. L., "Mass Assay and Uniformity Tests of Boron Targets by Neutron Beam Methods, Nucl. Instr. and Meth. Phys. Res., A 334, 149 (1993).
- Gilman, P.A., Canouts, V., Bishop, R.L., "The Production and Distribution of Classic Mimbres Black-On-White Pottery," American Antiquity, in press.
- Graessley, W.W., Krishnamoorti, R., Balsara, N.P., Lohse, D.J., Schultz, D.N., Sissano, J.A., "Effect of Deuterium Substitution on Thermodynamic Interactions in Polymer Blends," Macromol. 26, 1137 (1993).
- Greenberg, R.R., "Accuracy in Standards Preparation for Neutron Activation Analysis," J. Radional. and Nucl. Chem. Articles, in press.
- Greenberg, R.R., "Chemistry Problems for the Analysis of Chromium by Radiochemical Neutron Activation Analysis," Transactions of the American Nuclear Society 67 (1993).
- Greene, G.L., Arif, M., Dewey, M.S., Snow, W.M., "Facilities for Fundamental Neutron Physics at the NIST Cold Neutron Research Facility," J. Res. Natl. Inst. Stand. Technol. 98, 135 (1993).
- Hamley, I.W., Koppi, K. A., Rosedale, J.H., Bates, F.S., Almdal, K., Mortensen, D., "Hexagonal Mesophases Between Lamellae and Cylinders in a Diblock Copolymer Melt," Macromol., in press.
- Han, C.C., Hoon, H., "Statics and Kinetics of Phase Behavior in Polymer Blends," NATAS Polymer Blends and Copolymer Symposium Proc, 1993, p. 22.
- Hanley, H.J.M., Straty, G.C., Lindner, P., "Partial Scattered Intensities from a Binary Suspension of Polystyrene and Silica," Langmuir, in press.
- Hanley, H.J.M., Straty, G.C., Tsvetkov, F., "A SANS Study of a Clay Suspension under Shear," Langmuir, in press.
- Hashimoto, T., Jinnai, H., Hasegawa, H., Han C.C., "SANS Studies of Space-Time Organization of Structure in Polymer Blends," International Symposium on Advanced Nuclear Energy Research: Neutrons as Microscopic Probes, March 1993.

- He, M., Hill, R.M., Scriven, L.E., Davis, H.T., "Phase Behavior and Microstructure of Polyoxyethylene-trisiloxane Surfactants in Aqueous Solution," *J. Phys. Chem.* 97, 882 (1993).
- Henrickson, R.C., Blackman, M.J., "Style and Paste: Investigating the Production of Godin III Buff Painted Ware in Chemical Characterization of Ceramic Pastes in Archaeology," Prehistory Press, Madison, WI, edited by H. Neff (1992).
- Heuser, B.J., Spooner S., Glinka, C.J., Gilliam, D.L., Winslow, N.A., Boley, M.S., "Structural Investigation of Electrochemically Etched Silicon," *Mat. Res. Soc. Symp. Proc.* 283, 209 (1993).
- Hight, S.C., Anderson, D.L., Cunningham, W. C., Capar, S.G., Lamont, W.H., Sinex, S.A., "Multimethod Analysis of Food and Mineral Supplements for Major, Minor and Trace Elements," *J. Food Composition and Analysis* 6, 121-139 (1993).
- Hobbie, E.K., Reed, L., Huang, C.C., Han, C.C., "Asymptotic Crossover in Polymer Blends," *Phys. Rev. E* 48, 1579 (1993).
- Hodge, M.G., Neff, H., Blackman, M.J., Minc, L.D., "The Regional Structure of Black on Orange Ceramics Production in the Aztec Empire's Heartland," *Latin American Antiquity*, 4, 130-157, (1993).
- Hodge, M.G., Neff, H., Blackman, M.J., Minc, L.D., "A Compositional Perspective on Ceramic Production in the Aztec Empire in Chemical Characterization of Ceramic Pastes in Archaeology," Prehistory Press, Madison, WI, edited by H. Neff, (1992).
- Huang, J.S., Fetters, L.J., Richter, D., Hadjichristidis, N., Farago, B., Gast, A.P., "Structure and Dynamics of the Diblock Co-Polymer Aggregates in Solution," in *Physics of Complex Fluids and Biological Systems*, edited by W. Sung, Y.H. Jeong, S.I. Choi, (Min Eum Sa Press, 1993), p. 75.
- Ings, S.G., Gilliam, D.M., "Characterization of the Gamma Field in the B&W Owners Group Cavity Dosimetry Benchmark Experiment, in Reactor Dosimetry, ASTM STP 1228, American Society for Testing and Materials, Philadelphia, in press.
- Iyengar, G.V., Wolf, W.R., Demiralp, R., Greenberg, R.R., "Mixed Total Diet Slurry as a Prospective Reference Material," *Fresenius Z. Anal. Chem.*, in press.
- Jinnai, H., Hasegawa, H., Hashimoto, T., Han, C.C., "Time Resolved Small-Angle Neutron Scattering Study on Self-Assembling Processes of Deuterated and Protonated Polybutadiene Blends via Spinodal Decomposition: 1. Effect of Initial Thermal Fluctuation," *J. Chem. Phys.*, in press.
- Karim, A., Singh, N., Sikka, M., Bates, F.S., Dozier, W.D., Felcher, G.P., "Ordering in Asymmetric Poly(ethylene-propylene)-Poly(ethylene) Diblock Copolymer Thin Films," *J. Chem. Phys.*, in press.

- Kline, S.R., Kaler, E.W., "Colloidal Interactions in Water/2-Butoxyethanol Solvents," *Langmuir*, in press.
- Koppi, K.A., Tirrell, M., Bates, F.S., "Shear-Induced Isotropic-to-Lamellar Transition," *Phys. Rev. Lett.* 70, 1449 (1993).
- Koppi, K.A., Tirrell, M., Bates, F.S., Almdal, K., Colby, R.H., "Lamellae Orientation in Dynamically Sheared Diblock Copolymer Melts," *J. Phys. II France* 2, 1941 (1992).
- Lamaze, G.P., Downing, R.G., Pilione, L., Badzian, A., Badzian, T., "Analysis of Boron in CVD Diamond Surfaces Using Neutron Depth Profiling," *Applied Surface Science* 65/66, 587-592 (1993).
- Lamaze, G.P., Downing, R.G., Bobyak, L., Pilone, L.J., and Messier, R., "Analysis of Cubic Boron Nitride Thin Films by Neutron Depth Profiling," *Diamond and Related Materials*, in press.
- Liberman, A. D., Albats, P. Pftzner, H., Stoller, C., Gilliam, D. M., "A Method to Determine the Absolute Neutron Output of Small D-T Generators, *Nucl. Instr. and Meth. Phys. Res.*,B 79, 574 (1993).
- Lin, M.Y., Sinha, S.K., Drake, J.M., Thiyagarajan, P., Wu, X.-l, Stanley, H.B., "SANS Studies of Fluid Phase Transitions in Porous Media," *J. Physique (Paris)*, in press.
- Lin, M.Y., Sinha, S.K., Drake, J.M., Wu, X.-l, Thiyagarajan, P., Stanley, H.B., "Study of Phase Separation of a Binary Mixture in Confined Geometry," *Phys. Rev. Lett.*, in press.
- Lindstrom, R.M., "SUM and MEAN: Standard Programs for Activation Analysis," *Biol. Trace Elem. Res.*, in press.
- Lindstrom, R.M., Zeisler, R., Vincent, D.H., Greenberg, R.R., Mackey, E. A., Stone, C.A., Anderson, D.L., Clark, D.D., "Neutron Capture Prompt Gamma-Ray Activation Analysis at the NIST Cold Neutron Research Facility," *J. Radioanal. and Nucl. Chem.* 167, 121-126 (1993).
- Lindstrom, R.M., "Prompt-Gamma Activation Analysis," *NIST J. Research* 127-133 (1993).
- Lindstrom, R.M., Paul, R.L., Vincent, D.H., Greenberg, R.R., "Measuring Hydrogen by Cold-Neutron Prompt-Gamma Activation Analysis," *J. Radioanal. and Nucl. Chem. Articles*, in press.
- Lindstrom, R.M., Fleming, R.F., Paul, R.L., Mackey, E.A., "The  $k_0$  Approach In Cold Neutron Prompt-Gamma Activation Analysis," edited by F. DeCorte, Proc. Internal  $k_0$  Users Workshop, Universiteit Gent, Belgium, 121-124 (1992).



- Lindstrom, R.M., Yonezawa, C., "Prompt-Gamma Activation Analysis with Guided Neutron Beams," edited by Z.B. Alfassi and C. Chung, in Prompt Gamma Neutron Activation Analysis, CRC Press, Boca Raton, FL (1993).
- Lindstrom, R.M., Paul, R.L., Walters, W.B., Molnar, G., "Analytical Applications of Cold Neutron Capture and Opportunities for Nuclear Physics", in Proc. 8th Int. Sym. on Capture Gamma-Ray Spect. and Related Topics, Fribourg (1993).
- Lindstrom, R.M., "Accuracy in Gamma Spectrometry: Pileup, Dead Time, and Fast Electronics," Transactions of the American Nuclear Society 68, 12 (1993).
- Lindstrom, R.M., Mackey, E.A., Paul, R.L., "Analytical Applications of Guided Neutron Beams," Biol. Trace Elem. Res., in press.
- Lowenthal, D.H., Borys, R.D., Stevens, R.K., Pinto, J.P., Ondov, J.M., "A Fine-Particle Sodium Tracer for Long-Range Transport of the Kuwaiti Oil-Fire Smoke," J. Geophys. Res. Letters, 20 691-693, (1993).
- Mackey, E.A., Gordon, G.E., Lindstrom, R.M., Anderson, D.L., "Use of Spherical Targets to Minimize Effects of Neutron Scattering by Hydrogen in Neutron Capture Prompt Gamma-Ray Activation Analysis," Anal. Chem. 64 2366-2371 (1992).
- Mackey, E.A., Copley, J.R.D., "Scattering and Absorption Effects in Neutron Beam Activation Analysis Experiments," J. Radioanal. & Nucl. Chem. 167, 127-132 (1993).
- MacDonald, C.A., Abreu, C.C., Budkov, S., Chen, H., Fu, X., Gibson, W.M., Kardiawarman, Karnaukov, A., Kovantsev, V., Ponomarev, I. Rath, B. K., Ullrich, J. B., Vartanian, M., Xiao, Q.F., "Quantitative Measurements of the Performance of Capillary X-ray Optics", in Multilayer and Grazing Angle X-Ray/EUV Optics II, edited R.B. Hoover and A.B.C. Walker, Jr., SPIE Conference 2011, (San Diego, July, 1993).
- McConnell, G.A., Gast, A.P., Huang, J.S., Smith, S.D., "Disorder-Order Transitions in Soft Sphere Polymer Micelles," Phys. Rev. Lett. 71, 2102 (1993).
- Mildner, D.F.R., Arif, M., Stone, C. A., Crawford, R.K., "The Neutron Transmission of Single-Crystal Sapphire Filters, J. Appl. Cryst. 26, 438 (1993).
- Mildner, D.F.R., Chen, H., "The Neutron Transmission through a Cylindrical Guide Tube," J. Appl. Cryst., in press.
- Mildner, D.F.R., Chen, H., Downing, R.G., Sharov, V.A., "Focused Neutrons: A Point to be Made," J. Neut. Res. 1, 1 (1993).
- Mildner, D.F.R., Chen, H., Magerl, A., Gruning, U., "Promise of Silicon Wafer Microguides for Future Neutron Optical Elements," Neutron Optical Devices and Applications, eds., C.F. Majkrzak and J.L. Wood, SPIE Conference 1738, (San Diego, July 1992), p. 377.

- Mildner, D.F.R., Chen, H., Downing, R.G., Benenson, R.E., Glinka, C.J., "Low Resolution Small-Angle Scattering using Neutron Focusing Optics," IX International Meeting on Small-Angle Scattering, (Saclay, France, April, 1993), J. Phys. Coll., in press.
- Mildner, D.F.R., "The Focal Length of Neutron Lenses Using Capillary Optics," J. Appl. Cryst., in press.
- Mildner, D.F.R., "Neutron Focusing Optics for Low Resolution Small-Angle Scattering," J. Appl. Cryst., in press.
- Morrison, F.A., Mays, J.W., Muthukumar, M., Nakatani, I., Han, C.C., "Shear Induced Morphological Structures in Triblock Copolymers," Macromol. 26, 5271 (1993).
- Morrison, F.A., Mays, J.W., Nakatani, A.I., Han, C.C., "Flow-Induced Effects in a Microphase-Separated Styrene-Butadiene-Styrene Triblock Copolymer," ACS Polymer Preprints 34, 678 (1993).
- Motowoka, M., Jinnai, H., Hashimoto, T., Qui, Y., Han, C.C., "Phase Separation in Deuterated Polycarbonate/Poly(methylmethacrylate) Blend Near Glass Transition Temperature," J. Chem. Phys. 99, 2095 (1993).
- Nakatani, A.I., Douglas, J.F., Ban, Y-B, Han, C.C., "A Neutron Scattering Study of Shear-Induced Turbidity in Polystyrene/Dioctyl Phthalate Solutions at High Shear Rates," ACS Polymer Preprints 34, 554 (1993).
- Nakatani, A.I., Morrison, F.A., Mays, J.W., Muthukumar, M., Han, C.C., "Time Dependent Small Angle Neutron Scattering Behavior in Triblock Copolymers Under Steady Shear," ACS Polymer Preprints 34, 630 (1993).
- Norman, B.R., Iyengar, V., "Determination of Iodine in Diverse Botanical and Dietary Matrices by Preirradiation Combustion Followed by Neutron Activation Analysis," Fresenius J. Anal. Chem., in press.
- Ondov, J. M., Divita, F., "Size-spectra for Trace Elements in Urban Aerosol Particles by Instrumental Neutron Activation Analysis," J. Radioanal. Nucl. Chem., 167, 247-258, (1993).
- Ondov, J.M., Divita, F., Quinn, T., Dodd, J., "Comparison of Size Spectra of Elements in Urban and Rural Aerosol," J. Aerosol Sic., 24 S9-S10, (1993).
- Paul, R.L. Lindstrom, R.M., "Determination of Hydrogen in Titanium Alloy Jet Engine Compressor Blades by Cold Neutron Capture Prompt Gamma-Ray Activation Analysis," Rev. Progr. Quant. Nondest. Eval., in press.
- Paul, R.L., Mackey, E.A., "Neutron Scattering by Hydrogen in Neutron Prompt Gamma Activation Analysis," J. Radioanal. and Nucl. Chem. Articles, in press.

- Paul, R.L., Lindstrom, R.M., Vincent, D.H., "Cold Neutron Prompt Gamma Activation Analysis at NIST-A Progress Report," J. Radioanal. and Nucl. Chem. Articles, in press.
- Poentiz, W. P., Carlson, A. D., "The Data Base of the Standards and Related Cross Sections after ENDF/B-VI," International Symposium on Nuclear Data Evaluation Methodology, Brookhaven National Laboratory, USA, edited by Charles L. Dunford, World Scientific Publishing Company, p. 75 (1993),
- Rabeony, M., Peiffer, D.G., Dozier, W.D., Lin, M.Y., "Evolution of Structure in a Graft Copolymer-Homopolymer Blend under Strain," *Macromol.* 26, 3676 (1993).
- Reents-Budet, D., Bishop, R.L., MacLeod, B., "Acercamiento integrado a la ceramica pintada Clasica Maya," In VI Simposio de Investigaciones Arqueologicas en Guatemala 1992, Juan Pedro Laporte, H. L. Escobedo and S. Villagran de Brady, Eds., Museo Nacional de Arqueologia y Etnologia, Guatemala City, pp. 71-114, (1993).
- Rothman, M.J., Blackman, M.J., "Monitoring Administrative Spheres of Action in Late Prehistoric Northern Mesopotamia with the Aid of Chemical Characterization (INAA) of Sealing Clays, in Economy and Settlement in the Near East: Analysis of Ancient Sites and Materials," Supplement to V.7, 1990, MASCA Research Papers in Science and Archaeology, Univ. of Penn., Philadelphia, PA, N.F. Miller, Ed., 19-45, (1992).
- Sakurai, S., Jinnai, H., Hasegawa, H., Hashimoto, T., "Microstructure Effects on the Equilibrium Phase Behavior of Elastomer Blends Studied by SANS," *ACS PMSE* 68, 278 (1993).
- Shuto, K., Oishi, Y., Kajiyama, T., Han, C.C., "Preparation of 2-Dimensional Ultra Thin Polystyrene Film by Water Casting Method," *J. Polym.*, Japan, in press.
- Singh, N., Tirrell, M., Bates, F.S., "Applications of Fourier Synthesis Methods to the Analysis of Specular Reflectivity," *J. Appl. Cryst.*, in press.
- Soni, K.D., Williams, D.B., Newbury, D.E., Chi, P., Downing, R.G., Lamaze, G.P., "Depth-distribution of Lithium in Oxidized Binary Aluminum-Lithium Alloys Determined by Secondary Ion Mass Spectrometry and Neutron Depth Profiling," *Corrosion* 49, 31 (1993).
- Stein, G.S., Blackman, M.J., "The Organizational Context of Specialized Craft Production In Early Mosopotamian States," *Research In Economic Anthropology*, B. Isaac, Ed., JAI Press, V14, 29-59, (1993).
- Stevens, R., Pinto, J., Mamane, Y., Ondov, J., Abdurlraheem, M., al-Majed, W., Sadek, M., Cofer, W., Ellenson, W., Kellogg, R., "Chemical and Physical Properties for Emissions from Kuwaiti Oil Fires," *Water Sci. Techn.*, 27 223-233 (1993).

- Swider, J.R., Mustillo, D.M., Conticchio, L.F., Walters, W.B., Paul, R.L., Lindstrom, R.M., "Gamma-Ray Cascades in the Te-128  $n,\gamma$  Reaction Observed in Coincidence Measurements," in 8th International Symposium on Capture Gamma-Ray Spectroscopy and Related Topics, Fribourg, Switzerland (September 1993).
- Wu, Z-Y., Han, M., Lin, Z.C., Ondov, J.M., "Chesapeake Bay Atmospheric Deposition Study, Year 1: Spatial and Temporal Trends in the Concentrations of Selected Elements in Aerosol Particles," Atmos. Environ., in press.
- Xiao, Q.F., Chen, H., Mildner, D.F.R., Downing, R.G., Benenson, R.E., "A Comparison of Experiment and Simulation for Neutron Guidance through Glass Polycapillary Fibers", Rev. Sci. Instrum. 64, 3252 (1993).
- Yajima, H., Hair, D.W., Nakatani, A.I., Douglas, J.F., Han, C.C., "Dynamic Light Scattering Study of a Diluted Polymer Blend Near Its Critical Point," Phys. Rev. B 47, 12268 (1993).
- Ziesler, R., Demiralp, R., Koster, B., Becker, P., Ostapczuk, P., Wise, S.A., "Determination of Inorganic Constituents in Marine Mammal Tissues," Science of the Total Environment, in press.
- Ziesler, R., Demiralp, R., Makarewicz, M., "High Count Rate Gamma Spectrometry: A Recent Experiment in High Accuracy NAA Applications," J. Radioanal. and Nucl. Chem. Articles, in press.
- Zirkel, A., Urban, B., Richter, D., Fetters, D.J., Huang, J.S., Kampmann, R., Hadjichristidis, N., "Small Angle Neutron Scattering Evaluation of the Temperature Dependence of Atactic Polypropylene and Poly(1-Butene) Chain Dimensions in the Melt," Macromol. 25, 6148 (1992).



